Artificial Reefs: Effects on Wave Transformation and In-Canopy Flow

Insights from Large-Scale Wave Flume Experiments of a Fringing Reef

MSc thesis

Kjell Albers

Delft University of Technology

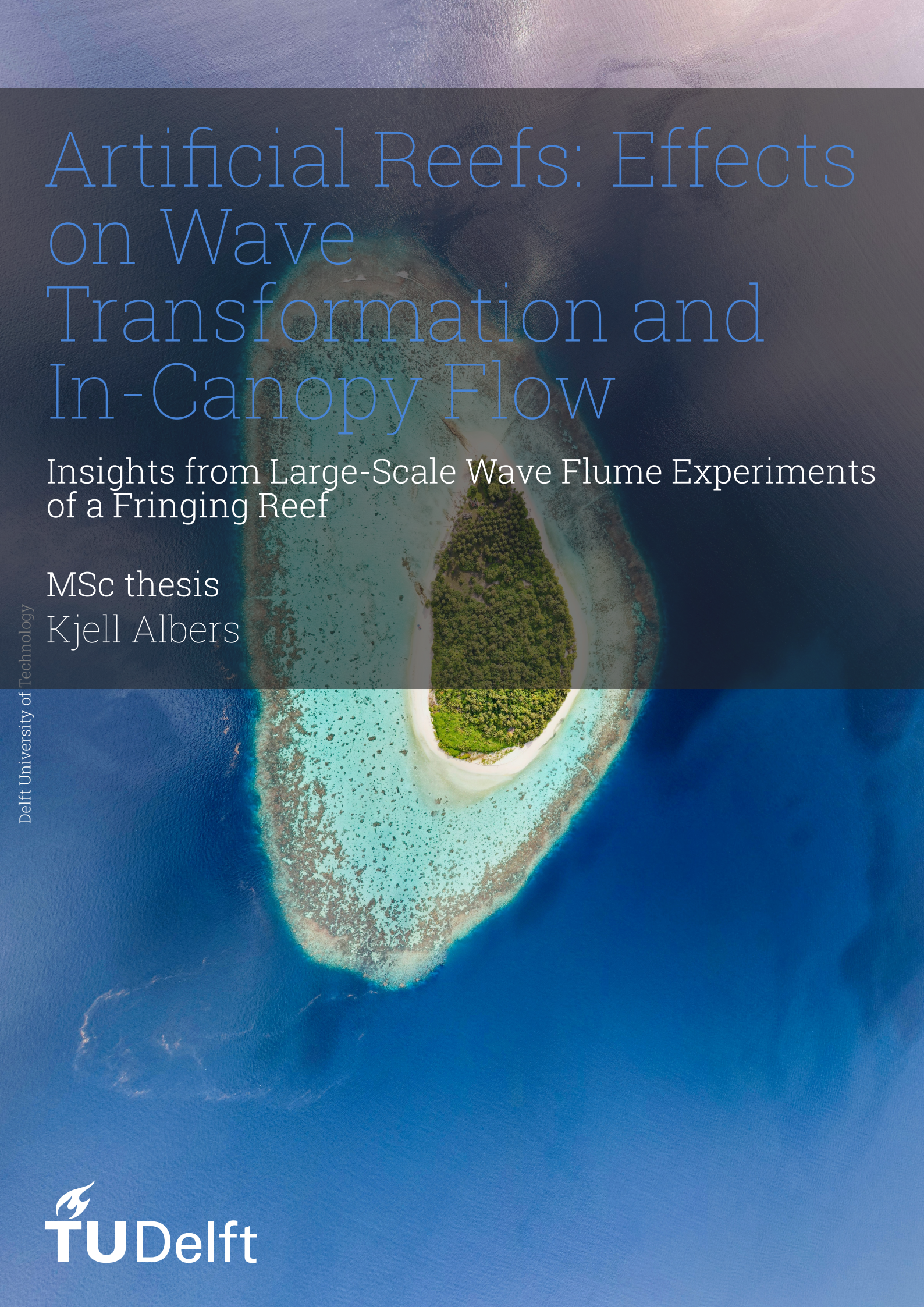

TU Delft

Artificial Reefs: Effects on Wave Transformation and In-Canopy Flow

Insights from Large-Scale Wave Flume Experiments of a Fringing Reef

by

Kjell Albers

Student Name	Student Number
K. Albers	4684850

Thesis committee:	Dr. M.F.S. Tissier	Delft University of Technology, chair
	Dr. ir. R.T. McCall	Deltares, daily supervisor
	Dr. ir. A.J.H.M. Reniers	Delft University of Technology
	Ir. F. Roelvink	Deltares
	Dr. ir. S.G. Pearson	Delft University of Technology
	Ir. S. Haage	Boskalis, external supervisor
Project Duration:	April, 2024 - February, 2025	
Faculty:	Faculty of Civil Engineering and Geosciences, Delft	

Cover: Unsplash, solitaroy atoll island by whosaynow

TU Delft

Preface

Before you lies my final work to obtain the title Master of Science in Hydraulic Engineering at the Faculty of Civil Engineering and Geosciences at Delft University of Technology. It also marks the end of my journey as a student at TU Delft. Along the way, many people have helped me and I'd like to take a moment to acknowledge them.

First and foremost, I would like to thank Marion, the chair of my committee, for her extensive guidance throughout my master's thesis. Working together on the wave flume experiments was a great experience and I will never forget your cheers when the first big waves started breaking on the forereef. To Ad, thanks a lot for the sharp questions you raised during the progress meetings and in the report feedback and of course for your help with installing the artificial reef elements. A lot of people came up with funny names for the elements, but your "stormtroopers" was definitely the most original. I would also like to thank Stuart Pearson for his positive energy and for emphasizing the obvious yet valuable reminder that "the best thesis is a finished thesis", which motivated me to finally wrap up things I had postponed for far too long.

I would like to thank Robert for giving me the opportunity to conduct this research at Deltares, which has been a great learning environment. Thank you for all the meetings during which you provided valuable discussions and feedback which has elevated the quality of my thesis. To Floortje, thanks a lot for always being available to brainstorm about my thesis. In many instances, your quick responses to data related issues really helped to streamline the process. I'd like to thank Samantha for her practical insights and for helping me see how this research connects to real-world applications at Boskalis.

To all other graduates and interns at Deltares, thanks for all the coffee breaks and shared laughs. To Vincent specifically, I had a great time working long hours at the Delta Flume together and braving the extreme sauna-like temperatures at the "snackbar" measurement station along the flume.

A huge thanks to the crew at the Hydraulic Engineering lab at TU Delft, Chantal, Arie, Arno and Pieter for making the experiments run so much smoother and always being solution-oriented. I'd also like to thank the Delta Flume team and all the others who helped during the experiments for their teamwork and dedication.

I would like to express my gratitude to my friends and family who supported me through my thesis and the rest of my studies. Big thanks to Jorrit and Johannes for making my report look way more aesthetic and providing the soundtrack to my thesis. To Daan, having you by my side throughout my thesis made everything so much more enjoyable. To my dad, despite your disappointment in discovering that I don't share your deep love for concrete, you've always supported me with great enthusiasm, and that has meant the world to me. To my sister, it was great sharing the experience of finishing our master's at TU Delft at the same time. Even though you were just one step ahead in the end, I'm proud that we'll soon be able to call ourselves the first engineers in our family. To mom, though you're not here with us, you are with me in my heart. I hope I'm making you proud.

Kjell Albers
Delft, February 2025

Abstract

Coral reefs provide vital coastal protection and ecosystem services but face growing threats from sea-level rise, warming seas, and ocean acidification. Coral reef restoration is proposed as a measure to reduce coastal hazards, yet there is currently insufficient evidence from field studies or appropriately scaled laboratory experiments to substantiate this claim. In particular, understanding the flow structure within such reef restorations is paramount as the rate at which wave energy is dissipated by a coral canopy is closely linked to this flow structure. Neglecting this flow in numerical models can lead to inaccuracies in predicting both wave dissipation and water level changes.

This thesis analyzes data from large-scale wave flume experiments conducted at Deltares' Delta Flume. The setup, a 1:3 scaled model of a Maldivian fringing reef, was tested under five wave conditions and two water levels. On a 45-meter wide reef flat, a 10-meter stretch was equipped with either 91 or 153 3D-printed artificial reef elements (0.25m high, 0.40m wide). Pressure sensors and flow meters measured wave transformation and dissipation, while two ADV arrays studied in-canopy flow. These CREST experiments, conducted with Plymouth University, Deltares, Boskalis, and Coastruction, extend the ARISE project, which investigates atoll island adaptation to sea-level rise.

This thesis addresses four main objectives: (a) examining the artificial reef's impact on wave transformation, frequency dependence, and water level response, (b) identifying in-canopy flow characteristics, (c) linking these characteristics to observed wave dissipation, and (d) evaluating an existing in-canopy flow model for accuracy.

As the relative height of the artificial reef decreases with rising water levels, its wave height reduction capacity declines, ranging from 8.5% to 15.2% at low water levels and 4.9% to 5.9% at high water levels. Although this reduction in incoming wave height, the placement of artificial reefs can still increase rather than decrease the onshore extreme water levels under specific forcing conditions, likely due to the artificial reef-induced drag force increasing wave setup.

The observed streamwise velocity variance differs considerably depending on the location of the ADV array. The total velocity variance decreases more in the ADV array behind the artificial reef elements than in the ADV array between the elements, where SS velocity variance even increases. Flow attenuation is observed to be higher at low water levels than high water levels, with longer and higher waves being attenuated more effectively than shorter and lower waves. The canopy wave dissipation rate modeled with the in-canopy flow theorem of Lowe et al. (2005b) is 43 - 87% lower than the dissipation added by the artificial reef but remains within the same order of magnitude. Particularly at higher frequencies, the modeled canopy dissipation rate is lower as it does not account for breaker dissipation. Another factor contributing to the discrepancy between modeled and observed dissipation per wave component is that the observed dissipation includes non-linear energy transfers, which are not included in the in-canopy flow model. The selection of ADVs for representing in-canopy flow has little impact on calculated flow attenuation and modeled canopy dissipation rates, whereas applying a flow convergence correction does considerably increase flow attenuation and decrease canopy dissipation rates.

According to the canopy flow classification by Lowe et al. (2005b), the tested runs fall between inertia-dominated and general flow. Reducing element spacing would push the flow more into the general flow regime, which would increase the frequency dependence of flow attenuation and wave dissipation.

Given its limited wave height reduction capacity, an artificial reef like this would be more effective as part of hybrid strategies. When combined with other coastal protection measures, these artificial reefs could be valuable in both providing coastal protection and improving ecology. All in all, the CREST experiments provide a valuable core dataset for model calibration and validation on reef island hydrodynamics as well as expanding our knowledge of reef nearshore hydrodynamics and its relation with in-canopy flow dynamics.

Contents

Preface i

Summary ii

Nomenclature v

1 Introduction 1

2 Theory 5
- 2.1 Reef characteristics & restorations . . . 5
  - 2.1.1 Coral ecology . . . 5
  - 2.1.2 Reef geometry and composition . . . 5
  - 2.1.3 Hydraulic and environmental conditions . . . 7
  - 2.1.4 Reef restoration . . . 8
- 2.2 Reef structural complexity & in-canopy flow . . . 9
  - 2.2.1 Canopy flow regimes . . . 11
  - 2.2.2 Canopy-induced wave dissipation . . . 13
  - 2.2.3 In-canopy measurements . . . 14
  - 2.2.4 Canopy parameters . . . 14
- 2.3 Reef hydrodynamics . . . 15
  - 2.3.1 Wave setup . . . 16
  - 2.3.2 Sea-swell (SS) waves . . . 17
  - 2.3.3 Infragravity (IG) waves . . . 17

3 Methodology 21
- 3.1 Research context . . . 21
- 3.2 Physical model . . . 22
- 3.3 Instruments . . . 30
  - 3.3.1 ADV placement . . . 32
  - 3.3.2 Pressure sensor (PS) . . . 37
  - 3.3.3 Electromagnetic flow meter (EMF) . . . 37
- 3.4 Data quality assessment . . . 37
  - 3.4.1 ADV data quality metrics . . . 37
  - 3.4.2 ADV data quality assessment . . . 38
  - 3.4.3 PS data quality . . . 40
- 3.5 Data processing . . . 42
  - 3.5.1 Timeseries filtering . . . 42
  - 3.5.2 Pressure to surface elevation . . . 44
  - 3.5.3 Separation incoming and outgoing waves . . . 45
  - 3.5.4 Measured velocity to depth averaged velocity . . . 46
- 3.6 Wave parameter calculation . . . 47
  - 3.6.1 Spectral characteristics . . . 47
  - 3.6.2 Wave non-linearity . . . 48
  - 3.6.3 Flow velocity attenuation . . . 48
  - 3.6.4 Wave dissipation rate or energy flux gradient . . . 50
  - 3.6.5 Extreme water level analysis . . . 51

4 Results 53
- 4.1 Results from PS and EMF measurements . . . 53
  - 4.1.1 Wave transformation . . . 53
  - 4.1.2 Effect of artificial reef on incoming wave height and mean water level . . . 56

4.1.3 Incoming wave energy reduction across artificial reef stretch . . . 58
4.1.4 Evolution of incoming energy density spectrum . . . 59
4.1.5 Wave dissipation rate . . . 62
4.1.6 Extreme water level analysis . . . 65
4.2 Results from ADV measurements . . . 67
4.2.1 Vertical velocity variance profiles . . . 67
4.2.2 Observed flow attenuation . . . 70

5 Discussion **74**
5.1 Potential drivers of increased wave setup and extreme water levels . . . 74
5.1.1 One-dimensional model simplification . . . 79
5.2 Comparing observed artificial reef effectivity with literature . . . 79
5.3 Linking observed dissipation to in-canopy flow using in-canopy flow theorem . . . 80
5.3.1 Modeled in-canopy wave dissipation . . . 80
5.3.2 Comparison to observed wave dissipation . . . 82
5.3.3 Spectral comparison to observed wave dissipation . . . 83
5.3.4 Flow attenuation comparison with in-canopy flow theory . . . 85
5.4 Limitations of the physical model . . . 87
5.4.1 Scale effects . . . 87
5.5 Limitations of data analysis methods . . . 88
5.5.1 ADV placement and representative flows . . . 88
5.5.2 Neglecting non-linear energy transfers . . . 92
5.6 Data quality and availability . . . 93

6 Conclusion & Recommendations **96**
6.1 Conclusions . . . 96
6.2 Recommendations . . . 99
6.2.1 Practical recommendations or implications . . . 99
6.2.2 Extending on or improving of the CREST experiments . . . 100
6.2.3 Conducting numerical modeling . . . 100
6.2.4 Performing field measurements . . . 101

A Lab experiments **108**

B Data processing techniques **115**
B.1 Fast Fourier Transform . . . 115
B.2 Wave number calculation . . . 116
B.3 Propagation of confidence intervals . . . 116

C Pressure sensor datasets **117**

D ADV results & data quality **119**

E Energy decrease and flow attenuation per wave component **128**
E.1 Wave energy decrease across artificial reef per wave component . . . 129
E.2 Flow attenuation per wave component . . . 131

Nomenclature

Abbreviations

Abbreviation	Definition
ADV	Acoustic Doppler Velocimeter
CREST project	'Coral reef RESToration to reduce island flooding' project
FFT	Fast Fourier Transform
IG	Infragravity (waves)
PS	Pressure Sensor
EMF	Electromagnetic Flow Meter
SS	Sea-Swell (waves)
RMS	Root mean square
SNR	Signal-to-noise ratio
Re	Real part

Symbols

Symbol	Definition	Unit
A_c	Open cross-section in artificial reef	[m^2]
A_f	Artificial reef element frontal area	[m^2]
A_p	Artificial reef element plan area	[m^2]
A_∞^{rms}	RMS orbital excursion length	[m]
C_D	Canopy drag coefficient	[-]
C_M	Canopy inertial coefficient	[-]
C_f	Canopy friction coefficient	[-]
c	Wave celerity	[m/s]
c_g	Wave group celerity	[m/s]
c_f	Bottom friction coefficient	[-]
D	Artificial reef element diameter	[m]
D_n	Nominal artificial reef element diameter	[m]
E	Energy density	[J/m^2]
$E_{uu}(f)$	Flow energy density spectrum	[m^4/s]
$E_{\eta\eta}(f)$	Wave energy density spectrum	[J/Hz]
f	Frequency	[Hz]
f_p	Peak frequency	[Hz]
f_e	Energy dissipation factor	[-]
F_c	Canopy-induced drag force	[N]
F_N	Nyquist frequency	[Hz]
F_S	Sampling frequency	[Hz]
GF	Groupiness factor	[GF]
g	Gravitational acceleration	[m/s^2]
h_0	Still water level	[m]
h_c	Canopy height	[m]
H_s	Significant wave height	[m]
H_{m0}	Significant (spectral) wave height	[m]
H_{IG}	Significant IG wave height	[m]

Symbol	Definition	Unit
H_{SS}	Significant SS wave height	[m]
I	In-canopy flow energy index	[-]
λ_f	Frontal area parameter	-
λ_p	Plan area parameter	-
k	Wave number	$[m^{-1}]$
K_p	Permeability	$[m^2]$
K_t	Transmission coefficient	[-]
m_0	Zeroth spectral moment	$[m^2]$
m_1	First spectral moment	$[m^2Hz]$
m_{-1}	First negative spectral moment	$[m^2/Hz]$
μ	Kinematic viscosity	$[m^2/s]$
n	Porosity	[-]
n_L	Spatial scaling factor	[-]
n_T	Temporal scaling factor	[-]
η	Free surface elevation	[m]
$\bar{\eta}$	Mean free surface elevation (setup)	[m]
ϵ_c	Modeled canopy wave dissipation rate	[J/s/m^2]
ϵ	Observed wave dissipation rate	[J/s/m^2]
ϵ_i	Observed wave energy flux gradient per wave component	[J/s/m^2/Hz]
α_w	Flow attenuation parameter	[-]
α_w^R	Representative flow attenuation parameter	[-]
$\alpha_{w.i}$	Flow attenuation parameter per wave component	[-]
ω	Angular frequency	[rad/s]
Q	Discharge	$[m^3/s]$
R	Reynolds number	[-]
ρ	Density	[kg/m^3]
S	Artificial reef element spacing	[m]
S_{xx}	Cross-shore radiation stress	[]
$S_{\eta\eta}(f)$	Wave variance density spectrum	$[m^2/Hz]$
T_p	Peak wave period	[s]
T_{m0}	Mean wave period	[s]
$T_{m-1.0}$	Mean wave frequency	[s]
U	Depth-averaged flow velocity	[m/s]
u	Point measured flow velocity	[m/s]
U_c	Spatially averaged in-canopy flow velocity	[m/s]
U_∞	Free-stream velocity	[m/s]
f	Frequency	[Hz]
$S_{\eta\eta}(f)$	Wave variance density spectrum	$[m^2/Hz]$
f_p	Peak frequency	[Hz]
F_N	Nyquist frequency	[Hz]
F_S	Sampling frequency	[Hz]

1

Introduction

Coral reefs, although covering only 0.2% of the ocean floor, support a remarkable diversity of marine life, estimated to encompass about 25% of known marine species (Cesar et al., 2003). Beyond their biodiversity, coral reefs offer valuable ecosystem services. For instance, they serve as critical sea-life spawning grounds utilized by fisheries, thereby providing nutrition and livelihood for millions of people, generating approximately $6.8 billion in annual revenues (Cesar et al. (2003); (Burke et al., 2011)). Additionally, countries with coral reefs attract substantial tourism, contributing an extra $35.8 billion in net benefits annually (Spalding et al., 2017). Moreover, coral reefs play a crucial role in coastal protection, safeguarding approximately 150,000 kilometers of shoreline resulting in a damage reduction of around $4 billion each year. Without these reefs, coastal flooding damages are projected to double (Beck et al., 2018).

One of the territories most vulnerable to this coastal flooding are coral reef islands, which are characterized by maximum elevations below 4 meters and average elevations of less than 2 meters above mean sea-level. With sea levels projected to rise faster in tropical regions, wave-driven flooding events are expected to become more frequent and increase in severity (Storlazzi et al., 2018). Contrary to popular belief, the primary threat is not the direct material damage due to inundation and wave impact, but rather the stress on the drinking water supply for which most coral island are dependant on groundwater contained in ”fresh groundwater lenses” (White and Falkland, 2010). Studies have demonstrated it is the salinisation of these freshwater aquifers caused by increased wave-driven flooding which will result in these islands becoming uninhabitable (Storlazzi et al., 2018).

Coral reefs reduce wave energy and therefore wave-driven flooding both by wave breaking near the reef crest and frictional dissipation on the reef slope and reef flat (Massel and Gourlay, 2000). Ferrario et al. (2014) suggests that reef crests, on average, attenuate 86% of the incident wave energy and reef flats dissipate the remaining wave energy by an average of 65%. However, feedback mechanisms between offshore boundary conditions, water levels and reef geometry and roughness can alter these ratios and even induce wave resonance which can make wave run-up difficult to predict (Monismith, 2007).

Coral reefs and its coastal protection services are under threat from local anthropogenic disturbances like vessel grounding, overfishing and nutrient loading which local effects are generally detrimental but of relatively minor impact compared to the consequences of persistent global stressors such as sea-level rise (SLR), increasing sea temperatures and ocean acidification (Pandolfi et al., 2011). These stressors are responsible for the average annual decline in coral cover of 1-2% over the last decades (Bruno and Selig, 2007). Within this decline in coral cover, significant fluctuations can be discerned which are depicted in Figure 1.1. Global coral bleaching events in 1998, 2009 and 2014, destroying 8%, 7% and 7% of coral cover worldwide, are alternated with periods of moderate recovery (Souter

et al., 2020) which underlines that not all is lost for the world's coral reefs.

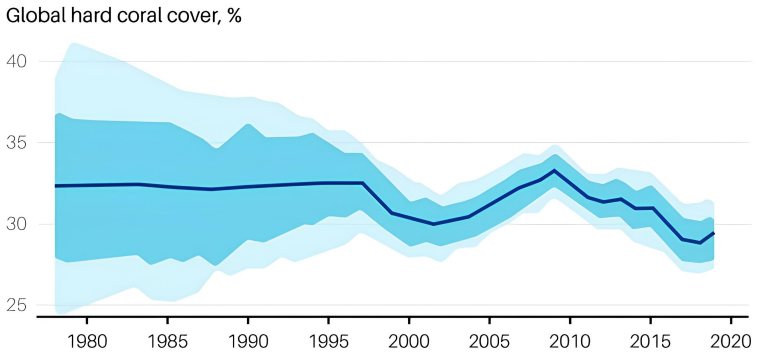

Figure 1.1: Decline in coral cover worldwide with clear periods of coral bleaching alternate with periods of recovery. Source: (encyclopedia, 2006)

A possible intervention, coral reef restoration, is increasingly being suggested and is expected to reduce coastal hazards (Rinkevich (2014), Rinkevich (2008)). Yet, there is currently a lack of evidence from field studies or appropriately scaled laboratory experiments to support this claim.

A review of Fabian et al. (2013) on reef restoration projects found that a vast majority of 90% of restorations were designed specifically for ecological value and found little quantitative information on coastal protection services. Due to costs and operational constraints, coral restorations are typically of limited spatial extent. This makes it crucial to understand which location, size and roughness of these relatively local modifications contributes most to reducing wave-driven flooding to ensure allocation of limited funds in the places where it will have most impact.

As of now, the few studies investigating the effect of coral restoration on wave-driven flooding were based on numerical modeling as in-field experiments modifying the coral cover are hard to perform. Numerical studies by Roelvink et al. (2021) and Storlazzi et al. (2021), investigating the effect of coral restoration on wave-driven flooding, indicate that the greatest wave-driven flooding reduction could be achieved with shallower coral restorations on the upper fore reef and reef flat. However, these studies opt for a highly schematized parametrization of the coral canopy, representing it as an impermeable local bed level increase in combination with a high friction coefficient allowing no interaction between wave-induced oscillatory flows and the complex coral canopy. (Lowe et al., 2007) stated that the rate at which wave energy is dissipated by a coral canopy is closely linked to the flow structure within the canopy. While modeling wave transformation, neglecting this in-canopy flow not only results in a different response in wave dissipation, but also affects the resulting water level response in terms of wave setup (van Rooijen et al. (2016), Buckley et al. (2018)). Several studies are conducted considering in-canopy flow (de Ridder (2018), Buckley et al. (2022)). However, these studies did not focus on reef restoration, which underlines the relevancy of this topic.

The CREST project, an initiative led by Delft University of Technology, aims to create a core dataset on the hydrodynamic response of a fringing reef environment including artificial reef elements installed on the reef flat. This data provides opportunity to analyze the interaction between wave-induced oscillatory flows and the complex coral canopy and its resulting wave dissipation and water level response. The aim of this analysis is to better understand the extent of this wave dissipation and water level response and its relation to in-canopy flow dynamics as a result of changing canopy density and hydrodynamic conditions, which is encapsulated in the main research question of this study:

How do artificial reefs with two different densities affect nearshore hydrodynamics and how does this relate to in-canopy flow as observed in large-scale wave flume experiment of a fringing reef?

To clarify this main research question a subdivision of 4 sub-questions is made accompanied by corresponding objectives:

1. What is the effect of an artificial reef restoration on wave transformation, its frequency dependence and resulting water level response?
2. What are the observed in-canopy flow characteristics?
3. How do the in-canopy flow characteristics relate to the observed wave dissipation?
4. How does the observed wave dissipation relate to existing in-canopy flow theory?

2

Theory

The objective of this theory chapter is to get a better understanding of the existing research on this topic and its underlying theoretical framework and identify possible knowledge gaps for further research. This chapter is divided into four sections. The first section focuses on the characteristics of coral and its environmental conditions, the components of a typical fringing reef, and the types of reef restoration projects that have already been carried out. The second section goes into depth on how the characteristics of a coral canopy can be quantified into parameters, and how these parameters aid in modeling the flow within the canopy and its effect on the depth-averaged flow. In the third section, the typical hydrodynamics and wave transformation over a fringing reef is described.

2.1. Reef characteristics & restorations

2.1.1. Coral ecology

Corals are the result of an intricate symbiotic relationship between coral polyps and dinoflagellate algae. A multitude of coral polyps, which are genetically identical sac-like animals, together form a coral ”group”, also referred to as a colony (Murphy, 2003). Each polyp excretes calcium carbonate near the base, eventually forming a hard exoskeleton. Typically, coral polyps harbor algae of the genus Symbiodinium, with which a mutualistic symbiotic relationship is formed. These algea supply corals with products of photosynthesis as well as benefiting corals by aiding calcification and waste removal. In turn, the algea benefit from a sheltered habitat and consumption of the polyp's carbon dioxide, phosphate and nitrogenous waste (Muscatine and Porter, 1977). The algae symbionts' photosynthetic systems experiences stress from rising sea temperatures and acidification caused by higher atmoshperic pCO_2, which results in overproduction of oxygen radicals damaging the algea symbionts and their coral hosts. As a result, the symbiotic algae are expelled as this increases the polyp's chance of surviving short-term stress. This leaves the corals without the characteristic yellow-brown pigmentation, hence the term coral bleaching (Goreau, 1964). As highlighted in the introduction, coral reefs have faced significant mass bleaching events in the last decades, but have proven able to bounce back. This resilience is reinforced by findings of Jones (2008), indicating that 71% of coral colonies transitioned their algae communities to more heat-tolerant types after bleaching events.

2.1.2. Reef geometry and composition

Darwin (1836), during his voyage on the Beagle, was the first to suggest atoll islands and its coral reefs develop within three distinct stages as can be seen in Figure 2.1. To this day, this theory is still in use to classify coral reefs and can be broken down in the following stages:

1. **Fringing reef**: These reefs extend straight from the shoreline of mid-ocean volcanic islands and can therefore be identified by its close proximity to the shoreline. With this geometry, waves tend to break relatively far onshore while the narrow lagoon dissipates little wave energy.
2. **Barrier reef**: While the coral reef is vertically accreting, the volcanic island subsides due to erosion and direct land subsidence eventually leaving a deeper and wider lagoon which is encircled

or bordered by the barrier reef.

3. **Atoll**: With full inundation of the volcanic island, only the coral rim is intact, leaving an atoll island encircling a deep lagoon.

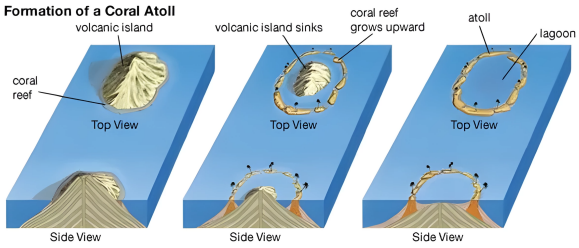

Figure 2.1: Development of coral reef stages. Source: encyclopedia (2006)

As coral reefs often reside on the edge of the continental shelf they form a steep transition from deep to shallow water. From offshore to onshore, the morphology of most reefs comprise of three main elements as can be seen in figure 2.2:

1. A steep fore reef, where waves shoal, refract and occasionally break. The fore reef is characterized by spurs (high elevation) and grooves (low elevation) (Kendal et al., 2001) which drive Lagrangrian circulation cells resulting in low-sediment, nutritious water being transported from ocean to reef and coral debris and sediment from reef to ocean (Rogers et al., 2013).
2. A reef crest, which emerges above the waterline during low tide and is most exposed to wave action. Wave dissipation here is dominated by depth-limited wave breaking and attenuates on average 86% of incident wave energy (Ferrario et al., 2014). The ecology of the reef crest is highly adapted and ranges from densely clustered coral colonies for moderate wave action to merely fast growing algae covering the calcareous crest in severe wave climates (NOAA, 2023).
3. A reef flat, lying sheltered behind the reef crest. The shallow nature of the reef flat leads to high temperatures and salinity, reducing the amount of coral on the reef flat (Chappell, 1980). Wave dissipation on the reef flat is dominated by frictional dissipation and dissipates the remaining wave energy with 65% on average. The width and roughness of the reef flat highly influences the actual amount of wave dissipation (Ferrario et al., 2014).

For fringing reefs, the most common reef type, the lagoon is either non-existent or very shallow and narrow as the reef flat extends further to the coastline. In the coral reef schematization implemented in this report, the lagoon is assumed to be non-existent as the reef flat is connected directly to the coastline.

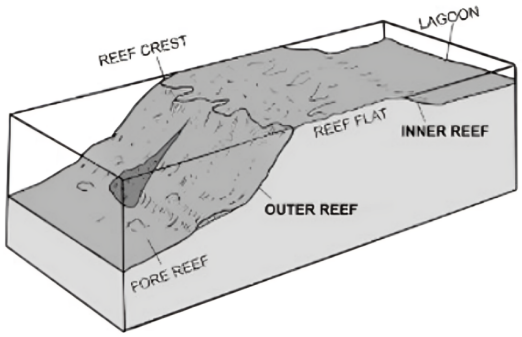

Figure 2.2: General classification of reef zones. Source: encyclopedia (2006).

Roelvink et al. (2021) subdivided a large dataset of 30.000 coral reef transects in four main characteristic reef profile types. These four types are classified as fringing reefs, convex reefs, linear reefs and three-slope reefs. In figure 2.3 . Within these profile classifications the following variability occurs:

1. fringing reef: reef flat width = (100 - 250 m), fore reef slope = (0.1 - 0.5)
2. convex reef: reef flat width = (100 - 250 m), fore reef slope = 0.1
3. linear reef: fore reef slope = (0.025, 0.1, and 0.5)
4. three-slope reef: shelf width = (100 and 250 m), offshore and nearshore slope = (0.1 and 0.5)

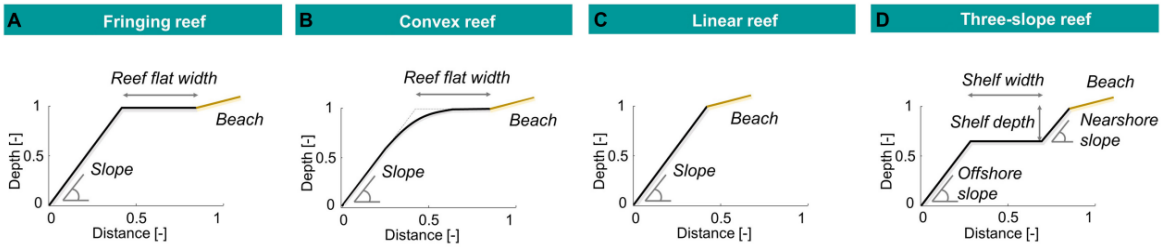

Figure 2.3: Main classifications of reef profile types according to Roelvink et al. (2021).

Besides the variation in reef geometry, a single reef can hold numerous coral species. The roughness of the reef and thereby frictional wave energy dissipation is determined by the coral species growing on it. A study by Chappell (1980) indicated that the degree of structural complexity is primarily determined by light intensity (and thus depth) and exposure to waves. Next to this, sediment concentration and subaerial exposure (exposure to air) are also of influence. To reflect on the reef zones in figure 2.2, on the fore reef branching corals dominate for shallow depths and more spherical species persist in deeper sections. On the reef flat and crest, branching corals are present in deeper parts but cannot persist in areas on the reef flat that emerge during low tide. Plate-like corals are better adjusted to this subaerial exposure and dominate shallow areas of the flat.

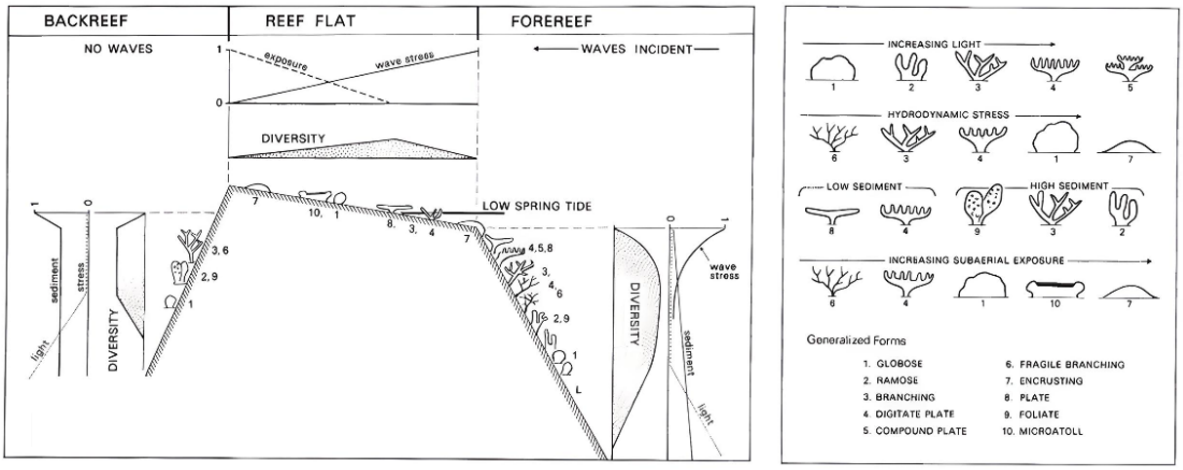

Figure 2.4: Zonation of different coral species on reef according to (Chappell, 1980).

2.1.3. Hydraulic and environmental conditions

Corals mostly exist in areas where the sea-surface temperatures are above 17-18 ◦C and below 33-34 ◦C for prolonged periods (Kennedy and Woodroffe, 2002). Due to narrow continental shelves on which coral reefs reside, storm surge is usually limited. However, significant wave height is high due to the virtually unlimited fetch on open ocean (van Dongeren, 2020). At the Maldives, the location of the island of Fiyoaree on which the island prototype is based, waves are predominantly from South-West ($205°$). Typical extreme wave conditions on the Maldives consist of a significant wave height H_s of 3 meters and a relatively long peak wave period T_p of 15 seconds, indicating remote swell waves. In addition to this, atolls in the Pacific Ocean are exposed to extreme wave conditions caused by cyclones with waves reaching a significant wave height H_s of 4.5 meters and a peak wave period T_p of 9 seconds.

The tidal climate of the Maldives can be classified in the micro-tidal regime with a semi-diurnal tidal cycle, with mean spring tidal ranges between 0.7 and 0.96 meters.

2.1.4. Reef restoration

Generally, reef restorations are either purely ecological in nature or involve the addition of artificial structures to provide more stable substrates for coral settlement. The purely ecological efforts, often termed “green” restorations, focus on repopulating reefs where coral populations have been decimated. In these cases, the areas targeted for restoration already have substrate properties suitable for coral attachment, so no artificial structural support for substrate stability is necessary (Shaver and Silliman, 2017). A review by Boström-Einarsson et al. (2020) recognizes three main methods of ’green’ restorations: (1) ’direct transplantation’ in which coral fragments are moved from a donor to recipient reef, (2) ’coral gardening’ where small fragments are raised in intermediate nurseries prior to out-planting on restoration sites and (3) ’micro-fragmentation’ in which fragments are cut from slowly growing encrusting corals are cut and mounted on tiles. Out-planting in micro-fragmentation is performed by securing micro-fragments to reef substrate after which a larger colony is formed by fusing of the fragments. Respectively, these three methods consist of 20%, 48% and 5% of the restorations covered in this review, with coral survival rates of 64%, 66% and 99%. Structural, or ”gray,” restorations utilize materials such as natural rocks, coral rubble, or metal and concrete structures to create reef roughness and stable substrates. These additions are designed to dissipate wave energy and provide habitats for corals and other reef organisms. If the structural restoration provides a suitable substrate for coral polyps to attach on, corals can be out-planted resulting in a ’gray-green’/hybrid restoration. Suitable substrate is considered to be consolidated matter while containing slight pores for coral polyps to anchor onto. Limestone occurring on coral reefs naturally has these desired properties (Madin and Madin, 2015). Without addition of artificial structures, substratum stabilization can be achieved either with mesh netting or electrical enhancement to encourage precipitation of calcium and magnesium (Boström-Einarsson et al., 2020).

Boström-Einarsson et al. (2020) also found that most restoration projects are of limited spatial extent, with a median restored area size of 100 m^2 composed of 10s of meters in alongshore direction and a few meters in cross-shore direction. This underlines the urgency to get a deeper understanding of these to optimize the potential benefits of these limited stretches of restoration. Coral restoration projects focused primarily (59% of studies) on out-planting fast-growing branching coral species. The limited spatial extent of these restorations underlines the urgency to get a deeper understanding of

Examples of artificial reefs are Reef Ball and MOSES, both designed to act as a habitat for marine life but oftentimes dissipating less energy then conventional submerged breakwaters due to limited structural complexity and thereby roughness. Many other artificial reef modules are currently being developed, like Coastruction units, which will be used in the CREST experiments. The three aforementioned artificial reef units can be seen before and some time after deployment in figure 2.5.

(a) Coastruction reef module

(b) MOSES reef module

(c) Reef Ball reef module

(d) Coastruction reef module deployed at Oostvoorne

(e) Deployed MOSES reef module

(f) Coral covered reef Ball reef module

Figure 2.5: Three different artificial reef modules (Reef Ball, MOSES, Coastruction/CREST unit) before and some time after deployment.

2.2. Reef structural complexity & in-canopy flow

On reefs, roughness elements are formed by communities of benthic organisms (e.g. corals, anemones, oyster), termed 'canopies'. The higher the structural complexity, the higher the roughness and associated wave dissipation. Jonsson (1966) proposed wave friction factors, which relate wave energy dissipation rates to near-bottom orbital velocities, depend on the ratio of the horizontal wave excursion amplitude A_{inf} to some roughness scale k_w. Numerous experimental studies have confirmed this assertion (Madsen, 1994; Nielsen, 1992; Swart, 1974). The wave excursion is intrinsic to the wave forcing and therefore relatively straightforward. Conversely, the definition of structural complexity and thereby the roughness scale is ambiguous and difficult to quantify. When modeling the effects of coral canopies on the wave attenuation it is crucial to utilize a set of parameters which effectively resemble the canopy's structural complexity.

Conventionally used parameters to describe the structural complexity are porosity and rugosity.

In Riera (2020), the porosity of an artificial reef structure is described as the ratio of the volume of pores V_p to the volume of the material V_t. If V_p if described as the difference between the volume of the bounded V_o and V_t, this equation follows:

$$n = \frac{V_o - V_t}{V_o} \tag{2.1}$$

Rugosity is typically determined using the widely-employed 'chain-tape' method due to its affordability and practicability. With a tape, the linear horizontal length over the reef L_t is measured. Next, the contour length of the canopy L_c is measured with a chain. The ratio between these measurements determines the rugosity index (Young et al., 2017):

$$RI = \frac{L_t}{L_c} \tag{2.2}$$

Another way of schematizing the canopy's roughness is described in Britter and Hanna (2003), which introduces dimensionless lambda parameters to describe canopies dispersing unidirectional air flows in urban environments:

$$\lambda_f = \frac{A_f}{A_T}$$
$$\lambda_p = \frac{A_p}{A_T} \tag{2.3}$$

Here, λ_f depicts the dimensionless frontal area of the canopy, whereas λ_p describes the dimensionless plan area. These two lambda parameters are determined with the canopy element frontal area A_f, the canopy element plan area A_p and the underlying surface area A_T (total area divided by the number of elements). λ_f is related to flow dispersion by drag as it describes the surface of the canopy facing the flow. In turn, λ_p describes the canopy's surface parallel to the flow, therefore being associated with flow dispersion by shear stress.

Building on the concept of these dimensionless lambda parameters, (Lowe et al., 2005b) concluded that oscillatory flow consistently generates higher in-canopy flow velocities compared to unidirectional flow. In this study, a theorem valid under unidirectional and oscillatory flow conditions was developed to predict the spatially averaged in-canopy velocity U_c as a function of the imposed free-flow velocity U_∞ and a collection of canopy geometry parameters:

$$\underbrace{\frac{dU_c}{dt}}_{\text{Local acceleration}} = \underbrace{-\frac{1}{\rho}\frac{dP}{dx}}_{\text{Pressure gradient}} + \underbrace{\frac{|U_\infty|\,U_\infty}{L_s}}_{\text{Shear stress}} - \underbrace{\frac{|U_c|\,U_c}{L_d}}_{\text{Form drag}} - \underbrace{\frac{C_M\lambda_p}{1-\lambda_p}\frac{dU_c}{dt}}_{\text{Inertial force}} \tag{2.4}$$

The canopy shear stress length scale L_s and the canopy form drag length scale are dependent on the aforementioned lambda parameters, the canopy height h_c, friction coefficient C_f and the drag coefficient C_d:

$$L_d = \frac{2h_c\,(1-\lambda_p)}{C_d\lambda_f}$$
$$L_s = \frac{2h_c}{C_f} \tag{2.5}$$

Lowe et al. (2008) proved this theorem to predict wave attenuation only 10% off observed values from lab experiments forcing monochromatic waves over a canopy of *Porites compressa*, a branching coral species. It was found that the attenuation is a function of the horizontal wave excursion amplitude A_∞ and the canopy geometry parameters in equation 2.5. In Lowe et al. (2007), this theorem is validated in an environment with spectral wave conditions by placing a model canopy comprising of cylindrical elements on a shallow reef flat. The theorem was shown to accurately predict the spectral distribution of flow attenuation: shorter period waves penetrated more readily into the canopy and therefore lose more energy than its long period counterparts.

An alternative to Lowe's theorem is the porous media theorem developed by Gu and Wang (1991). Here, the canopy is schematized as a porous medium with porosity n as described in equation 2.1 and a thickness or canopy height h_c. In the case of cylindrical or cubic canopy elements, the porosity n is directly related to the lambda plan parameter λ_p ($\lambda_p = 1 - n$). In the case of a more geometrically complex canopy element as the Coastruction element, the porosity n has to be determined via equation 2.1. The Gu and Wang (1991) theorem substitutes the 'shear' and 'drag' terms of equation 2.4 with 'laminar resistance' and 'drag' terms derived from the Forchheimer equation (Whitaker, 1996). (Lowe et al., 2008) added a shear stress term to the (Gu and Wang, 1991) theorem to account for long-period wave motions, resulting equation 2.6. It should be noted that, the upper case (canopy) friction coefficient C_f accounts the frictional stresses at the interface between the canopy and the free stream. It appears in the term that contains the velocity difference between the in-canopy flow and the free-stream flow. On the other hand, the lower case (bottom) friction coefficient c_f, accounts for the frictional stresses at the interface between bottom and near-bed flow.

$$\underbrace{\frac{d(U_c)}{dt}}_{\text{Local acceleration}} = \underbrace{-\frac{1}{\rho}\frac{dP}{dx}}_{\text{Pressure gradient}} - \underbrace{\frac{v(1-\lambda_p)}{K_p}U_c}_{\text{Laminar resisting force}} \underbrace{-\beta\,|U_c|\,U_c}_{\text{Form drag}} - \underbrace{\frac{C_M\lambda_p}{1-\lambda_p}\frac{dU_c}{dt}}_{\text{Inertial force}} + \underbrace{\frac{|U_\infty - U_c|\,(U_\infty - U_c)}{2h_c/C_f}}_{\text{Shear stress}} \tag{2.6}$$

in which
U_c : averaged in-canopy velocity $[\mathrm{m/s}]$
U_∞ : free-stream velocity $[\mathrm{m/s}]$
λ_p : dimensional plan area $(1-p)[-]$
K_p : permeability $[m^2]$
C_M : inertia force coefficient [-]
μ : kinematic viscosity $[\mathrm{m^2/s}]$
h_c : canopy height $[m]$
β : drag coefficient $[m^{-1}]$
C_f : empirical friction coefficient [-]
η : free-surface elevation $[\mathrm{m}]$
g: gravitational acceleration $[\mathrm{m/s^2}]$

As stated before, the rate at which wave energy is dissipated is closely linked to the flow structure within the coral canopy. To reflect this process, the in-canopy flow velocity following from either 2.4 or 2.6 can be used to determine the drag force induced by the canopy on the depth averaged flow as follows:

$$F_c = -\rho h_c \left[\beta \left| \overline{U}_c \right| \overline{U}_c + \frac{\mu (1-\lambda_p)}{K_p} \overline{U}_c + \frac{C_m \lambda_p}{1-\lambda_p} \frac{d\overline{U}_c}{dt} \right] \tag{2.7}$$

A more simplified representation of the time-varying canopy drag force is provided by Lowe et al. (2005b) as

$$F_c(t) = \frac{C_d \lambda_f}{2 h_c (1-\lambda_p)} \left| U_c(t) \right| U_c(t) \tag{2.8}$$

which incorporates the lambda parameters and canopy height. As it uses the spatially averaged in-canopy flow velocity $U_c(t)$ it is not required to compute a canopy flow gradient as in equation 2.7.

To account for the energy dissipation caused by the canopy, in an one-layer 1D model this canopy-induced force F_c is added to the depth-averaged horizontal momentum equation in the following manner:

$$\underbrace{\frac{\partial u}{\partial t}}_{\text{Local acceleration}} + \underbrace{u\frac{\partial u}{\partial x}}_{\text{Advection}} - \underbrace{v_h \frac{\partial^2 u}{\partial x^2}}_{\text{Diffusion}} = \underbrace{-g\frac{\partial \eta}{\partial x}}_{\text{Pressure gradient}} \underbrace{- c_f \frac{u|u|}{h}}_{\text{Bottom friction}} + \underbrace{\frac{F_c}{\rho h}}_{\text{Canopy-induced force}} + \underbrace{\frac{F_x}{\rho h}}_{\text{Wave-induced force}} \tag{2.9}$$

The aforementioned 1D method of accounting for the effect of canopies on hydrodynamics is also implemented in the phase-averaged and phase-resolving variants of nearshore hydrodynamics model XBeach. In this implementation, the canopy is represented as a subgrid cell, where the flow dynamics within this cell (equation 2.6) are used to calculate the force exerted by the canopy on the depth-averaged flow (equation 2.7). van Rooijen et al. (2022) compared the results of this canopy flow subgrid model, implemented in the phase-resolving version of XBeach, with wave flume experiments. They demonstrated that neglecting canopy flow can result in significant errors in wave predictions.

2.2.1. Canopy flow regimes

To understand the different possible canopy flow regimes, one must first understand how the canopy wave attenuation is defined and quantified in Lowe et al. (2005b). The wave attenuation parameter α_w is the ratio of the in-canopy velocity amplitude U_c to the free-stream velocity amplitude U_∞ and is therefore quantitative measure of the relative reduction of the in-canopy velocity from its above-canopy flow velocity. The precise definition of the above-canopy or free-stream flow velocity is that it remains unaffected by the roughness of the canopy.

For spectral waves, this wave attenuation parameter can also be expressed for each frequency component f_i as in equation 2.10. By doing this, the parameter can be used for assessing the artificial reef restoration's capability of attenuating wave energy in specific bandwidths. Furthermore, the velocity

amplitudes can be expressed as the square root of the corresponding velocity energy density spectra E_{uu}.

$$\alpha_{w,i} = \frac{U_{c,i}}{U_\infty} = \left(\frac{E_{uu_c,i}}{E_{uu_\infty,i}} \right)^{1/2} \tag{2.10}$$

The different canopy flow regimes result from contributions of the shear stress, drag and inertia force terms to this wave attenuation parameter. These contributions are respectively determined by the following dimensionless parameters as described in Lowe's theorem defined in equation 2.4:

$$\frac{A_\infty^{rms}}{L_s} \quad and \quad \frac{A_\infty^{rms}}{L_d} \quad and \quad \frac{C_M \lambda_p}{1-\lambda_p} \tag{2.11}$$

with A_∞^{rms} being the rms wave orbital excursion length with ω being calculated with the mean wave period in case of spectral wave conditions as follows:

$$A_\infty^{rms} = \frac{U_\infty^{rms}}{\omega} = \frac{U_\infty^{rms}}{\frac{2*\pi}{T_{m01}}} \tag{2.12}$$

Dependent on the magnitude of these 3 dimensionless parameters, the flow can either be classified as canopy independent, inertia force dominated, unidirectional limit or general flow:

1. Canopy independent: if all dimensionless parameters are negligibly small, the canopy flow is governed by potential flow and therefore unaffected by the presence of canopy elements. The attenuation parameter in this case is consistent with
   α_w = 1
2. Inertia force dominated: in case of negligible drag and shear, the inertia force contributes most to the attenuation of the oscillatory flow and gives a limiting attenuation parameter as frequency increases:
   $\lim_{\omega \to \infty} \alpha_w = \frac{1-\lambda_p}{1+(C_M-1)\lambda_p}$
3. Unidirectional limit: for infinite wave period T, excursion length A_∞^{rms} becomes very large, leading to a dominance of shear and drag over inertia. A force balance between the canopy shear stress and drag force terms leads to
   $\alpha_w = \frac{L_d}{L_c}$
4. General flow: none of the force terms can be neglected and the attenuation parameters is a function of the three dimensionless parameters:
   $\alpha_w = \alpha_w \left(\frac{A_\infty^{rms}}{L_s}, \frac{A_\infty^{rms}}{L_d}, \frac{C_M \lambda_p}{1-\lambda_p} \right)$

Only in the general flow regime, the wave attenuation parameters is dependent on the excursion length A_∞^{rms}. This is also reflected in Panel a) of Figure 2.6, where the wave attenuation parameter as a function of the ratio between excursion length and canopy element spacing A_∞^{rms}/S. In the general flow regime, the attenuation parameter is dependent on the aforementioned ratio and therefore the attenuation is frequency-dependent. For the inertia and unidirectional flow regime, converging to a constant value, the attenuation is solely dependent on the canopy's geometry.

These flow regimes were established for regular wave conditions. To account for spectral wave conditions, Lowe et al. (2007) used the same theorem and forced it with an uniformly distributed spectrum with frequencies ranging from 0 to 1 Hz. In Panel b) in Figure 2.6 the wave attenuation parameter per wave component is depicted as a function of the period T_j of its corresponding wave component for several values of U_{rms}^∞. Firstly, a wave component is attenuated more intensely as its corresponding wave period increases. Furthermore, this figure reveals that increasing the total velocity energy causes more attenuation of the in-canopy flow across all wave components. This can be explained by the fact that, analogous to monochromatic waves, α_w decreases as the free-stream wave excursion length

A_∞ increases. For spectral wave flow, the wave excursion rate spectrum $E_{AA,i}$ is dependent on the velocity spectrum and wave period as follows:

$$E_{AA,i} = \frac{E_{uu,i}}{\omega_i^2} = \frac{E_{uu,i}T_i^2}{(2\pi)^2} \tag{2.13}$$

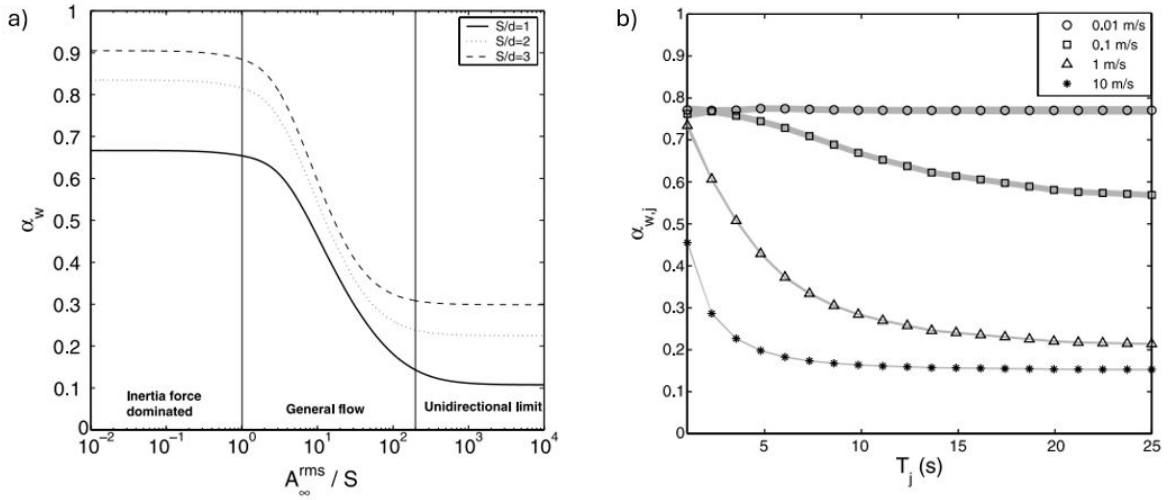

Figure 2.6: Panel a: Canopy flow regime classification of (Lowe et al., 2005b), showing the three possible flow regimes and the relation between flow attenuation parameter α_w and excursion length to spacing ratio A_∞^{rms}/S. Panel b: The relation of the attenuation parameter per wave component $\alpha_{w,i}$ and wave period T_i and orbital velocities (Lowe et al., 2007).

2.2.2. Canopy-induced wave dissipation

It is important to note that higher values of the flow attenuation parameter α_w result in increased dissipation rates, assuming the canopy geometry remains unchanged. This happens because higher flow attenuation parameter values correspond with lower flow attenuation, enhancing the flow through the canopy, which in turn lowers the work exerted by canopy forces (shear, drag, and inertia) responsible for wave dissipation. This is consistent with the fact that shorter waves penetrate more easily into the canopy and therefore dissipate more of its total energy. This does not imply that in a scenario with a bare reef, where the attenuation parameter approaches 1, dissipation is simply high because the flow is able to penetrate. This is because, the canopy must possess sufficient geometrical complexity to dissipate the penetrated flow. Therefore, dissipation by an artificial reef is maximized by finding an optimum between high drag and friction parameters and a high attenuation parameter. This is reflected in the way Lowe et al. (2007) links the wave attenuation parameter to wave dissipation. In this theorem, the dissipation factor $f_{e,i}$ determines the extent to which a wave component is dissipated by the canopy.

$$f_{e,i} = C_f + C_d\lambda_f\alpha_w^R\alpha_{w,i}^2 \tag{2.14}$$

The representative attenuation parameter α_w^R is calculated over the entire spectrum whereas $\alpha_{w,i}$ is associated with the ith wave component. With this dissipation parameter, the frequency-dependent wave dissipation induced by the canopy can be calculated by:

$$\varepsilon_{c,i} = \frac{1}{4}\rho f_{e,i}U_{\infty,w}^{rms}U_{\infty,i}^2 \tag{2.15}$$

In which the free-stream velocity amplitude per wave component $U_{\infty,i}$ can be calculated from the free-stream energy density spectrum as

$$U_{\infty,i} = \sqrt{2E_{uu_\infty,i}\Delta f} \tag{2.16}$$

The total in-canopy dissipation rate ϵ_c is calculated by integrating across all wave components:

$$\epsilon_c = \int \epsilon_c(f) df \tag{2.17}$$

2.2.3. In-canopy measurements

To gather information on in-canopy flow, flow measurement locations have to be chosen. To be able to pick locations representing all flow characteristics, some knowledge on the flow structure within the canopy is needed. Due to the structural complexity of the canopy and its resulting contraction and expansion of streamlines, there is significant spatial variability in flow velocities. Gijón et al. (2021) conducted in-canopy measurements within a dense array of wooden cylinders and identified two distinct regions of flow: an open region and a region directly behind a cylinder. Flow accelerates in the open region between the cylinders, while a wake forms directly behind each cylinder, reducing flow velocities as can be seen in Panel a) of Figure 2.7. Small lateral spacings accelerate flow and small streamwise spacings reduces flow velocities and reduces drag and shear forces on upstream elements. In Lowe et al. (2005b), the same two region were identified and two separate velocity profiles were collected to investigate the occurring spatial variations as can be seen in Panel b) of Figure 2.7. To approximate the spatially averaged velocity profile U(z), the average of both velocity profiles is constructed.

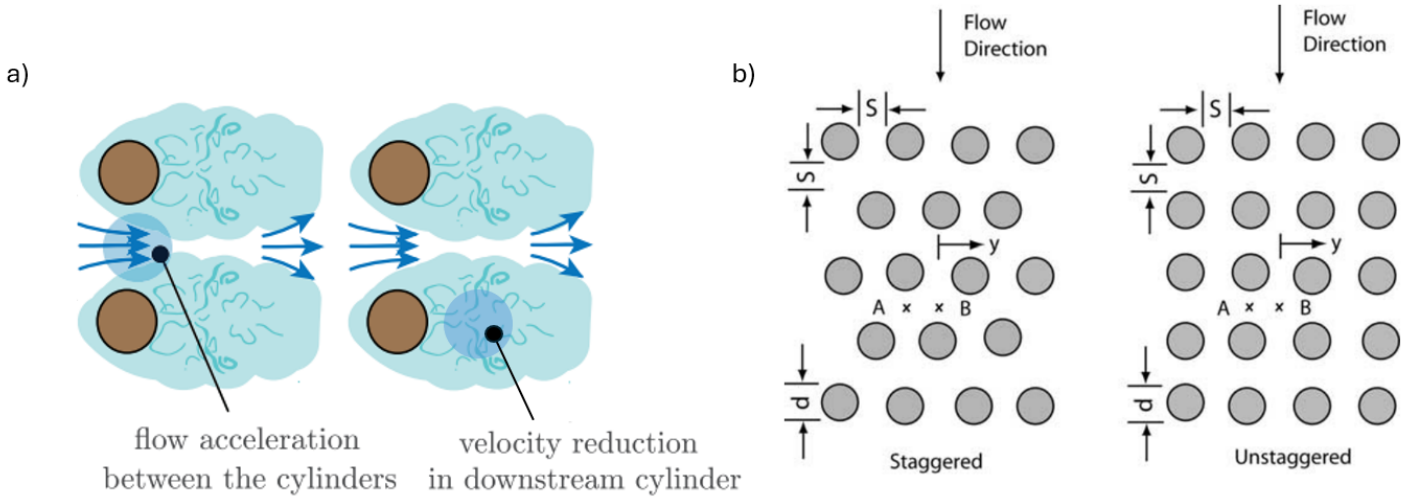

Figure 2.7: Panel a: Identification of two distinct regions of flow within a dense array of wooden cylinders. Modified from Gijón et al. (2021). Panel b: Cylinders used in experiments by Lowe et al. (2007), identifying two distinct flow regions to investigate flow variability.

2.2.4. Canopy parameters

For further understanding of the parameters used in the in-canopy flow theorem and get a foundation to choose a parameter space for calibration purposes, the physical basis and parameters ranges commonly used in literature are presented within this subsection.

Macdonald et al. (1979) proposed the 'modified Ergun equations' to determine the permeability parameter K_p and drag parameters β, which followed from experiments with a variety of porous medium geometries:

$$K_p = \frac{D_{eq}^2(1-\lambda_p)^3}{a_0\lambda_p^2} \tag{2.18}$$

$$\beta = \frac{b_0\lambda_p}{D_{eq}(1-\lambda_p)} \tag{2.19}$$

In the formulation of the 'modified Ergun equations', a_0 and b_0 are empirical constants and are respectively set to 180 and 1.8 in Lowe et al. (2008), resulting in prediction of K_p and β within 50%. A sensitivity

analysis conducted in de Ridder et al. (2021) demonstrated that a 50% uncertainty in the calculation of the drag force results in a 5% error in the in-canopy velocity u_c.

D_{eq} represents the characteristic length scale of the porous medium, also referred to as the 'equivalent mean sphere diameter' which is equal to six times the volume-to-surface ratio of the bed particles. For example, a bed composed of cylinders results in a characteristic length scale of $D_{eq} = 1.5D_{cylinder}$.

The drag coefficient β partly determines the magnitude of the drag forces exerted by the canopy on the flow in the canopy momentum equation 2.6. This drag term in the momentum balance is dependent on the in-canopy velocity u_c. When the canopy's surface parallel to the flow λ_f and surface parallel to the flow λ_p can be determined with reasonable accuracy, these parameters will hold information about the shape of the canopy and the shape parameter b_0 in the modified Ergun equations can be discarded. For this case, Coceal and Belcher (2004) described the following equation to determine the β-parameter,

$$\beta = \frac{\lambda_f}{\lambda_p} \frac{C_d}{2h_c} \tag{2.20}$$

Thus, as the lambda parameters canopy heights h_c are constant and a result of the artificial reef's geometry, β is determined by the drag coefficient C_d. Coceal and Belcher (2004), evaluated data from several experiments and found C_d to be in range 2 - 3, confirming this with direct numerical simulations. Lowe et al. (2005a) used a C_d of 2.5 in his research. In this research it is stated that C_d is greatly dependent on the canopy geometry and flow conditions thus this value serves only an initial guess if applied in models and calculations.

Furthermore, the laminar resistance term only becomes significant in very fine porous media, in this research the pores within the artificial coral restoration are relatively coarse and therefore the permeability K_p does not seem to have a large influence on the outcome of the in-canopy velocity U_c.

It should be noted that modeling studies investigating wave dissipation by coral canopies via a bottom friction model do not differentiate between bottom friction, laminar resistance, canopy drag, canopy friction and inertial forces and converge all information into the lower case bottom friction coefficient c_f (Storlazzi et al., 2022; Roelvink et al., 2021). Therefore, it can be expected that in an in-canopy flow model the parameter C_f will have to be set lower as it will only represent shear stress on the canopy-free-stream interface. This is reflected in the in-canopy flow study of Lowe et al. (2005a), in which $Cf\ O(0.01)$ is proposed as opposed to the general bottom friction coefficient range for oscillating flows over reefs of 0.01-0.3 (Nelson, 1996).

The inertia coefficient C_M partly determines the effect of the acceleration of the flow around the artificial reef elements as streamlines are expanding and contracting which result in the inertial forces in the in-canopy momentum equation 2.6. This parameter presents the most uncertainty in the in-canopy momentum equation, as is reflected in the greatly variable parameter ranges found in literature. Gu and Wang (1991) and Van Gent (1995) both proposed a C_M of approximately 0.5, while Mccorquodale et al. (1978) found a value of 0.2. Lowe et al. (2005a) found that a C_m of 1.7 lines up best with flow around cylindrical canopy elements and a value of 1.5 yields best result with flow around spherical canopy elements. de Ridder et al. (2021) used a range of 0.5-1.5 while modeling with the in-canopy flow model within XB-NH. In the same study it is shown that an uncertainty of 50% in the calculation of the inertia term results in a 10% error in the averaged in-canopy velocity U_c, making C_M the most influential canopy parameter after β.

2.3. Reef hydrodynamics

The characteristics that make (fringing) reef coastlines stand out to other coastlines, especially compared to dissipative beaches, is the steep transition from deep to shallow water combined with the shallow reef flat adjacent to the beach. This causes reef lines coastlines to encounter specific nearshore processes across both the low and high frequency bands of the wave spectrum (Van Dongeren et al.,

2013a). In this chapter, these nearshore processes are subdivided in wave setup, sea-swell waves (SS) and infragravity waves (IG).

2.3.1. Wave setup

While waves propagate toward the coast, shoaling and breaking result in local variations in wave energy. The radiation stress as described in equation 2.21 also varies due to this variation in wave energy, inducing a radiation stress gradient $\frac{\partial S_{xx}}{\partial x}$. When divided by the local water depth, this radiation stress gradient results in a onshore-directed horizontal force F_w acting on the water column. In absence of any canopy inducing drag forces on the water column, this horizontal force is balanced only by the pressure gradient as defined in equation 2.22. The continuous effect of this pressure gradient throughout the domain is essentially what results in wave setup. Due to the steep and rapid changes in bathymetry characteristic of fringing reef-lined coasts, the majority (90–99%) of incoming SS waves break at the reef crest, depending on the tidal stage (Péquignet et al., 2011). This SS wave breaking is the primary driver of the previously mentioned wave setup.

$$S_{xx}(f) = E(f)\left(1 + \frac{2k(f)h}{\sinh(2k(f)h)}\right) \tag{2.21}$$

$$\underbrace{\frac{\partial S_{xx}}{\partial x}}_{\text{Radiation stress gradient}} + \underbrace{\rho g h \frac{\partial \bar{\eta}}{\partial x}}_{\text{Pressure gradient}} = 0 \tag{2.22}$$

This wave setup, although being highly site and forcing dependent, can reach higher than typical value of up to 1.3 meters (Vetter et al., 2010). As such, it is an important driver for extreme onshore water levels. Understanding how canopies affect the magnitude of wave setup and its contribution to extreme water levels is therefore highly relevant. van Rooijen et al. (2016) identified three key mechanism of a canopy's influence on wave setup: **(1)** its direct impact on the radiation stress gradient, **(2)** the canopy-induced drag force on the return current, **(3)** net resulting wave-induced drag force due to emergent canopies, and **(4)** the wave-induced force resulting from skewed waves.

1) Regarding the canopy's direct impact on the radiation stress gradient, the wave energy dissipation caused by the canopy results in larger radiation stress gradients around the canopy and smaller radiation stress gradients further onshore as a larger fraction of the wave energy has already dissipated. As the wave force acting on the wave column F_w is dependent on water depth, the net influence of the canopy on the wave setup is also dependent on the relative water depth at the canopy's location.

2) The introduction of the canopy generates an onshore-directed force on the water column due to the offshore-directed mean near-bed current, also known as return current. This drag force combines with the horizontal force from the radiation stress gradient, F_w, requiring a greater pressure gradient for equilibrium. As a result, wave setup is expected to increase at locations with a significant return current, as has been observed in studies such as Luhar et al. (2010) and (Løvås and Tørum, 2001).

3) Using linear wave theory to integrate the wave-induced drag force on a submerged canopy over an entire wave cycle results in a net force of zero. However, for emergent vegetation, the net drag force is nonzero due to variations in the submerged canopy height throughout the wave cycle. Under the wave crest, a larger portion of the canopy is exposed to the drag force than under the wave trough, creating an offshore-directed force on the water column. As demonstrated by Dean and Bender (2006), this offshore force partially balances the radiation stress gradient, thereby reducing the pressure gradient's contribution and its resulting wave setup.

4) A similar setup reduction mechanism was found by Dean and Bender (2006) in skewed waves. These waves, generate higher depth-average flow velocities in the direction of wave propagation, due to their sharp peaks and flat troughs. Because drag force increases quadratically with velocity, the resulting drag force, working on the water column, integrated over a wave cycle is directed offshore. This effect occurs regardless of whether the canopy is submerged or emergent.

These four key mechanisms interfering with the radiation stress gradient-pressure gradient balance are clarified by van Rooijen et al. (2016) by looking at their proportional contributions to the setup gradient:

$$\text{setup gradient} \propto \frac{1}{h}\left(\frac{\partial En}{\partial x} + \tau_b + F_{v,m} - F_{v,w}\right) \tag{2.23}$$

Although providing a physical explanation for how a canopy affects wave setup helps with understanding the key mechanisms, the contribution of these mechanisms still greatly depends on the local geometry (e.g., bed slope and water depth), canopy characteristics (e.g., density, canopy height, and location), and wave conditions.

2.3.2. Sea-swell (SS) waves

Fresh wind waves are generated by disturbances of the sea surface due to wind stresses. In linear wave theory, as stated by the dispersion relationship $w^2 = gk\ tanh(gk)$, longer waves travel faster through the domain which results in frequency dispersion. Due to the additional directional spreading, wind waves encountered at great distances from their generation area are regular and long-crested (Casas-Prat et al., 2014), commonly referred to as sea-swell (SS, with frequencies > 0.04 Hz). Fiyoaree, the atoll acting as prototype for the lab experiment transect, mainly receives SS waves as it is located far away from wave generation areas. Due to the narrow spectrum encountered in SS waves, wave grouping is prominent.

When reaching the reef's steep foreshore, waves start interacting with the bottom. Wave energy is dissipation due to bottom friction and waves shoal shoal until reaching the wave breaking height ($H_b = \gamma h$), for which γ is usually between 0.4 and 0.6 (Jensen, 2004). Due to this wave breaking height, the reef crest acts as a wave height filter; solely waves lower than γh propagate onto the reef flat. On the reef flat, wave energy dissipation is dominated by frictional dissipation resulting from shallow water and high friction coefficient due to coral's structural complexity (Lowe et al., 2005a).

2.3.3. Infragravity (IG) waves

Roelvink and Stive (1989) classified infragravity (IG) waves as the wave components with a frequency lower than the spectrum-specific cutoff frequency of half the offshore peak frequency: $f_p/2 = 2 \cdot T_p$ Hz. This choice is based on the experience that in deep water, the majority of SS-wave energy is found at frequencies $> f_p/2$, while most IG-wave energy resides in the $< f_p/2$ part of the spectrum.

Numerous studies have established the importance of IG waves in wave run-up, defined as the maximum vertical extent of wave uprush on a beach, particularly under energetic wave conditions on mildly sloping beaches (Guza and Thornton, 1982; Raubenheimer and Guza, 1996; Ruggiero et al., 2004). More specifically, wave run-up on coasts fronted by coral reefs is often dominated by IG swash motions due to the dominance of IG-band and other low-frequency motions on the reef flat (e.g., Seelig, 1983, Nwogu and Demirbilek, 2010, Bricker and Roeber, 2015, Cheriton et al., 2016). According to Shimozono et al. (2015), the contribution of IG waves to wave run-up becomes more dominant as reefs become wider.

IG waves are generated by the interaction of wind waves or as previously stated, SS-waves (Longuet-Higgins and Stewart, 1962). In this study, two IG wave generation mechanisms are of importance: bound IG wave release and breakpoint forcing. Pomeroy et al. (2012b) found that break point forcing is dominant for reef coasts with a steep foreshore.

Bound IG wave

In deep water, irregular waves with different wavelength tend to travel in groups due to the interference between waves of different wavelengths. Figure 2.8 shows the case of two slightly different frequencies interfering and forming a wave group.

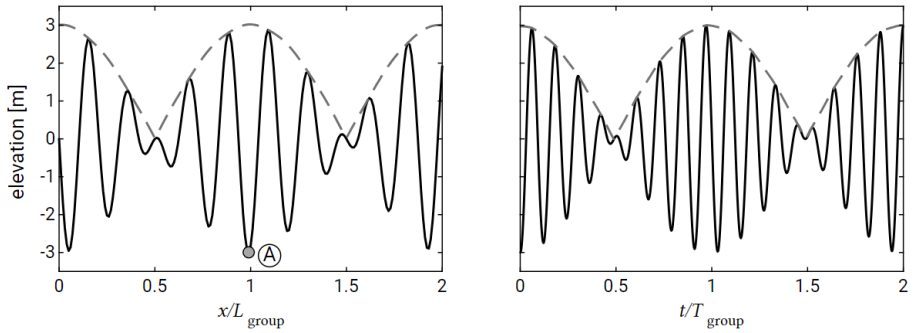

Figure 2.8: Wave grouping of waves with a slightly different period of 6.2 and 7.0 s, both with an amplitude of 1.5 m. The left panel shows the grouping in space at t = 0. The right panel shows the grouping in time at location A.

Due to variation in wave height, the radiation stresses vary within the wave group as well. As a result, the highest set-down in the shoaling zone is found under the highest waves in the wave group and lowest set-down under the lowest waves. The effect of this time-varying set-down is a long wave traveling at wave group celerity as can be seen in figure 2.9. The correlation between long wave and wave group is negative offshore from the breaker zone and turns positive inside the breaker zone, meaning that the long wave is 'released' and no longer moves at the wave group celerity.

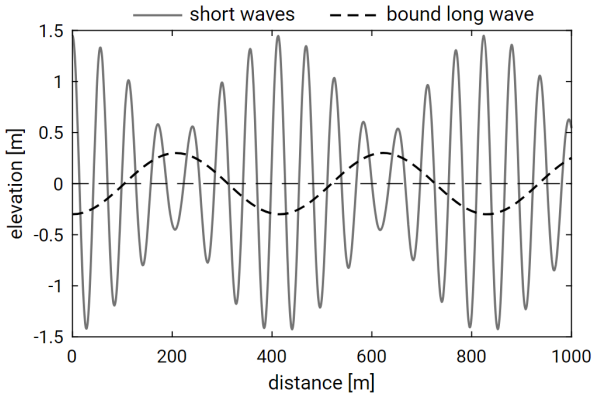

Figure 2.9: A bound long wave, perfectly out of phase with the wave group as the troughs of the bound long wave coincide with the maxima of the wave group envelope. A superposition of two waves (a1 = 0.5 m, T1 = 5.75 s and a2 = 1.0 m, T2 = 6.15 s) traveling in a water depth of 30 m is depicted. Note that the bound long wave is not scaled proportionally to the short waves within the wave group envelope.

Break point forcing

The location where waves reach shallow enough water to break (breakpoint) varies due to the variation of incoming SS wave heights in wave groups. Higher waves break further offshore and lower waves break further onshore, assuming a constantly sloping foreshore. While the breakpoint oscillates at the frequency of the wave group, the location of the wave set-down induced by radiation stresses also oscillates at the wave group's frequency (Bertin et al., 2018). This oscillation of the wave set-down location acts as an IG-wave generator propagating IG-waves on- and offshore from the breakpoint. A visualisation of this oscillation of this generation mechanism can be seen in Figure 2.10.

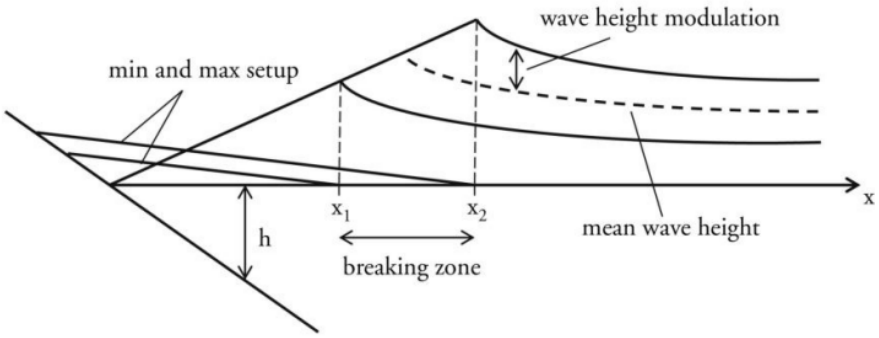

Figure 2.10: Visualisation of the shifting break point as an IG wave generating mechanism by Bertin et al. (2018)

Due to the breaking and frictional dissipation of SS-waves and the generation of IG-waves due to break point forcing and bound long wave releasing it is generally observed that energy is transferred from high to low frequency bands within the wave spectrum (Pomeroy et al., 2012b).

The combined processes of breaking SS-waves, breakpoint forcing and long bound wave generation result in a variety of short- and long-wave (Lowe et al., 2005a) propagating shorewards over the reef flat. Next to the fact that the majority (90-99%) of SS-waves have already broken at the reef crest, SS-waves are attenuated to a greater extent by frictional dissipation on the reef flat as they penetrate more readily into the coral canopy than their IG counterparts (Pomeroy et al., 2015). As a result, IG-waves tend to dominate the spectrum on the more onshore part of the reef flat (Van Dongeren et al. (2013b), Pomeroy et al. (2012a)), and therefore in most cases are the primary contributor to wave runup and subsequent resulting coastal flooding (Cheriton et al. (2016), Quataert et al. (2015)). Subsequently, enhancing reef restorations to dissipate energy in the IG band of the wave spectrum can be an effective strategy for reducing coastal flooding.

Due to their large wavelength, IG waves can trigger the resonance mode of the coastline. For resonance to occur in a semi open basin, a node should be present on the offshore, open boundary and an antinode should be present on the onshore closed boundary. (Péquignet et al., 2009) concluded that coral reefs are subject to the same resonance mechanism as described in the semi open basin example explained above. Equation 2.24 gives the theoretical wave frequency for which the resonance mode is triggered. Lower resonance modes (e.g. n = 0, 1) show the greatest amplification potential as their large wavelengths are least subject to frictional dissipation over the reef flats (Gawehn et al., 2016).

$$f_n = \frac{(2n+1)\sqrt{gh}}{4L} \; for \; n = 0, 1, ...N \tag{2.24}$$

3

Methodology

To answer the research questions defined in the introduction, a research methodology is laid out to provide sufficient and adequate data to discuss and ultimately draw conclusions from. To provide context for the methodology and explain the purpose of the Delta Flume experiments, this methodology chapter begins with a description of the research context in Section 3.1. This chapter first discusses the set up of the physical model in Section 3.2, covering the set-up of the fringing reef model within the flume, the design and metrics of the artificial reef elements and how these elements are placed on the reef platform. This Section also presents the wave and water level conditions. In Section 3.3, the instruments used to measure flow velocities and pressures in the flume are presented. The data obtained from these instruments is refined to a subset that meets the required quality standards through a data quality assessment, as detailed in Section 3.4. This subset of time series is then processed as outlined in Section 3.5. Within this data processing Section, Subsection 3.5.1 shows how outliers and erratic data are removed, Subsection 3.5.4 describes how point-measured velocity are converted to depth-averaged velocities, Subsection 3.5.2 presents how surface elevation timeseries are acquired from pressure measurements and Subsection 3.5.3 describes the decomposition of incoming and outgoing waves. With these processed timeseries of velocity and surface elevation data, wave parameters are calculated with methods presented in Section 3.6 in which methods of obtaining spectral characteristics, wave non-linearity, flow velocity attenuation and wave dissipation rates. Finally, methods of conducting an extreme water level analysis are presented in 3.6.5

The methodology used in this study builds on Vincent Takens' master's thesis (Takens, 2024), which, among other contributions, designed the artificial reef and optimized its placement and density for maximum coastal protection using the phase-resolving numerical model SWASH.

3.1. Research context

The lab experiments are conducted within the existing CREST and ARISE projects. ARISE is an initiative from the University of Plymouth and aims to enhance the capability to model impacts of sea-level rise on atoll island and hereby aid in developing climate change adaptation strategies. Simply put, the ARISE project will explore whether atoll islands can adapt to sea level rise.

The CREST project, an initiative led by Delft University of Technology, is an extension of the ARISE project and focuses specifically on wave transformation and run-up reduction provided by artificial reef restoration placed on reef flats encircling atoll islands. Through a TKI-proposal (public-private partnership), Deltares, Coastruction and Boskalis are involved in designing and testing reef elements used for artificial reef restoration.

Within these projects, the large-scale experimental data will act as a core dataset for model calibration and validation on reef island hydro- and morphodynamics. Through initiating the ARISE project, the University of Plymouth has designed the flume experiment in which the CREST project takes up a part of the experimental time. The CREST team is responsible for installing the artificial reef and providing in-canopy measurements.

The hydrodynamic boundary conditions which are used in the CREST part of the flume experiments are a subset of the conditions used in the ARISE part. Although these conditions are determined in discussion with all involved parties, these conditions are mainly follow from the aims of the ARISE project.

3.2. Physical model

As mentioned before, large-scale flume experiments are conducted to have a representation of reef hydrodynamics as near to a real fringing reef as possible. This section will give an elaborate overview of the setup of these flume experiments by means of introducing the fringing reef prototype and how this prototype translates to a transect applicable in a flume. Hydrodynamic boundary conditions, follow from the water levels this same prototype is typically exposed. Following, the design of the artificial reef elements is discussed below, along with how these elements interlock these elements to form the complete artificial reef. Finally, the types of instruments and their placement are introduced.

The large-flume scale experiments are performed in the Delta Flume, a unique testing facility on the premises of Deltares, a technological institute specializing in hydraulic engineering research and consulting. Despite being one of the largest wave flume in the world, the flume experiments are still somehow restricted by the dimensions of the Delta Flume. The flume has a length of 300 meters, height of 9.5 meters and a width of 5 meters.

The reef transect constructed in the Delta Flume is based on a prototype transect at the atoll island of Fiyoaree in the Maldives which is used a field study site within the ARISE project. This transect is specifically selected due to its relatively narrow reef flat and steep foreshore, a combination known to be susceptible to flooding as it allows a substantial amount of wave energy to reach the coastline. The location of this atoll island within the Maldives along with the structure and location of the fringing reef transect itself are shown in figure 3.1.

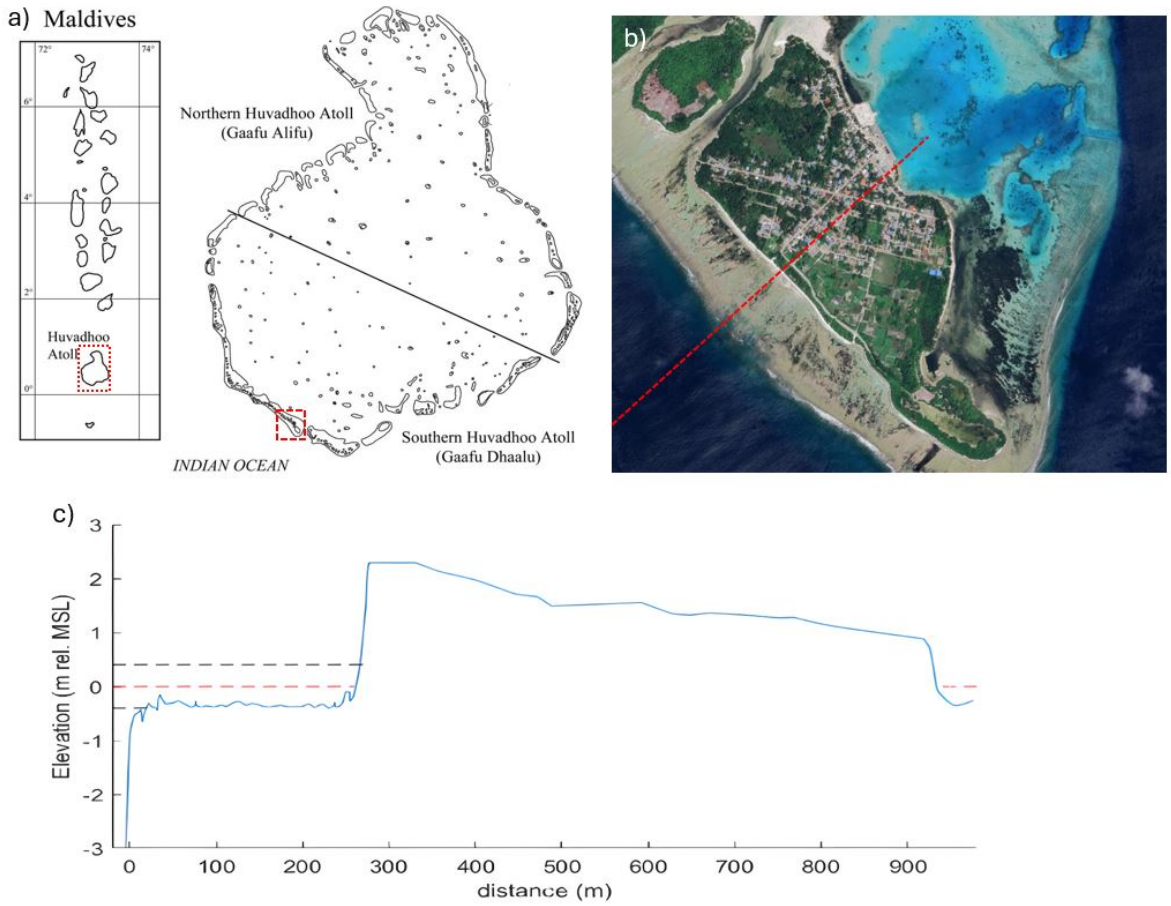

Figure 3.1: Dimensions and geometry of the Delta Flume reef platform and coral island based on a reef transect in Fiyoaree, Maldives (Russo and De Maddalena, 2021)

To move from this prototype transect to a transect applicable within the size restrictions of the flume, a downscaling factor has to be applied. To avoid scale effects, the ratio of flow inertia to gravitational forces is kept constant, expressed as the Froude number ($Fr = \frac{u}{\sqrt{gh}}$). This is known as Froude scaling, where all parameters are adjusted to ensure the Froude number remains constant. This method is preferred for larger experiments involving free-surface waves as they are dominated by gravitational forces. When opting for a spatial scaling factor of 3 to meet the size restrictions of the flume, the temporal scaling factor follows from the Froude scaling as follows:

$$Fr_p = Fr_m \tag{3.1}$$

$$\frac{u_p}{\sqrt{g_p * L_p}} = \frac{u_m}{\sqrt{g_m * L_m}} \tag{3.2}$$

$$n_L = \frac{L_p}{L_m} = 3, \quad n_T = \sqrt{n_L} = \sqrt{3}, \quad n_u = \sqrt{n_L} = \sqrt{3}$$

Meaning that flow velocities and wave periods, containing a temporal component, have to be scaled by their scaling factors n_u and n_T of $\sqrt{3}$.

Applying the spatial scaling factor of 3 to the Fiyoaree transect results in an island width and reef flat width of respectively 200 and 90 meters. Since the flume cannot accommodate these widths, the island and reef flat widths are further scaled down to 60 and 45 meters, respectively, representing prototype values of 180 and 135 meters. The island crest height and reef flat water depth can be scaled directly

with a factor 3 from the Fiyoaree transect, resulting in a crest height of 1 meter and a water depth range of 0.17 - 0.67 meters. Furthermore, the artificial reef installed in the Delta Flume covers a 10-meter stretch with a height of 0.25 meters resulting in a 30-meter wide, 0.75 meter high prototype artificial reef. An overview of the dimensions of both the Delta Flume, prototype and Fiyoaree dimensions can be seen in table 3.1.

Table 3.1: Dimensions of the reef transect as constructed in the Delta Flume, its prototype and the Fiyoaree fringing reef transect it is based on.

Variable	Delta Flume	Prototype	Fiyoaree
Coral island width [m]	60	180	600
Coral island crest height [m]	1	3	3
Reef flat width [m]	45	135	270
Initial reef flat water depth [m]	0.17 - 0.67	0.5 - 2.0	0.5 - 2.0
Artificial reef width [m]	10	30	n/a
Artificial reef height [m]	0.25	0.75	n/a

A visualization of how this geometry is represented in the Delta Flume is shown in figure 3.2. In this figure, it can be seen that the forereef has a steep slope of 1:5 and extends towards the reef flat which has a height of 5 meters with respect the flume's bottom. Furthermore, the island's beach has a gentle slope of 1:10 and is covered by a geotextile to prevent sediment transport and therewith provides a stable island. The artificial reef covers 10 meters on the reef flat, which reflects the limited spatial extent of artificial reef restorations. A central location on the reef flat is chosen as prior research showed the wave energy reduction capacity is greatest for shallow restorations on the reef flat. Furthermore, corals typically do not grow on the reef flat due to the absence of stable substrate. By providing this stable substrate with artificial reef elements, the roughness and height of the restoration area can increase even further via coral growth.

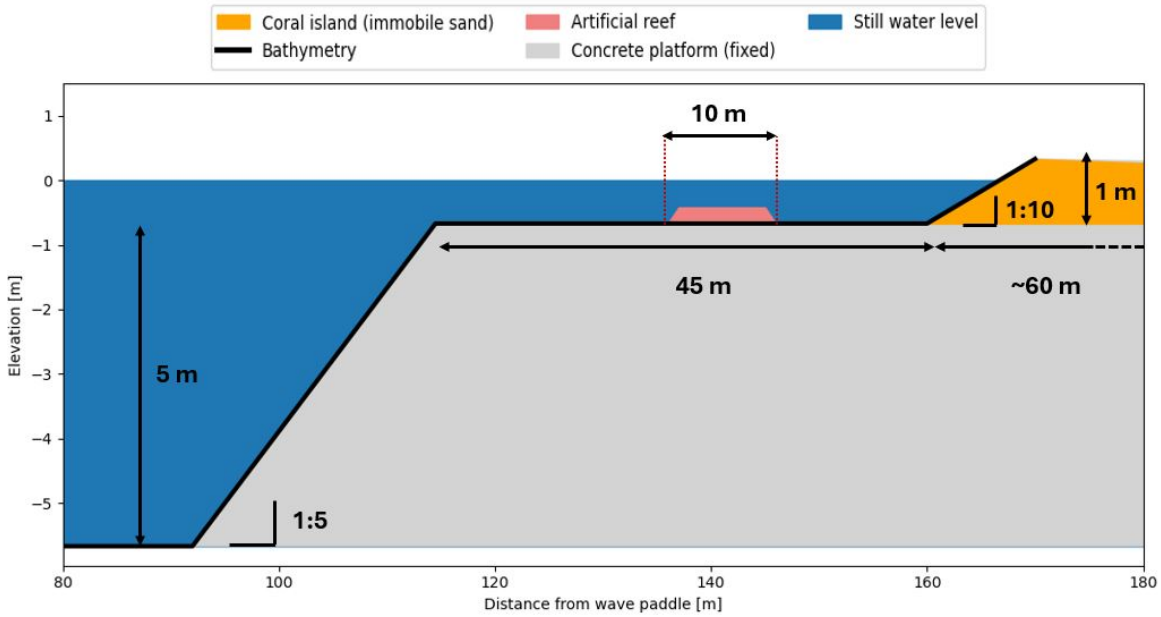

Figure 3.2: Representation of the reef transect as constructed in the Delta Flume, with the location of the artificial reef on the and the most relevant dimensions of the wave flume, reef platform and coral island.

As the effect of the artificial reef elements on the hydrodynamics will be tested for various wave conditions and water levels, a set of hydrodynamic boundary conditions is established. It should be noted that both the wave conditions and water levels are part of a broader set boundary conditions used within the ARISE project. Therefore, the numbering of wave conditions has jumps in it and the full range of water levels is not covered within the experiments presented in this thesis. Both wave conditions and water levels reflect the wave and tidal climates of the Indian and Pacific Oceans, aiming to closely replicate the hydrodynamics of a real fringing reef. Fiyoaree, located in the Indian Ocean, is mainly exposed to distant swell waves as it is at great distance from extreme wave generation areas. These waves are characterized by relatively low wave heights and long wave periods. As fringing reefs with the same characteristics as the Fiyoaree transect also occur in the Pacific Ocean, wave conditions representative to this specific location will also be tested. Fringing reef environments in the Pacific Ocean are typically located closer to areas of extreme wave generation. In particular, cyclones are a common feature in this region (Salvat and Wilkinson, 2011). As a result, the wave climate is characterized by shorter but higher waves.

In table 3.2, the wave conditions as tested in the flume are depicted alongside their prototype equivalent, which is scaled with the temporal scaling factor n_T of $\sqrt{3}$. C1, C7 and C11 represent the shorter period, Pacific Ocean wave conditions whilst C3 and C9 represent the longer period, Indian Ocean wave conditions. It was planned to have significant wave heights with increments of 0.5. However, the wave paddle could not accommodate a maximum wave height of $1.86 \cdot H_s = 1.86 \cdot 1.5 = 2.79$ meter. Therefore, a significant wave height of 1.3 meters is chosen for condition C11. Based on the provided significant wave height and peak period, a JONSWAP spectrum with a peak enhancement factor γ of 3.3 is generated and converted in a steering file which is fed to the wave generator. Bound harmonics generated by non-linear wave interactions are not accounted for in JONSWAP spectra. To overcome this limitation, the wave paddle uses second-order stirring which can only generate bound harmonics with frequencies higher than 0.2 Hz. On a real fringing reef, reflected waves propagating offshore will eventually move out of the domain. In experimental setups with closed domains, these waves will instead reflect back into the domain. To represent reality, active reflection compensation is employed to minimize the amplitude of these reflected waves.

Table 3.2: Wave conditions as tested in the flume, from which each pair of offshore significant wave height and peak period is used to construct a JONSWAP spectrum with γ=3.3. Note that the wave conditions are part of a broader set and the numbering of their IDs therefore has jumps in it.

ID	Delta flume		Prototype	
	H_s [m]	T_p [s]	H_s [m]	T_p [s]
C1	0.5	5.77	1.5	10
C3	0.5	9.24	1.5	16
C7	1.0	5.77	3.0	10
C9	1.0	7.51	3.0	13
C11	1.3	5.77	4.0	10

As could be seen in Table 3.1, reef flat water depths are within the range of 0.17 - 0.67 m. Within the ARISE project, four water levels are tested within this range. Due to limited experimental time in the CREST experiments, it is opted to test two separate water levels. A low tide of 0.33 meter and a high tide of 0.67 meter are chosen to have enough difference between the two tested water levels and to ensure continuous artificial reef element submergence. Although the reef flat water depth will eventually increase due to wave setup, the offshore water depth should stay constant over a full test run. This offshore water depth is equal to the sum of the height of the reef platform (5 meters) and the desired reef flat water depth at the start of the run. As the water volume in the flume is finite, the water which piles up on the reef flat due to wave setup is drawn from the more offshore part of the domain. To balance out this flux, a pump activates when the offshore water depth drops below either 5.33 or 5.67 meters, maintaining a constant offshore water depth. The applied offshore water levels and its corresponding reef flat water depth and prototype value are shown in table 3.3.

Table 3.3: Tested water levels, with in the first column the offshore water depth and the second column the still water depth over the reef flat.

ID	Offshore water depth flume [m]	Reef flat water depth flume [m]	Reef flat water depth prototype [m]
H533	5.33	0.33	1
H567	5.67	0.67	2

With reef flat water depths of 0.33 to 0.67 meters and peak wave periods ranging from 5.77 to 9.24 seconds, the shallow water wavelength, calculated using $L = T\sqrt{gh}$, falls between 10.4 and 23.7 meters. The reef flat constructed in the Delta Flume, which has a width of 45 meters, can accommodate 2 to 4 wavelengths. This range aligns closely with the 3 to 6 wavelengths common in natural fringing reefs.

Artificial reef element

The artificial reef elements used in the CREST experiments are originally designed by Takens (2024) and are 3D-printed by Coastruction. The design of the element aims to capture the geometric complexity of a natural coral reef while incorporating bio-receptive features. The key requirements that governed the element's design were as follows:

1. Tunnels of several sizes should be integrated to provide shelter for fish species.
2. Horizontal ledges should provide sufficient light and attachment area for coral polyps and algae to grow on the element.
3. The element needs to remain stable for all boundary conditions. If this is not the case, the element has to be fixed to the concrete reef platform.
4. The spacing of the elements should be selected to ensure that the flow within the artificial reef consistently falls within either the general flow regime or the inertial flow regime, as defined by

Lowe et al. (2007).

5. The element's dissipation capacity should be optimized by maximizing the element's frontal area and structural complexity.

The final geometry of the element as placed in the Delta Flume can be seen in Panel a) in Figure 3.3 alongside its placement within the full artificial reef in Panel b). The element includes ridges and openings promoting marine life habitation. The element has a height of 0.25 meters and in both directions has a width of 0.40 meters. The volume is equal to 0.0175 m^3. Next to these parameters, the plan area, frontal area and nominal diameter are shown in Table 3.4. The nominal diameter is calculated by determining the diameter of a cylinder with the same volume and height as the artificial reef element.

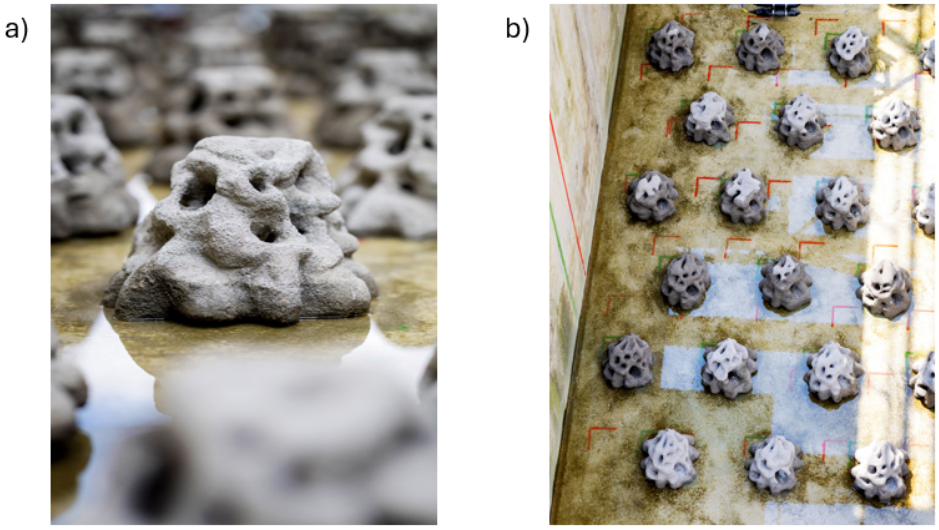

Figure 3.3: Artificial reef element 3d printed by Coastruction (a) and as placed in the Delta Flume in the low-density configuration (b). Photographs are courtesy of Deltares.

Table 3.4: Dimensions of one single Coastruction artificial reef element.

Height [m]	Length [m]	Width [m]	Volume [m^3]	Weight [kg]
0.25	0.40	0.40	0.0175	~30
Diameter D [m]	Nominal diameter D_n [m]	Frontal area A_f [m]	Plan area A_p [m]	
0.40	0.30	0.068	0.106	

Previously, the roughness of a canopy was defined either by the lambda parameters λ_f and or by the porosity n as defined in respectively equations 2.3 and 2.1.

From the artificial reef element's basic characteristics in table 3.4, these lambda parameters and porosity are computed as follows:

$$\lambda_f = \frac{A_f}{A_T} = \frac{A_f}{\frac{B_{flume} \cdot L_c}{n_{elements}}} \tag{3.3}$$

$$\lambda_p = \frac{A_p}{A_T} = \frac{A_p}{\frac{B_{flume} \cdot L_c}{n_{elements}}} \tag{3.4}$$

$$n = \frac{1 - (n_{elements} \cdot V_c)}{h_c \cdot B_{flume} \cdot L_c} \tag{3.5}$$

in which L_c is the length of the artificial reef restoration in the Delta Flume, equal to 10 meters. B_{flume} is the width of the Delta Flume, which is equal to 5 meters. Following these definitions, a set of roughness

parameters for each artificial reef configuration is presented in table 3.5. In this thesis, three different configurations will be covered, reference to as S0, S1, S3. S0 is the base case configuration, in which no artificial reef is present in the flume and is needed to quantify the net effect of introducing artificial reef elements to the system. S1 and S3 represent the low-density and high-density configurations, consisting of 91 and 153 elements, respectively. Additionally, a fourth configuration, S2, was tested, which is essentially the low-density setup supplemented with MOSES artificial reef units positioned just behind the standard 10-meter-long restoration. This configuration is not included in this report because the measurement locations were situated at the edges of the standard restoration, making it challenging to accurately quantify the net effect of the MOSES units.

Table 3.5: Values on the density and spacing of the two considered configurations S1 and S3, including its corresponding lambda parameters and porosity.

Configuration	Number of elements [-]	x-spacing S_x [m]	y-spacing S_y [m]	Frontal area parameter λ_f [-]	Plan area parameter λ_p [-]	Porosity n [-]
S1	91	0.42	0.42	0.1333	0.2078	0.87
S3	153	0.27	0.27	0.2081	0.3244	0.78

With these parameters a comparison can be made between the canopy elements used in the CREST experiments and those used in the experiments conducted in Lowe et al. (2005b) and Lowe et al. (2007). In these experiments, cylinders with a diameter of 5 centimeters and spacings of 5.0, 7.5, 10.0 and 15.0 cm were used. This results in the ratio S/d being in the range of 1-3. In the CREST experiments, the spacing and nominal diameter lead to a S/d_n ratio of 0.9 to 1.4. This is an indication that the spacing/density is selected as such that, although being dependent on A_∞^{rms} as well, the in-canopy flow will be roughly in the same flow regimes as Lowe's experiments and the energy dissipation can therefore be expected to be frequency-dependent.

Figure 3.4 provides a schematic overview of the low-density configuration S1, spanning approximately 10 meters of the reef flat and covering the entire width of the Delta Flume. A detail of this configuration is depicted in Figure 3.5, which shows the horizontal spacing between the elements and a distance from the element to the flume wall of 0.5 times the element's diameter.

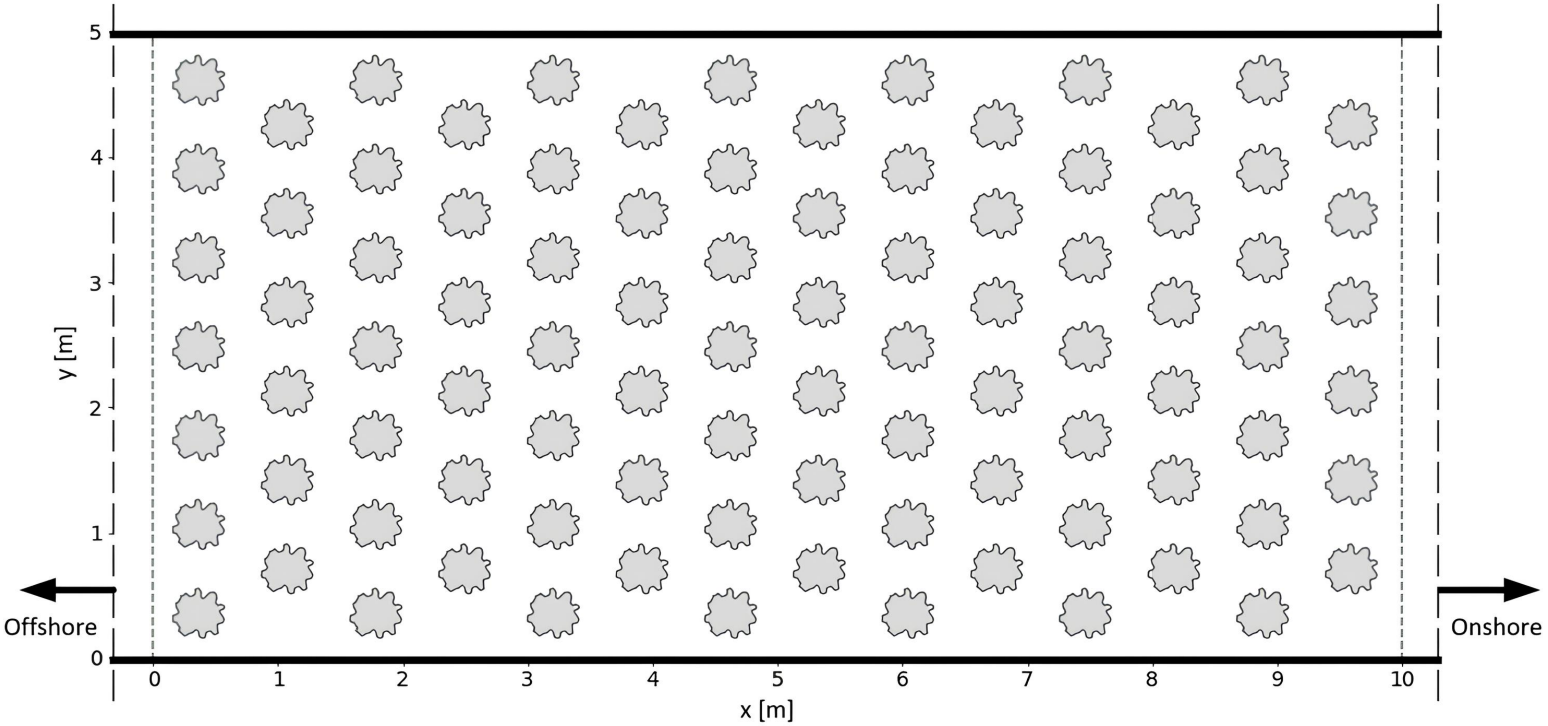

Figure 3.4: Schematic overview of the placement of 91 artificial reef elements over a section of 10 m in case of the low-density configuration S1.

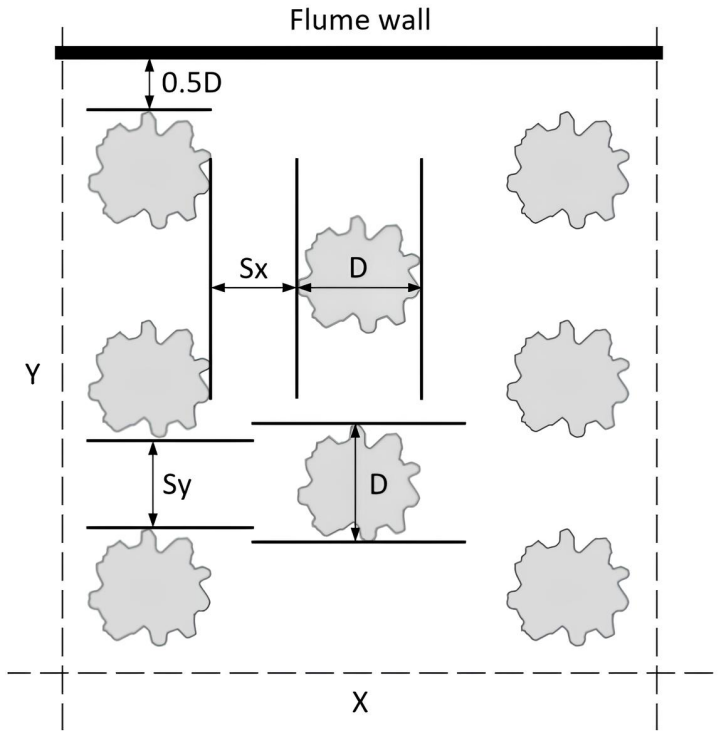

Figure 3.5: Spacing of the elements with respect to each other, vertical and horizontal spacing are equal to each other and boundary elements are placed 0.2 m, the distance of half their diameter off the flume wall. Adopted from Takens (2024)

To conclude on the setup of the physical model, all possible combinations of the 2 presented water levels and 5 wave conditions are ran. This results in 10 runs per artificial reef configuration. As this

thesis covers the three configurations S0, S1 and S3, a total number of 30 runs are analyzed. An overview of these runs is given in Table C.1. In addition to this dataset, wave conditions C3, C7, and C11 are repeated for both water levels, but only for the configurations S0 and S3. This results in an additional 12 runs. An overview of these 'reruns' is given in Table C.2. Section 3.4, diving into the data quality of the pressure sensors, explains the choice to perform the reruns.

3.3. Instruments

To collect flow velocity and water level data needed for quantitative insights in the wave transformation and water level response along the reef transect and hydrodynamics within the restoration canopy, a set of instruments are installed within the flume. Pressure sensors, wave height meters, and flow meters are placed to provide data of the evolution of the water level and flow velocities along the entire reef domain. To acquire a more detailed view of the hydrodynamics within the canopy itself, Acoustic Doppler Velocimeters are implemented. This subsection provides a technical description of each used instrument, along with details on their placement.

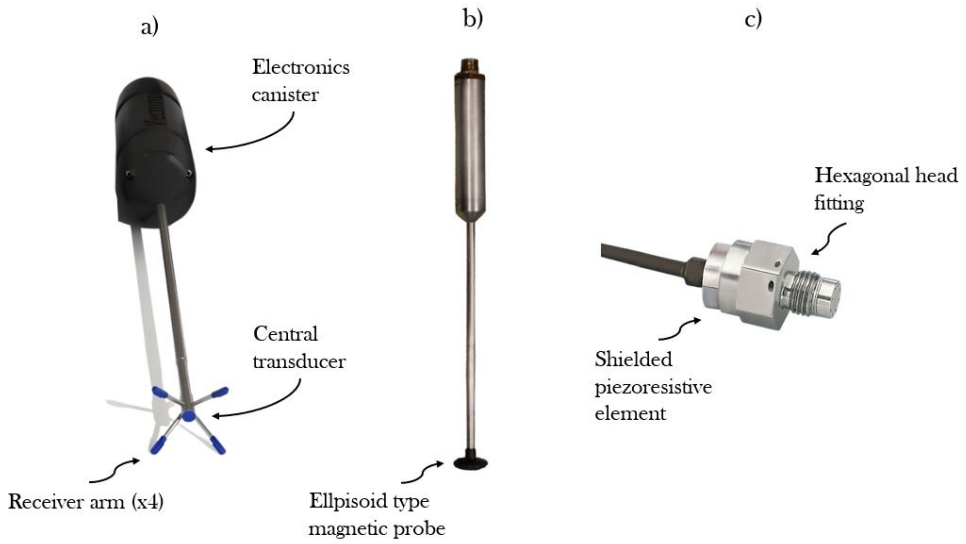

Figure 3.6: Instruments that are installed in the flume with a) an Acoustic Doppler Velocimeter (ADV), b) an Electromagnetic Flow Meter (EMF) and c) a Pressure Sensor (PS) with some elaboration on their key components.

The placement of these instruments within the flume is shown in Figure 3.7. The highest density of measurement locations is present at the forereef slope where the greatest gradients in the wave transformation are to be expected due to shoaling and breaking of waves. At all measurement locations, the EMF is positioned 15 cm above the seabed. Each EMF is installed at roughly the same location of a PS to provide directional measurements. It's important to note that the method described in section 3.5.3 using data from colocated PS and EMF instruments for separating incoming and outgoing waves relies on depth-averaged velocities. Since velocity amplitudes decrease closer to the seabed, the EMF's point deviate from the depth-averaged velocity, particularly in deeper waters offshore from the reef platform. Section 3.5.4 describes how this deviation can be accounted for.

Although the previously mentioned instruments operate with different sampling frequencies, the Deltares logger samples all data at a rate of 120 Hz, allowing for seamless integration for data analysis. After data collection by the Deltares logger, all data is subsampled to a rate of 20 Hz to ensure faster data processing.

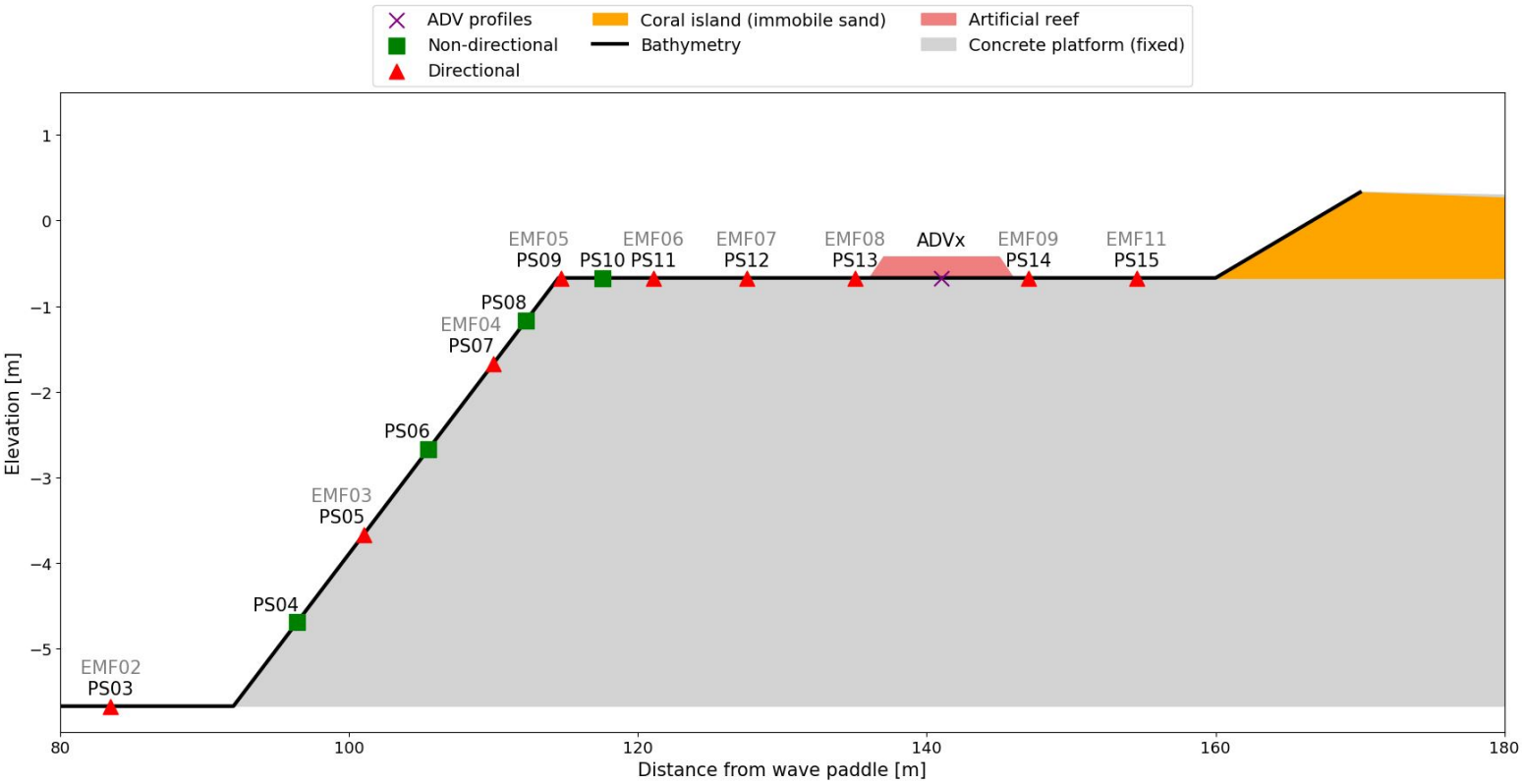

Figure 3.7: Location of standalone PSs and colocated EMFs and PSs as installed in the flume.

Acoustic Doppler Velocimeter (ADV)

Acoustic Doppler Velocimeters produced by Nortek (from now on referred to as ADVs) are used to quantify the velocity profile at the location of the reef restoration. More specifically, the 'vectrino' model of the available ADV models is used, as this model is more suitable for lab applications due to its limited size while still being robust enough to withstand substantial wave forces. The general design and assembly of the ADV can be seen in figure 3.6. The ADV consists of one central transducer and four receiver arms. The central transducer transmits a pair of ultrasound pulses with a frequency of 10 MHz towards a tiny sampling volume within the water column where it is reflected by very fine air bubbles after which the reflected signal is received by either of four receiver arms. The two ultrasound pulses are transmitted with a time lag between them. Therefore, a Doppler phase shift can be observed in the received signal, which is in turn converted to flow velocity by scaling with the speed of sound in water. For each receiver, a signal amplitude, signal-to-noise ratio and correlation are provided to determine the quality and accuracy of the velocity data. Each velocity component (x, y, z) is constructed with signals from two separate receivers. The velocity's z-component is constructed twice as the z-components are more difficult to record and therefore prone to error. In other words, the ADV gives both u_{z_1} and u_{z_2} as output. In figure 3.8 the types of ADVs used in the experiments are depicted. First of all, a side-looking ADV (type a) is used. Next to this, rigid head (type b) and flexible head (type c) ADVs are used. The flexible head ADV has a field probe and lab probe variant, with the field probe having a larger and sturdier probe than the lab variant as it is usually subject to higher hydrodynamic forces in the field.

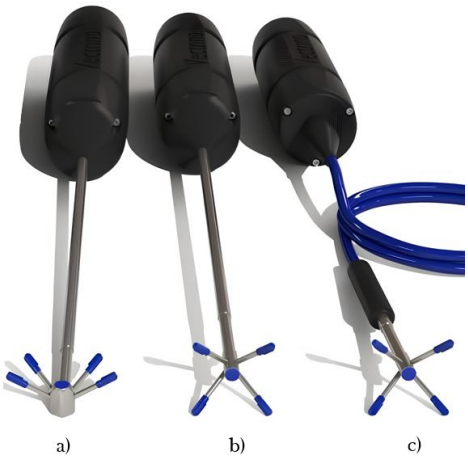

Figure 3.8: Different type of ADVs as installed in the ADV arrays with a) a rigid-head side-looking ADV, b) a rigid-head forward-looking ADV and c) a flexible-head forward-looking ADV. Of the flexible-head type ADVs a field variant has also been used, with a larger sturdier probe. **I now see that a) should be a flexible head ADV, will fix this in the final version of the report**

Table 3.6: Numbering of the used ADVs and their characteristics. ADV array A contains ADV1,2,3 and ADV array B contains ADV4,5,6.

ADV ID	Head type	Probe type	Probe direction	Distance probe-to-sampling volume [cm]
ADV1	Rigid	Lab	Side-looking	5
ADV2	Flexible	Field	Forward-looking	10
ADV3	Flexible	Lab	Forward-looking	5
ADV4	Flexible	Field	Forward-looking	5
ADV5	Rigid	Lab	Forward-looking	5
ADV6	Rigid	Lab	Forward-looking	5

3.3.1. ADV placement

The position in which the ADV is placed may dictate the magnitude of the observed velocities due to the flow patterns in and around the artificial reef elements in combination with the decay of wave-driven velocities within the water column. To aid in the choice of the exact ADV array locations, exploratory CFD simulations conducted by Akshay Patil are considered. These CFD simulations modeled turbulent channel flow, did not include a free surface flow like present in a wave flume. Instead, a rigid lid assumption is utilized, with unidirectional flow driven by a pressure gradient (Patil, 2023). Although the artificial reef setup in these simulations differs in density, spacing, and number of elements compared to the setup in the Delta Flume experiments, flow convergence and obstruction are expected to behave similarly. The flow patterns around the roughness elements is visualized in Figure 3.9.

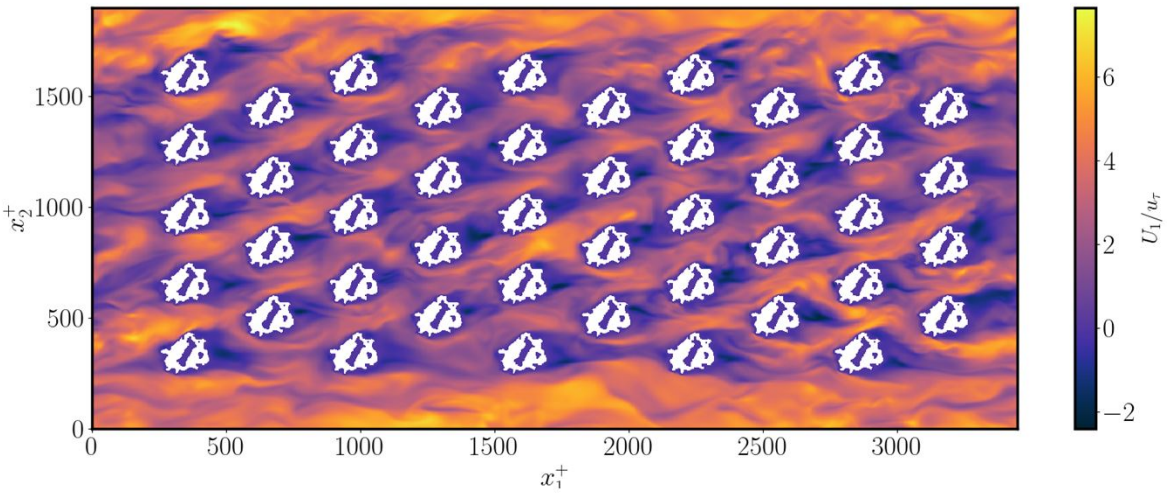

Figure 3.9: A snapshot of the top view of a high-resolution CFD model performed by Akshay Patil, capturing unidirectional flow over artificial reef elements.

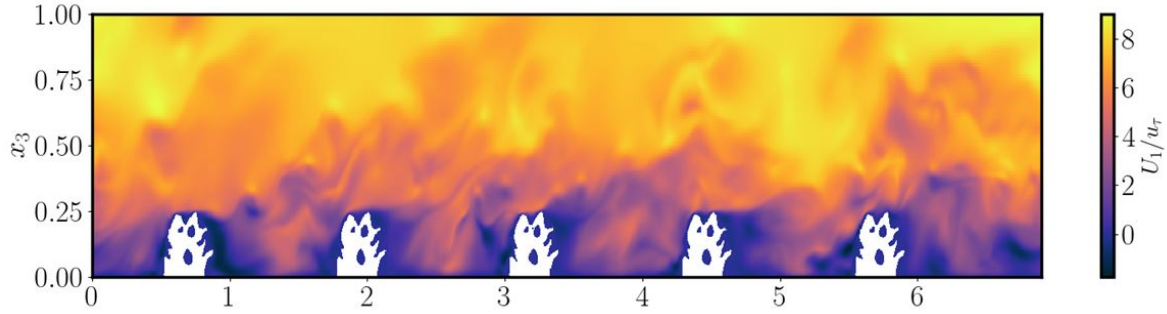

Figure 3.10: A snapshot of the side view of high-resolution CFD model performed by Akshay Patil, capturing unidirectional flow over artificial reef elements. This side view is a slice at x3 = 0.08 m in Figure 3.9

From this simulated flow pattern, it can be seen that the most distinct flow disturbances occur just behind the element (lower flow velocities due to flow obstruction) and right in between two elements (higher flow velocities due to flow convergence). Although the element geometry and spacing differs from the CREST experiments, the pattern of flow obstruction and convergence is expected to be roughly equal. To achieve two primary objectives — 1) understanding the flow's spatial variability and 2) identifying measurement points to calculating a representative average in-canopy flow velocity — the velocity profiles are positioned at these two locations. The choice for these specific measurement locations is in agreement with the experimental set-up of Lowe et al. (2005b) and findings of Gijón et al. (2021), as previously discussed in section 2.2.3. Additional requirements for placing the ADV instruments include ensuring that the ADV arrays are not too close to the wall to avoid flow disturbances, and that they are positioned at least 25 centimeters away from the flume centerline to prevent obstruction of the lines along which the laser scanners measure. The mounting system was also strategically designed to minimize flow disturbance caused by the ADV devices and the mounting system itself.

By taking into account the previously presented requirements, a final set up was designed. How this ADV array setup is placed within the staggered grid of the artificial reef can be seen in Figure 3.11 in which ADV array A is placed in the zone with expected flow acceleration and ADV array B in the zone with expected flow deceleration.

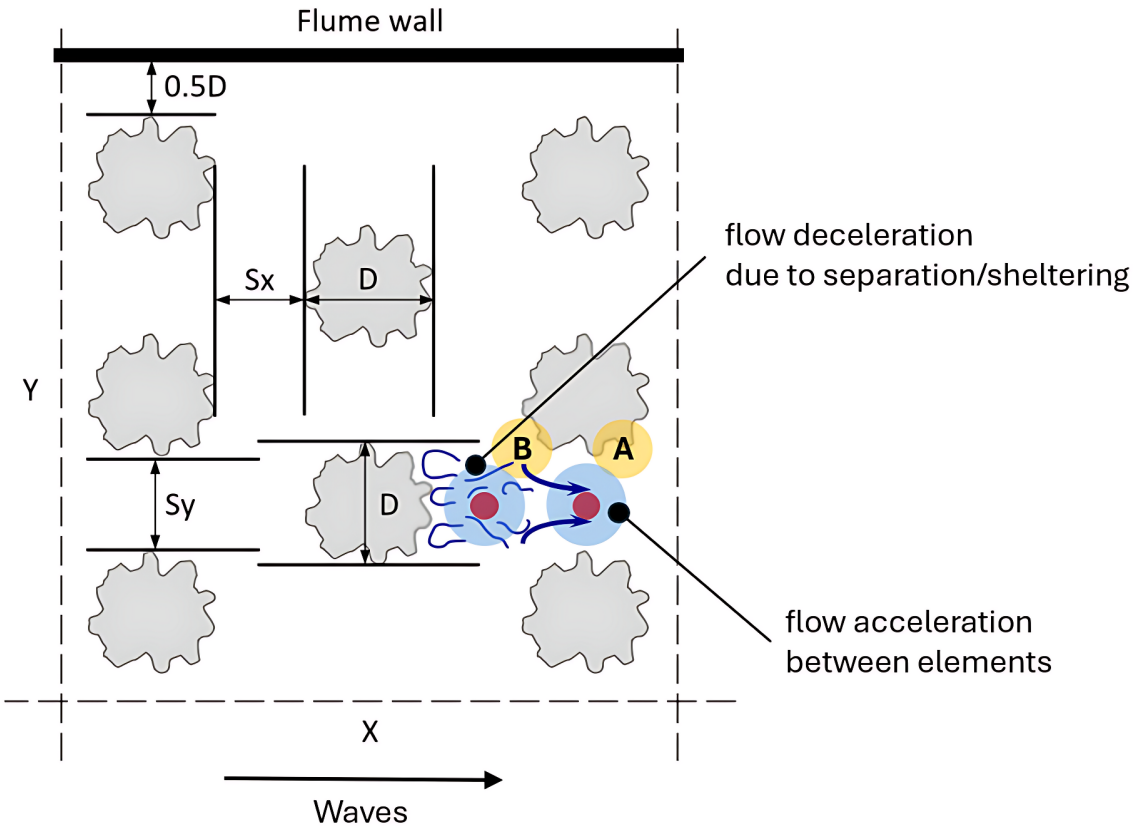

Figure 3.11: Spacing of the elements with respect to each other, with expected zones of flow acceleration and deceleration at which ADV array A and ADV array B will be placed. Adopted and modified from Takens (2024)

Figure 3.12 presents the complete artificial reef configurations S1 in blue and S3 in red. The locations of the two ADV arrays within this artificial reef setup is depicted with red dots. The canisters of ADV array A are embedded in one of the artificial reef elements to minimize flow disturbance. The configurations are designed as such that the 'embedded' element remains stationary. This ensures ADV array A does not have to be relocated when switching artificial reef configurations.

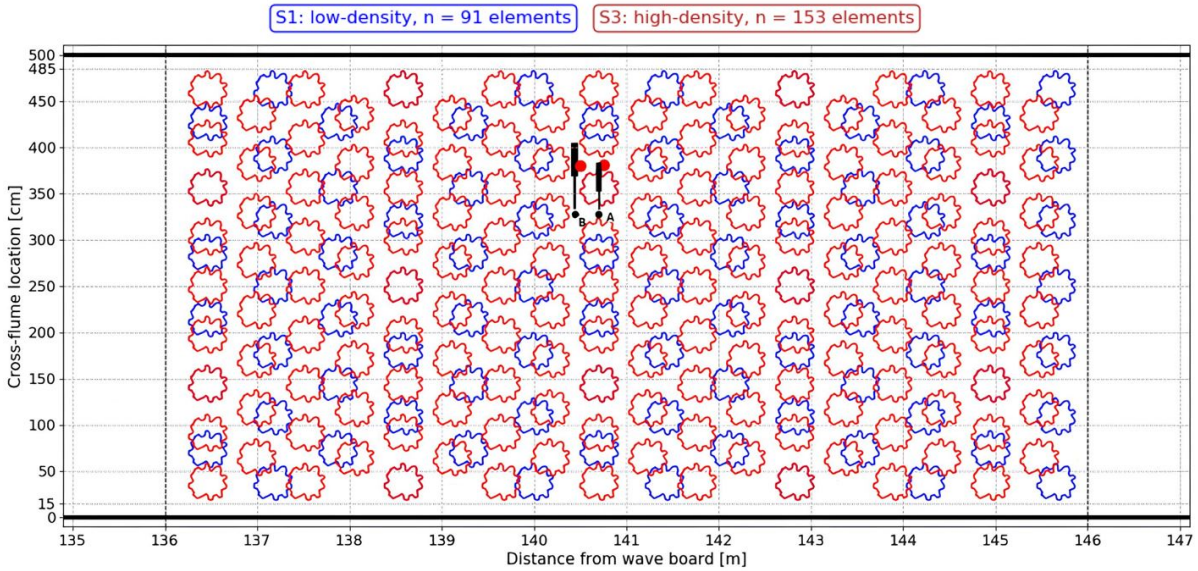

Figure 3.12: The location of the ADV array with respect to the low-density and high-density artifical reef. The location of the ADV arrays are depicted with a red dot and the placement of the ADVs itself can be seen in black. Note that the element in which ADV array A is embedded remains at the same place for both configuration. Figure adapted from Takens (2024).

ADV1 to ADV3 are placed in ADV array A. The mounting of ADV 2 and 3 are embedded in an artificial reef element and its canister are placed above the water surface. ADV1 is placed pointing down to ensure the mounting to be as high as possible, here again the canister is placed above the water. In turn, ADV4 to ADV6 are placed in ADV array B, just offshore of array B. As ADV5 and ADV6 are rigid head ADVs, the canister is fixed to the probe and can not be placed outside of the water. This will inevitably lead to flow obstruction. ADV4 has a flexible head and is positioned at the top of array B while its canister is placed outside of the water column.

Figure 3.13 and 3.14, respectively, show the top and side view of the ADV arrays as it was installed in the wave flume. In the ideal setup, the 3 ADVs making up a single array would have the exact same x and y-coordinates and only differ in height to measure in-canopy and free-stream flow. However, the practical constraints of the mounting system together with slight errors in placement resulted in offsets from this ideal setup. The ADV locations differ by a maximum of 2.1 cm in array A and 3.2 cm in ADV array B in the cross-shore direction. In the cross-flume direction, their positions deviate by up to 1.3 cm in array A and 4.2 cm in ADV array B. Furthermore, the ADVs are positioned slightly off from their target heights of 10, 20, and 30 cm above the flume bottom. In array A, the deviations from the desired heights are 1.4 cm, 0.2 cm, and 0.3 cm, respectively. In array B, the deviations are 0.3 cm, 0.3 cm, and 1.4 cm, respectively. The distance between ADV array A and array B is measured to be 36.8 cm.

These deviations from the ideal ADV array are manageable and won't cause serious inaccuracies in flow measurements.

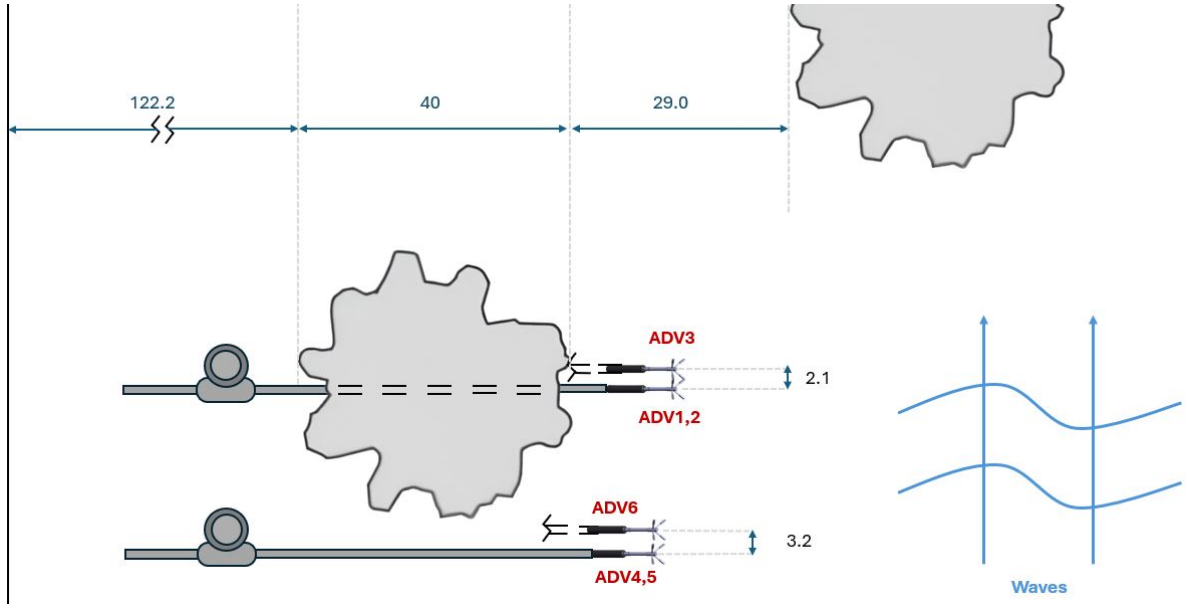

Figure 3.13: The location of the ADV and its mounting system as installed in the flume as seen from the top.

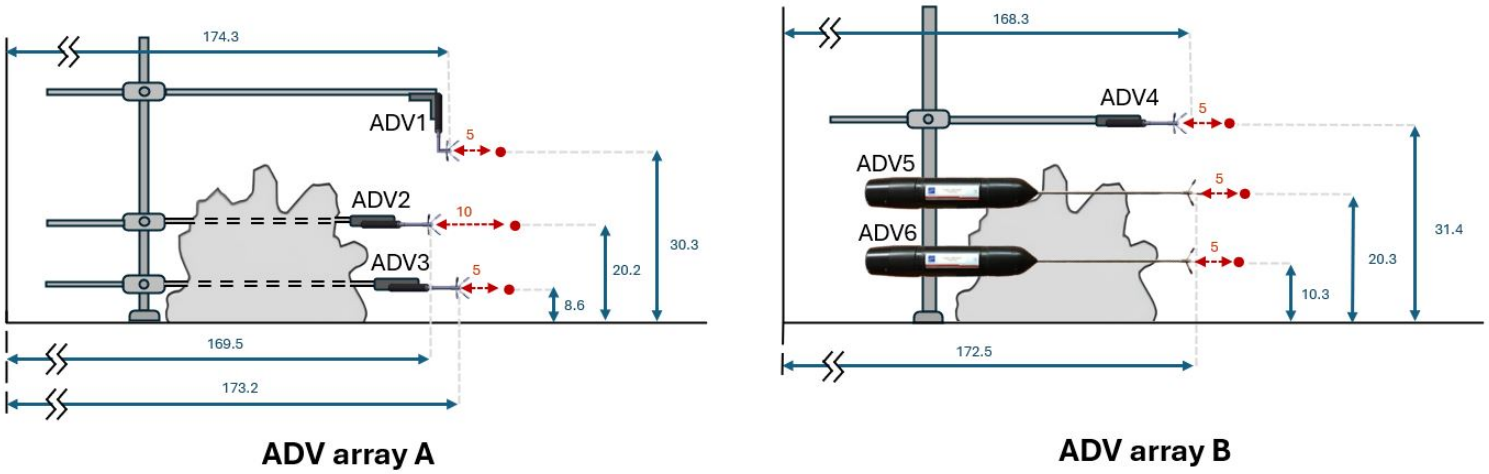

Figure 3.14: The location of the ADV and its mounting system as installed in the flume as seen from the side for both ADV array A and B.

Besides two exceptions, all ADVs are installed as such that receiver arms 1 and 3 construct the cross-shore velocity component. The first exception being the bottom ADV in array A (ADV3), which was rotated 90 during configuration S3 runs and all reruns. This adjustment was made to ensure that receiver arms 2 and 4 would construct the cross-shore velocity component as the receiver arms 1 and 3 had been performing poorly. Additionally, due to placement practicalities, the bottom ADV in ADV array B (ADV6) was rotated during initial installment and constructs the cross-shore velocity component with receiver arms 2 and 4 during all performed runs.

A picture of the actual set up in the flume can be seen in Figure 3.15.

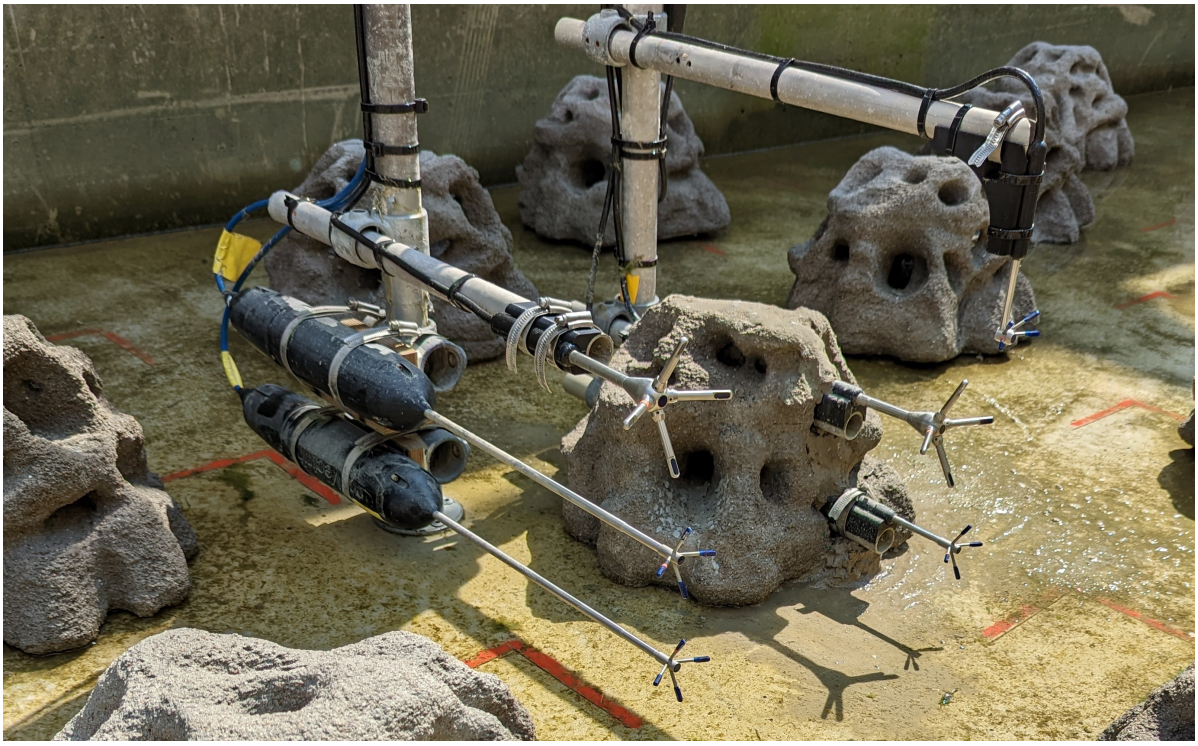

Figure 3.15: Picture of the actual ADV set up during testing.

3.3.2. Pressure sensor (PS)

Pressure sensors (from now on referred to as PS) are used to measure the relative pressure at the bottom of the flume. This pressure is consequently used to determine the water surface elevation in the flume. The pressure sensors used are from the model Kulite HK M375. The principle of operation of these pressure sensors is based on a piezoresistive silicon diaphragm. This diaphragm deforms when pressure is applied on it and the deformation is converted to a voltage output proportional to the applied pressure. The sensor includes a temperature compensation to neutralize the effect of temperature variations on the resistance of the silicon diaphragm. The accuracy of the Kulite HK M375 is +/- 1 bar (, https://kulite.com).

3.3.3. Electromagnetic flow meter (EMF)

Electromagnetic flow meters (from now on referred to as EMFs) can measure flow velocities by comparing two voltages measured by a probe consisting of two platinum electrodes at either end of the device. The basis of this method is the law of Faraday which states that a moving charge in a magnetic field creates a potential difference proportional to the velocity of the charge carried by the flow. The EMF's probe must be connected to a control unit to function, in this case it is connected to the Deltares system which can adjust the output's gain and zero shift as well as providing power to the probe. The accuracy of the EMF measurement is +/- 0.01 m/s +/- 1% of the measured value (Deltares, 2012). The EMFs provided by the University of Plymouth (EMF07 - EMF11) have a fixed time delay dependent on the sampling rate set for the instrument. The Plymouth EMFs were set to sample at a frequency of 16 Hz, corresponding with a time delay of 0.5 seconds. This time delay is taken into consideration during the data processing.

3.4. Data quality assessment

3.4.1. ADV data quality metrics

To aid in the selection of a data subset suitable for data analysis, data quality metrics are computed. These data quality metrics are determined prior to performing any data filtering steps presented in Section 3.5. The metrics which are computed are the percentage of outliers ($outliers$ [%]), the variance

Table 3.7: Requirements for ADV data quality for individual beams and the average of two beams. It is important to note that the requirements for the average of two beams are stricter than those for individual beams.

Metric	Requirement
% outliers	< 5
σ^2_{noise}	< 100
$\%_{corr.<70}$ individual beam	< 40
$\%_{corr.<70}$ average of beams	< 30
$\overline{SNR}$ beam 1	> 1
$\overline{SNR}$ average of beams	> 1.5

of the removed noise (σ^2_{noise}), total percentage of correlation below 70 ($corr._{<70}$ [%]) and mean signal-to-noise ratio ($\overline{SNR}$). The correlation and SNR are provided per ADV beam by the ADV acquisition software. The variance of the removed noise is calculated as the variance of the signal eliminated by applying a low-pass filter at 0.5 Hz, as outlined in Section 3.5.1. Similarly, the percentage of outliers is determined by the percentage of data points removed using the despiking method of Goring and Nikora (2002), as also described in 3.5.1.

Additionally, the measured velocity signals are visually compared to the nearest ADV to ensure data consistency and identify anomalies. The ADV timeseries is deemed of sufficient data quality to use for analysis purposes if, for all individual ADVs, the metrics from this timeseries satisfy 5 or more of the 6 requirements presented in Table 3.7. This table presents requirements for both individual beams and the combination of the two relevant beams. For instance, the mean SNR of a single beam can not be lower than 1, while the average of the mean SNRs of two beams must exceed 5.

3.4.2. ADV data quality assessment

To provide insight into the quality assessment of the ADVs, this section presents the quality metrics defined in Section 3.4.1. Since the ADV data quality remains relatively consistent across runs within a single configuration, run H533C3 is selected as a representative example. To illustrate the data quality assessment, the specific case of H533C3 is considered. Table 3.8 shows ADV data quality metrics across all ADVs and artificial reef configurations for H533C3. Data quality metrics from other runs can be seen in the data quality metrics tables in Appendix D

Table 3.8: Overview of the ADV quality metrics as defined in section 3.4.1 for runs SxH533C3. Note the poor data quality metrics for the low-density configuration S1 and the relatively low correlation in beam 1 and low mean SNR for ADV6 in both the bare-reef configuration S0 and the high-density configuration S3.

S0H533C3	outliers [%]	σ^2_{noise} $[m^2/s^-3]$	$corr._{<70,1}$ [%]	$corr._{<70,2}$ [%]	$\overline{SNR_1}$ [-]	$\overline{SNR_2}$ [-]
ADV1	0.28	1.35	2.45	6.19	27.7	27.4
ADV2	0.24	0.73	0.23	0.29	23.2	24.5
ADV3	0.15	0.75	4.26	1.64	14.9	19.5
ADV4	0.41	1.44	0.82	0.86	23.1	24.1
ADV5	0.21	1.14	1.37	4.27	21.9	21.8
ADV6	2.75	22.90	49.29	0.99	-2.3	-0.8
S1H533C3	outliers [%]	σ^2_{noise} $[m^2/s^-3]$	$corr._{<70,1}$ [%]	$corr._{<70,2}$ [%]	$\overline{SNR_1}$ [-]	$\overline{SNR_2}$ [-]
ADV1	0.24	2.13	4.80	8.21	27.5	27.3
ADV2	0.28	2.25	2.09	2.63	23.0	24.3
ADV3	0.00	1445.64	6.74	87.41	4.7	0.4
ADV4	0.33	2.48	2.52	3.00	23.8	24.0
ADV5	0.30	4.07	4.86	7.88	22.5	21.8
ADV6	1.99	9.78	53.57	3.51	17.7	18.9
S3H533C3	outliers [%]	σ^2_{noise} $[m^2/s^-3]$	$corr._{<70,1}$ [%]	$corr._{<70,2}$ [%]	$\overline{SNR_1}$ [-]	$\overline{SNR_2}$ [-]
ADV1	0.27	2.55	4.58	7.99	27.8	26.5
ADV2	0.30	2.99	3.30	4.23	23.1	24.5
ADV3	0.23	2.72	10.68	5.96	10.0	0.3
ADV4	0.32	2.74	2.98	3.90	23.9	24.2
ADV5	0.29	4.75	5.04	7.68	22.5	21.8
ADV6	1.67	7.30	44.74	3.27	12.1	8.4

The most notable anomaly in Table 3.8 is the data quality of ADV3 during configuration S1, note the extremely high noise variance and high percentage of points with correlation lower than 70%. These two poor data quality metrics make that only 4 out of the 6 data quality requirements are satisfied and the data of ADV3 during the configuration S1. To double-check this claim, the timeseries of ADV3 is compared with ADVs in the same array which did meet all data quality requirements. In this timeseries it can be seen that ADV3 indeed, as already indicated by the data quality metrics, produced erratic data which can not be used in analysis.

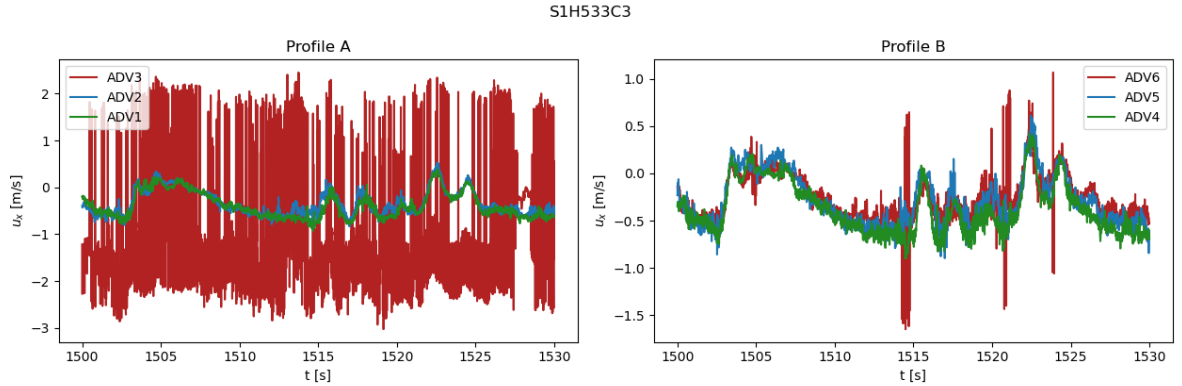

Figure 3.16: Snippet of the ADV velocity timeseries as measured during run S1H533C3. Note the erratic behaviour of ADV3.

Another notable anomaly in Table 3.8 is the high percentage of points with correlation lower than 70% for ADV6 in configurations S0 and S3. This low correlation results in the ADV6 timeseries satisfying 5 out of 6 data quality requirements. Failing to satisfy all 6 data quality requirements is deemed acceptable as long as the timeseries aligns relatively well with ADV timeseries in the same array. Figure 3.17 shows that the ADV6 timeseries does not deviate too much from the timeseries of ADV4 and 5. Although the ADV6 time series contains a large number of spikes and outliers, these can be filtered out. This is shown by Figure 3.19, which demonstrates that, despite the poor correlation for beam 1, filtering ADV6 for run S0H533C3 produces a time series suitable for data analysis.

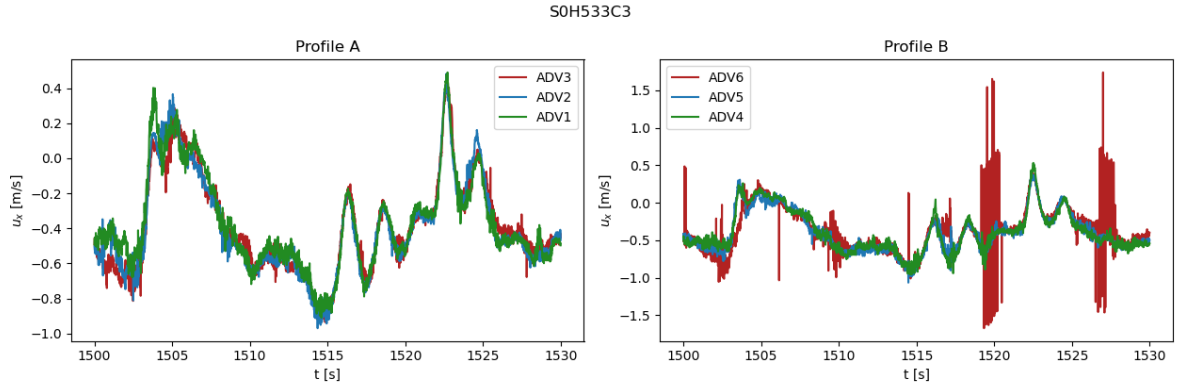

Figure 3.17: Snippet of the ADV velocity timeseries as measured during run S0H533C3. Note the large amount of spikes/outliers in ADV6.

In Appendix D, tables covering the data quality metrics of other runs reveal the same pattern in which ADV3 of the low-density configuration S1 does not meet the data quality requirements and ADV6 records data with low correlation across all tested artificial reef configurations. Furthermore, for some timeseries of ADV6, the requirement on mean SNR of beam 2 is not met. However, the timeseries proved to consistently align with other ADV timeseries which did meet all data quality requirements.

Concluding on this ADV data quality assessment, the time series from all six ADVs can be used to analyze the data for runs involving the bare reef case S0 and the high-density artificial reef. However, it should be noted that during these runs, ADV6 acquires velocity data with low correlation. On the contrary, when analyzing runs with low-density artificial reef configuration S1, only the timeseries of the upper four ADVs (ADV1, 2, 4, 5) can be used.

3.4.3. PS data quality

After performing the S0, S1, S2 and S3 test runs (in that order) in the physical model it was discovered that the signals retrieved by the pressure sensors contained a drift, i.e. after calibrating the pressure sensors to the offshore floater the pressure sensor output would diverge and present different still water levels. On top of that, the drift varied across pressure sensors. This indicates that, in addition to an absolute error in determining the mean water levels, there are also relative errors between pressure sensors, affecting the observed shape of wave setdown and setup.

Next to the drift, the standard deviation of the signal recorded by the pressure sensors was discovered to vary over time as well. Instead of affecting the observed mean water levels, wave heights and period determined from these recorded pressure signals will be unreliable as it is dependent on the measured standard deviation.

Both these effects were presumably caused by both the influence of suspended sand on the pressure sensors as well as the clogging of the geotextile sealing the box in which the pressure sensors were installed. Especially for PS4, 5 & 7, the suspended sand resulted in unreliable results. After finish-

ing the S1 tests, it was decided to install sand traps which clearly improved the data quality of some pressure sensors. However, PS7, 12 still showed erratic behaviour and others. After finishing the S3 tests, the decision was made to install the PSs in a pvc on top of the flume bottom. With this new PS installation, a set of dedicated wave conditions (C3, C7 and C11) would be repeated for both the S0 and S3 configuration and both water level cases. This repeated set of runs can be seen in Table C.2.

In figure 3.18, the significant wave height and wave setup of different artificial reef setups are compared for the same wave condition of C7 ($H_{m0} = 1.0, T_p = 5.77s$) with a water depth of 0.33 m. Note, for both variables, the differences within the runs with the original PS installment method. Panel a) illustrates that, for the reruns, significant deviations in significant wave height H_{m0} only begin to appear beyond PS13. These deviations can be attributed to the presence of the artificial reef elements. Furthermore, the even more delicate wave setup in Panel b) matches very well between the rerun conditions. Therefore it is reasoned that the new installment method results in reliable results for all PSs.

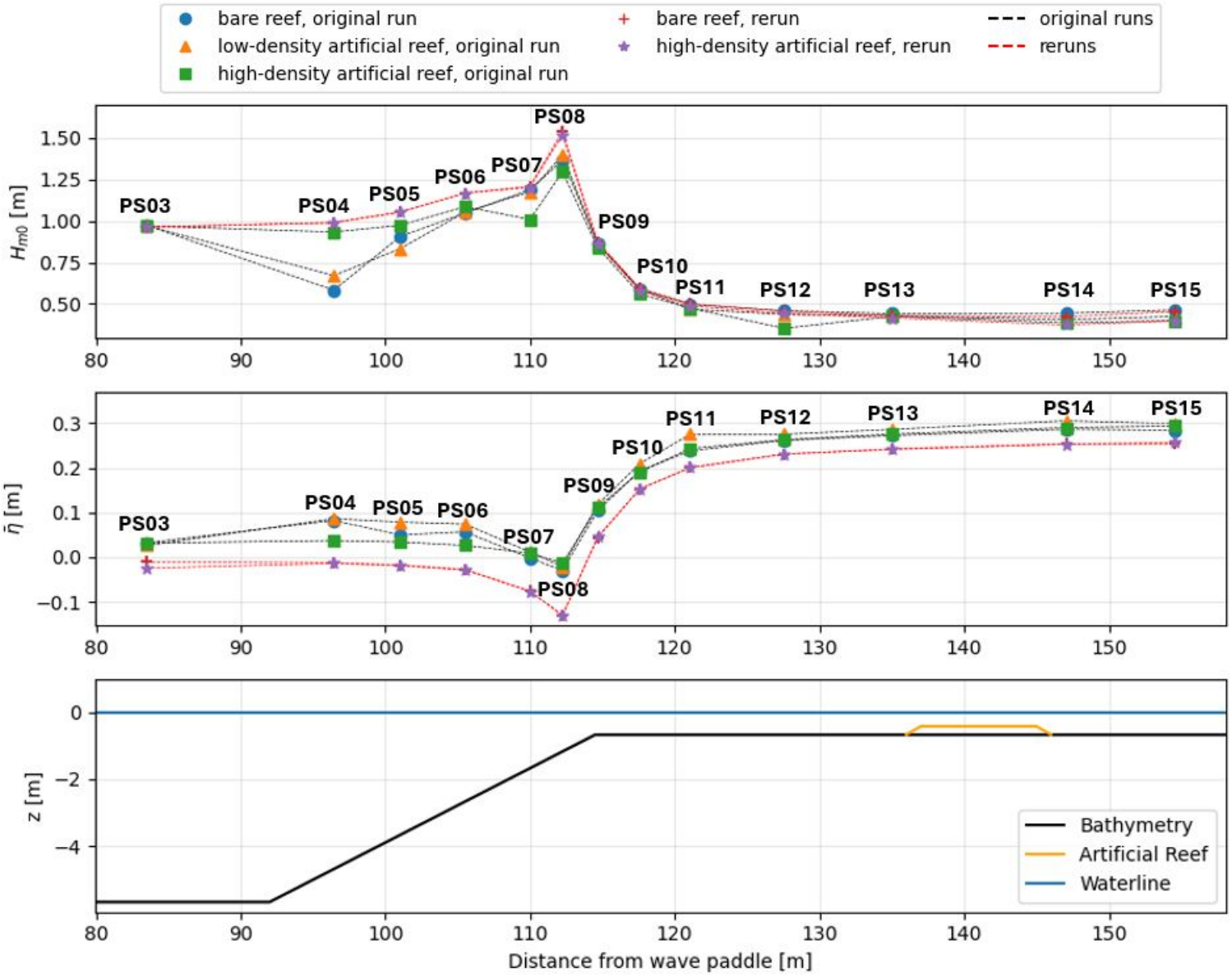

Figure 3.18: Transformation of the significant wave height H_{m0} and wave setup $\overline{\eta}$ for S0, S1, S2 and S3 runs for wave condition C7 during low water level. The S0 and S3 reruns are also included and denoted by a red dashed line.

The data of PS13 and PS14 are essential as the incoming water level series can be used to isolate the

direct effect of the artificial reef on the incoming wave energy. To assess the reliability of these sensors during the original runs, the incoming wave height of an original run is compared with that of a rerun with the same forcing. Table 3.9 indicates that, for more energetic wave conditions, the difference is on the order of O(1) cm, while for less energetic conditions, it is on the order of O(0.1) cm. Given $H_{m0,in}$ magnitudes of 30–50 cm, these deviations are relatively small. Therefore, it is concluded that the drift in the pressure sensors did not seriously affect sensors PS13 and PS14 and that, for all original test runs, its data can be utilized. With this data, the effect of the artificial reef on incoming wave energy from PS13 to PS14 (across the artificial reef) can be studied in detail.

Table 3.9: Differences in incoming wave height as measured at PS13 and PS14 for wave conditions C3 (column 1), C7 (column 2) and C11 (column 3). These differences are determined by comparing the incoming wave height observed in the repeated runs with that in the original runs. As the repeated runs are assumed to be the ground truth, errors in the original runs can be identified.

$h_0 = 0.33$ m		$H_{m0} = 0.5$ m, $T_p = 9.24$ s	$H_{m0} = 1.0$ m, $T_p = 5.77$ s	$H_{m0} = 1.3$ m, $T_p = 5.77$ s
PS13 $\Delta H_{m0,in}$ [cm]	S0	0.34	0.97	1.23
	S3	0.43	1.03	1.23
PS14 $\Delta H_{m0,in}$ [cm]	S0	0.30	1.71	2.34
	S3	0.28	1.18	1.69
$h_0 = 0.67$ m		$H_{m0} = 0.5$ m, $T_p = 9.24$ s	$H_{m0} = 1.0$ m, $T_p = 5.77$ s	$H_{m0} = 1.3$ m, $T_p = 5.77$ s
PS13 $\Delta H_{m0,in}$ [cm]	S0	0.06	0.87	0.38
	S3	1.29	0.49	0.29
PS14 $\Delta H_{m0,in}$ [cm]	S0	0.75	1.27	0.77
	S3	2.71	0.28	0.44

Concluding, this PS data analysis leads to two datasets:

- A limited dataset of reruns of which all PS and EMF data can be used. The relevant runs and their hydrodynamic conditions are displayed in an overview in Table C.2.
- A dataset including all original runs of which only the collocated PS and EMF data at x = 135 m (PS13, EMF8) and x = 147 m (EMF8, EMF9) will be used. The relevant runs and their hydrodynamic conditions are displayed in an overview in Table C.1.

3.5. Data processing

3.5.1. Timeseries filtering

The data obtained by the instruments might not always be usable due to noise or offsets. To obtain a subset of ADV, PS and EMF data with appropriate quality, post-processing steps have to be performed. Firstly, his subsection will elaborate on the steps performed to arrive at such a desirable data subset. Filtering of the data does not guarantee that the resulting data is of sufficient quality. Therefore, this subsection will also elaborate on the process of obtaining metrics to assess the data quality and selecting and removing test runs or with insufficient data quality. The filtering procedure is applied to the ADV data in the order as presented below.

Despiking algorithm

To remove spikes from the velocity timeseries provided by the ADVs, the despiking algorithm proposed by Goring and Nikora (2002) is used. This algorithm establishes a threshold based on the mean and standard deviation of the mean (μ) and standard deviation (σ) of the provided signal. A data point is removed from the signal, if the point falls outside this threshold ($\mu + -k \cdot \sigma$). I.e., if the deviation from the mean velocity exceeds $k\sigma$. In this case, a k value of 1.5 is applied. These thresholds are not only based on the velocity but also on its (higher) derivatives to filter out abnormal accelerations. The algorithm is applied in iterations, meaning that after the initial round of despiking, the data is checked for any new spikes that may have emerged due to the changes in the dataset after the first removal.

The values removed by the despiking algorithm are replaced by means of a cubic spline interpolation to ensure a smooth signal without gaps from missing data.

Low correlation filter

As mentioned in the ADV's description, a correlation coefficient is provided for each receiver arm. The correlation quantifies the similarity between the echoes from the initial and lagged pulse transmitted via the central transducer. These correlations are normalized to range from 0% to 100%, where higher values suggest greater confidence that the system measured its original pulses and correctly determined the Doppler phase shift. These correlations are used as a key data quality metric and a threshold is established to identify measurement with sufficient and insufficient data quality. Traditionally, although dependent on the specific dataset, a correlation threshold of 70% has been used to identify high-quality measurements (Nortek, 2025). In the ADV data quality overview in Table 3.8 it can be seen that in general the amount of measurements below the 70% threshold is in the order of single percents and visual inspection confirms measurements below this threshold correspond mostly with outliers. These findings confirms that the 70% threshold is a safe choice for this specific dataset.

It should be noted that for all ADVs except all runs for V6 and the S3 and repeated runs for V3, receiver arms 1 and 3 are used to construct the x-component velocity. For the aforementioned exceptions, receiver arms 2 and 4 are used. Consequently, the mean correlation provided for these two receiver arms is used to remove datapoints with a mean correlation lower than 70%. The removed data points are subsequently filled using cubic spline interpolation.

Low-pass filter

This filtering technique is applied to signals acquired by the PSs, EMFs and ADVs. The filter smooths out the signal by allowing only the lower-frequency components (those with frequencies below the cutoff frequency of 2 Hz) to pass through. Any higher-frequency components (those above the cutoff) are attenuated, meaning their influence on the signal is reduced. The higher the filter's order, the more sharply it will attenuate frequencies above the cutoff. In this case a Butterworth with an order of 4 is used, which is recognized as a moderate transition between passed and attenuated frequencies (Selesnick and Burrus, 1998).

In figure 3.19 it is shown what the 3 aforementioned filtering steps look like in practice when filtering a cross-shore velocity timeseries measured by an ADV. It can be seen that the despiking algorithm removes the greatest abnormalities in the signal but is not able to filter out sustained series of outliers. The data points with a mean correlation lower than 70% correspond with the regions with sustained noise and by removing and interpolating these the signal is smoothed out further. Finally, the low-pass filter removes all higher oscillations and therewith the sustained series of outliers as well.

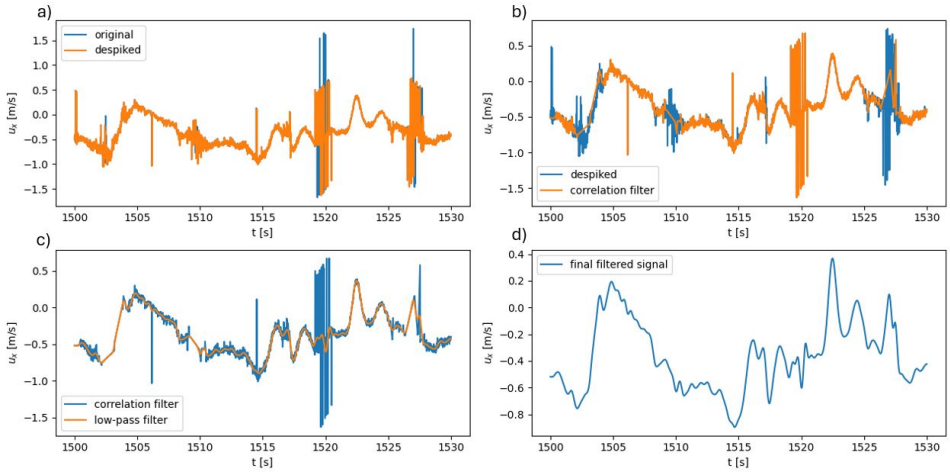

Figure 3.19: Step by step filtering of a velocity timeseries from run S0H533C3 measured by the lowest ADV in ADV array B (V6) with steps in chronological order:
a) Despiking the signal with the Goring and Nikora despiking algorithm and interpolating removed data points.
b) Removing all data points with a mean correlation lower than 70% and interpolating removed data points.
c) Attenuating all higher-frequency components (those above the cutoff frequency of 2 Hz).
d) The filtered, 120 Hz signal, which will be down-sampled to 20 Hz for faster data handling.
Note that before each filtering step the signal is showed in blue, whereas the signal after the filtering step is depicted in orange

Down-sampling

Since the Deltares system sampled all data at a rate of 120 Hz, but the focus of this thesis is on a time scale on the order of magnitude of 1 Hz, all data will be down-sampled to a sampling rate of 20 Hz. This adjustment results in significantly faster data processing. To arrive at this lower sample rate, a down-sampling technique with a rolling averaged is used. Firstly, for each new down-sampled value, this method computes the average of N original samples. In this case, N is equal to 6, the old sample rate divided by the desired lower sample rate. This results in a smoothed out version of the original signal, but still with a sample rate of 120 Hz. To arrive at a sample rate of 20 Hz only one value of every N values of the smoothed out signal is kept.

3.5.2. Pressure to surface elevation

To be able to do an elaborate analysis of the water level oscillations and therewith retrieve wave parameters, the raw pressure p retrieved by the pressure sensors in the Delta flume needs to be converted to free-surface elevation η on which a spectral analysis can be performed. The sampling frequency f_s of the pressure sensors is 120 Hz. Firstly, the rolling average of the fluctuations in the atmospheric pressures measured by a barometer on the premises of the Delta Flume are substracted from the PS signal. This is done to isolate the effect of the hydrostatic and hydrodynamic pressures on the PS.

To go from the pressure to actual surface elevation, a dynamic pressure correction is needed. The total pressure in the case of a wave is the hydrostatic pressure p_0 plus the wave-induced or dynamic pressure p_{wave}. In deep or intermediate water, the magnitude of this dynamic pressure p_{wave} caused by the oscillations in the water level are dampened out towards the bottom of the water column.

In deep or intermediate water, since the pressure sensors (PS) are positioned at the bottom of the flume, the recorded pressure is mainly a result by hydrostatic pressure, with only a fraction of the wave-induced pressure fluctuations reaching the sensors. Shorter-period waves require greater correction than longer-period waves because their velocity amplitude decreases more rapidly with depth. To account for this relationship between water depth and wavelength, the dynamic pressure is expressed as a function of kh:

$$p_{wave} = \frac{\rho g H}{2} \frac{cosh(k(h+z))}{cosh(kh)} \tag{3.6}$$

In this formulation the wave number k can be determined via the dispersion relationship as follows:

$$\omega^2 = gk \tanh(kh) \tag{3.7}$$

The wave number k is iteratively solved with the Newton-Raphson method as defined in Appendix B.2.

The first step in the dynamic pressure correction process involves using a Fast Fourier Transform (FFT) to determine the dynamic pressure amplitude, $\hat{p}_{wave,i}$, for each frequency component f_i. In this thesis, to be specific, a Welch's average periodogram method with a Hann filter with 50% maximum overlap is used for all applications where a FFT is needed. The amplitude of the free-surface elevation a_i can then be calculated by means of dynamic pressure correction factor K_i as defined in equation 3.8.

To calculate K_i, an accurate measure of the water depth is needed. The first step in obtaining this water depth, the pressure sensors have to be calibrated to a known water level. The still water levels of the pressure sensors are calibrated by utilizing the known still water level during the initial few minutes. During this time, the water level is stable, and the average water level, as measured by a floater positioned directly in front of the wave paddle, is used as a reference. This ensures that all pressure sensors start their measurements from a common baseline and the water level with respect to the flume's bottom is correctly determined. Subsequently, before applying the dynamic pressure correction, the mean water depth is extracted from the hydrostatic pressure timeseries. This can be done from the original pressure signal multiplied by ρg as the mean water depth is not influenced by the wave-induced variations in the dynamic pressure.

$$\frac{\hat{p}_{wave,i}}{\rho g} = a_i \cdot K_i \qquad with \qquad K_i = \frac{cosh(k_i(h+z))}{cosh(k_i h)} \tag{3.8}$$

As explained earlier, to account for dynamic pressures, shorter waves need a greater correction than longer waves. To avoid over-amplification of high-frequency wave components, a cut-off frequency is determined, beyond which the dynamic pressure correction is no longer applied. For sufficiently short waves, when the ratio of pressure sensor depth below the mean water surface level z_p to wave length L is greater than 0.2 ($z_p/L > 0.2$), the correction factor of K_i is set to 1 and the wave component's amplitude is not amplified.

3.5.3. Separation incoming and outgoing waves

The steep forereef is expected to reflect a significant amount of wave energy along with some reflection on the artificial reef and coral island beach. To both gain insight in the reflection of the reef system and obtain a purely incoming wave signal for the quantification, wave signals have to be decomposed into an incoming and an outgoing component. In this thesis, the decomposition is performed using the Guza method developed by Guza et al. (1985). The colocation of PSs and EMFs produces a time series of sea-surface elevation and velocity that are in phase with one another. The Guza method requires depth-averaged velocities, which are converted from EMF point-measured velocities as described in section 3.5.4. The Guza method assumes that both this depth-averaged velocity U and sea-surface elevation η are the superposition of their incoming (U^+, η^+) and outgoing (U^-, η^-) components as

$$\begin{aligned} \eta &= \eta^+ + \eta^-, \\ U &= U^+ + U^-, \end{aligned} \tag{3.9}$$

Assuming waves of constant forms propagating with wave celerities c^+ and c^-, the discharge can be presented as the product of wave celerity c and surface elevation η. This same discharge is equal to the dept-averaged velocity U times the water depth h. As in this report, the Guza method will be applied in the frequency domain, with the water depth set to the mean water depth. However, if the Guza method were applied in the time domain, the instantaneous water depth, including the wave surface elevation, should be used. This leads to the following equations:

$$\begin{aligned} Uh = Q = Q^+ + Q^- \\ Q^+ = c^+\eta^+ \quad \text{and} \quad Q^- = c^-\eta^- \end{aligned} \tag{3.10}$$

Combining and rewriting equations 3.9 and 3.10 yields the incoming and outgoing sea-surface elevations as functions of the total depth-averaged velocity U, water level η, and the celerity of incoming and outgoing waves c^+ and c^-:

$$\eta^+ = \frac{Uh + c^-\eta}{c^+ + c^-} \quad \text{and} \quad \eta^- = \frac{Uh - c^+\eta}{c^+ + c^-} \tag{3.11}$$

To be applicable to arbitrary water depths, the wave celerity is determined using linear wave theory as $c = \omega/k$, where the wave number k is derived from the dispersion relationship in equation 3.7. Using this frequency-dependent wave celerity, the decomposition method has to be performed in the frequency domain. To do this, the total water level and depth-averaged velocity timeseries are transferred to the frequency domain by performing a FFT as described in Appendix B.1:

$$\begin{aligned} \eta(f) &= \mathcal{F}\{\eta(t)\}, \\ U(f) &= \mathcal{F}\{U(t)\} \end{aligned} \tag{3.12}$$

The same relation with respect to discharge and wave celerity as in equation 3.11 holds in the frequency domain and therefore the incoming and outgoing components of the water level can be computed as:

$$\eta^+(f) = \frac{U(f)h + c^-(f)\eta(f)}{c^+(f) + c^-(f)} \text{and } \eta^-(f) = \frac{U(f)h - c^+(f)\eta(f)}{c^+(f) + c^-(f)} \tag{3.13}$$

The last step at obtaining the incoming and outgoing wave signals is obtaining the real part of the inverse Fast Fourier Transform ($\mathcal{F}^{-1}$) of the incoming and outgoing wave components as:

$$\begin{aligned} \eta^+(t) = Re(\mathcal{F}^{-1}\{\eta^+(f)\}) \quad \text{and} \quad \eta^-(t) = Re(\mathcal{F}^{-1}\{\eta^-(f)\}), \\ U^+(t) = Re\left(\mathcal{F}^{-1}\left\{\frac{c^+(f)\eta^+(f)}{h}\right\}\right) \quad \text{and} \quad U^-(t) = Re\left(\mathcal{F}^{-1}\left\{\frac{c^-(f)\eta^-(f)}{h}\right\}\right) \end{aligned} \tag{3.14}$$

3.5.4. Measured velocity to depth averaged velocity

As can be seen in section 3.5.3, a depth averaged velocity is used to decompose the water level and velocity timeseries into incoming and outgoing components. In the physical model, velocities are measured at the flume bottom, where higher-frequency orbital velocities are particularly attenuated. This leads to discrepancies between the measured velocity u and actual depth averaged velocity U, especially at the flow sensors located in relatively deeper waters offshore from the reef platform and on the reef slope. The measured velocities are converted by means of an algorithm utilizing the velocity profile over the vertical following from linear wave theory. It should be noted that in this method, the water depth h is defined as the mean water depth as the calculations are performed in the frequency domain. Firstly, the velocity in the frequency domain $u(f)$ is acquired by performing a FFT on the velocity timeseries $u(t)$:

$$u(f) = \mathcal{F}\left\{u(t)\right\} \tag{3.15}$$

From linear wave theory, the amplitude of a linear wave $a_u(f_i)$ per frequency component f_i at the depth of the flow sensor z_{EMF} is determined as,

$$a_u(f_i) = u(f_i)\frac{sinh(k_i h)}{\omega cosh(k_i z_{EMF})} \tag{3.16}$$

, where again the wave number k is determined via the dispersion relationship as presented in equation 3.7. This linear wave amplitude $a_u(f_i)$ per frequency component f_i is used to determine the horizontal velocity amplitude $u(f_i, z_j)$ per frequency component f_i at different heights z_j within the water column. A vertical grid with 100 points with grid size dz is constructed as $[0, dz, 2dz, , h]$, in water depths shallower than 1 meter the amount of grid points is less than 100 as a minimal grid size dz of 0.01 is set. The horizontal velocity amplitude per frequency component f_i at a specific height z_j is denoted as $u(f_i, z_j)$. A velocity profile is constructed by computing this amplitude for each vertical grid cell. The depth averaged velocity amplitude $U(f_i)$ per frequency component f_i is determined by taking the average of this velocity profile. This procedure is formulated in equation 3.17. To retrieve the depth averaged

velocity timeseries $U(t)$, the real part of the inverse FFT of the depth averaged velocity in the frequency-domain $U(f)$ is determined, as can be seen in equation 3.18.

$$U(f_i) = \frac{\sum_{j=1}^{n} u(f_i, z_j)}{n} = \frac{\sum_{j=1}^{n} \omega_i a_u(f_i) \frac{cosh(k_i(h+z_j))}{sinh(k_i h)}}{n} \tag{3.17}$$

$$U(t) = Re(\mathcal{F}^{-1}\{U(f)\}) \tag{3.18}$$

This method significantly intensifies high-frequency components of sensors with a high relative sensor depth kz_{EMF}, which may result in amplified noise. Therefore, the peak frequency of the most offshore velocity meter EMF02, is determined, and a high-frequency cut-off is set on 3 times this offshore peak frequency. Beyond this peak frequency, velocity amplitudes are no longer amplified. Generally, this cut-off frequency is equal to approximately 0.5 Hz which justifies this approach as most wave energy resides below 0.5 Hz and noise is generally found beyond this cut-off frequency. Visual inspection of the depth-averaged timeseries did not show any over-amplification of wave components.

3.6. Wave parameter calculation

To be able to effectively analyze the data from the physical model, a great deal of wave parameters can be used. In this section an overview is given of the parameters used in this thesis and how these are calculated.

3.6.1. Spectral characteristics

Firstly, at each pressure sensor, a variance density spectrum of the free-surface elevation ($S_{\eta\eta}(f)$) can be constructed by performing a FFT of the free-surface elevation signal. This FFT method is elaborated in Appendix B.1. By performing this transformation, the variance ($\frac{1}{2}a_f^2$) of each frequency component f_i is found. In this report, the frequency resolution of the wave parameter calculation is 0.0067 Hz. The wave energy per frequency bin is then subsequently found by multiplying the variance density spectrum by ρg as can be seen in equation 3.19.

$$E_{\eta\eta}(f) = \rho g S_{\eta\eta}(f) = \rho g \lim_{\Delta f \to 0} \frac{1}{\Delta f} E\left\{\frac{1}{2}a_f^2\right\} \tag{3.19}$$

In Section 2.3.3, it is mentioned that, according to the literature, IG waves are defined as wave components with frequencies lower than half of the offshore peak frequency f_p. In this thesis, the same classification is applied, with SS waves defined as wave components having a frequency higher than the cut-off frequency $f_p/2$. With these frequency bands, the IG- and SS-wave energy can be computed as in equation 3.20. In the case of the SS-, the energy density spectrum is integrated until half the sampling frequency f_s, known as the 'Nyquist frequency'. In this case, this Nyquist frequency equals 10 Hz as the acquired 120 Hz signal is down-sampled to a sample rate of 20 Hz.

$$E_{\mathrm{IG}} = \rho g \int_0^{f_p/2} S_{\eta\eta}(f)\mathrm{d}f \quad E_{\mathrm{SS}} = \rho g \int_{f_p/2}^{f_s/2} S_{\eta\eta}(f)\mathrm{d}f \tag{3.20}$$

The total energy present within the spectrum is then the sum of the energy present in the IG and SS frequency bands:

$$E_{tot} = E_{IG} + E_{SS} = \rho g \int_0^{f_s/2} S_{\eta\eta}(f)\mathrm{d}f \tag{3.21}$$

The integrated variance density spectra are classified as the zeroth spectral moment m_0, the first spectral moments m_1 and the first negative spectral moment $m_{-1.0}$. These spectral moments are deter-

mined as:

$$\begin{aligned} m_0 &= \int_0^{f_s/2} S_{\eta\eta}(f)df \\ m_1 &= \int_0^{f_s/2} f \cdot S_{\eta\eta}(f)df \\ m_{-1} &= \int_0^{f_s/2} f^{-1} \cdot S_{\eta\eta}(f)df \end{aligned} \tag{3.22}$$

These spectral moments can be used to conveniently determine wave parameters such as significant wave height H_{m0}, mean wave period T_{m0} and mean frequency $T_{m-1.0}$. These parameters relate to the spectral moments as follows:

$$\begin{aligned} H_{m0} &= 4\sqrt{m0} \\ T_{m01} &= \frac{m_0}{m_1} \\ T_{m-1.0} &= \frac{m_{-1}}{m_0} \end{aligned} \tag{3.23}$$

To obtain the spectral moments and the corresponding wave parameters for the IG and SS frequency bands, the same integration intervals as defined in 3.20 are used. The wave parameters of the incoming waves are calculated by simply constructing the variance density spectrum by FFT of the incoming surface elevation timeseries obtained with the decomposition method presented in Section 3.5.3.

3.6.2. Wave non-linearity

Skewness (Sk) is a measure of wave non-linearity can give valuable insights on the phasing of a wave signal, its resulting nonlinear behaviour and therefore shoaling/breaking point. Positive skewness indicates that wave crests are sharper and higher than wave throughs while negative skewness indicates the opposite. This skewness can be determined via equation 3.24. The wave asymmetry (As) is another measure of wave non-linearity and indicates the leaning forward or backward of the wave. Since wave skewness has been identified as one of the key factors of a canopy's effect on wave setup, the wave skewness around the artificial reef section will be examined. Wave asymmetry will not be explored further. As the dynamics of IG waves are primarily influenced by other factors that are less tied to skewness, the skewness is only calculated for the SS waves.

$$Sk = \frac{\langle(\eta - \bar{\eta})^3\rangle}{\langle(\eta - \bar{\eta})^2\rangle^{3/2}} \tag{3.24}$$

3.6.3. Flow velocity attenuation

To quantify the degree at which wave-induced flow is able to penetrate in the canopy the flow attenuation parameter is calculated as presented in equation 2.10, for which a free-stream and in-canopy velocity amplitude are needed. However, as six ADVs are deployed to measure flow velocities, the data needs to be slightly manipulated to arrive at both a single representative free-stream and in-canopy velocity amplitude.

The simplest and most intuitive approach to determine these representative velocity amplitudes is to average the measurements taken within the canopy, specifically from ADV2, ADV3, ADV5, and ADV6, as an approximation of the in-canopy flow. The approximate of the free-stream is then defined as the average of ADV1 & 3, which are located 5 centimeters above the canopy and is assumed to be unaffected by the artificial reef elements. Simply averaging the acquired time series directly is not feasible because the signals are out of phase due to differences in their respective cross-shore locations. Therefore, the velocity energy density spectra are averaged, obtained using the FFT method described in Appendix C. This ADV averaging method is visualized in Figure 3.20.

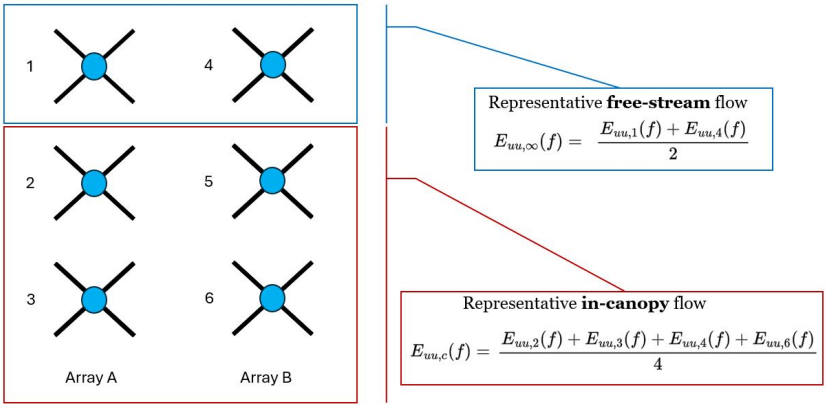

Figure 3.20: Method of approximating the representative free-stream and in-canopy flow, in this case the top two ADVs are used to construct the free-stream flow and the bottom four ADVs are used to construct the in-canopy flow.

However, the ADV data quality assessment presented in Section 3.4.2 revealed that the data recorded by the bottom ADV in array A (ADV3) contains high levels of noise. This means that all ADV3 for runs with the low-density artificial reef configuration S1 are deemed unusable for data analysis. Therefore, the method of approximating representative in-canopy flow as described above can not be applied to analyze low-density artificial reef runs. For these runs, an alternative approximation method representing the in-canopy flow with the two middle ADVs (ADV2 & 5) is used.

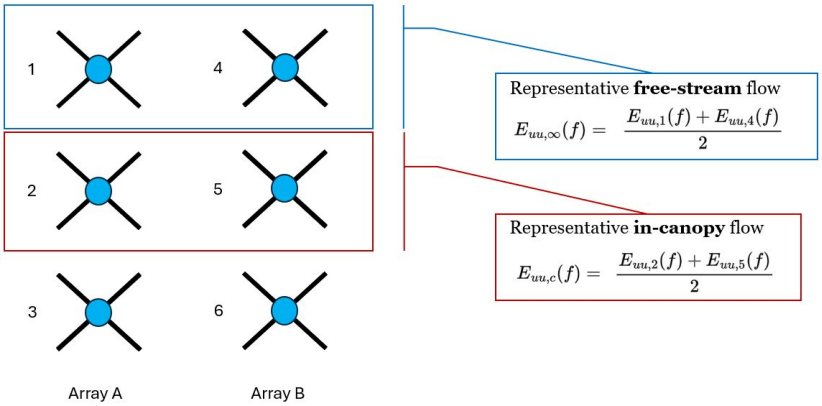

Figure 3.21: Method of approximating the representative free-stream and in-canopy flow, in this case the top two ADVs are used to construct the free-stream flow and the two ADVs in the middle are used to construct the in-canopy flow.

In summary, when comparing flow attenuation across configurations S0, S1, and S3, the approximation method using the two middle ADVs (ADV2 and ADV5) to represent in-canopy flow is applied. This method may lead to an underestimation of attenuation, as a greater portion of the flow is able to reach the higher-positioned ADVs. In contrast, when comparing only configurations S0 and S3, the approximation method utilizes the four bottom ADVs (ADV2, ADV3, ADV5, and ADV6) to represent in-canopy flow.

An alternative method for approximating the representative velocity amplitude, using a convergence correction to decrease the effects of flow convergence in ADV array A is explored in the discussion section. In the same section, it is explored how different methods of approximating a representative in-canopy flow influence the measured magnitude of energy penetration into the canopy.

To gain insight in which fraction of energy available in the free-stream flow is able to penetrate into the

canopy per wave component, the complement of the flow attenuation parameter is calculated:

$$(1 - \alpha_{w,i}) = \frac{E_{uu,\infty,i} - E_{uu,c,i}}{E_{uu,\infty,i}} \tag{3.25}$$

By putting the difference between the in-canopy flow energy and free-stream flow energy in the numerator, this metric represents the fraction of free-stream flow energy that gets blocked instead of the fraction that passes. This enables the layered plotting of flow energy changes, allowing for visualization of the net effect changing the artificial reef configuration has on the amount of flow energy that gets blocked.

3.6.4. Wave dissipation rate or energy flux gradient

To quantify the observed wave dissipation rate, the decay of the incoming wave energy flux over the full restoration width is considered. This wave energy flux is equal to the wave group celerity c_g times the wave energy E. Generally, the wave energy dissipation rate can be determined through the wave energy transport balance, as defined by (Holthuijsen, 2010):

$$\frac{\partial E(f,\theta;x,y,t)}{\partial t} + \frac{\partial c_{g,x} E(f,\theta;x,y,t)}{\partial x} + \frac{\partial c_{g,y} E(f,\theta;x,y,t)}{\partial y} + \frac{\partial c_\theta E(f,\theta;x,y,t)}{\partial \theta} = S(f,\theta;x,y,t) \tag{3.26}$$

As the experiments in the physical model were performed in a 1D flume, it can be assumed that there was no refraction and purely wave energy transfer in cross-shore direction while wave parameters are averaged over the run duration. This eliminates all wave direction (θ), cross-flume (y) and time (t) related derivatives. The remaining sink term $S(x)$ contains wave dissipation from breaking and bottom friction, frictional and drag losses caused by the canopy, and non-linear transfers resulting from interactions between individual wave components.

For each ith wave component, the sink term $S(x)$ can be expressed as 1) the sum of energy losses caused either by the flume bottom or artificial reef D_i and 2) the non-linear energy transfers $S_{nl,i}$. This simplifies the wave energy flux gradient ϵ_i [$J/m^2/s$] to

$$\epsilon_i = \frac{\partial c_{g,i} E_{\eta\eta,i}}{\partial x} = -D_i + S_{nl,i} \tag{3.27}$$

To compute the average wave energy flux gradient over the restoration stretch using observations from the Delta Flume experiments, the linear decline in the product of the total wave energy $E_i(x)$ and group celerity $c_{g,i}(x)$ per wave component can be divided by the restoration width. In the Delta Flume, pressure sensors were installed just offshore (x = 135 m) and just onshore (x = 147 m) of the artificial reef stretch, this results in the following discretized approximate of the wave dissipation rate:

$$\epsilon_i = \frac{c_{g,i}(x_{offshore}) E_{\eta\eta,i}(x_{offshore}) - c_{g,i}(x_{onshore}) E_{\eta\eta,i}(x_{onshore})}{x_{onshore} - x_{offshore}} \tag{3.28}$$

To arrive at a single representative energy flux gradient, the energy flux gradient per wave component is integrated over frequency. Note that by integrating over all wave components, the term containing non-linear interactions cancels out to zero as energy is just exchanged across frequencies.

$$\epsilon = \int \frac{\partial c_g E_{\eta\eta}}{\partial x}(f)\, df = -\int D(f) df + \underbrace{\int S_{nl}(f) df}_{=0} \tag{3.29}$$

Strictly speaking, only the total energy flux gradient ϵ, integrated over all wave components, can be referred to as the **wave dissipation rate**. In contrast, the energy flux gradient per wave component ϵ_i includes non-linear transfers and is therefore simply referred to as the **wave energy flux gradient**. In

this thesis, this specific definition is used.

To make an estimate how much bottom friction and wave breaking contribute to the total wave dissipation rate, an estimate of the bottom friction dissipation can be made. A commonly used formula to approximate wave energy dissipation due to bottom friction is based on the work of Hasselmann et al. (1973) and Collins (1972):

$$D_{f,i} = \frac{2}{3} c_g \rho f_b E_{\eta\eta,i} \tag{3.30}$$

A reasonable approximation of the bottom friction parameter f_b would be 0.002 (Sabatier, 2007). The total bottom friction dissipation rate D_f is calcualted by integrating the dissipation across all wave components:

$$D_f = \int D_f df \tag{3.31}$$

To isolate the energy lost due to dissipation mechanisms from other effects like wave reflection, the incoming wave energy $E_{in,i}$ instead of the total wave energy is used to calculate the wave dissipation rates and wave energy flux gradients presented above. Regarding limits of integration, the total wave dissipation rate is calculated by integrating over [0, f_s/2], whereas the energy flux gradients corresponding to the IG- and SS-wave frequency band are respectively integrated over [0, f_p/2] and [$f_p/2$, f_s/2].

To gain understanding in the change in incoming wave energy across the reef restoration as presented in Appendix Figures A.1 and A.2 and its frequency dependence, the relative change in incoming wave energy per wave component is investigated. This is done by calculating, for every frequency component, the relative change in incoming wave energy as in equation 3.32. Note that this metric does not represent wave dissipation (as it lacks multiplication by the group wave celerity) but the change in wave energy itself. It is chosen to

$$\Delta E_{\eta\eta,in}(f) = \frac{E_{\eta\eta,in,PS13} - E_{\eta\eta,in,PS14}}{E_{\eta\eta,in,PS13}} \cdot 100\% \tag{3.32}$$

3.6.5. Extreme water level analysis

While the findings on wave dissipation and attenuation caused by the artificial reef can be valuable, they do not directly address the reef's implications for flood risk. As we lack wave run up and overtopping data, the closest we can come to a quantification of flood risk is an extreme water analysis close to the beach toe. This extreme water level analysis is conducted by sorting the total surface elevation timeseries of the most onshore placed pressure sensor, PS15. The timeseries is sorted from low to high and the 2% of highest values are selected. The contribution of both the SS and IG-waves to the extreme water levels can be determined by determining, at the same point in time t_i ($\eta_{2\%}(t_i)$), the value of the IG- and SS- surface elevation time series for each 'extreme' surface elevation value in this selection. The contribution of the wave setup to the extreme water levels is assumed to be constant and thus equal to the total wave setup. Next, the mean of the 2% highest water levels is calculated and the same can be done for the

This results in the mean of the 2% highest water levels $\overline{\eta}_{2\%}$ and its contributions $\overline{\eta}_{2\%,IG}$, $\overline{\eta}_{2\%.SS}$ and $\overline{\eta}_{2\%,setup} (= \bar{\eta})$ by respectively IG- and SS-waves and wave setup where

$$\overline{\eta}_{2\%} = \overline{\eta}_{2\%,IG} + \overline{\eta}_{2\%.SS} + \overline{\eta}_{2\%,setup} \tag{3.33}$$

By comparing the mean extreme water levels of the high-density artificial reef configuration with those of the bare reef case, the impact of placing artificial reef elements on extreme water levels can be quantified, along with identifying the key components driving this change in extreme water level.
Furthermore, the relative contribution of a component can be calculated as a fraction of the mean extreme water level as $\overline{\eta}_{2\%,IG}/\overline{\eta}_{2\%}$ The relative contributions of the three components (IG, SS, setup) should than add up to 1.

4

Results

This chapter presents a data analysis to provide results addressing the posed research questions. In the first part of this data analysis, the data collected from the PSs and EMFs is analyzed to examine wave transformation across the fringing reef transect. Additionally, the the impact of the artificial reef on onshore extreme water levels and the frequency dependence of wave energy dissipation are investigated. The second part focuses on the data collected by the ADVs, from which the in-canopy flow dynamics and flow attenuation are studied. Concluding each section, an overview of the key takeaways from that section is provided.

4.1. Results from PS and EMF measurements

4.1.1. Wave transformation

The first part of the analysis covers the general hydrodynamics by studying how wave height and mean water levels vary horizontally across the fringing reef transect. Secondly, the impact of the artificial reef is investigated by the absolute wave dissipation rate ϵ and the percentage decrease of incoming wave energy. To better understand the artificial reef's impact on flood risk, the extreme water levels at the most onshore measurement location are analyzed, along with the main components contributing to these extreme levels. Finally, to get a full view of the dissipation's frequency dependence the energy decrease across the artificial reef is analyzed per frequency component.

As presented in the previous section, the general wave transformation and water level response can only be presented with the runs that were reran after reinstalling the pressure sensors. These nearshore hydrodynamic processes, with and without artificial reef elements, are depicted in Figures 4.1 and 4.2, respectively, for a water level on the reef flat of 0.33 and 0.67 m. In the first two panels a and b the transformation of the significant wave height H_{m0} and the significant IG wave height $H_{m0,IG}$ are illustrated. With a sparser spreading, at the location of the colocated sensors, the incoming significant wave height $H_{m0,in}$ and incoming significant IG wave height $H_{m0,in,IG}$ are depicted in panel c and d. In panels e) and d), the wave setup $\bar{\eta}$ is shown alongside a bathymetry plot, providing a reference for the locations of the measurement points within the reef transect.

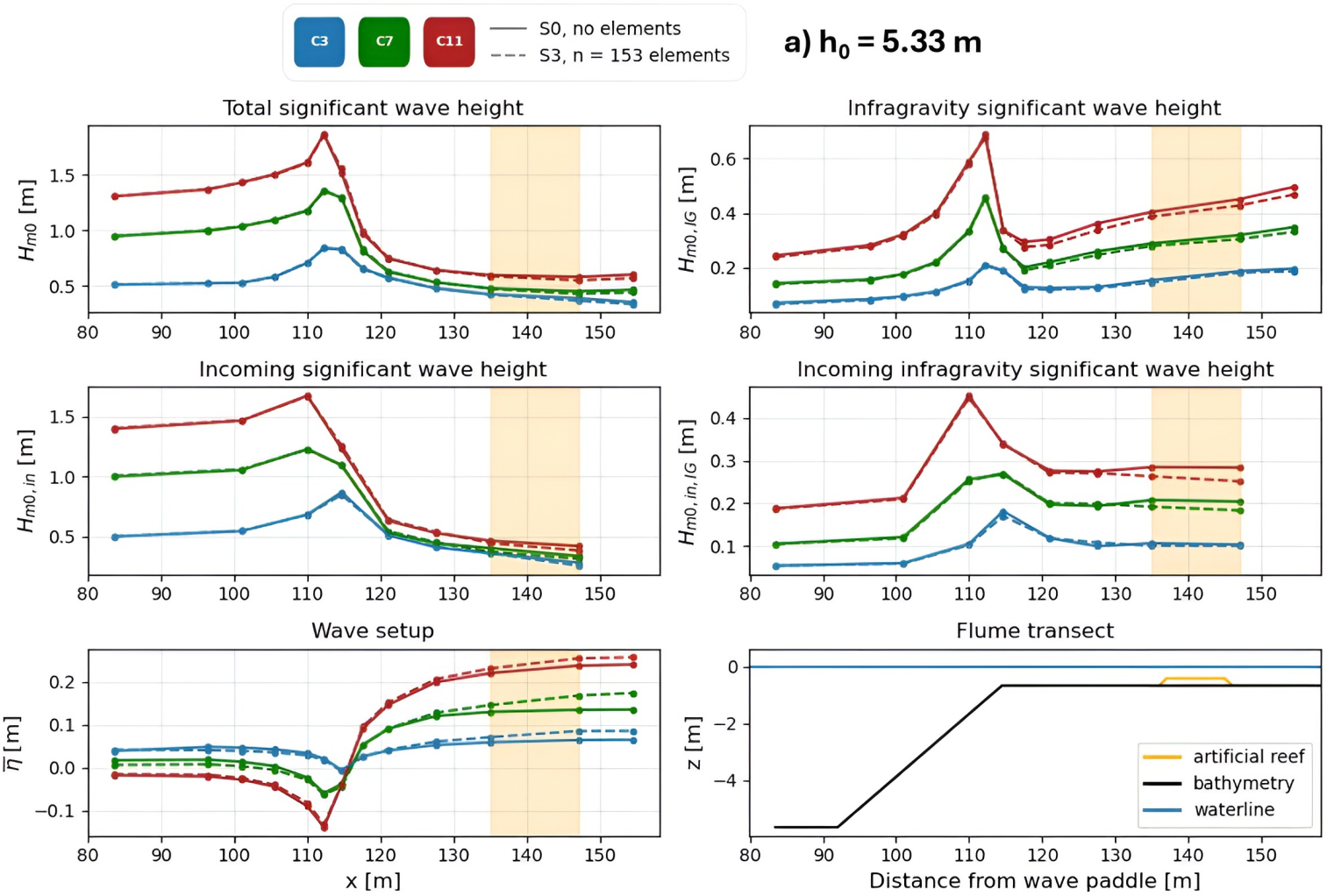

Figure 4.1: Transformation of significant wave height, IG significant wave height, incoming significant wave height, incoming IG significant wave height and wave setup as observed along the flume transect, all for the **low water level** case of h_0 = 0.33 m. The artificial reef stretch is marked in orange/yellow. See Table 4.1 for a quantitative summary of the artificial reef's effect on wave height and setup at x = 147 m for wave conditions C3, C7, C11.

Wave transformation: low water level runs

In the IG-related panels b) and d) in Figures 4.1 and 4.2 it can be observed that the IG wave height increases more significantly than the total wave height. This a combination of shoaling and IG wave generation by break-point forcing. In intermediate and deep waters, where the dispersion relationship applies, long waves such as IG waves have a higher wave group celerity compared to shorter waves. While these waves propagate into shallower water, their celerity decreases more significantly, with all wave celerities approaching the shallow water wave celerity $c = \sqrt{gh}$. This convergence leads to more intense wave shoaling. However, after shoaling, the IG wave height does not decline as sharply as the total wave height as longer waves are affected less by nonlinear effects that tend to steepen and break these waves. Furthermore, in the breaker zone the net effect of IG wave dissipation is reduced by the generation of IG waves via break-point forcing. Similarly, the IG wave height increases throughout the entire reef flat, indicating either energy transfer from higher frequencies (S_{nl} in equation 3.27), reflection or a combination of both.

In panel d the reflective component of the IG waves is eliminated by the method presented in Section 3.5.3. This wave transformation plot shows that on the reef flat the incoming IG wave height is relatively stable with only a slight increase just offshore of the artificial reef. This slight increase in incoming IG wave height indicates energy transfer from higher frequencies as the reflective component is eliminated.

Across the artificial reef section from x = 54.5 to x = 63.5, the incoming IG wave height decreases again, with a greater reduction observed in the presence of the high-density artificial reef.

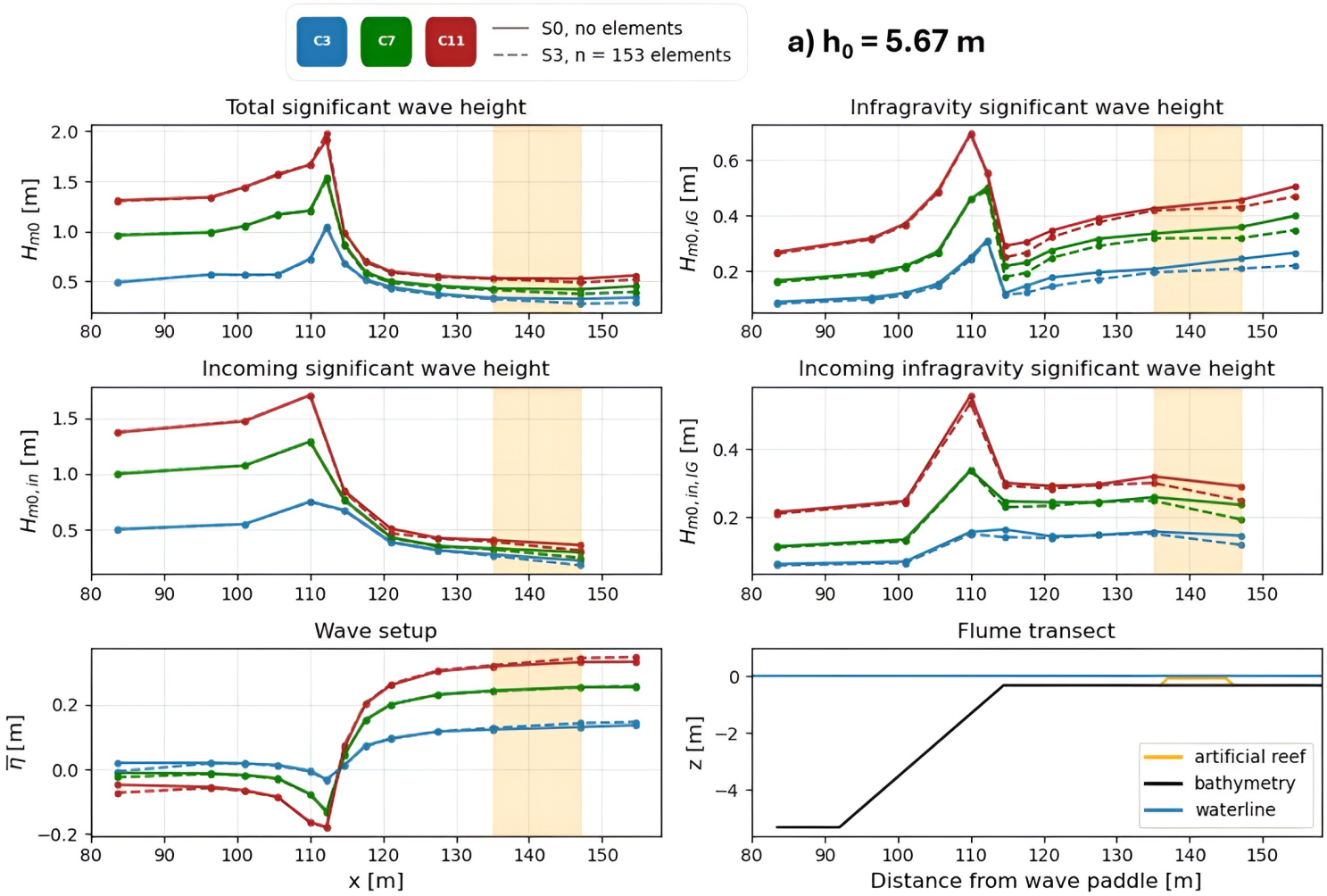

Figure 4.2: Transformation of significant wave height, IG significant wave height, incoming significant wave height, incoming IG significant wave height and wave setup as observed along the flume transect, all for the **high water level** case of h_0 = 0.67 m. The artificial reef stretch is marked in orange/yellow. See Table 4.1 for a quantitative summary of the artificial reef's effect on wave height and setup at x = 147 m for wave conditions C3, C7, C11.

Wave transformation: high water level runs

The IG-related panels b and d in Figure 4.2 again show that the IG wave height increases more intensely than the total wave height in panel a. Due to the higher water level on the reef crest the increase in total significant wave height starts later and the wave height decline in the breaker zone is less severe resulting in slightly larger wave heights on the reef flat.

Again, discrepancies in the total incoming wave height (panel c) only occur after x = 54.5, the location where the artificial reef starts. Panel d shows that incoming IG waves lose their energy later in the domain. Beyond x = 40 m on the reef flat, their wave height remains even more stable than during the low water level runs. Across the artificial reef, between x = 54.5 and x = 63.5, the reduction in incoming IG wave height appears only very small. For the C3 wave condition, even slight IG-wave growth can be observed over the artificial reef stretch.

For high water levels, the effect of the artificial reef is less clear and The differences in IG wave heights just onshore of the artificial reef between the S0 and S3 runs are somewhat inconsistent. This highlights that measuring slowly varying water levels on the reef flat is challenging and, therefore, it is difficult to

isolate the actual effect of the artificial reef.

> On the reef flat, total incoming wave height decreases while incoming IG wave height stays stable. A slight increase in incoming IG wave height just offshore of the artificial reef suggests energy transfer from higher frequencies. Across the artificial reef (x = 54.5 to x = 63.5), incoming IG wave height decreases, especially in the presence of the artificial reef. At high water levels, the effect of the artificial reef is less clear.

4.1.2. Effect of artificial reef on incoming wave height and mean water level

To get a more quantitative insight in the net effect of the restoration on wave heights and mean water levels, a simple comparison is made between the runs without artificial and with high-density artificial reef, while keeping the forcing conditions constant. For each forcing condition covered in the repeated runs, the following are determined: (1) the incoming wave height just offshore of the artificial reef stretch in the case of a bare reef, (2) the incoming wave height at the same location in the presence of a high-density artificial reef, and (3) the absolute change in these two incoming wave height values (in meters) as well as the relative change (in percentage). This method is repeated to determine the change in wave setup. In Table 4.1, an overview of these absolute and relative changes in incoming wave height and setup is presented.

Low water level runs

Figure 4.3 shows the relative incoming wave height reduction as a function of offshore significant wave height H_{m0} and offshore peak period T_p, for all low water level runs. This figure reveals that while keeping the offshore wave period constant, higher values of offshore significant wave height will decrease the relative incoming wave height reduction. Similarly, while keeping the offshore wave height constant, higher values of offshore peak period will increase the relative incoming wave height reduction.

Furthermore, per wave combination, the spread in incoming wave height reduction per frequency band can be seen. This reveals that the incoming wave height reduction is relatively uniformly distributed over the IG- and SS-waves as the highest discrepancy is highest at the C11 ($H_m0 = 1.3m$ and $T_p = 5.77s$) wave condition with 1.4 percentage points. Although this does not include the distribution of wave height reduction across all wave components, it does indicate a lack of frequency-dependency of the wave height reduction.

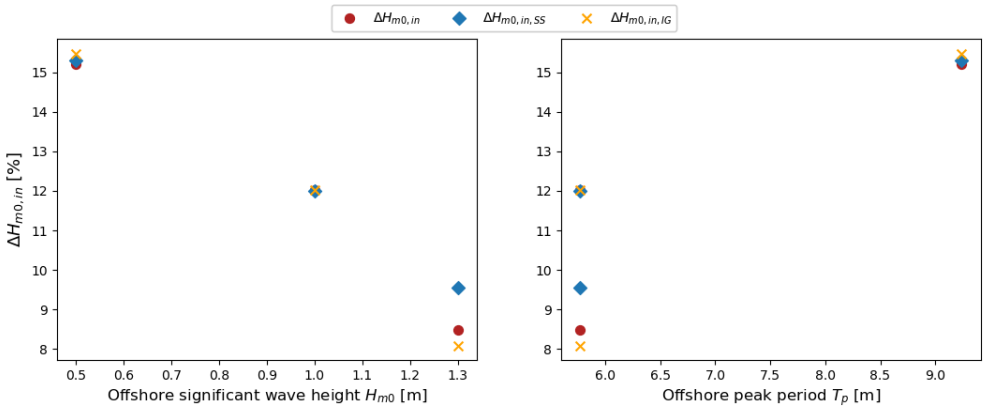

Figure 4.3: Relative incoming wave height reduction as a function of offshore significant wave height (left) and offshore peak period (right) during the **low water level runs**.

High water level runs

Figure 4.4 shows the relative incoming wave height reduction as a function of offshore significant wave height and offshore peak period, for all low water level runs. Compared to the high water level runs, the reduction in incoming wave height exhibits the same dependence on offshore significant wave height H_{m0} and offshore peak period T_p. The exception to this is the for the C11 ($H_m0 = 1.3m$ and $T_p = 5.77s$) wave condition, where increasing the offshore significant wave height from 1.0 m results in

higher relative incoming wave height reduction.

The same figure shows that the relative reduction in incoming wave height is less uniformly distributed over the IG- and SS-waves than during low water level runs. For low, long waves, the relative reduction in IG-wave height is relatively smaller than that of SS-wave height, whereas for high, short waves, it is greater.

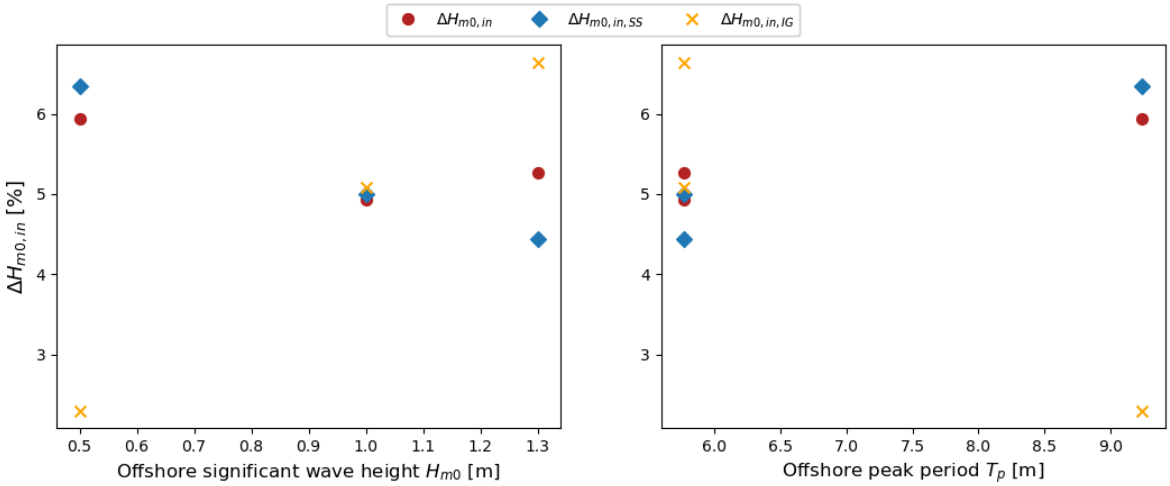

Figure 4.4: Relative incoming wave height reduction as a function of offshore significant wave height (left) and offshore peak period (right) during the **high water level runs**.

Table 4.1: The absolute and percentage difference in incoming wave height and wave setup when comparing the base case S0 to the high-density artificial reef case S3 for the reran wave conditions C3, C7, C11 (from left to right in the table's columns). The presented setup and wave heights are observed at x = 147 by PS14, just onshore of the artificial reef

$h_0 = 0.33$ m	$H_{m0} = 0.5$ m, $T_p = 9.24$ s	$H_{m0} = 1.0$ m, $T_p = 5.77$ s	$H_{m0} = 1.3$ m, $T_p = 5.77$ s
$\Delta Hm0,in$ [m]	-0.034	-0.034	-0.030
$\Delta Hm0,in$ [%]	-15.2	-12.0	-8.5
$\Delta Hm0,in,SS$ [m]	-0.024	-0.018	-0.017
$\Delta Hm0,in,SS$ [%]	-15.3	-12.0	-9.5
$\Delta Hm0,in,IG$ [m]	-0.023	-0.029	-0.025
$\Delta Hm0,in,IG$ [%]	-15.5	-12.0	-8.1
$\Delta\bar{\eta}$ [m]	+0.012	-0.001	+0.013
$\Delta\bar{\eta}$ [%]	+9.2	-0.4	+3.8
$h_0 = 0.67$ m	$H_{m0} = 0.5$ m, $T_p = 9.24$ s	$H_{m0} = 1.0$ m, $T_p = 5.77$ s	$H_{m0} = 1.3$ m, $T_p = 5.77$ s
$\Delta Hm0,in$ [m]	-0.017	-0.018	-0.024
$\Delta Hm0,in$ [%]	-5.9	-4.9	-5.3
$\Delta Hm0,in,SS$ [m]	-0.016	-0.015	-0.015
$\Delta Hm0,in,SS$ [%]	-6.4	-5.0	-4.4
$\Delta Hm0,in,IG$ [m]	-0.003	-0.011	-0.02
$\Delta Hm0,in,IG$ [%]	-2.3	-5.0	-6.6
$\Delta\bar{\eta}$ [m]	+0.021	+0.033	+0.017
$\Delta\bar{\eta}$ [%]	+32.9	+24.6	+7.2

Artificial reef's effect on mean water level

As could already be seen in panel e from Figure 4.1 and Figure 4.2, the pattern of wave setdown and setup changes by the presence of the high-density artificial reef. Both the wave setdown and setup become greater by introducing the artificial reef elements. This effect is more pronounced in high water level runs compared to low water level runs.

When interpreting the values in Table 4.1, it is remarkable that for all high water level runs, the increase in wave setup in absolute terms exceeds the absolute decrease in incoming wave height. For the low water level runs, the absolute increase in wave setup does not exceed the absolute decrease in incoming wave height.

It should be noted that for both water levels, the offshore water levels are not consistent which makes it tricky to cross-compare wave setup between different test runs. The variation of this offshore water level is within 0.1 meter, which is significant compared to the initial reef flat water depths of 0.33 and 0.67 m. These inconsistent offshore water levels can have an effect on wave transformation and wave setup as these are both depth-dependent. The variation in offshore water levels between S0 and S3 under identical wave conditions is however minimal.

- The incoming wave height reduction just onshore of the artificial reef stretch ranges from 8.5% to 15.2% for low water level runs and from 4.9% to 5.9% for high water level runs.
- Both decreasing the offshore wave height and increase the offshore peak period results in higher relative wave height reduction.
- For low water level runs, the relative reduction in incoming wave height is particularly well distributed between IG- and SS-waves, whereas for high water level runs, this distribution is less balanced.
- In the high water level cases, the absolute increase in wave setup is higher than the absolute reduction in incoming wave height.

4.1.3. Incoming wave energy reduction across artificial reef stretch

Section 4.1.2 examined the wave height reduction at the same location in the domain by comparing the bare reef and high-density artificial reef runs. Another way of quantifying incoming wave reduction is calculating the percentage decrease in incoming wave energy from PS13 to PS14, which are the pressure sensors placed just offshore and just onshore the artificial reef. Figure 4.5 shows the energy reduction for each forcing condition, showing the bare reef case (S0), low-density case (S2), and high-density case (S3). This allows for differentiating the energy reduction caused by the artificial reef from the 'background' energy reduction of the bare reef. In this figure, the height of the blue bar represents the net effect the artificial has on the incoming wave energy reduction.

First of all, it is notable that increasing the water depth in the flume results in lower net effect of the artificial reef. During **high water level** runs, as shown in panel b, the initial energy reduction in the bare reef case is higher as more SS-wave energy propagates onto the reef flat and is able to be attenuated. However, when artificial reef elements are introduced, the wave energy reduction increases only slightly. In contrast, during **low water level** runs, as shown in panel a, the wave height reduction for the bare reef is smaller, but the net effect on wave energy reduction of the artificial reef is significant enough to result in greater overall wave energy reduction compared to the high water level runs. Therefore, increasing the reef flat water depth decreases the wave energy reduction capacity of the artificial reef.

For both water levels, Figure 4.5 shows that increasing either the offshore wave height or the offshore peak period reduces the relative wave energy reduction caused by the artificial reef (represented by the blue bar in the figure).

Figure 4.3 shows the relative incoming wave height reduction as a function of offshore significant wave height H_{m0} and offshore peak period T_p, for all low water level runs. This figure reveals that while keeping the offshore wave period constant, higher values of offshore significant wave height will decrease the relative incoming wave height reduction. Similarly, while keeping the offshore wave height constant, higher values of offshore peak period will increase the relative incoming wave height reduction.

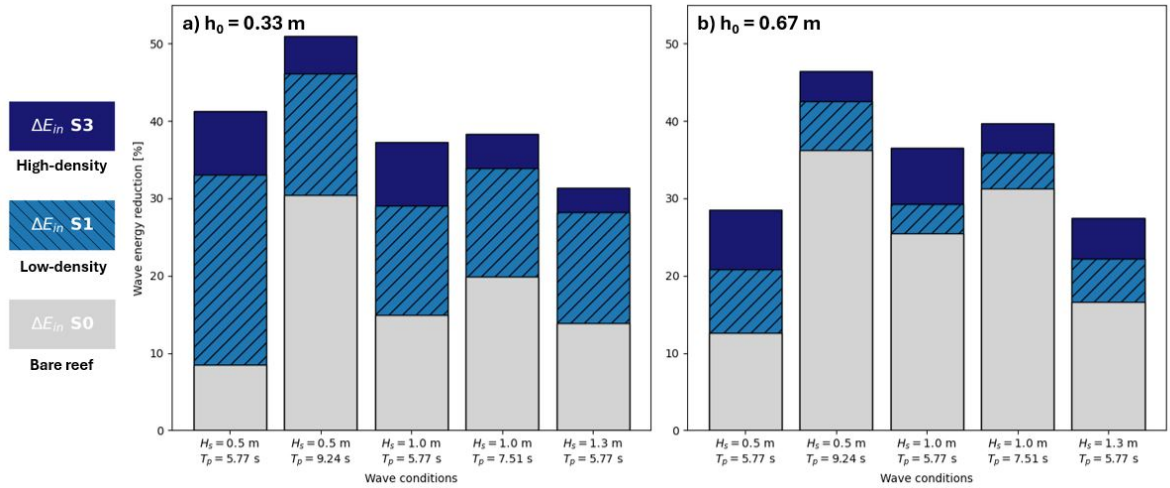

Figure 4.5: Relative reduction in incoming wave energy from just before to just after the artificial reef (PS13 to PS14) for all wave conditions at reef flat water depths of **a)** 0.33 m and **b)** 0.67 m.

Within the tested forcing conditions, the incoming wave energy reduction across the artificial reef increases when either the offshore wave height, offshore peak period, or reef flat water depth is increased while keeping the other forcing parameters constant.

4.1.4. Evolution of incoming energy density spectrum

Although the transformation of the IG-wave height is already covered, more information on the frequency dependence of the wave transformation is needed. For this purpose, the incoming energy density along the flume's transect is analyzed. Figure 4.6 depicts the energy density spectra for the wave condition $H_{m0} = 1.0$ m, $T_p = 5.77$ s at several measurement locations along the reef slope and reef flat. In general, a slight increase in SS-wave energy is observed on the reef slope due to shoaling and a subsequent decrease due to depth-dependent breaking. From these energy density spectra it is again confirmed that the reef flat water depth dictates the amount of SS-wave energy reaching the flat. This same water depth seems to influence the wave transformation at the location of the artificial reef as well. In the lower water depth case, the energy density decreases for all frequency components. However, when the water depth is 0.67 m, the abundance of SS-wave energy leads to an increase in IG-wave energy over the artificial reef (from PS13 to PS14).

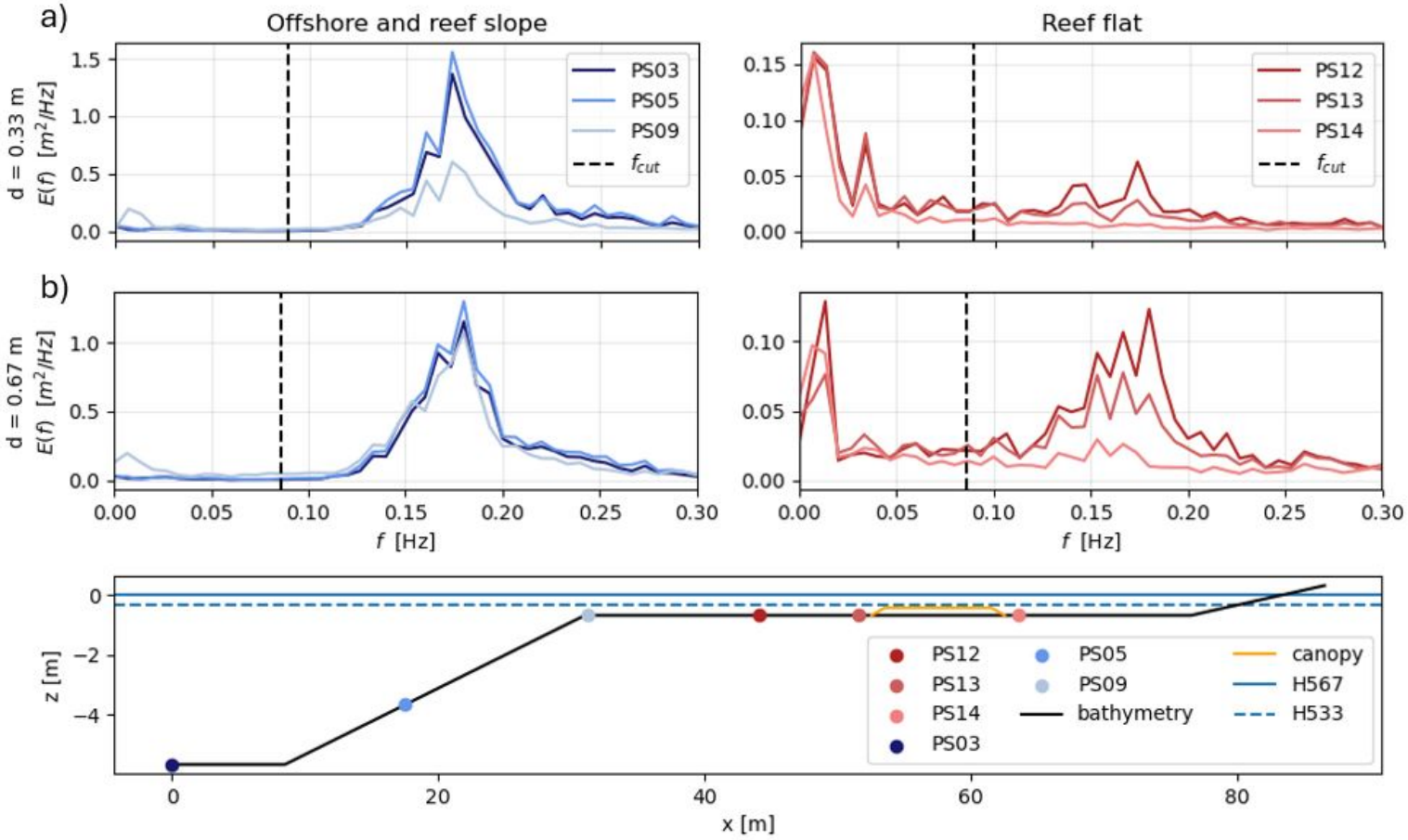

Figure 4.6: Evolution of the incoming wave energy density spectra offshore over the fringing reef transect in the Delta Flume. For wave condition C7 ($H_{m0} = 1.0$ m & $T_p = 5.77$ s at reef flat water levels of **a)** 0.33 m and **b)** 0.67 m.

By only looking at the incoming wave energy density spectra just offshore and onshore of the artificial reef stretch, the effect of the artificial reef on each wave component is more clearly visible. Figure 4.8 presents the spectra for the low water level case of wave condition C9 ($H_s = 1.0$m, $T_p = 7.51$s), comparing the bare reef, low-density, and high-density artificial reef scenarios. From this figure, it becomes clear that in general the greatest absolute decrease in wave energy between PS13 and PS14 concentrates in the most energetic frequency components. The presence of a (higher-density) artificial reef only has a small effect on the energy decrease for the SS-waves. Although the limited amount of available SS-wave energy, the absolute amount of SS-wave energy reduction is roughly equal to the decrease of more readily available IG-wave energy.

Figure 4.7: Flow energy per wave component as measured above (blue $E_{uu,\infty}$) and within (yellow $E_{uu,c}$) the artificial reef canopy (for S0 and S3) for wave condition C9 during **low water level** runs. The red line is the absolute difference between the flow energy measured offshore and onshore of the artificial reef. Shaded regions denote the 95% confidence intervals of the calculations.

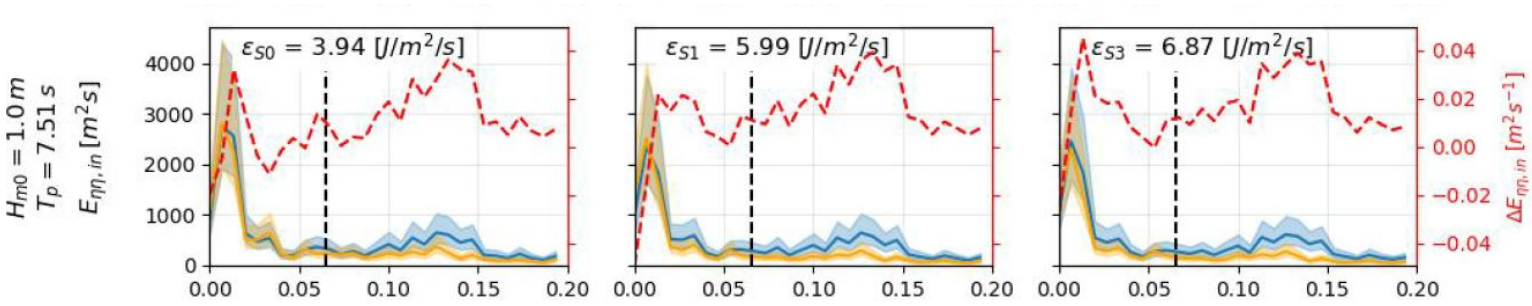

Figure 4.8

The same spectra but for the high water level case is presented in Figure 4.9. As can also be seen in this figure, the greatest decrease in wave energy is in the most energetic frequency components. Relatively speaking, the SS-wave energy decrease becomes more dominant over the IG-wave energy decrease compared to the high water level case. This results from two key observations: (1) Reduced depth-limited breaking allows more SS-wave energy to reach the artificial reef, leading to a greater absolute dissipation of SS-wave energy, and (2) Energy at the lowest frequencies (< 0.025 Hz) increases rather than decreases, likely due to nonlinear transfers from higher frequencies, as incoming wave energy is shown.

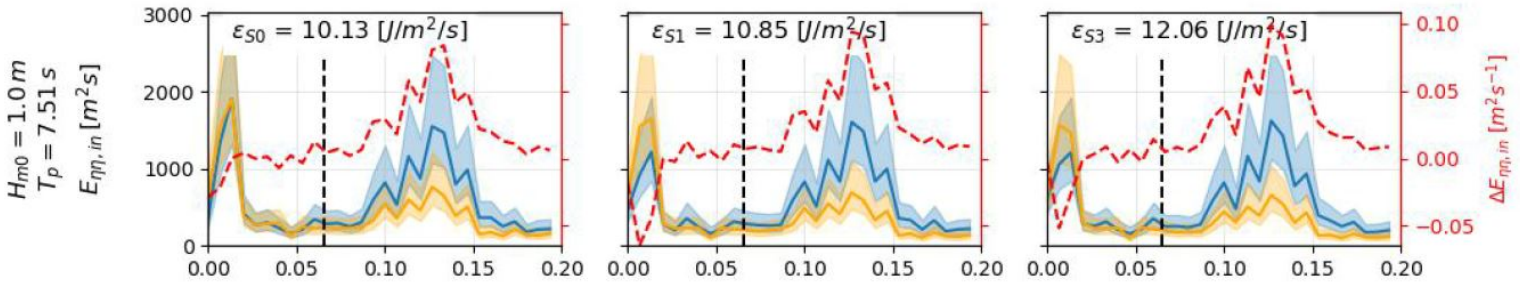

Figure 4.9: Flow energy per wave component as measured above (blue $E_{uu,\infty}$) and within (yellow $E_{uu,c}$) the artificial reef canopy (for S0 and S3) for wave condition C9 during **high water level** runs. The red line is the absolute difference between the flow energy measured offshore and onshore of the artificial reef. Shaded regions denote the 95% confidence intervals of the calculations.

In Appendix Figures A.1 and A.2, a complete overview of the evolution of the energy density for all forcing conditions is presented. This overview shows that the evolution of incoming wave spectra across the artificial reef is consistent with the observations described above, with SS-wave energy decreasing more significantly than IG-wave energy at high water levels compared to low water levels across all forcing conditions. For high water level runs, slight IG-wave energy growth is observed in the presence of an artificial reef for all forcing conditions.

In the low water level case (panel a), the greatest energy loss of SS-waves is observed in the bare reef scenario. The presence of the artificial reef further reduces SS-wave energy by approximately 10% beyond the bare reef's energy dissipation. However, around f $\approx$ 0.07 Hz, an additional energy loss peak of roughly 40% is observed. Increasing the density of the artificial reef results in only a marginal further reduction in SS-wave energy. For IG-waves, the bare reef case shows minimal energy decrease. However, the effect of introducing the artificial reef is greatest for these waves, as it adds energy decrease of up to 40%.

In the high water level case (panel b), the artificial reef contributes to an approximately 10% reduction

in SS-wave energy, distributed relatively evenly across wave components. The most notable difference compared to the low water level case is in the IG-waves, where the addition of the artificial reef results in an energy increase, suggesting a nonlinear energy transfer from higher frequencies.

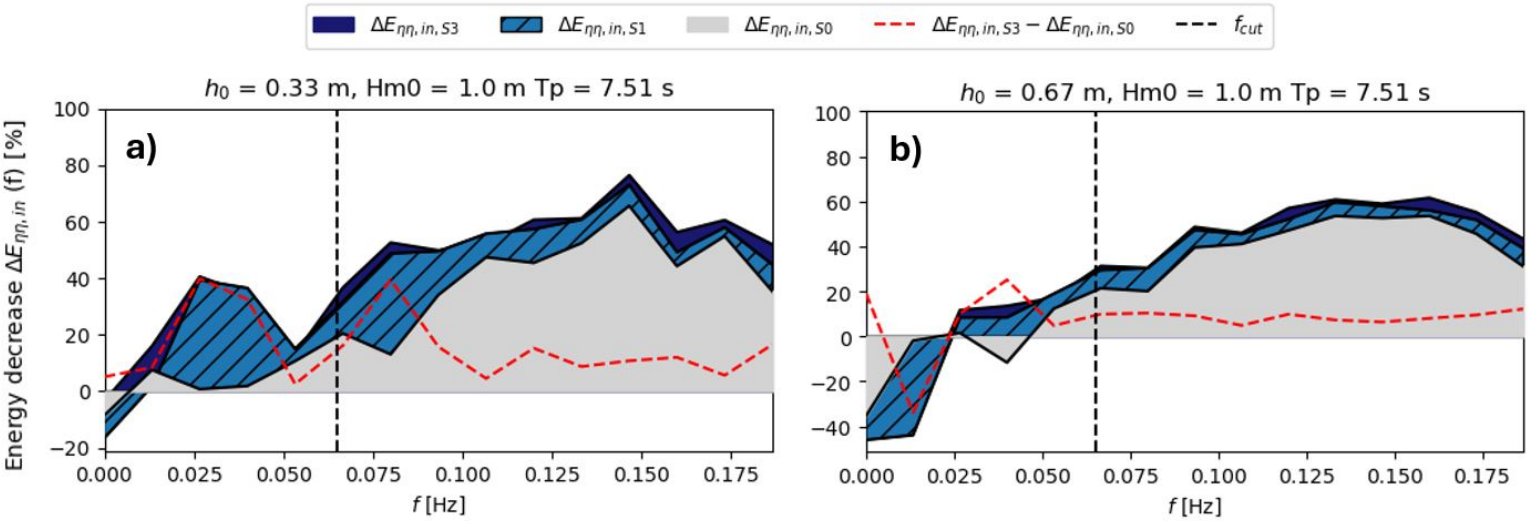

Figure 4.10: Energy change per wave component as observed over the artificial for wave condition C9, during low water level (panel a) and high water level (panel b). Note that the percentages of energy changes are layered over each other. By visualizing this way, the grey area is the initial energy change during the bare reef case and the added blue area is the energy change added by introducing the artificial reef elements.

The same figures, but for all forcing conditions, are presented in Figures E.1 and E.2 in Appendix E.1.

During low water levels, SS wave energy is being transferred to IG wave energy throughout the reef flat. During high water levels, reduced depth-limited breaking allows more SS wave energy to reach the artificial reef while the amount of IG wave energy increases by adding the artificial reef.

4.1.5. Wave dissipation rate

The wave dissipation rate as presented in Section 3.6.4 is determined across the artificial reef stretch for all original runs. Figure 4.11 shows the observed dissipation rate in the same manner as the relative wave energy reduction was presented in Figure 4.5. First of all, across all wave conditions, the total wave dissipation rate is greater at high water level (panel b) than at low water level (panel a). At low water levels, the net increase of wave dissipation by introducing the artificial reef (represented by the blue bar in the figure) increases either by increasing the offshore wave height or the offshore peak period. At high water levels however, this does not apply. Here, the net increase in dissipation is not a clear function of offshore significant wave height and peak period. Still, the total dissipation rate is greater than at low water levels, although this is primarily an effect of greater 'background' dissipation already present in the bare reef case (represented by the grey bar).

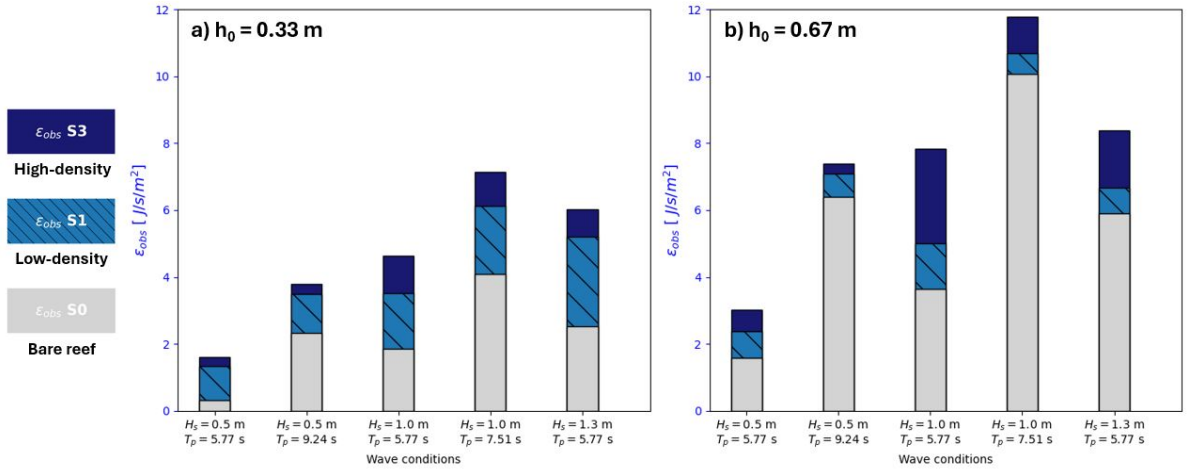

Figure 4.11: Absolute wave dissipation rate ϵ (calculated with incoming wave energy from just before to just after the artificial reef (PS13 to PS14)) for all wave conditions during low water level runs (panel a) and high water level runs (panel b).

By using the expression for bottom friction dissipation D_f in equation 3.30, the contribution of bottom friction to the total wave dissipation rate is estimated. Figure 4.12 shows, for the bare reef runs, the observed wave dissipation rate and its share of bottom friction. This figure reveals that, during low water level runs, bottom friction accounts for **6 – 22%** of the observed dissipation, with an average contribution of **12%**. At higher water levels, the bottom friction's contribution is **4 - 22%**, averaging **8 %**. Since total dissipation in the bare reef case is solely due to wave breaking and bottom friction, wave breaking dissipation dominates over bottom friction dissipation on the reef flat.

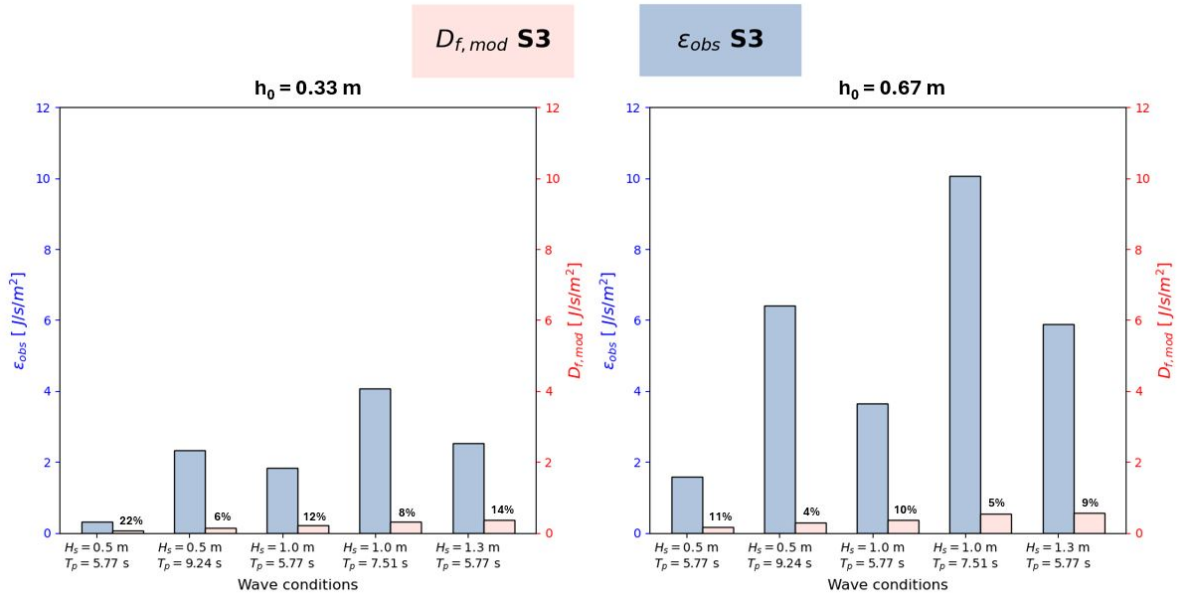

Figure 4.12: Absolute wave dissipation rate ϵ during the bare reef case (light blue) for all wave conditions during low water level runs (panel a) and high water level runs (panel b) compared to the estimated bottom friction dissipation D_f (light red) during the same bare reef case.

Comparing the observed dissipation rates in Figure 4.11 to the relative wave energy reduction in Figure 4.5, the absolute dissipation rate does not appear to follow the reef's wave energy reduction capacity. Namely, dissipation rates are higher at high water levels while relative energy reduction capacity is lower at high water levels. During high water levels, the relatively higher wave dissipation rate can not

keep up with the higher available amount of wave energy propagating on the reef flat and the relative wave energy reduction is therefore lower.

In Figure 4.13, the total wave dissipation rate is shown as a function of offshore significant wave height and peak period. It can be seen that while keeping the other variable constant, the dissipation rate increases both with wave height and peak period. Notable is the fact that in the low water level case with an artificial reef almost as much energy is dissipated as in the high water level case without elements. This highlights the already relatively high level of 'background' dissipation during the bare reef runs.

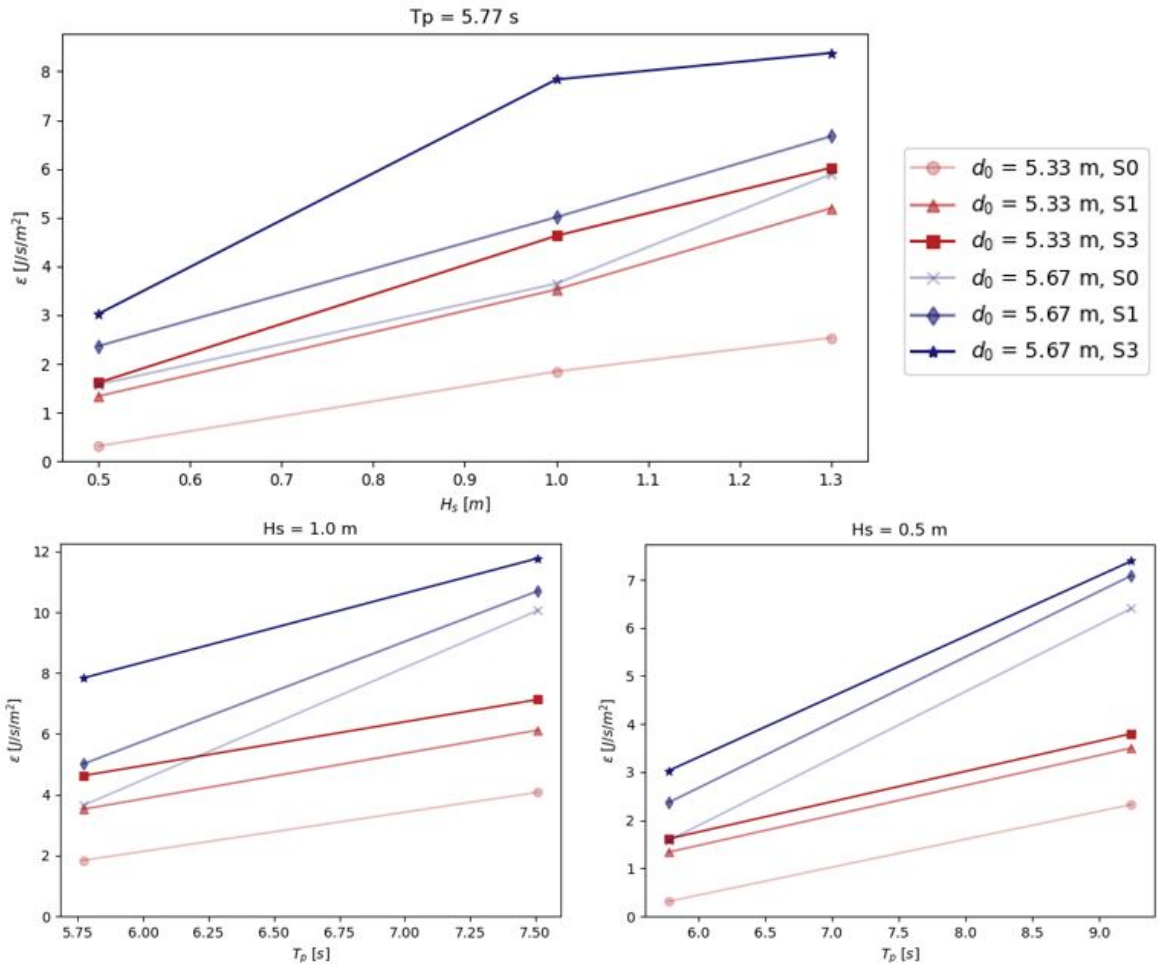

Figure 4.13: Wave dissipation rates as observed over the restoration as a function of offshore significant wave height and offshore peak period while keeping the other offshore wave variable constant. Note that the lines connecting data points do not indicate a linear relationship, they are presented solely to group related data points.

Appendix Figure 4.14 presents ϵ as a function of offshore significant wave height, this time showing the IG and SS-waves separately. Due to this separation, the ϵ-values presented are referred to as wave energy flux gradient as non-linear transfers are included (see equation 3.27. Differentiating between IG-bandwidth and SS-bandwidth has an apparent impact on the previously observed patterns. For example, the SS energy flux gradient increases even stronger with rising offshore significant wave height. The most significant effect, however, is observed in the IG energy flux gradient in Panel a), where the dependency on water depth is reversed. In other words, the energy flux gradients are larger for low water depth than for high water depth as IG energy flux gradient is more readily available at low water depths due to stronger break-point forcing. The IG flux gradient in the high water depth is just above zero or even negative, indicating IG-wave growth. Even more remarkable is that, for a high significant wave height of 1.3 m, adding the artificial reef results in more IG-wave amplification instead of less growth.

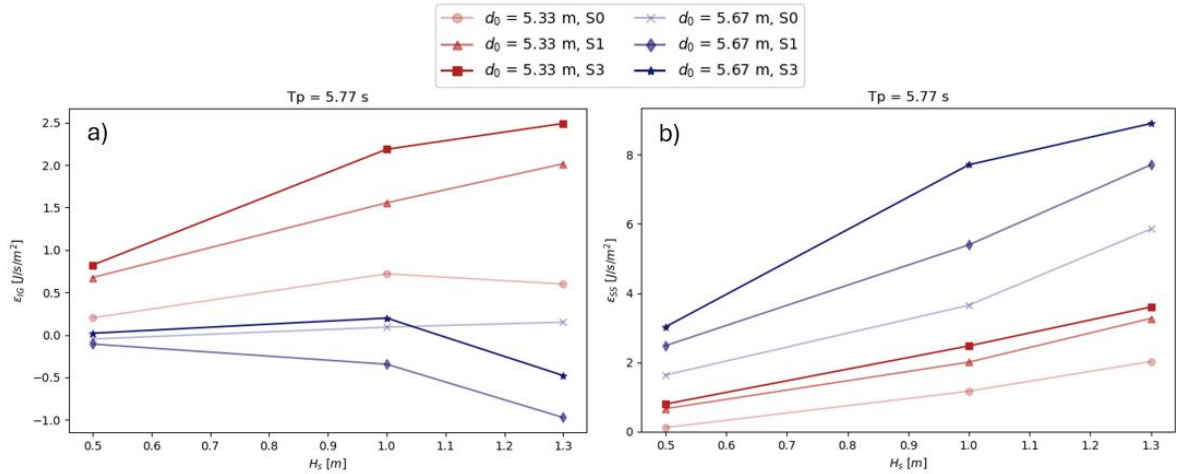

Figure 4.14: Wave energy flux gradients ϵ_{IG} and ϵ_{SS} as a function of offshore significant wave height for IG-waves in Panel a) and for SS-waves in Panel b).

During low water levels, the artificial reef significantly increases wave dissipation as compared to high water levels were the added wave dissipation is only small. At high water levels, the increased wave dissipation can not keep up with the higher available amount of wave energy, leading to low relative wave height reduction. Bottom friction is estimated to contribute only a small part of the total wave dissipation.

4.1.6. Extreme water level analysis

Although it is apparent that the artificial reef effectively reduces incoming wave energy, the fact that the observed increase in wave setup exceeds the incoming wave height reduction as can be seen in table 4.1, requires further investigation. It raises concerns that the increase in wave setup could counteract the reef's effectiveness in reducing extreme water levels at the beach toe. To test this, the water level timeseries of the most onshore pressure sensor (PS15 at x = 72.5) is further analyzed. In this case, the total water level timeseries are considered as neglecting the reflective component can lead to underestimation of extreme water levels. For the analysis, the method presented in Section 3.6.5 is applied. This approach allows the influence of wave height reduction and wave setup increase on extreme water levels to be visualized in Figure 4.15. From panel b, it can be seen that placing the artificial reef on the reef flat during high water level runs leads to an increase in the mean of the 2% extreme water levels, making the artificial reef counterproductive. In other words, the reef's beneficial effect on the wave height is overturned by the increase in wave setup. However, in the case of lower water levels, as shown in panel b, the extreme water levels decreases as expected due to the combined effect of the artificial reef dissipating more wave energy and causing a smaller increase in wave setup.

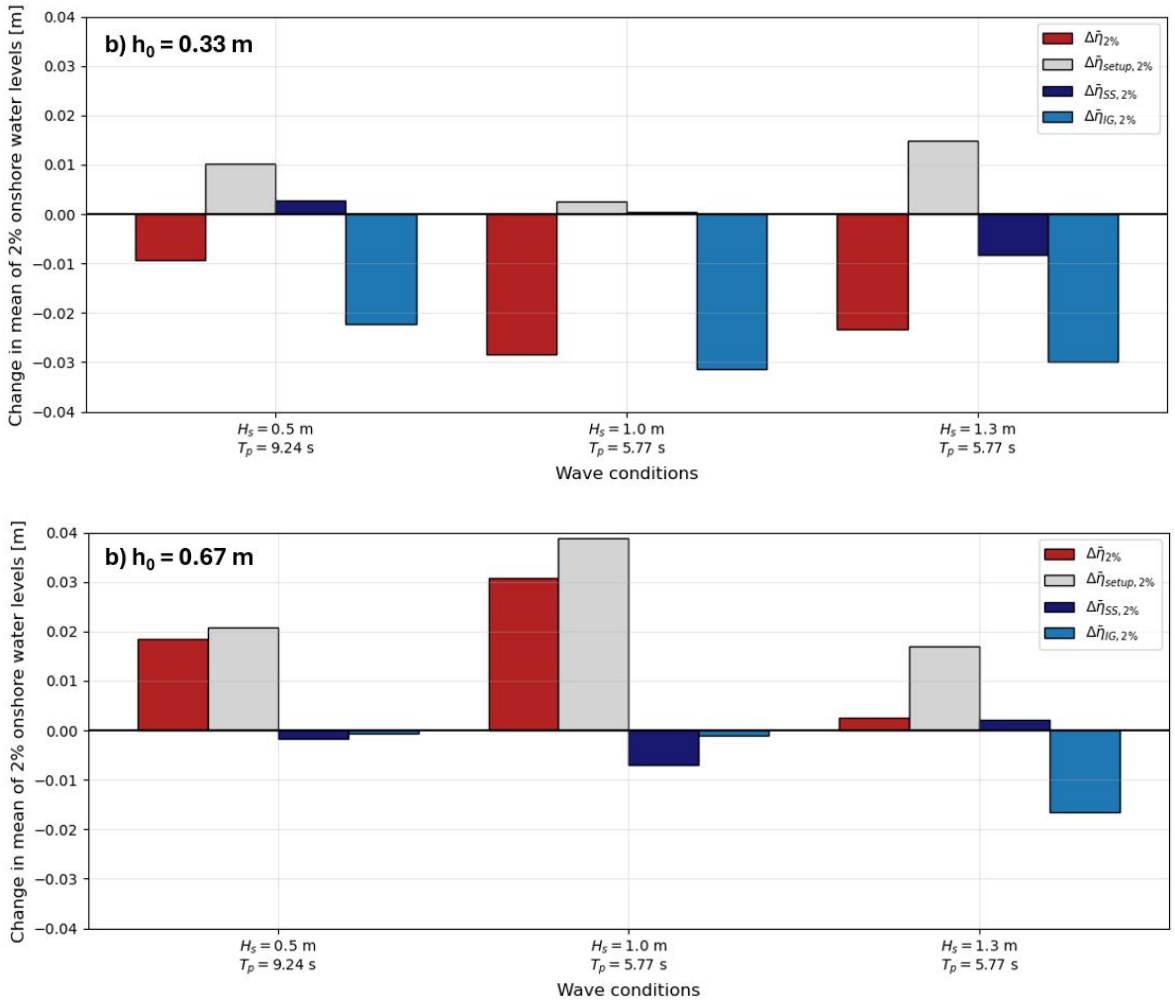

Figure 4.15: The change in mean of 2% extreme water level due to **addition** of the high-density artificial reef S3. For the three reran wave conditions C3, C7, C11 (left to right) during low water level runs (panel a) and high water level runs (panel b).

To provide more context for interpreting the extreme water levels previously presented, the relative contributions of setup, SS-waves and IG-waves are depicted in Figure 4.16. Regardless of water depth, it can be observed that a higher offshore wave height results in an increase in the wave setup contribution to onshore extreme water level. Furthermore, the wave setup consistently is a more important driver for extreme water levels at lower reef flat water depths compared to higher depth. Regarding the influence of waves, the SS-wave height has a significantly higher contribution to the wave setup at the high water depth case, likely because a larger amount of SS-wave energy reaches the reef flat. In the low water depth case, SS-wave contribution is minimal. This is compensated by increased wave setup and IG-waves. Stronger depth-induced wave breaking at the reef crest leads to increased wave setup and greater IG-wave generation through break-point forcing. The placement of the artificial reef has a relatively small effect on the distribution of the contributions, a small increase in the contribution of wave setup and a decrease in the wave-related contributions can be observed.

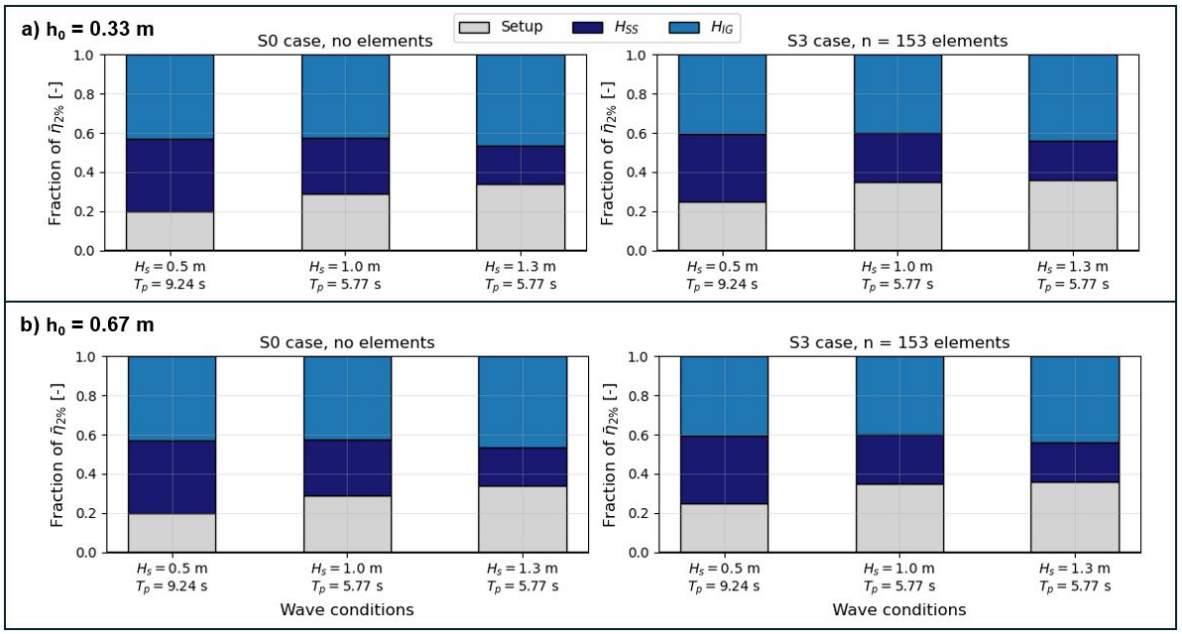

Figure 4.16: The contributions of SS waves, IG waves and setup to the change in mean of 2% extreme water level due to addition of the high-density artificial reef S3. For the three reran wave conditions C3, C7, C11 (left to right) during low water level runs (panel a) and high water level runs (panel b).

During high water levels, the introduction of artificial reefs can generate increased wave setups that counteract the reduction in wave height, leading to an increase in extreme water levels observed onshore. This increade in extreme water levels is not observed during low water levels.

4.2. Results from ADV measurements

By analyzing the data acquired by the ADVs more insight in the in-canopy flow dynamics can be gained. First of all, the individual measurement points in the velocity variance profile will be analyzed separately to reveal the spatial variability of the in-canopy flow. Thereafter, the energy density of each ADV pair located on the same height are averaged and a representative velocity variance profile is constructed. By doing this, the velocity profiles of different configurations and forcing conditions can be compared. From these representative velocity variance profiles, the wave attenuation is determined and presented. Additionally, for each wave component, the change in wave energy from free-stream to in-canopy is visualized to get an insight into which wave components are attenuated most.

4.2.1. Vertical velocity variance profiles

First of all, the velocity profiles for the H533C1 and H567C3 runs are analyzed both without (S0) and with artificial reef elements (S3). Runs H533C1 and H567C3 are selected because they represent the smallest and greatest relative depths, respectively, while maintaining the same offshore wave height. To quantify the wave energy at each measurement point, the variance σ^2_{uu} is calculated from the velocity timeseries. In Figure 4.17, ADV arrays A and B are shown in separate rows. For both runs, the total variance decreases more significantly in ADV array B than in ADV array A due to the presence of the artificial reef. This agrees with the region of flow convergence where ADV array A is located. This stark difference highlights the importance of measuring at multiple profile location within the canopy. To identify which bandwidth is most affected by the presence of the artificial reef, the first column presents the total variance, while the second and third columns show the IG-wave variance and SS-wave variance, respectively. It can be seen that for run H533C1, the IG-bandwidth contains most energy. In the other run, this is reversed, with the SS-bandwidth containing most energy. For the IG-wave bandwidth,

the observed velocity decay is consistent, regardless of available energy. For the SS-wave bandwidth however, the velocity profiles exhibit deviating behavior. By introducing artificial reef elements, the energy in the SS-bandwidth increases in ADV array A, indicating that the flow convergence affects these frequencies most. In the high water level case, where SS-waves dominate on the reef flat, this convergence effect also emerges in the total variance in Profile A. Especially the difference in SS velocity profiles underline the importance of measuring and accounting for the spatial-variability of the in-canopy flow structure.

In the total and IG-wave variance profiles, it can be seen that the flow measured by ADV4 (assumed to be representative of the free-stream flow in ADV array B) is slightly attenuated by the artificial reef. On the contrary, the flow measured by ADV1 (assumed to be representative of the free-stream flow in ADV array A) is amplified. This is an indication that the flow velocities measured by the upper ADVs do not comply with the strict definition of the free-stream flow that it remains completely unaffected by the presence of the artificial reef. However, this discrepancy can also be a result of differences in hydrodynamic conditions between the base case and artificial reef run. As these differences in forcing conditions are assumed to be small, it is decided to not investigate this in further detail.

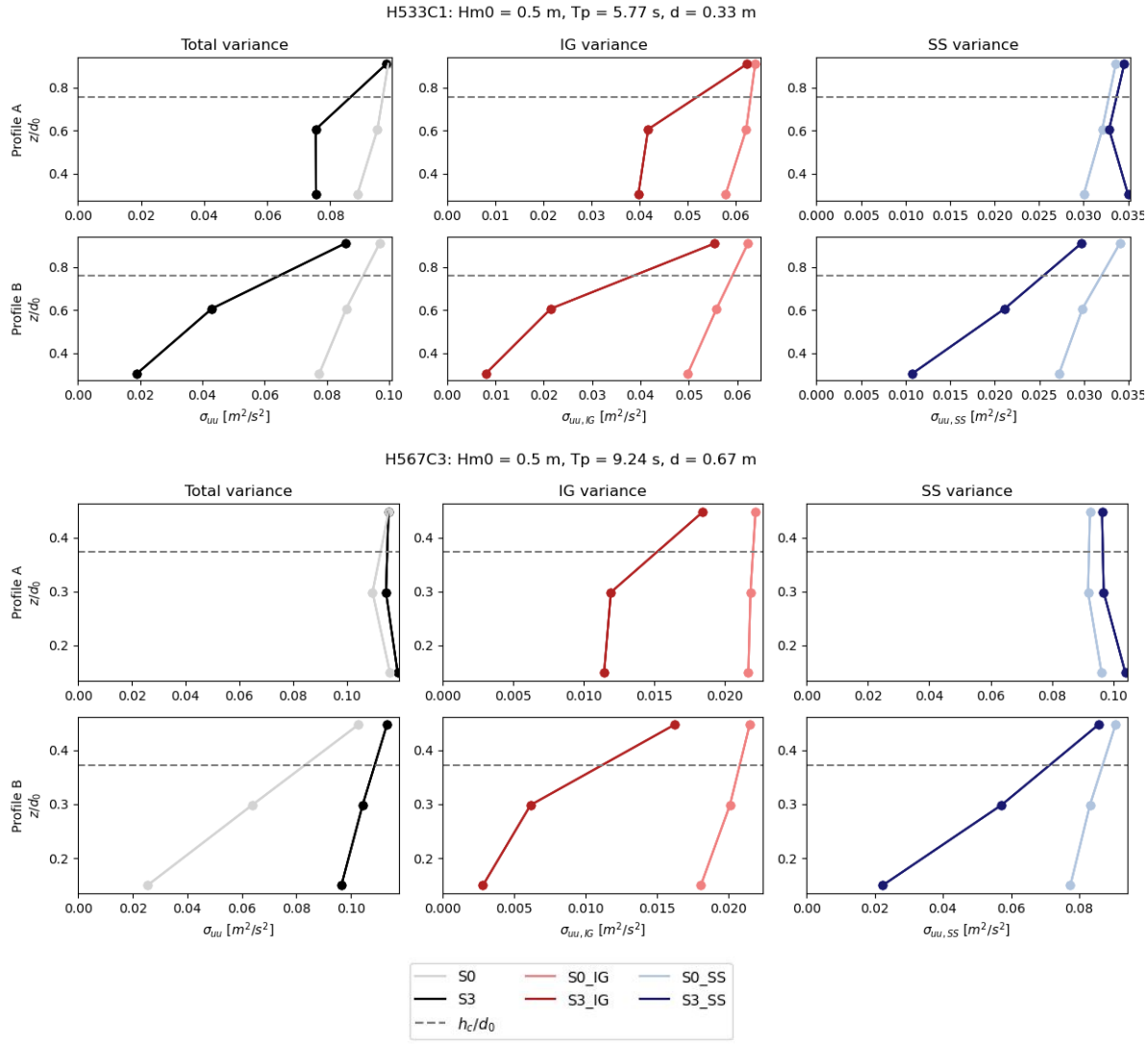

Figure 4.17: Vertical profiles of streamwise velocity variance as measured by the ADVs, for each measurement point the variance in velocity is shown. The three different columns depict the total, IG and SS velocity profile while the two rows depict the velocity profiles of profile A and B. In the upper window, the velocity profiles belonging to run H533C1 are shown while the bottom window shows the velocity profiles of H567C7.

By constructing an average variance for the ADV measurements conducted at z = 0.1, 0.2 and 0.3 m height, the effect of spatial variability is accounted for and the representative velocities used to compute wave attenuation can be seen. Figure 4.18 shows the vertical velocity variance profile for wave conditions C1 ($H_{m0} = 0.5$m, $T_p = 5.77$s) and C11 ($H_{m0} = 1.3$s, $T_p = 5.77$s), both with and without the artificial reef. Similarly, Figure 4.19 presents the vertical velocity variance profile for wave conditions C1 ($H_{m0} = 0.5$m, $T_p = 5.77$s) and C11 ($H_{m0} = 0.5$s, $T_p = 9.24$s).

By comparing the velocity profiles with and without the artificial reef, the effect of the canopy can be visualized. With only three points along the velocity profile, identifying gradients is challenging. However, certain features can still be discerned. Initially, for a bare reef, the vertical velocity variance profile tends to follow a hyperbolic as expected from linear wave theory. With the introduction of the artificial reef, the flow velocity variance measured by the upper ADVs experiences slight attenuation, while the in-canopy velocities are significantly reduced, indicating diminished flow within the reef's canopy. The initial reduction within the canopy is substantial, followed by a slower rate of decrease, with the velocity variance showing only a minor reduction at the lowest measurement point.

Figure 4.18 reveals that increasing the offshore peak period results in greater flow velocity attenuation over the vertical by the artificial reef and leads to steeper gradients in the velocity variance profile. Similarly, Figure 4.18 shows that increasing the offshore wave height also results in steeper gradients in the velocity variance profile.

Furthermore, it is observed that in the low water case compared to the high water case, more wave energy is 'available' at the upper ADVs as the measured velocity variance in the low water case is higher here. For the high water level, the upper ADVs are situated further away from the water surface and it is likely that not all flow energy present in the free-stream flow is able to reach the upper ADVs.

Appendix Figure D.2 shows the averaged vertical velocity variance profiles for all forcing conditions. The aforementioned observations are consistent with the forcing conditions not yet presented in Figure 4.18 and 4.19.

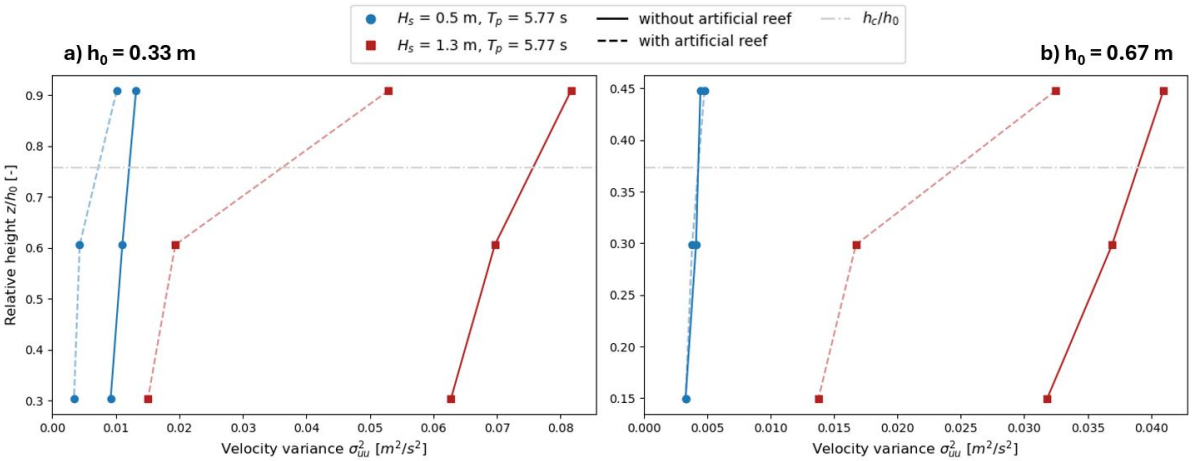

Figure 4.18: Velocity profiles for wave conditions C1 (blue) and C11 (red) with on the left the low water case and right the high water case. The variances are determined by averaging the variance of two ADVs at the same height. The solid lines depict the velocity profiles without artificial reef while the dashed lines depict the velocity profiles with artificial reef.

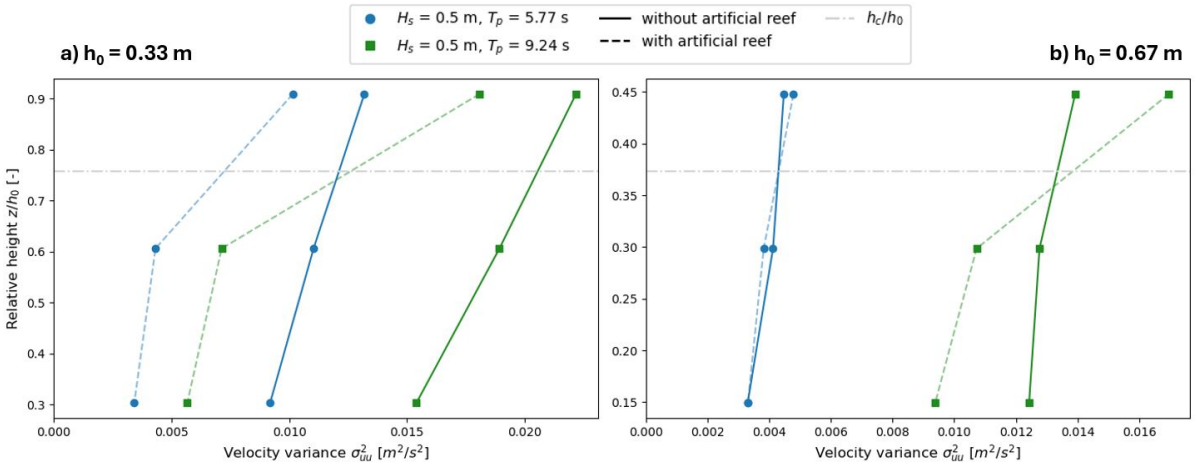

Figure 4.19: Velocity profiles for wave conditions C1 (blue) and C3 (green) with on the left the low water case and right the high water case. The variances are determined by averaging the variance of two ADVs at the same height. The solid lines depict the velocity profiles without artificial reef while the dashed lines depict the velocity profiles with artificial reef.

The total velocity variance decreases more significantly in ADV array B than in ADV array A due to the artificial reef, even increasing SS wave energy in ADV array A, highlighting the importance of measuring at multiple locations within the canopy. Increasing the offshore peak period and wave height leads to steeper gradients in the velocity variance profile, indicating greater flow attenuation by the artificial reef.

4.2.2. Observed flow attenuation

Figure 4.20 shows the observed flow attenuation parameter α_w per forcing condition. Note that a low value of this flow attenuation parameter corresponds to **high** flow attenuation. The overview of attenuation parameters reveals that the attenuation is consistently higher at low water levels where the canopy is closer to the water surface. Furthermore, it can be seen that increasing the offshore significant wave height or peak period results in a decrease in flow attenuation parameter and thus larger flow attenuation.Increasing the artificial reef density by 62 elements from configuration S1 to S3 reduces the flow attenuation parameter by approximately 0.05 to 0.08. This indicates that 5–8% less flow energy from the representative free-stream flow reaches the canopy.

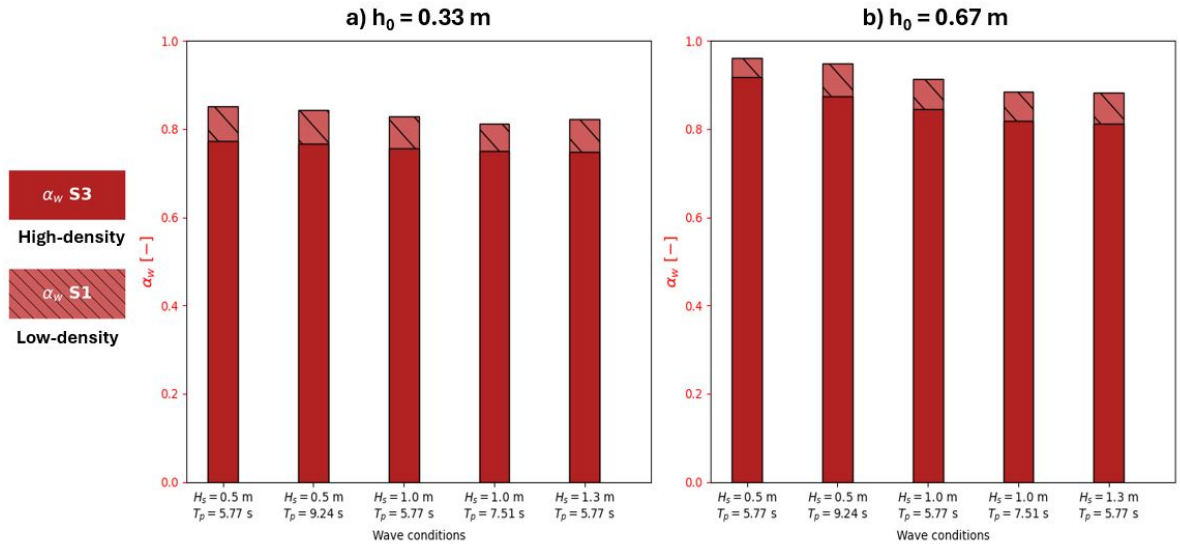

Figure 4.20: Flow attenuation paramter ϵ for all wave conditions during low water level runs (panel a) and high water level runs (panel b) for the low-density (S1) and high-density (S3) configuration.

By calculating the complement of the flow attenuation parameter $(1-\alpha_w)$ for each wave component and comparing it between the bare reef case and the high-density artificial reef, the frequency dependence of the flow attenuation can be determined. Figure 4.21 shows the flow attenuation per wave component and how much it increases due to the artificial reef's presence for both low water levels (panel a) and high water levels (panel b). Note that a higher value of $1-\alpha_w$ represent greater flow attenuation. The figure shows that the flow is minimally attenuated in the bare reef case. In some cases the flow attenuation even becomes negative, although this is likely an artifact of the low measured energy in the top 'free-stream' ADVs. The Figure also shows that the flow attenuation for the IG waves is roughly double that of the attenuation observed for the SS-waves.

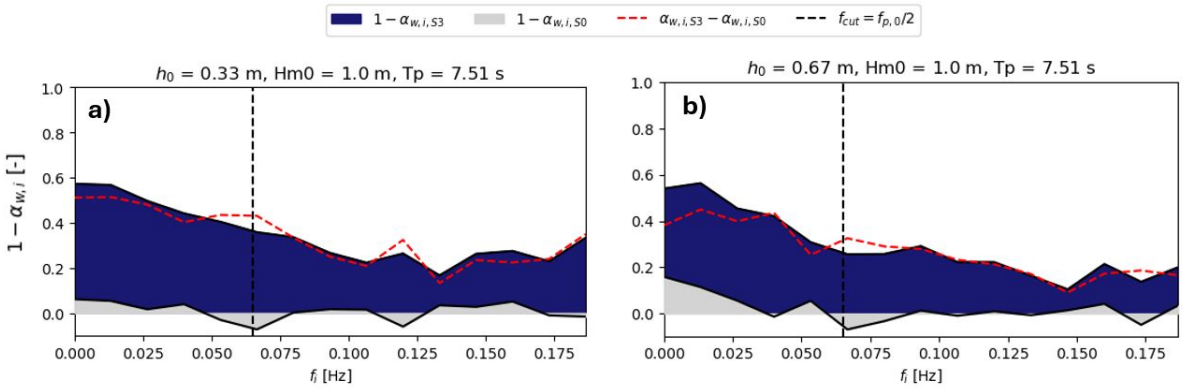

Figure 4.21: Energy change per wave component as observed comparing the free-stream flow and in-canopy flow (**represented by the four bottom ADVs**) for wave condition C7 during low water level (panel a) and high water level (panel b). Note that the percentages of energy changes are layered over each other. By visualizing this way, the grey area is the initial energy change due to bottom friction and the added blue area is the energy change added by introducing the artificial reef elements. Higher values mean that less wave energy is able to penetrate into the canopy. The red line depicts the increased flow attenuation by placing the artificial reef elements.

The same figures but for all forcing conditions are presented in Figures E.1 and E.2 in Appendix E.1.

Flow attenuation is consistently higher at low water levels, where the canopy is closer to the water surface. Increasing the artificial reef density leads to a 5-8% reduction in the amount of flow energy from the free-stream that reaches the canopy. IG waves are attenuated more than SS waves and therefore shorter waves penetrate into the canopy more easily.

5

Discussion

In this chapter, the previously presented results are examined and discussed in further detail, the observations are compared to existing literature and the limitations of the physical model and data analysis methods are discussed. First of all, the possible drivers of the observed increase in wave setup are discussed in Section 5.1. Secondly, the observed wave height reduction is compared to other literature investigating the effect of artificial reefs on wave transformation in Section 5.2. Consequently, in Section 5.3, the observed flow attenuation rates are used to model canopy-induced dissipation rates after which these modeled dissipation rates are compared to the observed dissipation rates. Furthermore, the observed flow attenuation is compared to the in-canopy flow model of Lowe et al. (2005b). The limitations the physical model and data analysis methods has and what implications these limitations have on the drawn conclusions are presented in Section 5.4 and 5.5. Finally, the limitations of the data quality is presented in 5.6.

5.1. Potential drivers of increased wave setup and extreme water levels

As was presented in the extreme water level analysis in Section 4.1.6, the increase in wave setup counteracts the reef's effectiveness in reducing extreme water levels at the beach toe. Specifically during the high water level cases, placing the artificial reefs led to an increase in the mean of the 2% extreme water levels, making the artificial reef counterproductive. In other words, the reef's positive impact on wave height is counteracted by the increase in wave setup.

To gain insight in what drives this increase in wave setup and how such a counterproductive effect can be prevented, key mechanism affecting wave setup as introduced in Section 2.3.1 are considered. These key mechanisms—wave skewness, radiation stress, canopy emergence, and mean canopy drag force—will be examined in greater detail in this section.

First of all, the effect of the artificial reef on the wave skewness is investigated. Figure 5.1 shows the wave skewness across the artificial reef stretch for three wave conditions during high water level runs. First of all, it can be seen that skewness decreases across the artificial reef because the steepest, most skewed waves break will break due to instabilities. Highly nonlinear waves, such as steep, breaking waves, typically display skewness on the order of O(0.1) (Marthinsen and Winterstein, 1992), so the observed SS-wave skewness of 0.15 - 0.45 can be classified as steep, breaking waves. The figure also shows that, due to the presence of the artificial reef, the wave steepness decreases by approximately 0.05. This change is deemed not substantial enough to affect the wave setup to the extent observed during the experiments.

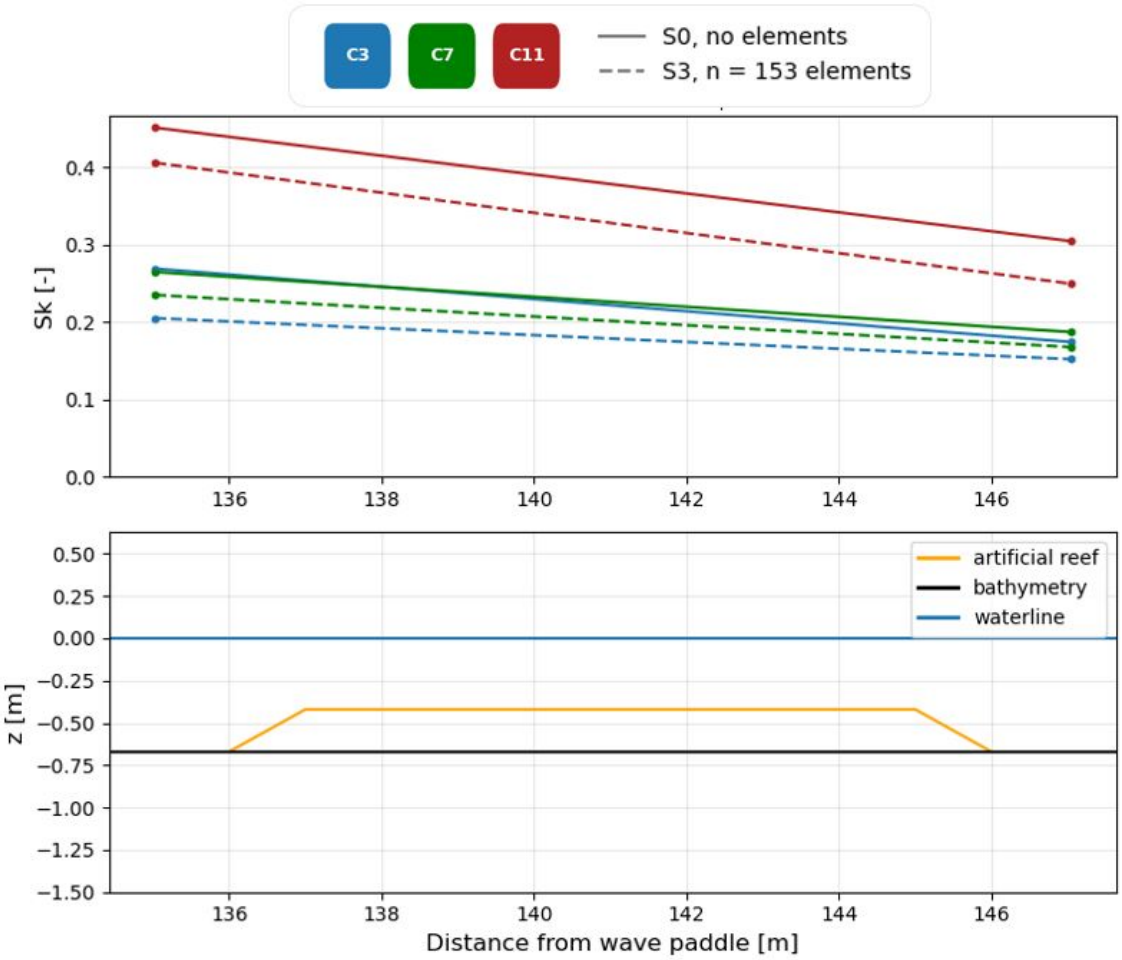

Figure 5.1: Transformation of the wave skewness across the artificial reef for the rerun wave conditions C3, C7 and C11 during the high water level runs.

The emergence of the artificial reef elements is investigated by showing the water level timeseries and canopy height of 0.25 meters. Figure 5.2 shows this water level timeseries and canopy height for run S0H533C1, which is the only run in which the artificial reef emerges above the water surface. This plot reveals that, even during this run, there is only one single moment when the canopy becomes slightly emerged. At this point, the water level is just $3.3 \cdot 10^{-5}$ m below the canopy height. Thus, artificial reef emergence is excluded as a driver of the observed increase of wave setup.

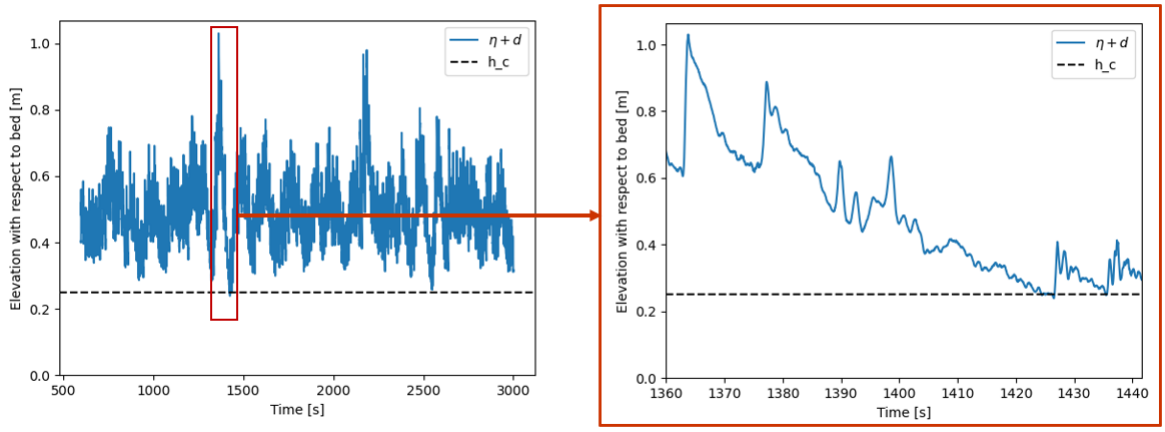

Figure 5.2: Surface elevation timeseries of run S0H533C1 with canopy height of 0.25 m plotted alongside. Zoom shows the single moment when the artificial reef becomes becomes emerged.

In Table 5.1, the mean value of the flow velocity measured by EMF09, within the artifial reef. This instrument was chosen because it directly measures the return current impacting the artificial reef. As the instrument is placed 0.15 m above the bed, it is a good indicator of the magnitude of the near-bed current as the depth at this location is roughly 0.85 m for run S3H567C7. To conduct this analysis, the velocity timeseries of EMF09 are post-processed as such that the velocity is 0 during still water to ensure 0 offset. The presented values reveal two important features of the return current as occurring in the physical model. First of all, an increase in water depth consistently results in an increase in return current. At higher water levels, more wave energy and therefore mass transport reaches the shoreline. According to the principle of continuity, this increased flow must return offshore, leading to a stronger return current. Secondly, comparing runs with and without an artificial reef shows that introducing the artificial reef has little effect on the return current. However, a canopy drag force is added to the momentum balance when the artificial reef is introduced, potentially influencing the wave setup.

Table 5.1: Increase of return current by increasing the initial reef flat water depth from 0.33 to 0.67 meter for the repeated wave conditions C3, C7 and C11.

		$H_{m0} = 0.5m, T_p = 10.39s$		$H_{m0} = 1.0m, T_p = 5.77s$		$H_{m0} = 1.5m, T_p = 5.77s$	
Configuration		S0	S3	S0	S3	S0	S3
u_{return} [m/s]	d = 0.33 m	0.049	0.037	0.055	0.058	0.085	0.078
	d = 0.67 m	0.068	0.052	0.076	0.074	0.105	0.114
Δu_{return} [%]		+39	+41	+38	+28	+24	+46

A resistance force exerted by the canopy on the water column, varying in time with the canopy averaged flow velocity, can be parametrized by equation 2.8 as defined in Lowe et al. (2005b). To ensure the correct order of magnitude, a bulk drag coefficient C_d value of 2.5 is used for the calculations, as suggested by Lowe et al. (2005b), used on cylindrical elements in oscillatory flow, with a similar grid and spacing.

To get an idea of the magnitude of the effect of both this canopy drag force, the depth-averaged 1D momentum balance as defined in equation 2.9 is considered. As in this case the only interest is the effect on the canopy drag force and radiation stress, the inertial, advective, diffusive, shear terms can be crossed out. Under the assumption of steady flow and normally incident wave forcing can be formulated as presented in equation 5.1. The average canopy drag force F_c

$$\cancel{\frac{\partial u}{\partial t}} + \cancel{u\frac{\partial u}{\partial x}} - \cancel{v_h\frac{\partial^2 u}{\partial x^2}} = -g\frac{\partial \eta}{\partial x} - \cancel{c_f\frac{u|u|}{h}} + F_c + \frac{F_x}{\rho h} \tag{5.1}$$

averaged over many wave cycles:

$$\rho g h\frac{\partial \overline{\eta}}{\partial x} + \frac{\partial S_{xx}}{\partial x} + \overline{\tau}_b + \overline{F}_c = 0 \tag{5.2}$$

The contribution of the canopy drag force and radiation stress terms on the change in water level can than be estimated by integrating this simplified momentum balance as

$$\overline{\eta}(x) = \frac{1}{\rho g h}\int -\frac{\partial S_{xx}}{\partial x}dx + \frac{1}{g}\int \bar{F}_c\, dx \tag{5.3}$$

if both the radiation stress gradients $\frac{\partial S_{xx}}{\partial x}$ and the canopy drag force $\bar{F}_c$ are measured in units of N/m.

To be able to use the canopy drag force in the provided momentum balance, the drag force needs to be averaged over many wave cycles. To compute this averaged canopy drag $\bar{F}_c$ force the following steps are followed:

1. The timeseries of ADV2 and ADV3 in ADV array A are averaged to approximate the average in-canopy flow velocity $U_c(t)$.
2. The absolute value of the square of this timeseries is determined.
3. By filling in the parameters corresponding to the relevant artificial reef configuration from Table 3.5 in equation 2.8, it is found that the average canopy drag force $\bar{F}_c$ is equal to 0.84 (low-density artificial reef) or 1.54 (high-density artificial reef) times the value determined in step 2.

For run S3H567C7, with the greatest observed increase in wave setup from its corresponding bare reef case, these steps result in the following averaged canopy drag force (for the high-density artificial reef):

$$\overline{F_c(t)} = \frac{C_d\lambda_f}{2h_c(1-\lambda_p)}\overline{\left|\overline{U}_c(t)\right|\overline{U}_c(t)} = 1.54\overline{\left|\overline{U}_c(t)\right|\overline{U}_c(t)} = 0.04\ N/m \tag{5.4}$$

As the calculated canopy-induced drag force is measured in units of m/s^2, it does not have to be divided by ρh like the radiation stress gradient which is measured in units of N/m. The contribution of the canopy-induced drag force to the wave setup can than be calculated as $\frac{F_c}{g}\cdot L_{restoration} = \frac{0.04}{9.81}\cdot 10 = 0.041$. This is close the observed increase in onshore mean water level of 0.033 m for the considered run.

To quantify the effect of the wave-induced force F_x on the wave setup, the differences in radiation stress gradients is determined. It should be noted that the radiation stresses used in this thesis are calculated using equation 2.21, which is derived from linear wave theory. However, radiation stresses in non-linear waves deviate from this linear approximation. With the available data, this is the best approximation that can be made. In Figure 5.3, the blue curves show the radiation stresses on the reef flat with and without the artificial reef. From these curves, the radiation stress gradients can be determined. This is done with central differences in the interior points and backward differences at the onshore boundary. The spacing between data points may be too large to accurately address the local variations in radiation stress. Furthermore, the radiation stresses have been calculated from discrete data on the reef flat by using finite differences. For sparse data, these numerical methods (e.g., forward or central differences) can introduce significant errors.

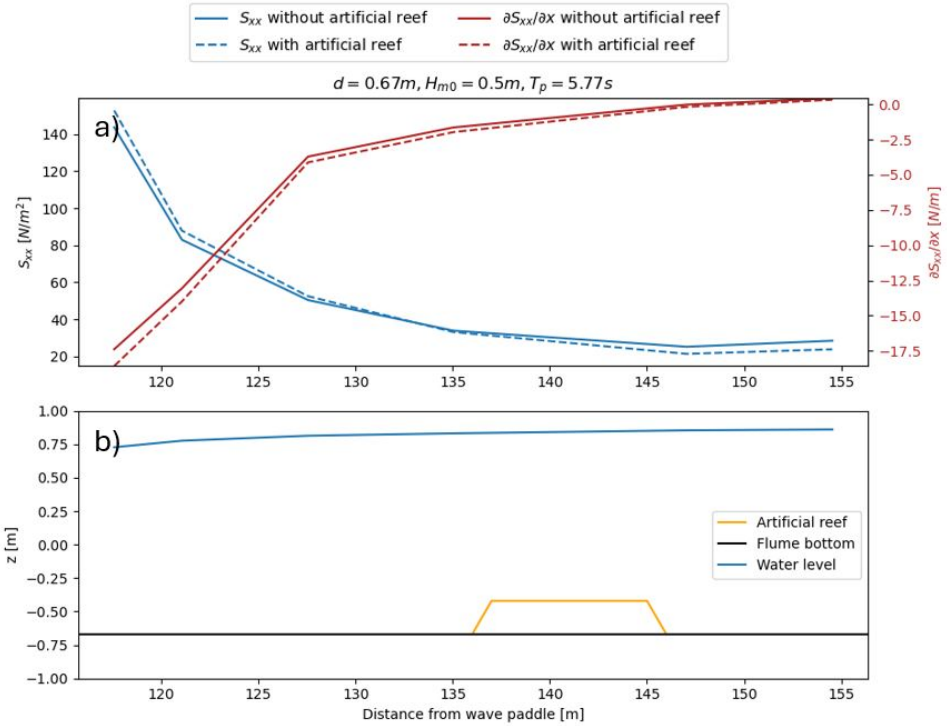

Figure 5.3: Radiation stress and radiation stress gradient on the reef flat for run S3H657C7, in which the largest increase in wave setup was observed.

By subtracting the stress gradient vectors with the reef with the stress gradients without the reef, this vector follows:

$$\Delta \partial S_{xx}/\partial x = [-1.19, -0.93, -0.41, -0.33, -0.16, -0.10], \tag{5.5}$$

meaning that the introduction of the artificial reef makes the radiation stress gradients more negative, thereby leading to higher radiation stresses in absolute terms. Applying the trapezoidal rule to the integral in equation 5.3 reveals that this decrease in radiation stress gradients results in a calculated onshore mean water level increase $\Delta\overline{\eta}$ of 0.002 m. However, the observed increase in onshore mean water level for the considered run is 0.033 m which is a difference of O(10), indicating that the change in radiation stresses is unlikely to be the main contributor to the observed increased wave setup.

Considering the aforementioned findings on radiation stress, the minimal wave skewness over the artificial reef, and the fact that the reef remains consistently submerged, these three potential contributors to the increased wave setup can be ruled out. This strongly suggests that the canopy-induced drag force is the primary factor in driving the observed increase in wave setup by introducing artificial reef elements.

However, it is important to note that the impact of changes in bottom friction due to the artificial reef has not been considered. The cross-shore pressure gradient associated with the wave setup $\bar{\eta}$ also balances the bottom stress τ_b and therefore an increase in bottom friction will lead to an increase in wave setup. Apotsos et al. (2007) highlights that bottom friction plays a crucial role in setup predictions. Ignoring bottom friction leads to an underestimation of the observed setup across all water depths. When investigating wave dissipation by coral canopies using a bottom friction model, the lowercase 'bulk' friction coefficient c_f (which accounts for bottom friction, inertial forces, canopy drag, and canopy friction) increases, as the combined roughness of the canopy and bottom is greater than that of the bottom alone. Consequently, the increase in bottom friction caused by the artificial reef in the CREST experiments may contribute to the observed wave setup increase. However, without further analysis, the extent of this contribution remains uncertain.

5.1.1. One-dimensional model simplification

As seen in the extreme water level analysis, the observed increase in wave setup by introducing the artificial reef counteracts wave height reduction and even increase extreme onshore water levels. The drag force induced by the artificial reef was identified as the primary factor driving force of the observed increase in wave setup. Although this finding is based on an 'order of magnitude' calculation, it is valuable to compare the hypothesis that the return flow induces a canopy drag force, leading to an increase in wave setup, with existing literature.

Van Dongeren et al. (2013a) demonstrated that mean wave-driven return flows influence wave setup, which ties in with the hypothesis that the return flow induces a canopy drag flow resulting in increased wave setup as observed in the CREST experiments. In this study, one-dimensional cross-shore numerical modeling of a fringing reef significantly overestimated wave setup compared to field data and wave setup estimates from other coral reef systems. The outcome of a horizontal two-dimensional model closely matched with observed wave setup in the field due to significant return flows, which led to reduced setup across the reef. This return flow was also observed by numerical modeling by Lowe et al. (2009), where the spatial distribution of the wave setup resulted in persistent wave-driven return flows.

The observed increase in wave setup in the physical model could therefore be caused by a limitation of measuring in a wave flume, where mean wave-driven flow can not freely flow offshore through the artificial reef stretch. By obstructing this mean return flow, the mass transported onshore over the artificial reef by Stokes drift accumulates behind the artificial reef, appearing as a rise in mean water level.

Another limitation of the one-dimensional nature of the physical model is the absence of refraction and diffraction effects. Particularly diffraction can negatively influence the wave reduction of an artificial reef. In the field, an artificial reef typically has a limited extent alongshore-wise. This means that at the edges, diffraction will cause waves to "bend" around the structure, resulting in increased wave transmission over the artificial reef. As the artificial reef in the CREST experiments was installed over the full flume width, diffraction effects are absent, which could result in the physical model overestimating wave height reduction.

5.2. Comparing observed artificial reef effectivity with literature

In the introduction, a reference was made to Ferrario et al. (2014), claiming that reef crests, on average, attenuate 86% of the incident wave energy and reef flats dissipate the remaining wave energy by an average of 65%. The difference in context compared to this research is that Ferrario et al. (2014) investigated the effect of the presence of the entire reef platform (reef crest and reef flat) instead of only an artificial reef, explaining the large differences in observed wave energy reduction.

Takens (2024) reproduced the CREST experimental setup using the phase-resolving hydrodynamic model SWASH. In this numerical model, relative wave height reduction at the location just onshore of the artificial reef (as presented in Table 4.1) was overestimated by 200% when using uncalibrated parameters and a porous-medium representation of the artificial reef.

Roelvink (2019) adopted a conventional 'bottom friction' model (increase in bed level combined with a higher friction coefficient) in the phase-resolving version of the hydrodynamic model XBeach. Transmission coefficient (K_T) across an artificial reef of height 1.25 meters and width of 10 meters are predicted to be 0.58 for SS-waves and 0.66 for IG-waves. Respectively, this corresponds to a wave energy reduction of 42% and 34%. These are results of forcing it with a wave height of 4.0 meters and a wave period of 7.16 seconds. These parameters are all at prototype scale. The closest wave condition C11 (prototype scale H_s = 3.0 m, T_p = 10 s) in the CREST experiments resulted in wave energy reductions of 26 and 31%, which is relatively close. Background dissipation is included in both the values from Roelvink (2019) and the CREST experiments, thus it is difficult to compare the net effect of the artificial reef.

It is also relevant to look compare the artificial reef geometry to other artificial reefs applied in experiments or in the field. Diederen (2022) used interlocking blocks with a height of 0.01 m, 5 layers to achieve a height of 0.05 m. These were tested on a scale of 1:20 so the prototype block height is be 0.2 m per interlocking block which results in a total artficiail reef height of 1 m. Other artificial reef structures like Reef Balls are available within the size range 0.30 - 1.83 m (Reefball, 2025). The prototype height of the Coastruction elements is 0.75, indicating that the artificial reef used in the CREST

experiments is relatively low. As the geometrical complexity of the artificial reef element is already high (boosting C_d and C_f), the two remaining methods to increase wave energy reduction capacity are to either increase the element height or increase the artificial reef density. As decreasing the ratio of canopy height over total water depth reduced the relative wave energy reduction significantly (Figure 4.5), increasing the element height seems the most promising option of these two.

Quick calculation to show effect increasing density and increasing relative height on wave height reduction?

5.3. Linking observed dissipation to in-canopy flow using in-canopy flow theorem

After quantifying the in-canopy flow dynamics in terms of velocity variance profiles and flow attenuation in Section 4.2, the canopy-induced wave dissipation rate is determined via the in-canopy flow theorem of Lowe et al. (2005b) and presented in Section 5.3.1. This modeled canopy wave dissipation rate is then compared to both the observed dissipation rate in Section 5.3.2 and the observed wave energy flux gradient per wave component in Section 5.3.3.

5.3.1. Modeled in-canopy wave dissipation

Using the in-canopy flow model of Lowe et al. (2005b), the wave dissipation rate induced by the canopy itself can be calculated as presented in equation 2.15. The analysis in this section follows the same steps as made in the calculation of this canopy wave dissipation rate. First, the observed values of the flow attenuation parameter α_w are presented, with which the dissipation factor f_e is calculated as presented in equation 2.14. By analyzing the dissipation rate for each wave component, a quantification is made on which wave components are affected most by the canopy according to the in-canopy flow model. Finally, the canopy-induced wave dissipation rate is presented.

For these calculations, a C_d of 2.5 is used for the calculations, as suggested by Lowe et al. (2005b). In the same study, a C_f of 0.02 was used. However, Lowe was dealing with significantly smoother plastic canopy elements than the Coastruction elements used in the CREST experiments. Therefore, a C_f of 0.05 is chosen, which remains on the order of O(0.01).

Figures 5.4 and 5.5 display the dissipation factors for both the low-water case (panel a) and the high-water case (panel b) for the S1 and S3 configurations. To incorporate the low-density configuration S1 in this analysis, the middle ADVs (ADV2 and ADV5) represent the in-canopy flow, with the method visualized in Figure 3.21. The figure reveals that, as expected, waves are affected more by the high-density configuration compared to the low-density artificial reef. It can also be observed that IG-wave components are affected less by the artificial reef than the SS-wave components are. As artificial reef density increases, the dissipation factor difference between IG- and SS-wave components increases. In other words, the frequency dependence of the dissipation factor increases. Additionally, since attenuation is lower at higher water levels as seen in Figure 4.20, wave-induced flow energy can penetrate more easily, causing wave components to be more influenced by the canopy in the high water level scenario.

Figure 5.4 shows that the dissipation factor decreases with increasing offshore significant wave height, regardless of water level, while Figure 5.5 indicates a similar decline with increasing offshore peak period. As the dissipation parameters C_d and C_f stay constant, this decrease is a logical consequence of the lower fraction of flow energy able to penetrate into the canopy for longer and higher waves, as shown in Figure 4.20.

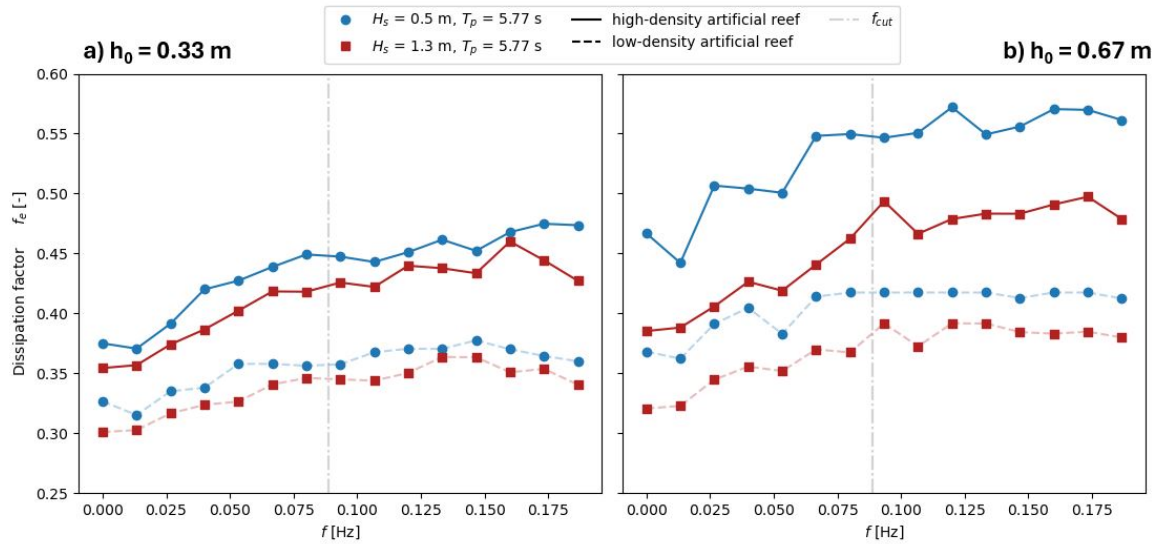

Figure 5.4: Dissipation factor f_e per wave component for wave condition C1 (blue) and C11 (red) indicating to which extent a wave component is affected by the artificial reef. Panel a shows the dissipation factors for the high water level run, while panel b presents them for the high water level run.

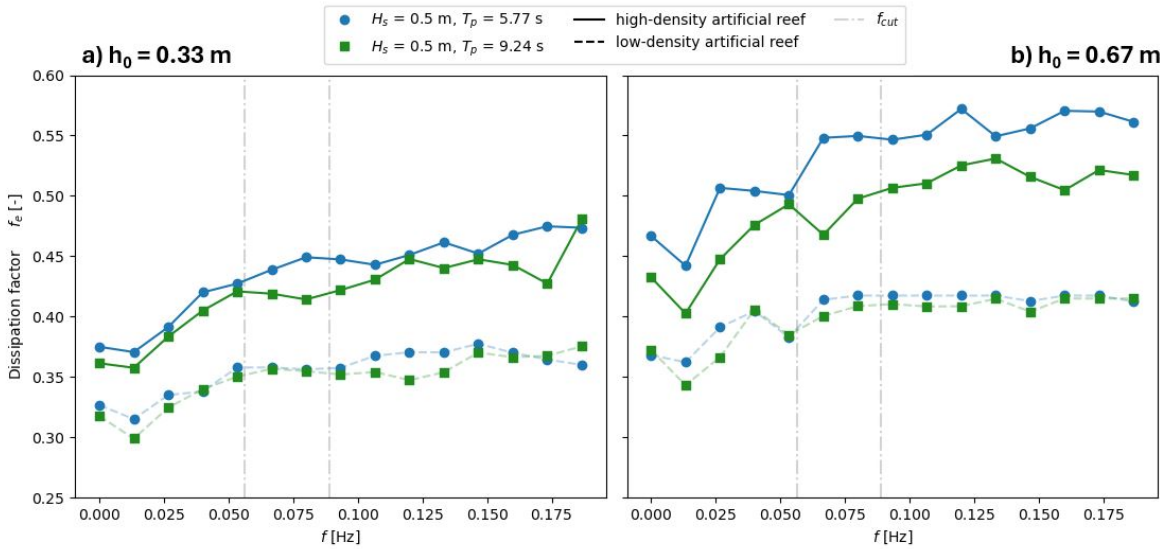

Figure 5.5: Dissipation factor f_e per wave component for wave condition C1 (blue) and C3 (green) indicating to which extent a wave component is affected by the artificial reef. Panel a shows the dissipation factors for the high water level run, while panel b presents them for the high water level run.

Figure 5.6 the canopy wave dissipation rate modeled via the in-canopy flow theorem (ϵ_{mod}) are plotted alongside the observed flow attenuation parameter (α_w) for all forcing conditions. This figure shows that, first of all, canopy wave dissipation rates are consistently lower during high water level runs. Increasing the density of the artificial reef slightly increases the canopy wave dissipation rate. Furthermore, the canopy wave dissipation rate is higher for forcing conditions with higher and longer waves. This suggests that, despite greater flow attenuation for higher and longer waves, the increased available wave-induced flow energy results in higher canopy wave dissipation rates.

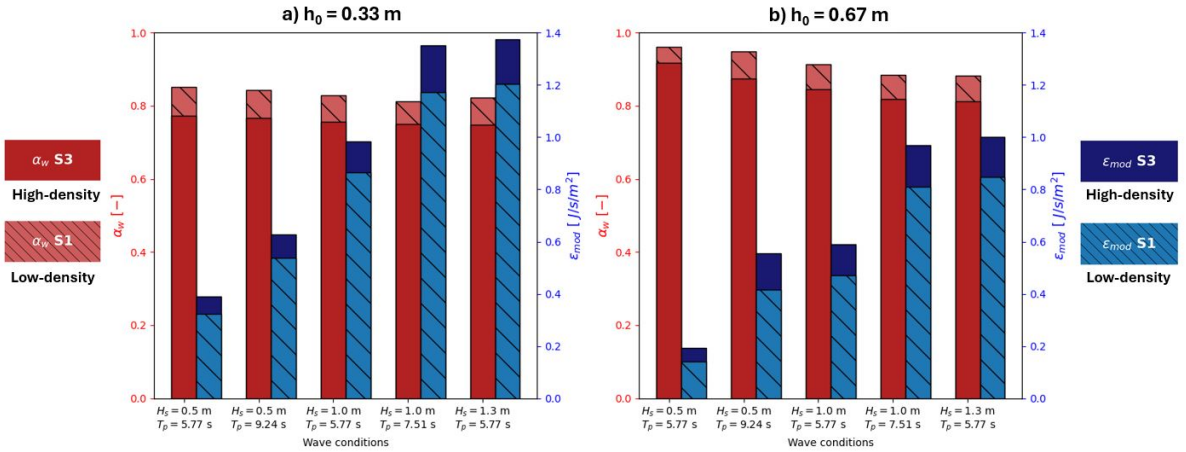

Figure 5.6: Flow attenuation paramter ϵ and its modeled canopy dissipation rate ϵ_{mod} for all wave conditions during low water level runs (panel a) and high water level runs (panel b) for the low-density (S1) and high-density (S3) configuration.

5.3.2. Comparison to observed wave dissipation

The observed wave dissipation rates are presented alongside the modeled canopy wave dissipation rates in Figure 5.7. To provide a clear comparison with the observed artificial reef-induced wave dissipation rate, the canopy wave dissipation rate is plotted from the same height as the observed increase in wave dissipation. The error bar presented above the canopy wave dissipation rates indicates the value the wave dissipation rate would have if both the bulk drag coefficient C_d and friction coefficient C_f are increased by 50%. Figure 5.2 presents the percentage of modeled canopy wave dissipation relative to the observed artificial reef-induced wave dissipation. This table shows that during low water level runs, the modeled canopy wave dissipation accounts for **30–44%** of the observed artificial reef-induced wave dissipation. In high water level runs, this percentage varies between **13%** and **57%**, indicating greater inconsistency in the prediction.

The same table reveals that the lowest discrepancies between observed and modeled dissipation rate are present at the forcing conditions with long waves, namely wave condition C3 ($H_s = 0.5$m, $T_p = 9.24$s) and C9 ($H_s = 1.0$m, $T_p = 7.51$s). This is an indication that wave breaking is partly responsible for the discrepancy between the observed and modeled dissipation rates as wave breaking is more likely to occur with short, high waves. Theoretically, if no extra wave breaking is added by the presence of the artificial reef, the observed net increase in dissipation by the artificial (the blue bar) and the canopy-induced dissipation rate (the red bar) should be equal in height. However, as the in-canopy flow model likely has its inaccuracies and the amount of wave breaking is unlikely to remain unchanged by introducing the artificial reef elements, the bar heights deviate from each other. The most likely scenario is that the artificial reef enhances wave breaking and this results in larger discrepancies between modeled and observed dissipation rates.

Table 5.2

h_0 = 0.33 m	$H_s = 0.5$ m, $T_p = 5.77$ s	$H_s = 0.5$ m, $T_p = 9.24$ s	$H_s = 1.0$ m, $T_p = 5.77$ s	$H_s = 1.0$ m, $T_p = 7.51$ s	$H_s = 1.3$ m, $T_p = 5.77$ s
$\Delta\epsilon$ [%]	30	43	35	44	39
h_0 = 0.67 m	$H_s = 0.5$ m, $T_p = 5.77$ s	$H_s = 0.5$ m, $T_p = 9.24$ s	$H_s = 1.0$ m, $T_p = 5.77$ s	$H_s = 1.0$ m, $T_p = 7.51$ s	$H_s = 1.3$ m, $T_p = 5.77$ s
$\Delta\epsilon$ [%]	13	57	14	57	40

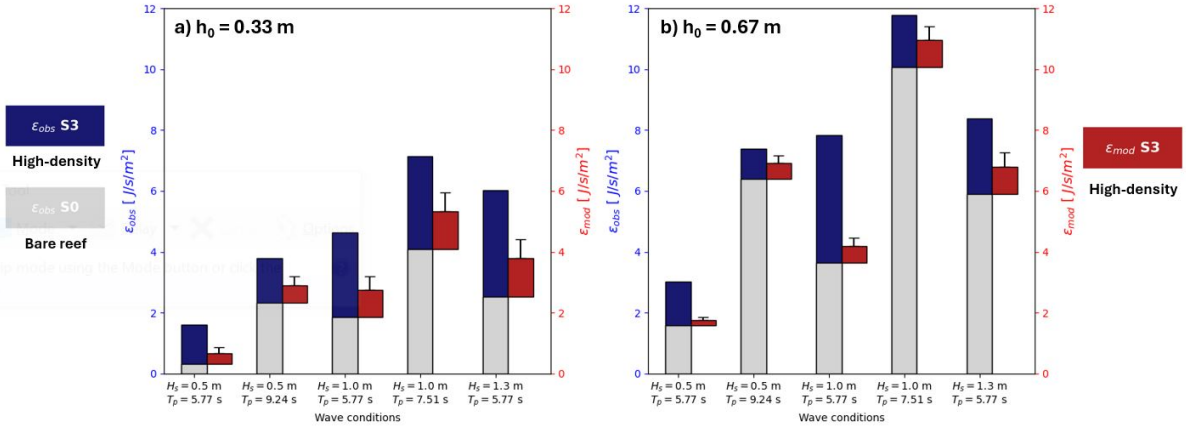

Figure 5.7: Absolute observed wave dissipation rate ϵ_{obs} (calculated with incoming wave energy from just before to just after the artificial reef (PS13 to PS14)) compared to modeled canopy wave dissipation rate ϵ_{mod} for all wave conditions during low water level runs (panel a) and high water level runs (panel b).

5.3.3. Spectral comparison to observed wave dissipation

To get an idea at which frequencies the canopy model predicts most wave dissipation and how this is linked to the observed wave dissipation, the canopy wave dissipation rate per wave component $\epsilon_{c,i}$ as presented in equation 2.15 is compared to the observed energy flux gradient per wave component ϵ_i as presented in equation 3.29. As this comparison is conducted in the frequency domain, the observed energy flux gradients is now the sum of dissipation by the canopy, dissipation by breaking and bottom friction and energy added or removed by non-linear energy transfers.

Figure 5.8 shows the energy flux gradients during a low water level run (panel a) and a high water level run (panel b), both with an offshore wave height of 0.5 m and peak period of 5.77 s. In panel a, the energy flux gradients of the longer waves align closely. However, the peak around 0.1 Hz in the observed energy flux gradients is not represented in the modeled canopy wave dissipation rates. In the high water level case, it can be seen that the observed energy flux gradients becomes negative, indicating non-linear transfers from higher frequencies. Now, the in-canopy flow model does not match the wave energy flux gradient observed in the longer wave components. This is a logical consequence of the fact that the in-canopy flow model only covers dissipation by

It should be noted that the dissipation following from the in-canopy flow dynamics only accounts for drag and friction losses within the canopy and not for dissipation by wave breaking and bottom friction. The large discrepancy at higher frequencies between the two dissipation curves could be a cause of this absence of a wave breaking in the formulation of in-canopy wave dissipation. Even more so, the introduction of a canopy within wave-induced flow does enhance wave breaking and discrepancies could get even larger when canopy density or complexity is increased.

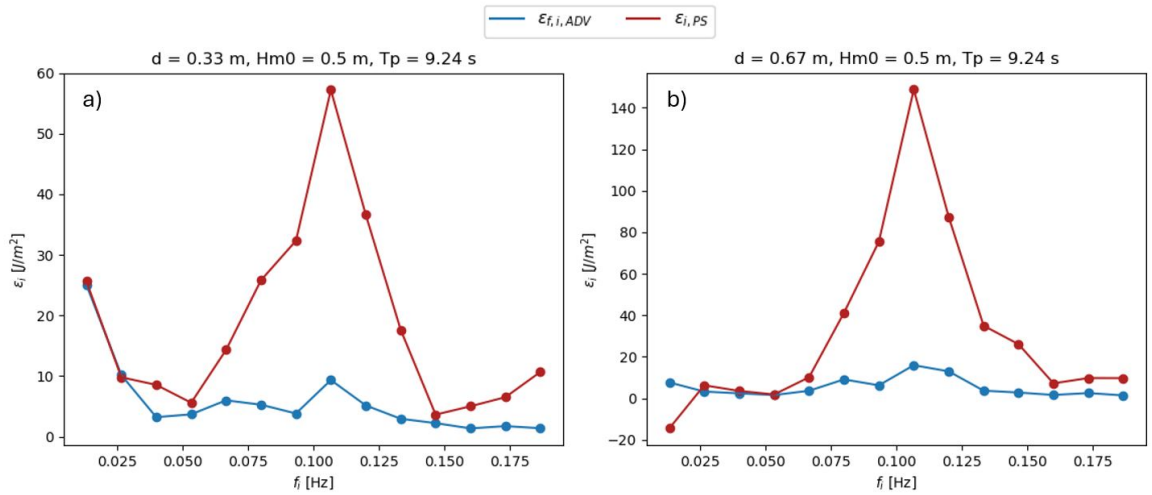

Figure 5.8: Observed wave energy flux gradients per wave component (red curve) compared to dissipation rates per wave component following from the in-canopy flow observations (blue curve) for both run S3H33C3 (Panel a) and run S3H567C3 (Panel a) showing the effect of increased water levels on the matching of the dissipation rate curves

To investigate whether the lack of accounting for wave breaking dissipation in the in-canopy flow model is causing discrepancies, two test runs from the high-water case are compared in Figure 5.9. These runs are chosen because much SS-wave energy is known to propagate on the reef flat during this case. In Panel a) wave dissipation rates with H_{m0} = 1.0 m and Panel b) for H_{m0} = 1.5 m, both with an offshore peak period of 5.77 seconds. Figure E.2 shows that the $H_{m0} = 1.0$ m case exhibits an SS-wave amplitude variance approximately an order of magnitude greater than the $H_{m0} = 0.1$ m case, indicating steeper and breaking waves. For frequencies > $f_p/2$, the discrepancy between the two dissipation curves is depicted by the green dashed line. Plotting this line reveals that increasing the SS-wave amplitude does decrease the capability of the in-canopy flow model to match observed SS-wave energy flux gradients.

Overall, comparing these two different quantifications of wave dissipation is challenging, as they inherently describe different processes. Additionally, the contributions of wave breaking, bottom friction, canopy drag, and nonlinear transfers to the total energy flux gradient remain unclear.

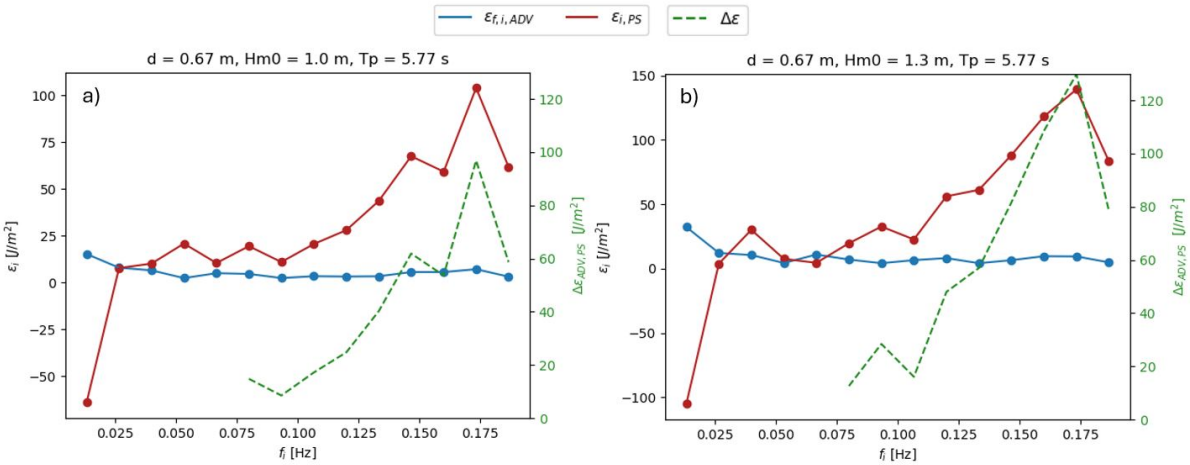

Figure 5.9: Observed wave energy flux gradients per wave component (red curve) compared to dissipation rates per wave component following from the in-canopy flow observations (blue curve) and their discrepancy at higher frequencies (green dashed curve) for both run S3H33C3 (Panel a) and run S3H567C3 (Panel a) showing the effect of increased wave steepness on the matching of the dissipation rate curves

5.3.4. Flow attenuation comparison with in-canopy flow theory

To compare the observed in-canopy flow dynamics to existing literature, the in-canopy flow theorem by Lowe is considered. First of all, it can be determined in which flow regime the CREST experiments reside. These flow regimes are elaborated in section 2.2.1. The ratio A_{∞}^{rms}/S governs in which flow regime the test run can be classified. As Lowe considered monochromatic waves for this analysis and could therefore use a single angular frequency ω, a bulk as the forcing in the CREST experiments are based on spectral waves. This bulk angular frequency ω can either be computed with the mean frequency T_{m01} or the mean period $T_{m-1.0}$. These metrics differ in weighing of wave components: T_{m01} is more influenced by shorter waves, while $T_{m-1.0}$ gives more weight to longer waves.

To prevent the mean period $T_{m-1.0}$ from becoming too large, the very low frequency (VLF) waves are neglected. Typically, these VLF waves are classified as waves with a frequency lower than the offshore peak frequency divided by 20 (Roelvink and Stive, 1989). Thus, the mean period $T_{m-1.0}$ will be calculated by only considering the frequency range [$f_p/20,\ f_s/2$]. This results in Table D.11, in which the mean frequency and period and their resulting excursion rate A_{∞}^{rms} are also shown. The ratio A_{∞}^{rms}/S as determined with the mean frequency T_{m01} are in a range of 0.42 - 2.36, while being in a range of 4.11 - 86.412 if determined with the mean period $T_{m-1.0}$. Respectively, this would classify the flow observed in the test runs in the transition from inertia force dominated to general flow regime (mean frequency) or in the middle of the general flow regime (mean period). In the general flow regime, the attenuation parameter is dependent on wave frequency. As the observed attenuation parameters did not show much frequency-dependency, it is likely that the calculation based T_{m01} is closer to the truth. This difference shows that, in spectral wave conditions, the flow regime classification is very sensitive to the choice of a representative period.

From Table 3.4, it is known that the ratios S/d_n are 1.4 and 0.9 for respectively the S1 and S3 configuration. Together with the determined ratio A_{∞}^{rms}/S and attenuation parameter α_w, the attenuation's frequency-dependency can now be compared within the framework of Lowe's theorem (Lowe et al., 2005b). This can be visualized by plotting the aforementioned parameters within the flow regime graph in Figure 5.10. In panel a of this figure, the four bottom ADVs represent the canopy flow, which limits the analysis to the high-density S3 configuration. In panel b, the two middle ADVs represent the canopy flow, extended the analysis to the low-density S1 configuration. This analysis reveals the A_{∞}^{rms}/S - α_w to behave similarly compared to Lowe's in-canopy theorem. In Panel a), the observed attenuation parameters are clustered closely around the S/d = 1 curve. Additionally, for the low-water case, the attenuation shows a dependence to A_{∞}^{rms}/S similar to the theoretical curve, while for the high-water case, it deviates more. This discrepancy makes sense as the high water case position the top ADVs as such that the measured velocities are already affected and do not represent the actual free-stream flow. This makes that the shorter waves are already attenuated more when its energy reached the top ADVs, resulting in a higher frequency dependency of the attenuation.

For the alternative representative in-canopy flow in Panel b), the observed attenuation corresponding low-density configuration with S/d = 1.4 lies between the theoretical S/d = 1 and S/d = 2 curves. Again, for the high water case, the frequency-dependency is larger. The key difference from the original representative in-canopy flow in Panel a) is that Lowe's theorem consistently overestimates attenuation relative to the observed values. This can be attributed to the in-canopy flow being measured by ADVs positioned higher in the canopy, resulting in lower observed attenuation. Consistent with this observation, the predicted attenuation in Lowe et al. (2005b) consistently overestimated the observed attenuation by 5 to 10%.

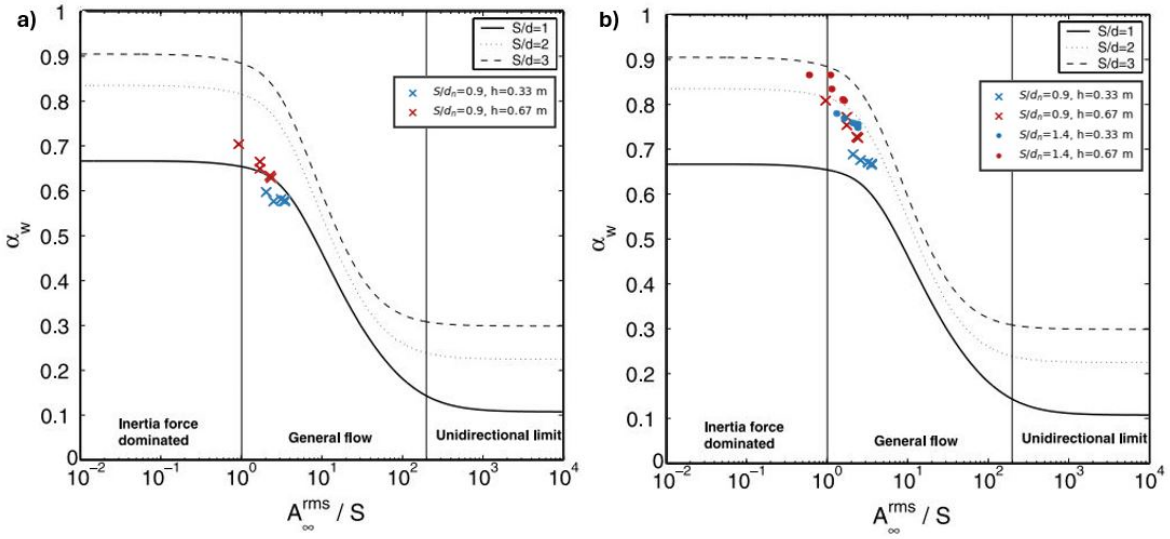

Figure 5.10: Relation between observed wave attenuation parameters and A_{∞}^{rms}/S plotted within the theoretical attenuation curves of Lowe et al. (2005b). In panel a, the wave attenuation parameter are determined by approximating the in-canopy flow with the bottom four ADVs while in panel b the in-canopy flow is approximated only with the two middle ADVs. Modified from Lowe et al. (2005b).

The fact that the wave attenuation is on the transition between inertia force dominated and general flow can be explained by the fact that the elements are placed sufficiently sparse (S is high, A_{∞}^{rms}/S is low) that all wave components can penetrate the canopy relatively easy. A natural coral reef or breakwater typically has much lower porosity and narrower spacing (Wang and Sun, 2010; Fernando et al., 2008). Without changing the wave conditions, this narrow spacing would lead to a general flow regime and therefore more frequency-dependent attenuation and dissipation.
To investigate how the assumption of these canopy parameters influences the match between the dissipation rates, the same comparison can be made but with an increase in both parameters of 50% to $1.5C_d$ and $2.0C_d$. For run S3H533C3, the in-canopy flow dissipation rate is determined with these adjusted parameters, while keeping the other parameter constant. The result of which can be seen in Figure 5.11, with the left panel showing dissipation curves for varying C_f and right panel for varying C_d. This dependence on the canopy drag parameter is in accordance with research by de Ridder et al. (2021), which demonstrated that 50% uncertainty in the calculation of the drag force results in a 5% error in the in-canopy velocity U_c. This showed that C_d is the most sensitive canopy parameter after the inertial parameter C_M.

The modified dissipation curves indicate that increasing the drag parameter has a much larger effect on dissipation due to in-canopy flow compared to adjusting the friction parameter by the same percentage. Additionally, when attempting to match the dissipation rates at higher frequencies, the IG-wave dissipation rates are overestimated for both the increased drag and friction parameters.

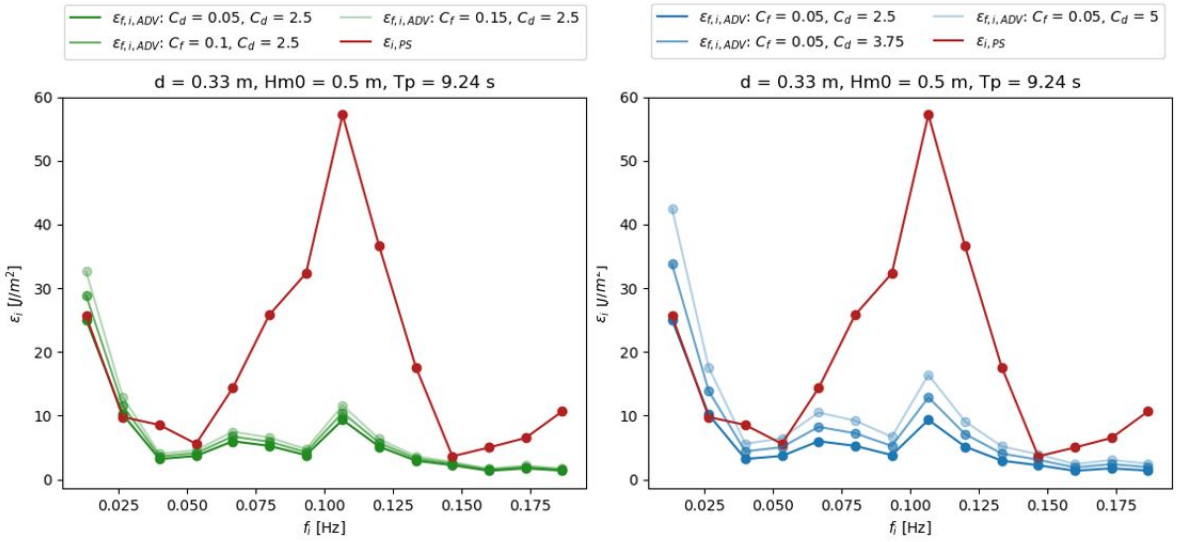

Figure 5.11: Left panel: observed wave energy flux gradients per wave component (red curve) compared to the dissipation rate per wave component following from the in-canopy flow (green curve) with canopy drag parameter C_f values of 0.05, 0.1 and 0.15.
Right panel: observed wave energy flux gradients per wave component (red curve) compared to the dissipation rate per wave component following from the in-canopy flow (blue curve) with canopy drag parameter C_d values of 2.5, 3.75 and 5.
Both for wave condition C7.

5.4. Limitations of the physical model

To be able to know which conclusions one can draw from acquired data, it is important to know its limitation and deficiencies. Knowing these limitations also aids in providing targeted recommendations on how to improve a future similar model.

5.4.1. Scale effects

As previously mentioned, the physical model is designed using Froude scaling with a spatial scaling factor of 3. This scaling method accurately scales the ratio between inertial and gravitational forces. In larger, free-surface flows, this appropriately scales the governing forces. For smaller, boundary-layer flow dominated experiments such as pipe flow studies, Reynolds scaling is typically used. This accurately scales the ratio between inertial and viscous forces.
Considering in-canopy flow, frictional losses are governed by boundary layer flow and drag losses by separation flow. As one of the main objectives of thesis is investigation these wave energy losses, it is relevant to discuss the implications of not scaling for turbulence. To do this, the Reynolds number of the model and prototype (R_m and R_p) are calculated to give an idea how big the discrepancies in viscous forces between the model and prototype are.

$$R_m = \frac{u_m \cdot l_m}{\nu}$$
$$R_p = \frac{u_m/\sqrt{n_L} \cdot (l_m/n_L)}{\nu}$$

In this definition, the viscosity v of water at 20°C equals $1.010^6\ m^2/s$. With the smallest length scale l_m of the artificial reef elements being 0.015 m, the dimension of the smallest horizontal ledge. The velocity scale in the model u_m is calculated as the mean velocity measured by ADV1 during the high-density runs. Within these runs, this mean velocity is between 0.23 and 0.42 m/s. This results in the following ranges of model Reynolds R_m and prototype Reynolds number R_p:

$$R_m = 4200 - 6300$$
$$R_p = 7274 - 10911$$

First of all, it can be confirmed that both the flow in the model as well as in the prototype are in the turbulent flow regime, as Re > 4000. The implications of the lower Reynolds number in the model are that the flow is more influenced by viscous forces relative to inertial forces. The viscous boundary layer thickness in turbulent flow δ is inversely proportional to the Reynolds number as

$$\delta \approx \frac{0.37}{R_x^{1/5}} x$$

Given that the Reynolds number in the prototype is twice that of the model, the effect on the boundary layer thickness can be determined as follows:

$$\left.\begin{aligned} \delta &\approx R^{-1/5} \\ \Delta R &= 2 \end{aligned}\right\} \quad \Delta\delta = 2^{-1/5}\delta = \frac{1}{32}\delta \tag{5.6}$$

Although the boundary layer thickness increases by approximately 3%, this slight change suggests that the wave dissipation rates observed in the CREST experiments do not deviate significantly from the prototype.

5.5. Limitations of data analysis methods

The decisions and assumptions made in data analysis can have an effect on the conclusions drawn from the collected data. More specific, the representation of the individual ADVs as 'free-stream' and 'in-canopy' flow and which effects this may have on presented results and conclusions is discussed in Section 5.5.1. Furthermore, the method of calculating the wave dissipation rate and its limitations of not accounting for non-linear energy transfers are discussed in Section 5.5.2.

5.5.1. ADV placement and representative flows

The spatial variability in flow structure and construction of a representative in-canopy and free-stream velocity affect the results and therefore the conclusion drawn from it. To investigate how seriously these conclusions can be affected, different methods of accounting for spatial flow variability and in-canopy flow representation will be compared in this section.

First of all, a method of accounting for the convergence is discussed. This method is based on the MSc thesis of van Wiechen (2020), in which flow convergence due to a canopy's presence was also observed. van Wiechen (2020) reasoned that the cross-sectional flow area varies along the cross-shore axis but that the mass flux/discharge remains constant. With a coefficient, the accelerated flow timeseries can then be corrected.

The physical basis and description of this method as used in this thesis is as follows: Firstly, the cross-sectional area in the flume through which free flow is allowed, changes over the length of the reef restoration. More specifically, the presence of the artificial reef elements reduces this cross-sectional area. Within this reduced cross-section, streamlines are contracting and expanding. As the ADV flow measurements are influenced by these accelerations and decelerations, a correction factor is set up. By assuming there is no mass transfer between the canopy and the remainder of the water column. This assumption is enforced by the fact that vertical orbital velocities are typically negligibly small lower in the water column (Grue and Jensen, 2012). This means that the mass flux in the canopy Q_c does not change over the length of the reef restoration, which can be represented in a canopy continuity equation as

$$\frac{\delta A_c(x) \cdot u_c(x)}{\delta x} = 0 \qquad with \qquad A_c(x) \cdot u_c(x) = Q_c \tag{5.7}$$

The correction factor can now be determined by setting the mass fluxes at the position of the ADV array equal to that at a position without elements. The cross-section at which ADV array A recorded data is defined as $A_{c,ADV}$ whereas a cross-section of the canopy layer unaffected by the artificial reef elements is defined as A_c. In Figure 5.12 it can be seen how A_{ADV} gets reduced by the presence of the artificial reef. Filling in the definitions of these cross-sectional areas yields:

$$u_c \cdot A_c = u_{c,ADV} \cdot A_{c,ADV} \qquad with \qquad A_c = W_{flume} \cdot h_c \quad \& \quad A_{c,ADV} = A_c - n \cdot A_{f,element} \tag{5.8}$$

in which n is the number of elements, W_{flume} the width of the flume and $A_{f,element}$ the frontal area of the artificial element as the arrays are located at the the widest point of the elements. Rearranging equation 5.8 gives the following correction factor γ_c:

$$u_c = \gamma_c \cdot u_{c,ADV} \qquad with \qquad \gamma_c = \frac{W_{flume} \cdot h_c - n \cdot A_{element}}{W_{flume} \cdot h_c} \tag{5.9}$$

This correction factor is applied to all ADV data from profile A, as this ADV array is influenced by its reduced cross-sectional area due to its location in the convergence zone between two elements. Although the highest ADV in this array is located 5 centimeters above canopy height, it is assumed that this will not have a significant influence. The low- and high-density configurations have 6 and 8 elements at the location of ADV array A, respectively. The canopy cross-sectional areas corresponding to both of these configurations are depicted in figure 5.12.

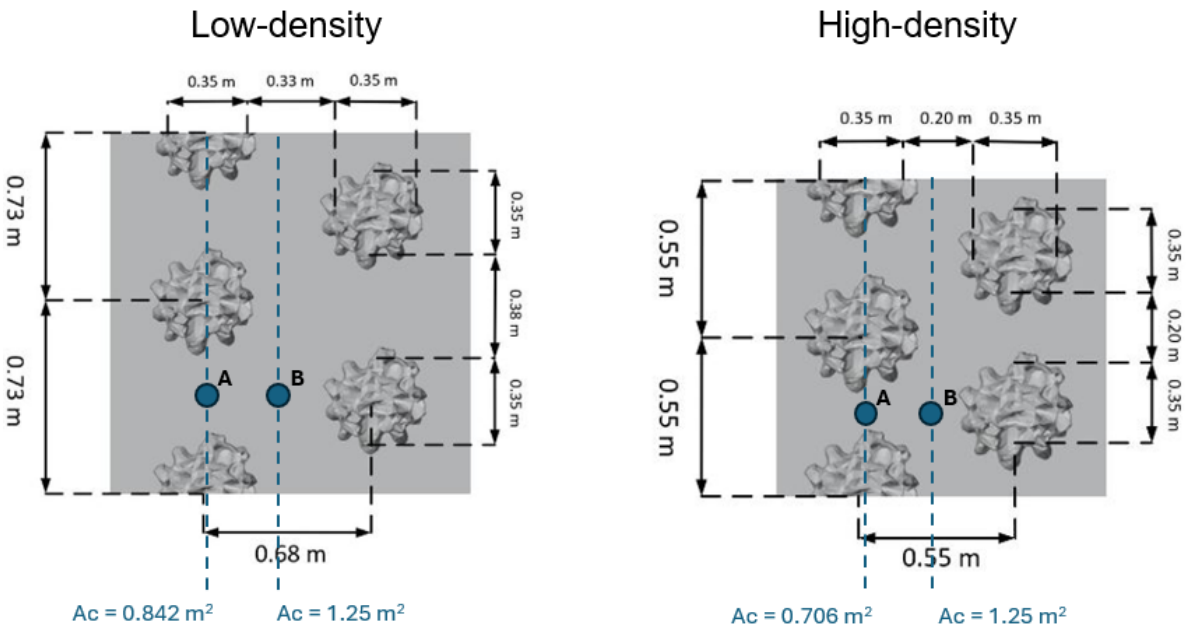

Figure 5.12: Reduced cross-sections of the canopy due to obstruction by reef elements for the low- and high-density artificial reef restorations.

As observed in the velocity profiles in Figure 4.17, the convergence effect is most distinct at the lowest ADV in Profile A. This is as expected as the cross-sectional area is reduced most here. To account for the difference in cross-sectional area reduction and its resulting extent of flow convergence, each ADV in Profile A has a different correction factor. Within the free-stream flow, ADV1 is positioned in an open area where the cross-sectional area reduction is zero, meaning the correction factor γ_c is also zero. It is assumed that at ADV2, the cross-sectional area is reduced by 50% of the total reduction. At ADV3, the reduction in cross-sectional area is as shown in equation 5.9. The approach for approximating the representative in-canopy and free-stream flow using the correction factor is illustrated in Figure 5.13.

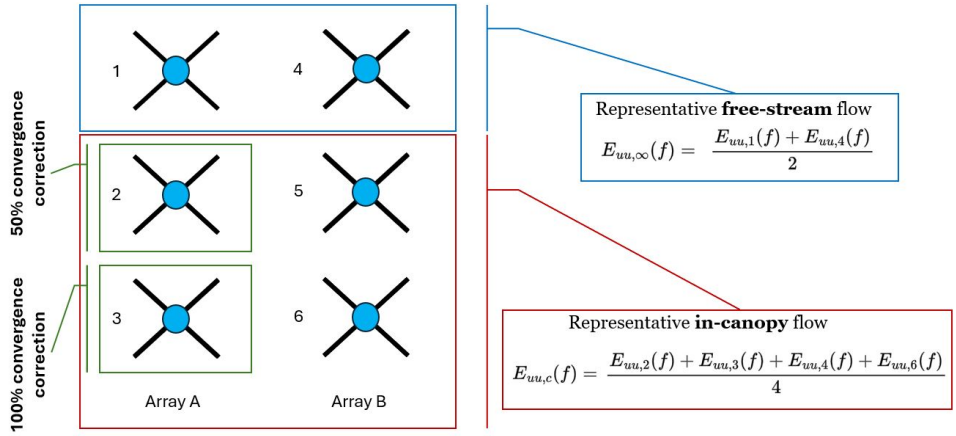

Figure 5.13: Method of approximating the representative free-stream and in-canopy flow, in this case the top two ADVs are used to construct the free-stream flow and the bottom four ADVs are used to construct the in-canopy flow and a flow convergence correction of respectively 50 and 100% is applied to ADV2 and ADV3 in ADV array A.

To assess the impact of each of the averaging/representation methods, the flow attenuation parameters α_w and the modeled canopy wave dissipation rate ϵ_c are compared across the different methods. To ensure clarity, the methods will be referred to as follows:

- Method A: representing the in-canopy flow with the four bottom ADVs as presented in Figure 3.20.
- Method B: representing the in-canopy flow with the two middle ADVs as presented in Figure 3.21.
- Method C: representing the in-canopy flow with the four bottom ADVs but with a convergence correction as presented in Figure 5.13.
- Method D: This method is identical to Method D, but with a 75% cross-sectional reduction at ADV1 and a 37.5% reduction at ADV2 ($0.75 \cdot 50\%$).

Figure 5.14 shows the flow attenuation parameter α_w per wave condition for all four methods. It can be seen that, as expected, the flow attenuation increases if we choose ADVs deeper in the canopy (from method B to method A). Similarly the flow attenuation increases if we apply the convergence correction (from method A to method C). Slightly reducing the convergence correction with 25% already decreases the flow attenuation significantly. Overall, the convergence correction has a greater effect on the calculated flow attenuation than the choice in which ADVs represent the in-canopy flow.

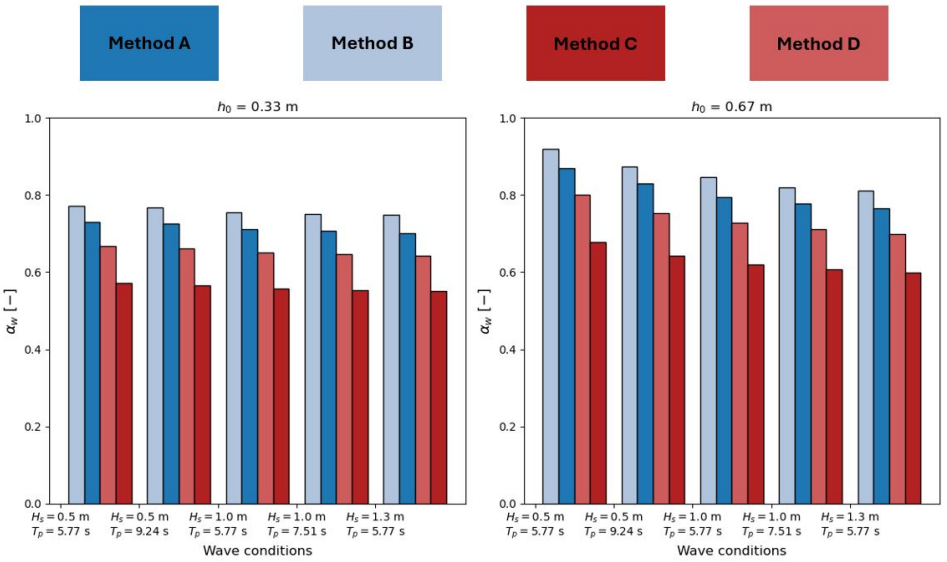

Figure 5.14: The effect of selecting which ADVs represent the in-canopy flow and applying a convergence correction on the calculated flow attenuation α_w for each wave condition, during both low water level (left panel) and high water level (right panel) runs.

Figure 5.14 shows the modeled canopy wave dissipation rate ϵ_c per wave condition for all four methods. The differences between the methods are more pronounced for wave dissipation rates than for flow attenuation. It can be seen that opting for the two middle ADVs to represent the in-canopy flow (from method A to B) only slightly increases the dissipation rate. This increase is not enough to alter the conclusions drawn from this data. Opting for the flow convergence correction gives a relatively large decrease in dissipation rate (from method A to C) while decreasing the flow convergence correction only decreases the dissipation rate by a little (from method C to D). Still, the modeled canopy wave dissipation rate is of the same order of magnitude as the observed wave dissipation rates presented in Figure 4.11.

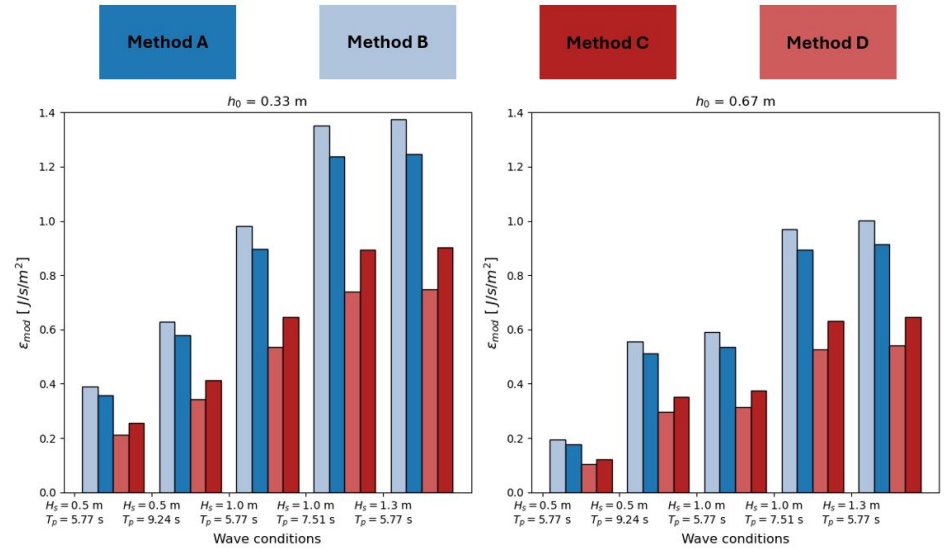

Figure 5.15: The effect of selecting which ADVs represent the in-canopy flow and applying a convergence correction on the modeled canopy wave dissipation rate ϵ_{mod} for each wave condition, during both low water level (left panel) and high water level (right panel) runs.

Similarly, the flow attenuation per wave component $\alpha_{w,i}$ is compared across the different methods. Fig-

ure 5.16 shows $1 - \alpha_{w,i}$ for method A, B and C during the low water level run of wave condition C9 ($H_s = 1.0$m, $T_p = 7.51$s). Again, the difference in attenuation between the methods differing which ADVs represent the canopy flow is relatively small. On the contrary, applying a convergence factor significantly increases flow attenuation. In Figure 5.16, the most notable difference between the methods is the difference in the flow attenuation's frequency dependency. If no convergence correction is applied, IG waves are significantly more attenuated than SS waves. With convergence correction however, this difference in attenuation is a lot smaller. One possible explanation is that the flow convergence mainly suppresses the SS-waves, as they show the highest amplification in ADV array A, as seen in the vertical velocity variance profiles.

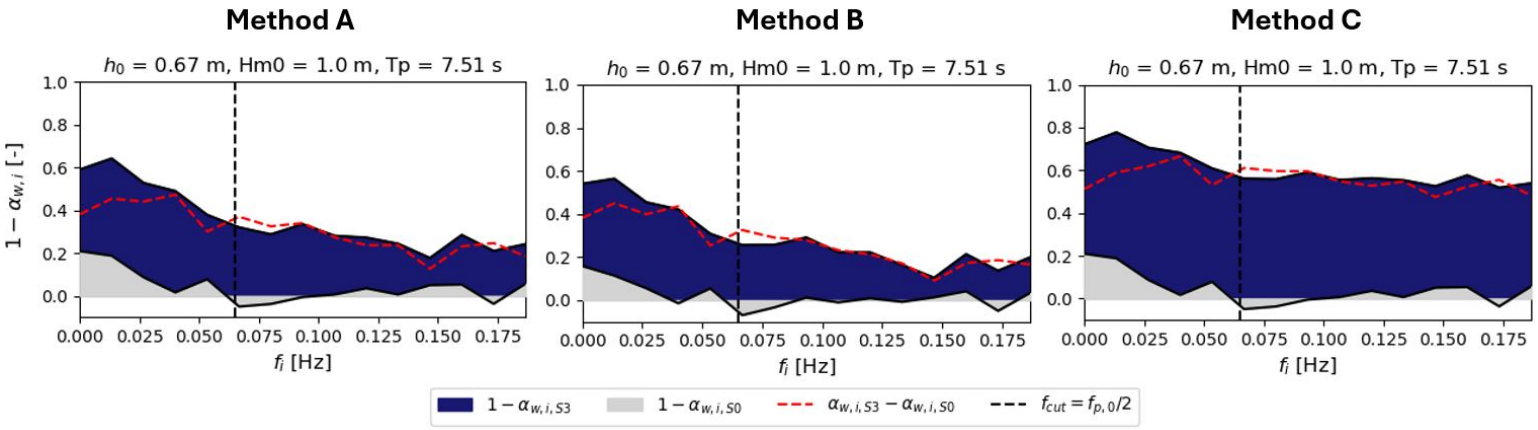

Figure 5.16: Energy change per wave component as observed comparing the free-stream flow and in-canopy flow (**represented by three different methods A, B an C**) for wave condition C9, for the high water level case. Note that the percentages of energy changes are layered over each other. By visualizing this way, the grey area is the initial energy change due to bottom friction and the added blue area is the energy change added by introducing the artificial reef elements. Higher values mean that less wave energy is able to penetrate into the canopy. The red line depicts the increased flow attenuation by placing the artificial reef elements.

For all other wave conditions during the high water level runs, the flow attenuation parameter per wave component is presented in Appendix Figure E.5 for method B and in Appendix Figure E.6 for method C.

5.5.2. Neglecting non-linear energy transfers

As IG-waves are the most important contributor to wave run-up, it is very important to design artificial reefs to dissipate energy in this bandwidth as this will have the biggest impact on flood risk reduction. As observed in the evolution of the incoming wave energy density spectra in Figure 4.6, these IG-waves are generated due to non-linear energy transfers from higher frequencies. During high water level runs, the incoming IG-wave height even grow across the artificial reef.

The MSc thesis of Takens (2024), showed that the limitations of the wave paddle during the CREST experiments plays a large role in the amount of IG-wave energy on the reef flat. In this thesis, the peak in low-frequency energy as observed in the model was compared to results of a numerical model with a resolution of 10 layers. As discussed in the Theory chapter, the wave paddle cannot generate subharmonics with frequencies lower than 0.02 Hz. To mimic this behavior, the numerical model was adjusted to stop imposing bound subharmonics with a frequency of 0.02 Hz and lower. Without this cut-off frequency, the model was poorly predicting the peak in low-frequency energy. With this cut-off frequency, discrepancies in IG-wave energy still appeared but were much smaller.

Waves of frequencies lower than 0.02 Hz are essentially just slow oscillations of the water level, therefore being able to seriously impact the water depth over the artificial reef. As the IG-wave height at the reef restoration area is between 0.2 and 0.5 m for both water levels, the amplitude of this slow water level oscillation is very significant compared to the initial reef flat water depths of 0.33 and 0.67 m. As observed, the wave dissipation and incoming wave height reduction are strongly tied with the water level on the reef flat. The observed peak in low-frequency energy can seriously affect the observed

dissipative capacity of the artificial reef and it is important to better understand the IG-wave generation mechanisms.

To gain insight in this IG-wave generation and how it influences the performance of the artificial reef, the wave groupiness can be considered. Wave groups with a larger wave groupiness are expected to transfer more energy to IG-wave components and can therefore be an explanation for the observed IG-wave increase. The wave groupiness factor GF is defined by List (1991) as:

$$GF = \frac{\sqrt{2}\sigma_A}{\overline{A(t)}} \tag{5.10}$$

in which the wave envelope $A(t)$ is the variation of wave amplitude on the timescale of wave groups. The standard deviation of the wave envelope is defined σ_A and $\overline{A(t)}$ is the mean of the wave envelope.

Similarly, a bispectral analysis could pose a solution to quantifying nonlinear interactions and estimate energy transfers within the spectra. By performing such an analysis, the dissipation can be isolated from the wave energy flux gradient. The bi-spectral analysis computes a parameter called the bicoherence, which measures the degree of non-linear interaction between two wave components at different frequencies. It helps identifying whether energy is being transferred from one frequency to another. De Bakker et al. (2015) stated that the bicoherence provides a normalized measure of the strength of the coupling and the phase relationship of the interacting wave components. This same study analyzed high-resolution data from a gently sloping laboratory beach utilizing a bispectral analysis of which two bispectra are shown in Figure 5.17. In this figure, red highlights areas where strong nonlinear interactions occur between wave components with frequencies shown on the x- and y-axis.

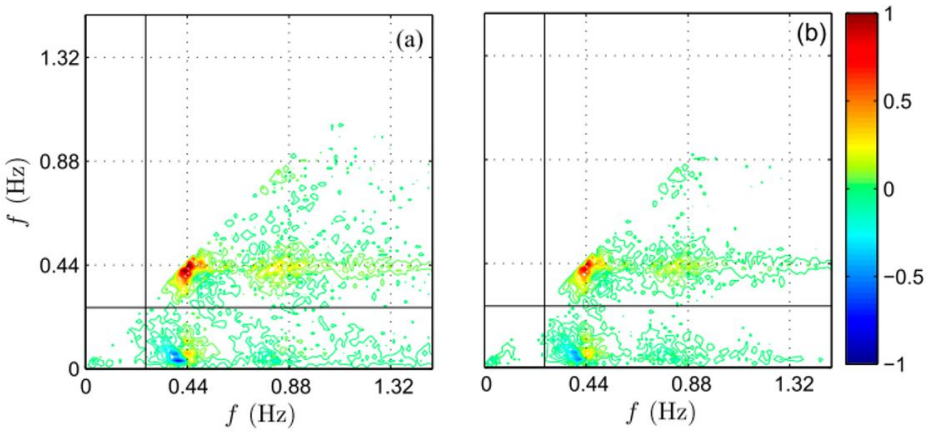

Figure 5.17: Imaginary part of the bispectra of one tested wave condition for the (a) total wave signal and (b) incoming wave signal. The colored bar depicts the range of bicoherence values. Adopted from De Bakker et al. (2015)

5.6. Data quality and availability

As previously mentioned, not all of the acquired data could be used for analysis. For instance, some pressure sensors in the original test data showed poor performance due to pressure drift. Once the drift was identified, measures were taken such as using sediment traps and placing sensors on top of the flume bottom. Still, this drift is able to seriously affect the conclusions drawn from the calculated mean water levels. In particular, the findings presented on the observed increase in wave setup are very sensitive to errors in measurements. Given that the wave setup changes due to the artificial reef are very small, at most just a few centimeters, even a small measurement error can significantly impact the results. This should be kept in mend when interpreting the presented results and its resulting conclusions.

Next to the drift, there were also pressure amplitude related issues. This means that data on wave heights and wave dissipation rates, using the variance of the pressure signal, can also be affected.

Although no anomalies in terms of wave growth or decay are observed, careful interpretation of the data is recommended.

A brief analysis on the usability of the PS data is conducted in the results chapter, from which it seemed that PS13 and PS14 were not affected seriously by the aforementioned issues. Therefore, it was decided to use the data of these PSs to investigate the net effect of the artificial for all tested wave conditions. However, too little is known about the effect of the poor data quality on the signals acquired by the pressure sensors. Exclusion of this issue can be achieved by defining and testing quality metrics, as well as visually inspecting each pressure time series. This would solidify the conclusions drawn from the experimental data.

Regarding the collected ADV data, the data acquired by the bottom ADVs (ADV3 & 6) showed problems with data quality. One of the beams of ADV6 consistently showed low correlation values, while ADV3 displayed high levels of noise for runs with the low-density artificial reef. The other ADVs however, had very stable and good data quality. As is shown in Section 5.5, the choice of which ADVs represent the in-canopy flow does not have a significant influence on the calculated flow attenuation and modeled canopy wave dissipation rates. Therefore, it is advised to represent the in-canopy flow with the middle ADVs (ADV2 & 5) for further analysis of the ADV data.

6

Conclusion & Recommendations

Now that the limitations of the physical model results are described and the findings compared to existing literature, this chapter will address the research questions posed in the introduction of this thesis. Building on the answers to the research questions, suggestions for future research are presented.

6.1. Conclusions

For clarity's sake the main research question is repeated:

> How do artificial reefs with two different densities affect nearshore hydrodynamics and how does this relate to in-canopy flow as observed in large-scale wave flume experiment of a fringing reef?

This research question is covered by answering three sub-questions, key results are addressed for each sub-question.

> What is the effect of an artificial reef restoration on wave transformation, its frequency dependence and resulting water level response?

Wave dissipation and wave height reduction strongly decrease by decreasing the relative height of the artificial reef in relation to the water depth

By placing the artificial reef, the incoming wave height is reduced by **8.5 - 15.2 %** at low water levels and by **4.9 - 5.9 %** at high water levels. By placing the low-density artificial, the bulk wave dissipation rate is increased by **50.0 - 332.3 %** at low water levels and by **6.4 - 50.0 %** at high water levels. Increasing the density of the artificial reef from 91 to 153 elements, the wave dissipation increases for the same water levels of respectively **8.6 - 31.5 %** and **4.2 - 56.3 %**.

Greater bulk wave dissipation is observed at higher water levels. However, due to the higher amount of wave energy reaching the reef flat this increased wave dissipation can not keep up with the available amount of wave energy and the relative reduction of wave energy diminishes at high water depths. In other words, the dissipative capacity of the artificial reef depends on its relative height. As water levels rise, its relative height decreases, causing wave energy concentrated at the surface to propagate over the reef.

During low water level runs, the relative reduction in incoming wave height is particularly well distributed between IG- and SS-waves, whereas for high water level runs, this distribution is less balanced.

If incoming wave height is split into two main bands (IG and SS) based on a cutoff-frequency equal to half the offshore peak frequency, the wave height reduction is relatively uniformly distributed over the bandwidth. For example, for wave condition C3 at **low water depth**, the incoming wave height reduction is **15.2%** while its SS- and IG-counterparts equal respectively **15.3%** and **15.5%**. In the high

water level run of wave condition C3, the reduction in incoming wave height is **5.9%**, with the SS- and IG-wave components showing reductions of **6.4%** and **2.3%**, respectively. This increased frequency dependency is probably an effect of stronger non-linear interactions across the artificial reef during the high water level runs.

When considering all wave components, the frequency dependence of wave energy change is more evident. As the IG-wave bandwidth consists of less frequency bins, this does not translate to the small differences between IG- and SS-wave reduction as presented before. Initially, on the bare reef, most of the energy decrease can be found in the SS-bandwidth. The net effect of the artificial reef on the wave energy decrease is however greatest for IG-waves. Although the net effect in the SS-bandwidth is smaller, the magnitude of energy decrease is still greatest for these wave components. For the higher water case, the differences per wave component are even greater. For the longest wave components, energy increase is observed of which the extent of growth is very sensitive to the specific reef configuration and wave condition.

For specific forcing conditions, artificial reefs are able to increase rather than decrease extreme water levels
At high water levels, the artificial reef not only reduces wave height by several centimeters but also leads to an increase in wave setup by several centimeters. In the extreme water level analysis, this wave setup was able to counteract wave height reduction and increase extreme water levels onshore. An order-of-magnitude calculation indicated that the drag force generated by the artificial reef likely resulted in the observed increase in wave setup. Supporting this hypothesis, a study on the numerical modeling of fringing reef wave transformation by Van Dongeren et al. (2013a) suggest that one-dimensional models tend to overestimate wave setup because they do not account for offshore-directed mean flows, which result in drag forces. Consequently, the wave setup observed in the physical model can be overestimated due to the obstruction of these return flows.

What are the observed in-canopy flow characteristics?

Flow variance differs considerably depending on the location of the ADV array and higher and longer offshore waves result in greater changes to the velocity variance profiles.
The total velocity variance decreases more significantly in the ADV array behind the artificial reef element than in the ADV array between the artificial reef elements due to the artificial reef, even increasing SS velocity variance in the array between the artificial reef elements, highlighting the importance of measuring at multiple locations within the canopy.

The more SS wave energy is present on the reef flat, the more SS wave energy is able to penetrate into the canopy meaning that the total flow attenuation. Therefore, high water levels where much SS-wave energy propagates onto the reef flat show less flow attenuation as the readily available SS wave energy can reach the canopy. Similarly, the vertical velocity variance profiles are affected less by the artificial reef during high water level runs.

Furthermore, higher and longer offshore waves lead to steeper gradients in the velocity variance profile due to the presence of the artificial reef, indicating greater flow attenuation caused by the artificial reef.

Flow attenuation is consistently higher at low water levels, where the canopy is closer to the water surface and IG waves are attenuated more than SS waves. Therefore shorter waves penetrate into the canopy more easily.
During the high water level runs, **89 - 97%** of the free-stream energy reaches the low-density artificial reef canopy. During low water levels, this gets lowered to **81 - 84%**, also showing less variability across the wave conditions. Increasing the artificial reef density leads to a 5-8% reduction in the amount of flow energy from the free-stream that reaches the canopy.

Furthermore, an analysis of flow attenuation per wave components shows that IG waves are attenuated more than SS waves and therefore shorter waves penetrate into the canopy more easily. This has its effect via the dissipation factor f_e which is higher for shorter wave components, indicating shorter waves are affected more by the canopy. Furthermore, the dissipation factor f_e is consistently higher at higher water levels as the flow is attenuated less at higher water levels, which results in flow energy

more easily being able to penetrate the canopy and lose its energy.

Choices in which ADVs represent the in-canopy flow do not significantly influence flow attenuation and modeled canopy wave dissipation, correcting for flow convergence does.
The flow convergence correction demonstrates that flow convergence significantly influences the magnitude and frequency dependence of observed flow attenuation. Convergence effects allow SS wave-induced flow to penetrate the canopy more easily. Correcting or reducing these effects lowers in-canopy flow velocities, reduces SS-wave penetration, and underestimates SS-wave dissipation, reducing the frequency dependence of attenuation. These effects are essential for accurately capturing in-canopy wave dissipation. Removing them could notably affect the frequency distribution of attenuation, as IG waves no longer experience greater attenuation than SS waves.

On the other hand, the choice of which ADVs represent the in-canopy flow does not have a significant influence on the calculated flow attenuation and modeled canopy wave dissipation rates. Furthermore, the frequency dependence of the flow attenuation is not affected. Therefore, further analysis of the ADV data could be carried out by representing the in-canopy flow using the middle ADVs, while the application of a flow convergence factor should be approached with caution.

How do the in-canopy flow characteristics relate to the observed wave dissipation?

The modeled canopy wave dissipation rates are lower than the observed dissipation rates, but remain within the same order of magnitude.
During low water level runs, the modeled canopy wave dissipation accounts for **30–44%** of the observed artificial reef-induced wave dissipation. In high water level runs, this percentage varies between **13%** and **57%**, indicating greater inconsistency in the prediction. Despite this difference, the modeled canopy wave dissipation rate and observed dissipation rate are of the same order of magnitude. It is likely that wave breaking is partly responsible for the discrepancy between the observed and modeled dissipation rates as wave breaking is more likely to occur with short, high waves which are more frequently occurring across the artificial reef stretch during high water level runs.

The modeled canopy wave dissipation rates per wave component deviates more significantly from the observed energy flux gradients as the calculation of these gradients does not account for non-linear energy transfers and the in-canopy flow does not account for breaker dissipation.
Regarding dissipation per wave component, the in-canopy model is able to accurately capture observed wave energy flux gradients at low frequencies. This is valid on the condition that there is no IG wave increase across the artificial reef stretch due to non-linear interactions. In the low frequencies during the high water level runs, observed energy flux gradients get negative which the modeled canopy wave dissipation rate can not match as the calculation of the observed energy flux gradients does not account for energy transfer due to non-linear interactions.

At higher frequencies, the observed energy flux gradients are significantly larger than the modeled canopy dissipation rates. This is likely due to the in-canopy flow not accounting for breaker dissipation as it only accounts for frictional and drag dissipation as a direct result of the presence of the canopy. Discrepancies between observed an in-canopy model dissipation become larger when the steepness of SS-waves increase, affirming the suspicion that the difference arises from the fact that the modeled canopy wave dissipation rates do not account for breaker dissipation.

How does the observed wave dissipation relate to existing in-canopy flow theory?

Canopy parameter sensitivity:
The dissipation factor and wave dissipation rate are a function of the canopy parameters C_d and C_f and the wave attenuation parameter α_w. It has been shown that by adjusting the canopy parameters, the discrepancy between the in-canopy flow dissipation rate and observed wave dissipation rate can be reduced for SS wave components. However, the accuracy of the in-canopy flow model for describing the IG wave dissipation rate is compromised by the same canopy parameter adjustment. It must be

noted that the observed IG wave dissipation rate contain non-linear energy transfers, therefore not purely representing wave dissipation. This analysis also showed that the in-canopy wave dissipation rate is more sensitive to changes in the drag parameter C_d than it is to the friction parameter C_f, which is in accordance with observations by de Ridder et al. (2021).

Flow regime classification:
The observed attenuation parameters and ratios A_{∞}^{rms}/S are used to classify the test runs in flow regimes as defined by Lowe et al. (2005b). From this analysis it followed that the flow consistently resides on the transition between inertia-dominated flow and general flow meaning that the attenuation is only slightly frequency dependent according to the in-canopy flow model. Opting to determine the attenuation parameter with a representative in-canopy flow constructed with the middle ADVs slightly overestimates flow attenuation compared to in-canopy flow theory by Lowe et al. (2005b). In contrast, constructing the representative in-canopy flow with the four bottom ADVs slightly overestimates the attenuation parameter. For low water level runs, the frequency dependency matches better than for high water level cases. This is a result of the flow attenuation parameter being more variable across the high water level runs.

6.2. Recommendations

Based on the conclusions drawn, the following recommendations are provided to either build upon these conclusions or improve the results leading up to these conclusions. These recommendations are categorized into four areas:

1. Practical recommendations on how to implement the tested artificial reef element for ecological benefits and coastal protection strategies.
2. Extending the analysis on data from the CREST experiments or improving its methodology for further applications.
3. Conducting numerical modeling to complement this research.
4. Performing field measurements to complement this research.

6.2.1. Practical recommendations or implications

Utilizing the CREST artificial reef in hybrid solutions Due to the limited decrease in incoming wave height provided by the CREST artificial reef, consideration should be given to hybrid solutions that incorporate the CREST artificial reef or explore other ways in which it can contribute. The CREST artificial reef alone is not sufficient to effectively protect coastlines. However, when integrated with larger structures, the hybrid system not only provides coastal protection but also contributes to ecological improvement.

If a project requires ecological rehabilitation, the CREST artificial reef could pose a solution as the elements are specifically designed to provide ecological benefits. In this context, the coastal protection function would be an additional advantage.

For contractors, cutting costs on shoreline protection with rock armour or concrete elements is an important objective. For context: a reduction of just one centimeter in the nominal diameter of shoreline protection can already have a considerable impact on project costs. Elements as used in the CREST artificial reef have the capacity to decrease hydrodynamic loads on shoreline protection. A financial analysis could determine whether the cost of installing an artificial reef is justified by the savings in shoreline protection expenses.

Implications of sea-level rise on artificial reef effectivity As presented before, wave dissipation and wave height reduction strongly decrease by decreasing the relative height of the artificial reef in relation to the water depth. The projection of 1 meter sea level rise by the end of the century (Lee et al., 2023), makes prototype water levels of 2 meters or higher more likely, further decreasing the effectivity of the artificial reef.

The bioreceptivity of the CREST artificial reef could mitigate these effects. Corals are known to grow upward in response to rising water levels, which could help counteract the reduced effectiveness caused by sea level rise by increasing both the height and roughness of the CREST artificial reef.

6.2.2. Extending on or improving of the CREST experiments

Physical modeling in a wave basin:
By increasing the width of the wave flume, an artificial reef can be installed which is not cross-shore uniform. In this situation, diffraction effects and two-dimensional currents like return currents draining off the reef flat around the artificial reef. For this purpose, a wave basin could be used.

Investigate non-linear interactions: To be able to investigate the wave dissipation per wave component, the non-linear interactions in the wave spectrum should be better understood, or preferably, quantified. The groupiness factor (GF) can be calculated to identify regions within the domain where non-linear interactions play a significant role, as wave groups with higher groupiness are expected to transfer more energy to IG-wave components. To quantify the energy transfer due to non-linear interactions, a bispectral analysis can be conducte. If this non-linear interaction energy transfer is calculated per wave component ($S_{nl,i}$), the actual wave dissipation rate can be isolated from the wave energy flux gradient.

Further investigation on drift and amplitude variation in pressure sensor data: In this thesis, a brief analysis of the pressure sensor data is done to assure the incoming surface elevation timeseries of the pressure sensors just offshore and just onshore of the artificial reef stretch could be used to quantify the net effect of the artificial reef for all tested wave conditions. A more elaborate analysis on its data quality is needed to be completely sure that the results and drawn conclusions are not affected by the drift and amplitude variation in the pressure signals.

Experiments with a adjustable free-stream ADV: It was observed that the water level significantly influenced the wave attenuation parameter α_w. At higher water levels, the observed wave attenuation was lower and matched the in-canopy flow theorem of Lowe et al. (2005b) less accurately. This is likely also due to the fact that the spacing of the ADVs relative to water depth changes when water level increases. The measured free-stream flow is already influenced by the canopy, leading to reduced observed wave attenuation. Adjusting the height of the ADVs could align with the strict definition of free-stream flow as being unaffected by the canopy. Adjusting the top ADV when a new water level is tested would solve this issue, which comes with its own challenges regarding design of the mounting system and determining an ideal new ADV measuring height.

Wave run-up analysis: To more quantitatively and specifically assess the potential coastal protection provided by the CREST artificial reef, wave run-up on the beach measured during the CREST experiments can be analyzed. Wave run-up measurement were conducted in the flume, which can be linked to propagation and generation of IG-wave energy on the reef flat. This can provide more insights on how the density, location and height of the artificial canopy is able to reduce flood risk.

Perform experiments more clearly in the general flow regime: As the flow in the CREST experiments was on the transition between inertia-dominated and general flow, only little frequency dependent attenuation has been observed. To get more insight in the frequency dependency of wave attenuation by artificial reefs, the ratio A_{∞}^{rms}/S. This can be achieved by increasing the wave height or length or decreasing the spacing S of the configuration. As the wave paddle was already on its limits with regards to wave generation, the more realistic option is to decreasing the spacing and test artificial reef configuration with higher densities.

6.2.3. Conducting numerical modeling

Conduct higher dimension numerical modeling: Similarly to testing in a wave flume, two dimensional horizontal modeling (2DH) allows for the consideration of diffraction effects and two-dimensional currents, such as return currents that drain off the reef flat around the artificial reef. This is expected to respectively enhance the transmission of incoming wave and reduce the wave setup, both influencing the ability of the artificial reef to dissipate energy and reduce extreme onshore water levels. Extending on 2DH modeling, 3D modeling is possible. Firstly, this would enable for more accurate wave dispersion. Introducing multiple vertical layers would also allow for the modeling of more complex canopies,

rather than representing the canopy as a single block with uniform porosity. However, these improvements would come at the cost of increased computational resources, raising the question of whether extending to a 3D model is worth it.

Calibrate a XBeach model with experimental CREST data: XBeach Non-Hydrostatic+ contains an in-canopy flow representation of coral reefs based on Lowe's in-canopy flow theorem (Lowe et al., 2005b), which incorporates canopy parameters such as C_f and C_d. By calibrating a model like this on the CREST experimental data, these parameters can be determined and with the calibrated model more hypotheses can be tested which couldn't be tested with the experimental data alone. A comparison of the XBeach in-canopy flow model with a conventional model, which represents the canopy as a bed level step with increased roughness, would also be valuable. This could help determine whether an in-canopy flow model enhances predictions of wave transformation and its water level response. This report demonstrated that the in-canopy flow model, despite having uncalibrated parameters C_f and C_d, accurately predicts the order of magnitude of canopy-induced dissipation and the impact of canopy-induced drag force on wave setup. These findings are promising for the use of the XBeach in-canopy flow model.

Perform high-resolution CFD simulations: To be able to gain more understanding of the in-canopy flow structure a high-resolution CFD simulation can be performed. Figure 3.10 gave a good indication in the flow pattern around the implement artificial reef elements but is limited to unidirectional flow. A similar model, with wave-induced flow, would give detailed informed on the in-canopy flow structure. This can be used to compare with the measurements from the ADV arrays and give information if the spacing of the ADVs captured the spatial flow variability and how good the representation of the in-canopy flow was. Compared to 2DH modeling, this would provide a more detailed view of the flow structure within the artificial reef, instead of a single flow velocity value representing the in-canopy flow.

Investigate the inflection point of artificial reef density: As reef restoration projects are typically of limited extend, resources have to be carefully considered when constructing such restorations. Therefore, overdesigning is not advisable. The wave dissipation curves in Figure 4.13 show that the increase in dissipation from increasing the restoration density by 62 elements is minimal. This thesis provides data for only one such increment, but testing a larger range of densities could reveal an inflection point where the dissipation increment per density increase starts to level off. Norris et al. (2024) showed that for a given set of wave conditions an inflection point exists where wave energy dissipation balances element spacing. When this inflection point is known, an ideal artificial reef density can be designed based for the governing wave conditions a coastline is exposed to.

6.2.4. Performing field measurements

Conduct a long-term field pilot: A long-term pilot of field measurements could provide additional insights compared to a physical model. First of all, the pilot could provide information on the degradation of the elements and its bio-receptivity. A high bioreceptivity could increase roughness of the artificial reef element by coral, algae and other benthos growth, potentially increasing its dissipation capacity. This also gives information on the provided ecosystem services of the artificial reef. Furthermore, during a field campaign, the low-frequency energy peak would not be as pronounced as in the CREST experiments, since there are no wave paddle limitations. Subharmonics with frequencies below 0.02 Hz will be present in the wave field, eliminating the supposed influence of the slowly varying water level on the artificial reef's effectiveness.

Bibliography

Apotsos, A., Raubenheimer, B., Elgar, S., Guza, R., and Smith, J. A. (2007). Effects of wave rollers and bottom stress on wave setup. *Journal of Geophysical Research: Oceans*, 112(C2).

Beck, M. W., Losada, I. J., Menéndez, P., Reguero, B. G., Díaz-Simal, P., and Fernández, F. (2018). The global flood protection savings provided by coral reefs. *Nature Communications*, 9.

Bertin, X., de Bakker, A., Van Dongeren, A., Coco, G., André, G., Ardhuin, F., Bonneton, P., Bouchette, F., Castelle, B., Crawford, W. C., et al. (2018). Infragravity waves: From driving mechanisms to impacts. *Earth-Science Reviews*, 177:774–799.

Bevington, P. R. and Robinson, D. K. (2003). Data reduction and error analysis. *McGrawâ€“Hill, New York*.

Boström-Einarsson, L., Babcock, R. C., Bayraktarov, E., Ceccarelli, D., Cook, N., Ferse, S. C. A., Hancock, B., Harrison, P., Hein, M., Shaver, E., Smith, A., Suggett, D., Stewart-Sinclair, P. J., Vardi, T., and McLeod, I. M. (2020). Coral restoration – a systematic review of current methods, successes, failures and future directions. *PLOS ONE*, 15(1):1–24.

Britter, R. E. and Hanna, S. R. (2003). Flow and dispersion in urban areas. *Annual Review of Fluid Mechanics*, 35.

Bruno, J. F. and Selig, E. R. (2007). Regional decline of coral cover in the indo-pacific: Timing, extent, and subregional comparisons. *PLoS ONE*, 2.

Buckley, M. L., Lowe, R. J., Hansen, J. E., Dongeren, A. R. V., and Storlazzi, C. D. (2018). Mechanisms of wave-driven water level variability on reef-fringed coastlines. *Journal of Geophysical Research: Oceans*, 123.

Buckley, M. L., Lowe, R. J., Hansen, J. E., van Dongeren, A. R., Pomeroy, A., Storlazzi, C. D., Rijnsdorp, D. P., da Silva, R. F., Contardo, S., and Green, R. H. (2022). Wave-driven hydrodynamic processes over fringing reefs with varying slopes, depths, and roughness: Implications for coastal protection. *Journal of Geophysical Research: Oceans*, 127. Lab experiment data from Scheldt flumeValidation:RMSE lower in lab experiments as your scale is offRMSE normalized (dimensionless) to for example mean wave heightBias: how much are you off in general (consistency)Also look at multiple components:mean wave height–> am I looking only at low frequencies or at high frequencies?mean water level on reef flat2

Burke, L., Reytar, K., Spalding, M., and Perry, A. (2011). *Reefs at Risk Revisited*.

Casas-Prat, M., Wang, X. L., and Sierra, J. P. (2014). A physical-based statistical method for modeling ocean wave heights. *Ocean Modelling*, 73:59–75.

Cesar, H., Burke, L., and Pet-soede, L. (2003). The economics of worldwide coral reef degradation. *Cesar Environmental Economics Consulting, Arnhem, and WWF-Netherlands*, 14.

Chappell, J. (1980). Coral morphology, diversity and reef growth. *Nature*, 286.

Cheriton, O. M., Storlazzi, C. D., and Rosenberger, K. J. (2016). Observations of wave transformation over a fringing coral reef and the importance of low-frequency waves and offshore water levels to runup, overwash, and coastal flooding. *Journal of Geophysical Research: Oceans*, 121(5):3121–3140.

Coceal, O. and Belcher, S. (2004). A canopy model of mean winds through urban areas. *Quarterly Journal of the Royal Meteorological Society*, 130(599):1349–1372.

Collins, J. I. (1972). Prediction of shallow-water spectra. *Journal of Geophysical Research*, 77(15):2693–2707.

Darwin, C. (1836). *THE STRUCTURE AND DISTRIBUTION OF CORAL REEFS*.

De Bakker, A., Herbers, T., Smit, P., Tissier, M., and Ruessink, B. (2015). Nonlinear infragravity–wave interactions on a gently sloping laboratory beach. *Journal of Physical Oceanography*, 45(2):589–605.

de Ridder, M. (2018). Non-hydrostatic wave modelling of coral reefs with the addition of a porous in-canopy model.

de Ridder, M. P., Smit, P. B., van Dongeren, A. R., McCall, R. T., Nederhoff, K., and Reniers, A. J. (2021). Efficient two-layer non-hydrostatic wave model with accurate dispersive behaviour. *Coastal Engineering*, 164:103808.

Dean, R. G. and Bender, C. J. (2006). Static wave setup with emphasis on damping effects by vegetation and bottom friction. *Coastal engineering*, 53(2-3):149–156.

Deltares (2012). Programmable electromagnetic liquid velocity meter, version 1.1.

Diederen, C. (2022). Experimental wave flume study: the stability of an artificial reef.

encyclopedia, B. (2006). An atoll is a ring of land surrounding a pool of water called a lagoon. this kind of island forms from a volcanic island circled by a coral reef.

Fabian, R., Beck, M., and Potts, D. (2013). Reef restoration for coastal defense: A review.

Fernando, H., Samarawickrama, S., Balasubramanian, S., Hettiarachchi, S., and Voropayev, S. (2008). Effects of porous barriers such as coral reefs on coastal wave propagation. *Journal of Hydro-environment Research*, 1(3-4):187–194.

Ferrario, F., Beck, M. W., Storlazzi, C. D., Micheli, F., Shepard, C. C., and Airoldi, L. (2014). The effectiveness of coral reefs for coastal hazard risk reduction and adaptation. *Nature Communications*, 5.

Gawehn, M., van Dongeren, A., van Rooijen, A., Storlazzi, C. D., Cheriton, O. M., and Reniers, A. (2016). Identification and classification of very low frequency waves on a coral reef flat. *Journal of Geophysical Research: Oceans*, 121(10):7560–7574.

Gijón, A. M., Jansen, W., Uijttewaal, W., Reniers, A., van Rooijen, A., Suzuki, T., Etminan, V., and Winterwerp, J. (2021). Wave transmission and drag coefficients through dense cylinder arrays: Implications for designing structures for mangrove restoration. *Ecological Engineering*, 165:106231.

Goreau, T. F. (1964). Mass expulsion of zooxanthellae from jamaican reef communities after hurricane flora. *Science*, 145.

Goring, D. G. and Nikora, V. I. (2002). Despiking acoustic doppler velocimeter data. *Journal of hydraulic engineering*, 128(1):117–126.

Grue, J. and Jensen, A. (2012). Orbital velocity and breaking in steep random gravity waves. *Journal of Geophysical Research: Oceans*, 117(C7).

Gu, Z. and Wang, H. (1991). Gravity waves over porous bottoms. *Coastal engineering*, 15(5-6):497–524.

Guza, R., Thornton, E., and Holman, R. (1985). Swash on steep and shallow beaches. In *Coastal Engineering 1984*, pages 708–723.

Guza, R. T. and Thornton, E. B. (1982). Swash oscillations on a natural beach. *Journal of Geophysical Research: Oceans*, 87(C1):483–491.

Hasselmann, K., Barnett, T. P., Bouws, E., Carlson, H., Cartwright, D. E., Enke, K., Ewing, J., Gienapp, A., Hasselmann, D., Kruseman, P., et al. (1973). Measurements of wind-wave growth and swell decay during the joint north sea wave project (jonswap). *Ergaenzungsheft zur Deutschen Hydrographischen Zeitschrift, Reihe A*.

Holthuijsen, L. H. (2010). *Waves in oceanic and coastal waters*. Cambridge University Press, Cambridge, England.

(https://kulite.com), K. . (2025). Miniature High Pressure Pressure Transducer | Product Advisor | Kulite | The Leader in Pressure Transducer Technology — kulite.com. https://kulite.com/products/product-advisor/product-catalog/miniature-high-pressure-pressure-transducer-hkm-375m/. [Accessed 12-02-2025].

Jensen, M. S. (2004). Breaking of waves over a steep bottom slope.

Jones, R. J. (2008). Coral bleaching, bleaching-induced mortality, and the adaptive significance of the bleaching response. *Marine Biology*, 154.

Jonsson, I. G. (1966). Wave boundary layers amd friction factors. *Coastal Engineering Proceedings*.

Kendal, M. S., Monaco, M. E., Buja, K., Christensen, J., Kruer, C., Finkbeiner, M., and Warner, R. (2001). *Methods Used to Map the Benthic Habitats of Puerto Rico*. NOAA National Ocean Service Center for Coastal Monitoring and Assessment Biogeography Team. page 45.

Kennedy, D. M. and Woodroffe, C. D. (2002). Fringing reef growth and morphology: A review. *Earth-Science Reviews*, 57.

Lee, H., Calvin, K., Dasgupta, D., Krinner, G., Mukherji, A., Thorne, P., Trisos, C., Romero, J., Aldunce, P., Barrett, K., et al. (2023). *Climate change 2023: synthesis report. Contribution of working groups I, II and III to the sixth assessment report of the intergovernmental panel on climate change*. The Australian National University.

List, J. H. (1991). Wave groupiness variations in the nearshore. *Coastal Engineering*, 15(5-6):475–496.

Longuet-Higgins, M. S. and Stewart, R. (1962). Radiation stress and mass transport in gravity waves, with application to 'surf beats'. *Journal of Fluid Mechanics*, 13(4):481–504.

Løvås, S. M. and Tørum, A. (2001). Effect of the kelp laminaria hyperborea upon sand dune erosion and water particle velocities. *Coastal Engineering*, 44(1):37–63.

Lowe, R. J., Falter, J. L., Bandet, M. D., Pawlak, G., Atkinson, M. J., Monismith, S. G., and Koseff, J. R. (2005a). Spectral wave dissipation over a barrier reef. *Journal of Geophysical Research: Oceans*, 110(C4).

Lowe, R. J., Falter, J. L., Koseff, J. R., Monismith, S. G., and Atkinson, M. J. (2007). Spectral wave flow attenuation within submerged canopies: Implications for wave energy dissipation. *Journal of Geophysical Research: Oceans*, 112.

Lowe, R. J., Falter, J. L., Monismith, S. G., and Atkinson, M. J. (2009). A numerical study of circulation in a coastal reef-lagoon system. *Journal of Geophysical Research: Oceans*, 114(C6).

Lowe, R. J., Koseff, J. R., and Monismith, S. G. (2005b). Oscillatory flow through submerged canopies: 1. velocity structure. *Journal of Geophysical Research: Oceans*, 110.

Lowe, R. J., Shavit, U., Falter, J. L., Koseff, J. R., and Monismith, S. G. (2008). Modeling flow in coral communities with and without waves: A synthesis of porous media and canopy flow approaches. *Limnology and Oceanography*, 53(6):2668–2680.

Luhar, M., Coutu, S., Infantes, E., Fox, S., and Nepf, H. (2010). Wave-induced velocities inside a model seagrass bed. *Journal of Geophysical Research: Oceans*, 115(C12).

Macdonald, I., El-Sayed, M., Mow, K., and Dullien, F. (1979). Flow through porous media-the ergun equation revisited. *Industrial & Engineering Chemistry Fundamentals*, 18(3):199–208.

Madin, J. S. and Madin, E. M. (2015). The full extent of the global coral reef crisis. *Conservation Biology*, 29.

Madsen, O. S. (1994). Spectral wave-current bottom boundary layer flows. In *Coastal Engineering 1994*, pages 384–398.

Marthinsen, T. and Winterstein, S. R. (1992). On the skewness of random surface waves. In *ISOPE International Ocean and Polar Engineering Conference*, pages ISOPE–I. ISOPE.

Massel, S. R. and Gourlay, M. R. (2000). On the modelling of wave breaking and set-up on coral reefs. *Coastal Engineering*, 39.

Mccorquodale, J. A., Hannoura, A.-A. A., and Sam Nasser, M. (1978). Hydraulic conductivity of rockfill. *Journal of Hydraulic Research*, 16(2):123–137.

Monismith, S. G. (2007). Hydrodynamics of coral reefs. *Annual Review of Fluid Mechanics*, 39.

Murphy, P. (2003). Coral reefs: cities under the sea. *Choice Reviews Online*, 40.

Muscatine, L. and Porter, J. W. (1977). Reef corals: Mutualistic symbioses adapted to nutrient-poor environments. *BioScience*, 27.

Nelson, R. (1996). Hydraulic roughness of coral reef platforms. *Applied Ocean Research*, 18(5):265–274.

Nielsen, P. (1992). *Coastal bottom boundary layers and sediment transport*, volume 4. World scientific.

NOAA (2023). What are coral reefs.

Norris, B. K., Storlazzi, C. D., Pomeroy, A. W., and Reguero, B. G. (2024). Optimizing infragravity wave attenuation to improve coral reef restoration design for coastal defense. *Journal of Marine Science and Engineering*, 12(5):768.

Nortek (2025). The Comprehensive Manual - Velocimeters. https://support.nortekgroup.com/hc/en-us/articles/360029839351-The-Comprehensive-Manual-Velocimeters#:~:text=Covers%20Principles%20of%20Operation%2C%20Troubleshooting%2C%20the%20Service%20Manual,Velocimeter.%20Covers%20Principles%20of%20Operation%2C%20Troubleshooting%2C%20the%20Service. [Accessed 12-02-2025].

Pandolfi, J. M., Connolly, S. R., Marshall, D. J., and Cohen, A. L. (2011). Projecting coral reef futures under global warming and ocean acidification.

Patil, A. L. (2023). *Direct Numerical Simulations of Wave-Current Interactions Over Bumpy Walls*. Stanford University.

Péquignet, A.-C., Becker, J. M., Merrifield, M., and Boc, S. (2011). The dissipation of wind wave energy across a fringing reef at ipan, guam. *Coral Reefs*, 30:71–82.

Péquignet, A. C. N., Becker, J. M., Merrifield, M. A., and Aucan, J. (2009). Forcing of resonant modes on a fringing reef during tropical storm man-yi. *Geophysical Research Letters*, 36(3).

Pomeroy, A., Lowe, R., Symonds, G., Van Dongeren, A., and Moore, C. (2012a). The dynamics of infragravity wave transformation over a fringing reef. *Journal of Geophysical Research: Oceans*, 117(C11).

Pomeroy, A. W., Lowe, R. J., Van Dongeren, A. R., Ghisalberti, M., Bodde, W., and Roelvink, D. (2015). Spectral wave-driven sediment transport across a fringing reef. *Coastal Engineering*, 98:78–94.

Pomeroy, A. W. M., Van Dongeren, A., Lowe, R., de Vries, J. v. T., and Roelvink, J. (2012b). Low frequency wave resonance in fringing reef environments. *Coastal Engineering Proceedings*, (33):25–25.

Quataert, E., Storlazzi, C., Van Rooijen, A., Cheriton, O., and Van Dongeren, A. (2015). The influence of coral reefs and climate change on wave-driven flooding of tropical coastlines. *Geophysical Research Letters*, 42(15):6407–6415.

Raubenheimer, B. and Guza, R. (1996). Observations and predictions of run-up. *Journal of Geophysical Research: Oceans*, 101(C11):25575–25587.

Reefball (2025). Reef Ball Sizes - Chart of all basic Reef Ball sizes — reefballfoundation.org. https://reefballfoundation.org/sizes/. [Accessed 12-02-2025].

Riera, E. (2020). *Towards a purposeful construction of a new generation of artificial reefs: Comparative analyses of the intrinsic factors favouring their colonization from micro to macro-scale*. PhD thesis, Université Côte d'Azur.

Rinkevich, B. (2008). Management of coral reefs: We have gone wrong when neglecting active reef restoration. *Marine Pollution Bulletin*, 56.

Rinkevich, B. (2014). Rebuilding coral reefs: Does active reef restoration lead to sustainable reefs?

Roelvink, F. (2019). Coral restoration for coastal hazard risk reduction: the effect of coral restoration on wave transformation over various reef morphologies and the resulting runup. *Delft University of Technology*.

Roelvink, F. E., Storlazzi, C. D., van Dongeren, A. R., and Pearson, S. G. (2021). Coral reef restorations can be optimized to reduce coastal flooding hazards. *Frontiers in Marine Science*, 8.

Roelvink, J. and Stive, M. (1989). Bar-generating cross-shore flow mechanisms on a beach. *Journal of Geophysical Research: Oceans*, 94(C4):4785–4800.

Rogers, J. S., Monismith, S. G., Feddersen, F., and Storlazzi, C. D. (2013). Hydrodynamics of spur and groove formations on a coral reef. *Journal of Geophysical Research: Oceans*, 118.

Ruggiero, P., Holman, R. A., and Beach, R. (2004). Wave run-up on a high-energy dissipative beach. *Journal of Geophysical Research: Oceans*, 109(C6).

Russo, F. and De Maddalena, A. (2021). On the presence of the spinner shark carcharhinus brevipinna (müller henle, 1839) (chondrichthyes: Carcharhinidae) in maldivian waters. *Marine Biological Journal*, 6:87–91.

Sabatier, F. (2007). U.s. army corps of engineers, coastal engineering manual (cem), engineer manual 1110-2-1100: U.s. army corps of engineers, washington, d.c. (6 volumes). *Méditerranée*, page 146.

Salvat, B. and Wilkinson, C. (2011). Cyclones and climate change in the south pacific. *Revue d'Écologie*, 66(2):105–115.

Selesnick, I. W. and Burrus, C. S. (1998). Generalized digital butterworth filter design. *IEEE Transactions on signal processing*, 46(6):1688–1694.

Shaver, E. C. and Silliman, B. R. (2017). Time to cash in on positive interactions for coral restoration. *PeerJ*, 2017.

Shimozono, T., Tajima, Y., Kennedy, A. B., Nobuoka, H., Sasaki, J., and Sato, S. (2015). Combined infragravity wave and sea-swell runup over fringing reefs by super typhoon haiyan. *Journal of Geophysical Research: Oceans*, 120(6):4463–4486.

Souter, D., Planes, S., Wicquart, J., Logan, M., David, O., and Staub, F. (2020). Status of coral reefs of the world: 2020 executive summary. *Global Coral Reef Monitoring Network*.

Spalding, M., Burke, L., Wood, S. A., Ashpole, J., Hutchison, J., and zu Ermgassen, P. (2017). Mapping the global value and distribution of coral reef tourism. *Marine Policy*, 82:104–113.

Storlazzi, C. D., Gingerich, S. B., Dongeren, A. V., Cheriton, O. M., Swarzenski, P. W., Quataert, E., Voss, C. I., Field, D. W., Annamalai, H., Piniak, G. A., and McCall, R. (2018). Most atolls will be uninhabitable by the mid-21st century because of sea-level rise exacerbating wave-driven flooding. *Science Advances*, 4.

Storlazzi, C. D., Reguero, B., Cumming, K., Cole, A., Shope, J., L., C. G., Viehman, T., , Nickel, B., and Beck, M. (2021). Rigorously valuing the potential coastal hazard risk reduction provided by coral reef restoration in florida and puerto rico. *U.S. Geological Survey*.

Storlazzi, C. D., Rey, A. E., and van Dongeren, A. R. (2022). A numerical study of geomorphic and oceanographic controls on wave-driven runup on fringing reefs with shore-normal channels. *Journal of Marine Science and Engineering*, 10(6):828.

Swart, D. (1974). Sediment dynamics field experiment: Sunday's river. In *Coastal Engineering 1984*, pages 1371–1385.

Takens, V. (2024). Optimising artificial reef design through large-scale experiments.

van Dongeren, A. (2020). Waves on reefs: How coral reefs transform ocean waves and help protect coasts. *Coastal Engineering Proceedings*.

Van Dongeren, A., Lowe, R., Pomeroy, A., Trang, D. M., Roelvink, D., Symonds, G., and Ranasinghe, R. (2013a). Numerical modeling of low-frequency wave dynamics over a fringing coral reef. *Coastal Engineering*, 73:178–190.

Van Dongeren, A., Lowe, R., Pomeroy, A., Trang, D. M., Roelvink, D., Symonds, G., and Ranasinghe, R. (2013b). Numerical modeling of low-frequency wave dynamics over a fringing coral reef. *Coastal Engineering*, 73:178–190.

Van Gent, M. (1995). Porous flow through rubble-mound material. *Journal of waterway, port, coastal, and ocean engineering*, 121(3):176–181.

van Rooijen, A., Lowe, R., Ghisalberti, M., McCall, R., and Hansen, J. (2022). Modelling wave attenuation through submerged vegetation canopies using a subgrid canopy flow model. *Coastal Engineering*, 176:104153.

van Rooijen, A. A., McCall, R. T., van Thiel de Vries, J. S., van Dongeren, A. R., Reniers, A. J., and Roelvink, J. A. (2016). Modeling the effect of wave-vegetation interaction on wave setup. *Journal of Geophysical Research: Oceans*, 121.

van Wiechen, P. (2020). Wave dissipation on a complex coral reef: an experimental study.

Vetter, O., Becker, J. M., Merrifield, M. A., Pequignet, A.-C., Aucan, J., Boc, S. J., and Pollock, C. E. (2010). Wave setup over a pacific island fringing reef. *Journal of Geophysical Research: Oceans*, 115(C12).

Wang, H. and Sun, Z. (2010). Experimental study of a porous floating breakwater. *Ocean Engineering*, 37(5-6):520–527.

Whitaker, S. (1996). The forchheimer equation: a theoretical development. *Transport in Porous media*, 25(1):27–61.

White, I. and Falkland, T. (2010). Management of freshwater lenses on small pacific islands. *Hydrogeology Journal*, 18.

Young, G., Dey, S., Rogers, A., and Exton, D. (2017). Cost and time-effective method for multi-scale measures of rugosity, fractal dimension, and vector dispersion from coral reef 3d models. *PloS one*, 12(4):e0175341.

A

Lab experiments

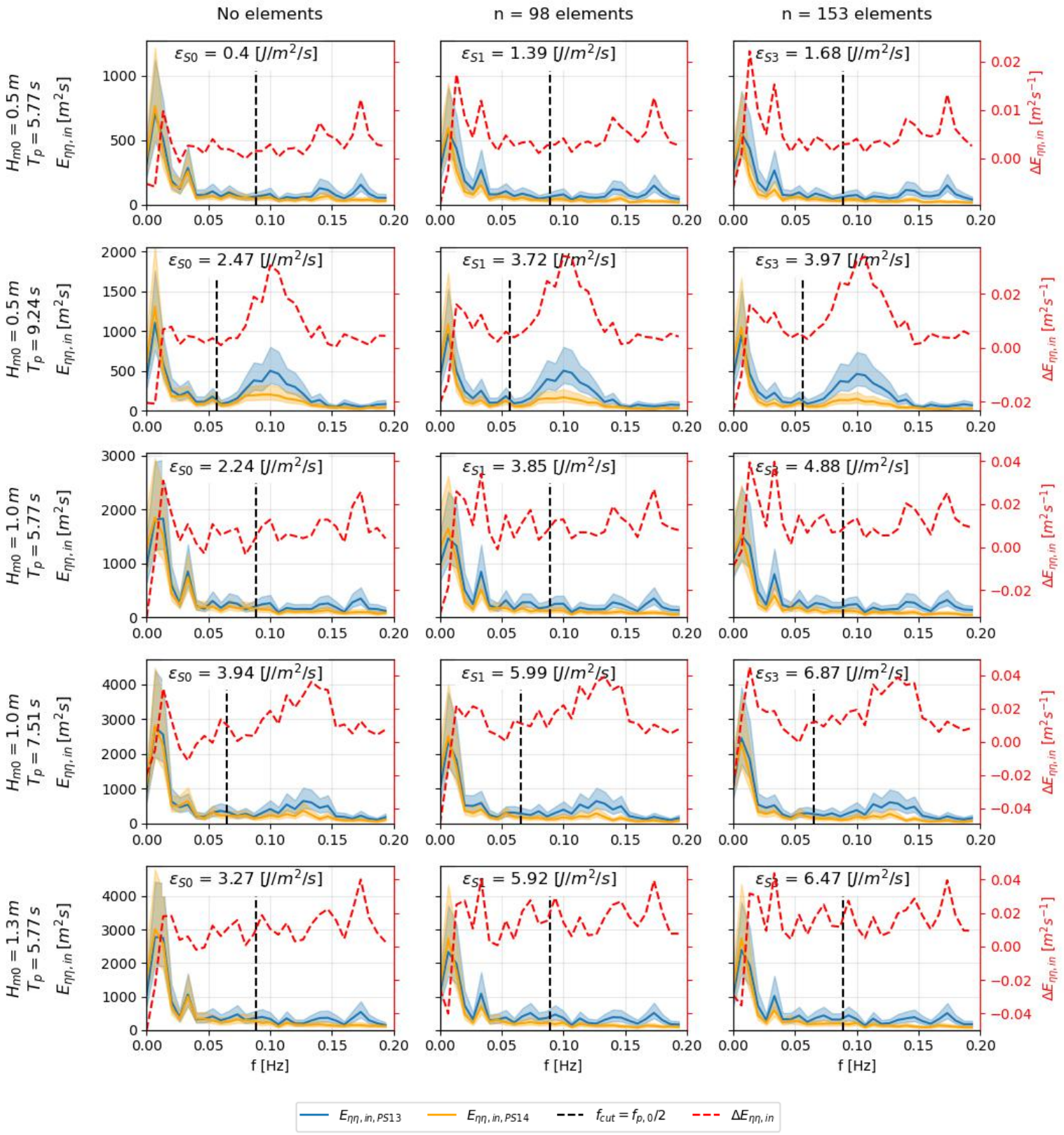

Figure A.1: Incoming wave energy per wave component as measured before (blue $E_{\eta\eta,in,PS13}$) and after (yellow $E_{\eta\eta,in,PS14}$) the artificial reef (for S0, S1 and S3) at **low water level**. The red line is the absolute difference between the flow energy measured offshore and onshore of the artificial reef. Shaded regions denote the 95% confidence intervals of the calculations.

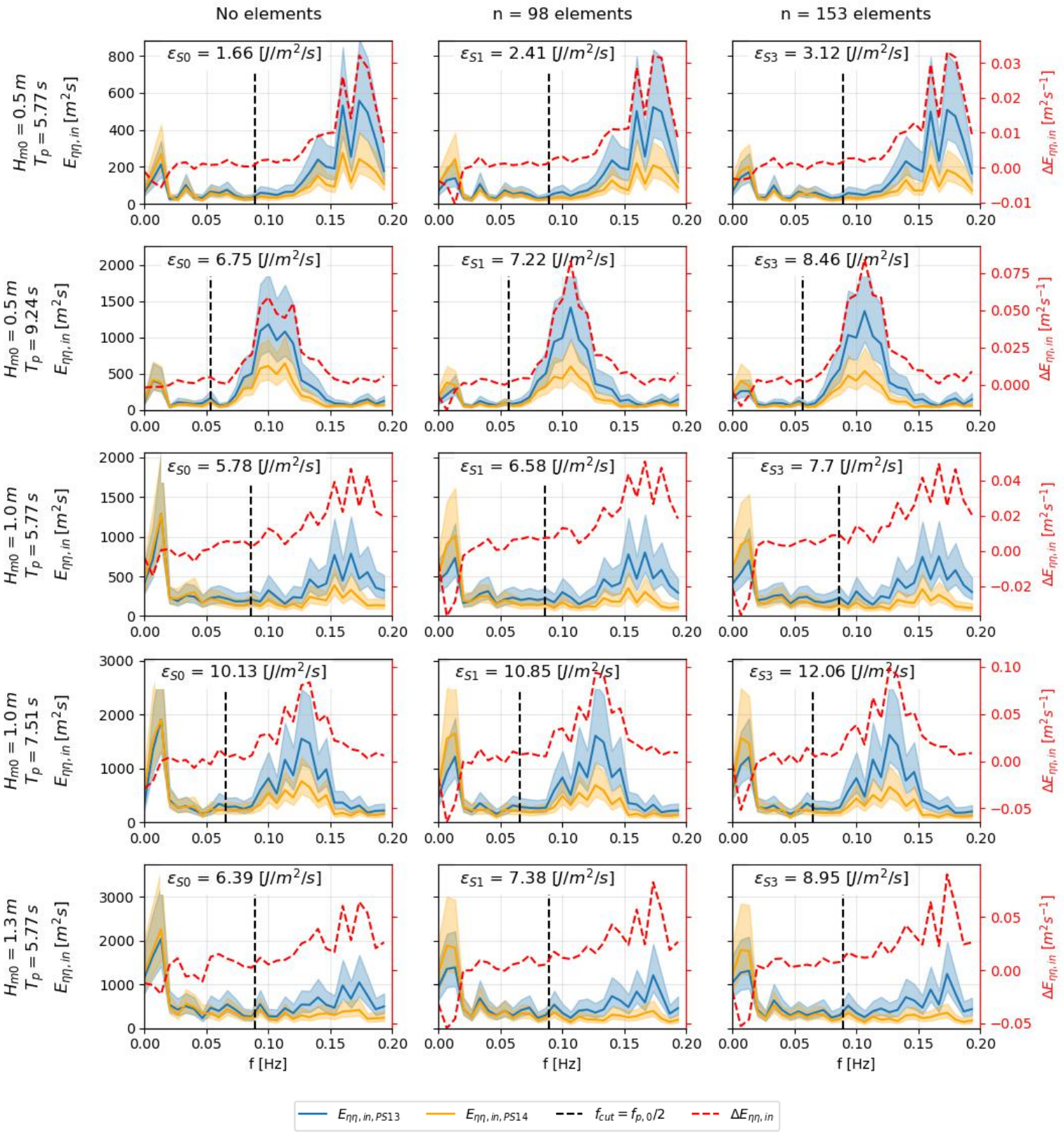

Figure A.2: Incoming wave energy per wave component as measured before (blue $E_{\eta\eta,in,PS13}$) and after (yellow $E_{\eta\eta,in,PS14}$) the artificial reef (for S0, S1 and S3) at **high water level**. The red line is the absolute difference between the flow energy measured offshore and onshore of the artificial reef. Note the increase of SS-wave energy. Shaded regions denote the 95% confidence intervals of the calculations.

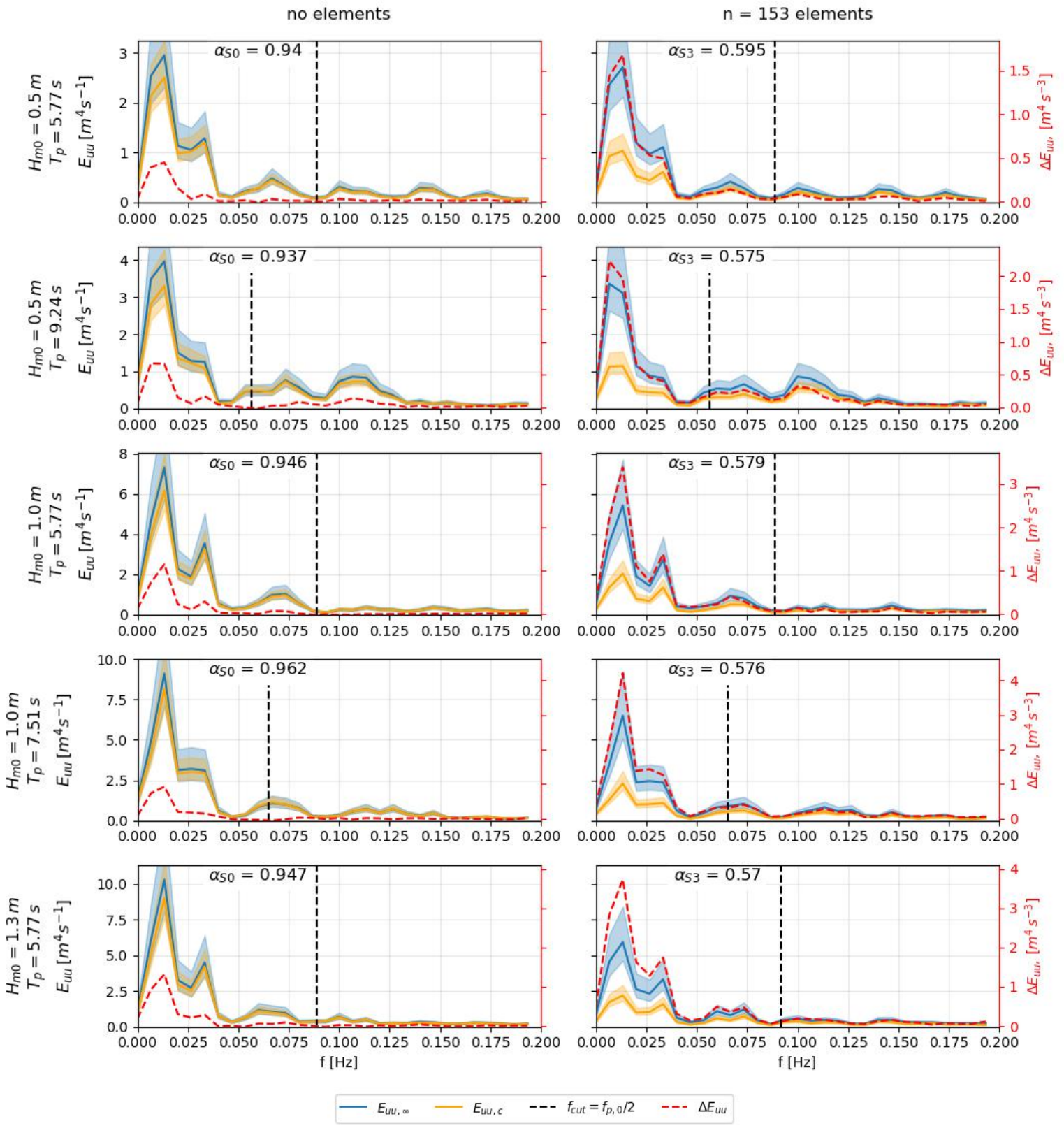

Figure A.3: Flow energy per wave component as measured above (blue $E_{uu,\infty}$) and within (yellow $E_{uu,c}$) the artificial reef canopy (for S0 and S3) during **low water level** runs. The red line is the absolute difference between the flow energy measured above and within the canopy. Shaded regions denote the 95% confidence intervals of the calculations.

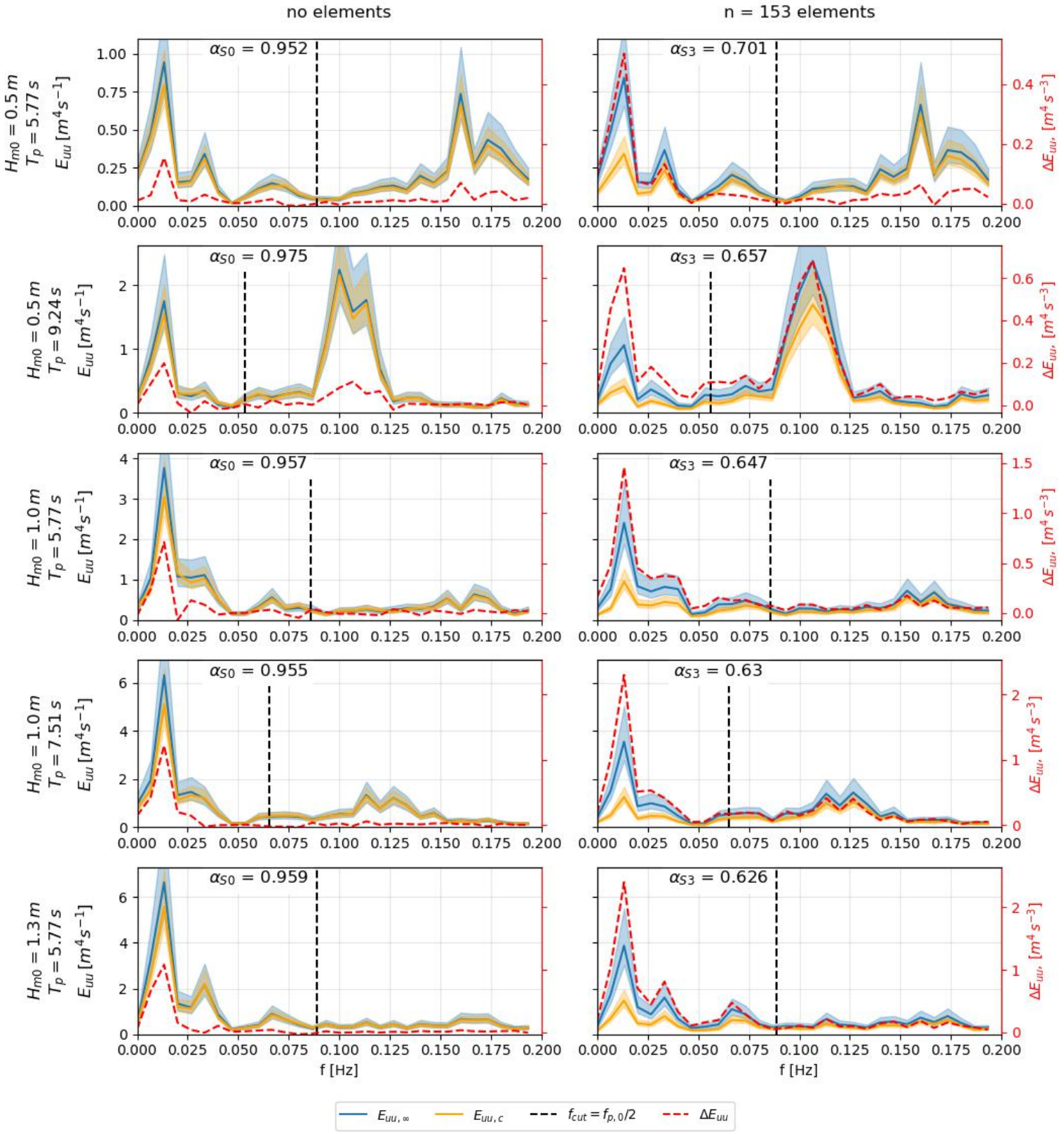

Figure A.4: Flow energy per wave component as measured above (blue $E_{uu,\infty}$) and within (yellow $E_{uu,c}$) the artificial reef canopy (for S0 and S3) during **high water level** runs. The red line is the absolute difference between the flow energy measured above and within the canopy. Shaded regions denote the 95% confidence intervals of the calculations.

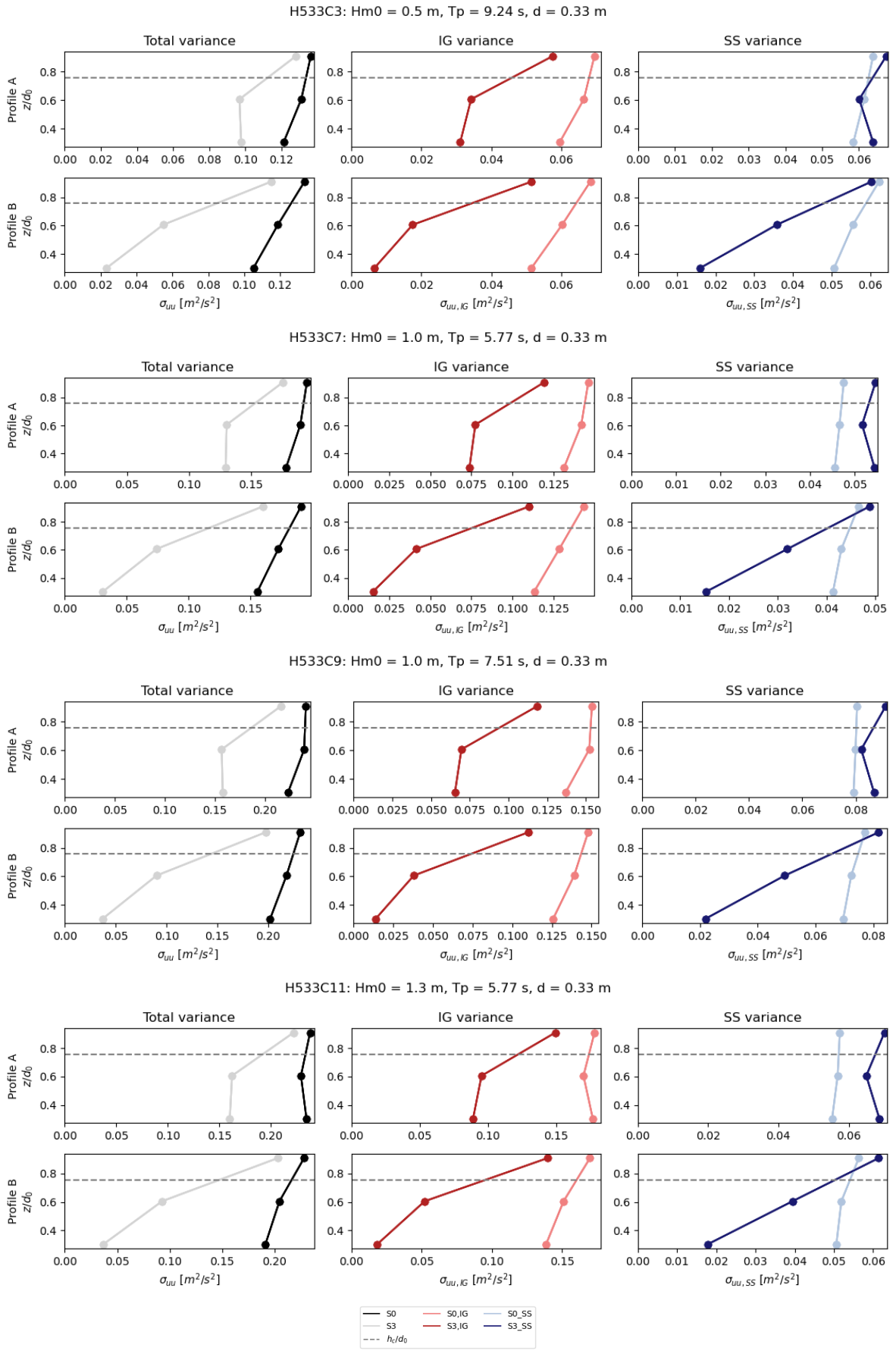

Figure A.5: Velocity profiles as measured by the ADVs, for each measurement point the variance in velocity is shown. The three different columns depict the total, IG and SS velocity profile while the two rows depict the velocity profiles of profile A and B. All the low water case (H533) runs which where not shown in the results sections are shown here.

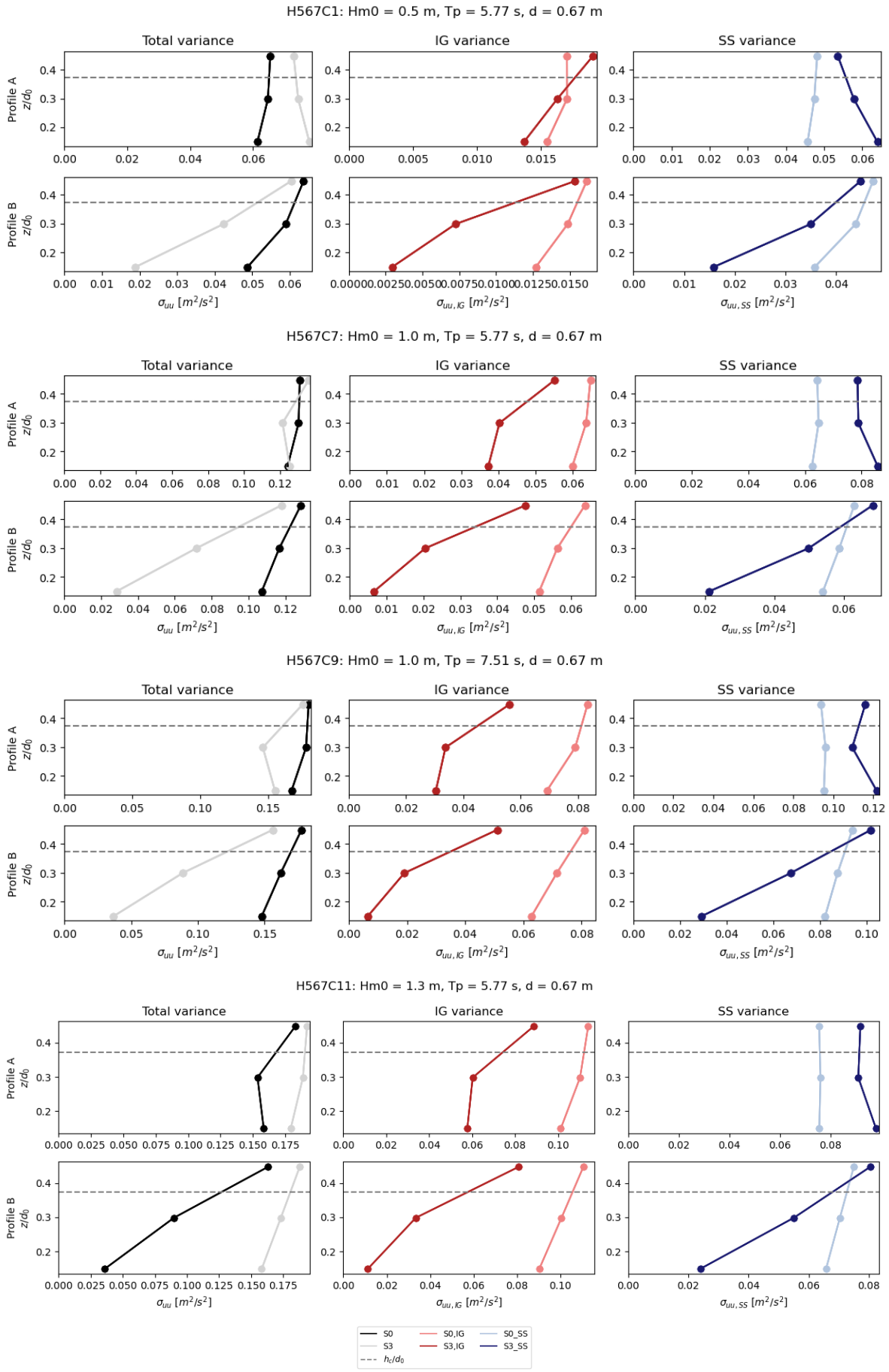

Figure A.6: Velocity profiles as measured by the ADVs, for each measurement point the variance in velocity is shown. The three different columns depict the total, IG and SS velocity profile while the two rows depict the velocity profiles of profile A and B. All the high water case (H567) runs which where not shown in the results sections are shown here.

B

Data processing techniques

B.1. Fast Fourier Transform

The Fast Fourier Transform is performed via the following steps:

1. Clipping and detrending the timeseries:

In the flume experiments, the model is forced by a stationary JONSWAP spectrum. However, as the system has to adapt itself to this forcing, non-stationary conditions can be. This starting up (spin-up time) is removed from the timeseries by removing the first 10 minutes of the timeseries. From this point onward, 40 minutes of sea-surface elevation data are analyzed, ending well before wave generation stops. This approach eliminates the non-stationary adjustment period to still water conditions (spin-down time). Despite the stationary JONSWAP spectrum and removal of spin-up and spin-down time, the timeseries is detrended using a second-order polynomial to remove potential non-stationary artifacts.

2. Splitting up the timeseries in blocks:

The resulting 40-minute timeseries is split into either 16 or 32 blocks of length $nfft$. To improve stability of the FFT, each block shares 50% of its data with its adjacent blocks. The laboratory instruments were sampled at 120 Hz by the Deltares logging system, which is subsampled to 20 Hz for faster data processing. The frequency resolution Δf is determined by the dividing the sample frequency of 20 Hz by the block length: $\Delta f = F_s/nfft$. For 16 and 32 blocks the frequency resolution equals respectively 0.0067 Hz and 0.0134 Hz.

Whereas almost all applications in this thesis are performed with a number of 16 blocks, the plots in which the energy change per wave component is depicted are performed with 32 blocks to get more wave energy within each frequency bin preventing results to be altered too much by for example dividing by a infinitesimally amount of wave energy. In these cases, the amount of blocks used and resulting frequency resolution are specified in the description of the plot.

3. Applying the Hamming window:

To each of these timeseries blocks, a Hamming window is applied by tapering the edges of the timeseries. To do this, the timeseries is multiplied by the Hamming window function, which smoothly reduces the amplitudes within the timeseries near the boundaries of the block to zero. This method maintains a high frequency resolution and reduces artifacts caused by the finite length of the signal while staying computationally efficient.

4. Performing the Fast Fourier Transform:

This Fast Fourier Transform enables to estimate the amplitude per frequency and relies on defining the sea-surface elevation as the sum of harmonic wave components (a Fourier series) with unknown amplitudes a_i and phases α_i as is visualized in Figure B.1:

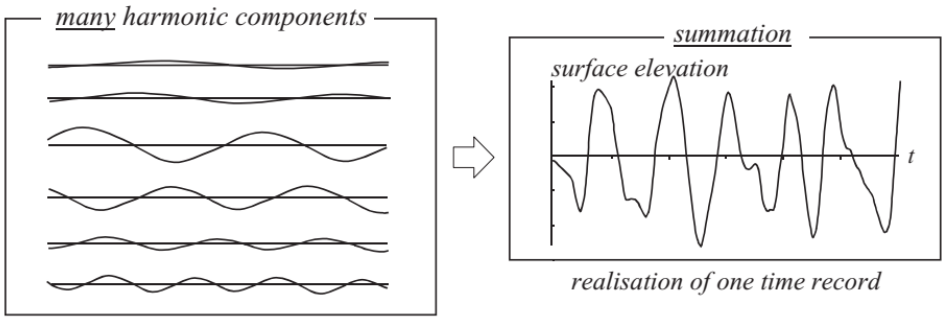

Figure B.1: Summation of many harmonic components with random amplitude and phase results in a surface elevation timeseries as could be acquired from a pressure sensor data in the wave flume.

Performing the Fast Fourier Transform results in either the variance density spectrum of the water level timeseries $E_{\eta\eta}(f)$ $[m^2 \cdot s^{-1}]$ or velocity timeseries $E_{uu}(f)$ $[m^4 \cdot s^{-3}]$, which can be used to compute a variety of wave parameters. The resulting frequency vector is of range $[0, f_N = \frac{F_s}{2}]$, with the maximum frequency being the Nyquist frequency divided by 2. This capped frequency range prevents aliasing and therefore all bulk wave parameters are integrated over this specific range instead of $[0, \infty]$.

B.2. Wave number calculation

To approximate the wave number k, the linear dispersions equation as defined in equation 3.7 is solved iteratively with the Newton-Rhapson method. First of all, an initial guess of kh is computed as:

$$q = \frac{w^2 h}{g \cdot \left(1 - \exp\left(-\left(\frac{w^2 h}{g}\right)^{5/4}\right)\right)^{2/5}} \tag{B.1}$$

which ensures a good starting point for iteration. The Newton-Rhapson method uses the adjustment principle

$$kh_{i+1} = kh_i - \frac{f(kh)}{f'(kh)} \tag{B.2}$$

in which

$$f(kh) = kh \tanh(kh) - \frac{w^2 h}{g} \tag{B.3}$$

$$f'(kh) = \tanh(kh) + kh\left(1 - \tanh^2(kh)\right) \tag{B.4}$$

The method performs two iterations, after which the adjustment between two steps is sufficiently small and kh has converged. The wave number is simply calculated as $k = kh/h$. The absolute error in kh for this method is smaller than 5.0e-16 for all kh.

B.3. Propagation of confidence intervals

The propagation of a confidence interval (CI) when taking the average of its associated variable (Bevington and Robinson, 2003):

$$\begin{aligned} \bar{E} &= \frac{1}{n}\sum_{i=1}^{n} E_i \\ CI_{\bar{E}} &= \frac{\sqrt{\sum_{i=1}^{n} \left(CI_{E_i}\right)^2}}{n} \end{aligned} \tag{B.5}$$

C

Pressure sensor datasets

Table C.1: Original runs for which the surface elevation data acquired by PS13 and PS14 is used to determine energy change and wave dissipation rates over the restoration area.

Configuration	Water level	Wave condition		
ID	ID	ID	Hs [m]	Tp [s]
S0, S1, S2, S3	H533	C1	0.5	5.77
S0, S1, S2, S3	H533	C3	0.5	9.24
S0, S1, S2, S3	H533	C7	1.0	5.77
S0, S1, S2, S3	H533	C9	1.0	7.51
S0, S1, S2, S3	H533	C11	1.3	5.77
S0, S1, S2, S3	H567	C1	0.5	5.77
S0, S1, S2, S3	H567	C3	0.5	9.24
S0, S1, S2, S3	H567	C7	1.0	5.77
S0, S1, S2, S3	H567	C9	1.0	7.51
S0, S1, S2, S3	H567	C11	1.3	5.77

Table C.2: Runs which were repeated, specifically the wave conditions C3, C7 and C11 were repeated. With these extra runs, the general wave transformation and wave reduction can be determined.

Run	Configuration	Water level	Wave condition		
	ID	ID	ID	Hs [m]	Tp [s]
1	S0	H533	C3	0.5	9.24
2	S0	H533	C7	1.0	5.77
3	S0	H533	C11	1.3	5.77
4	S0	H567	C3	0.5	9.24
5	S0	H567	C7	1.0	5.77
6	S0	H567	C11	1.3	5.77
7	S3	H533	C3	0.5	9.24
8	S3	H533	C7	1.0	5.77
9	S3	H567	C11	1.3	5.77
10	S3	H567	C3	0.5	9.24
11	S3	H567	C7	1.0	5.77
12	S3	H567	C11	1.3	5.77

D

ADV results & data quality

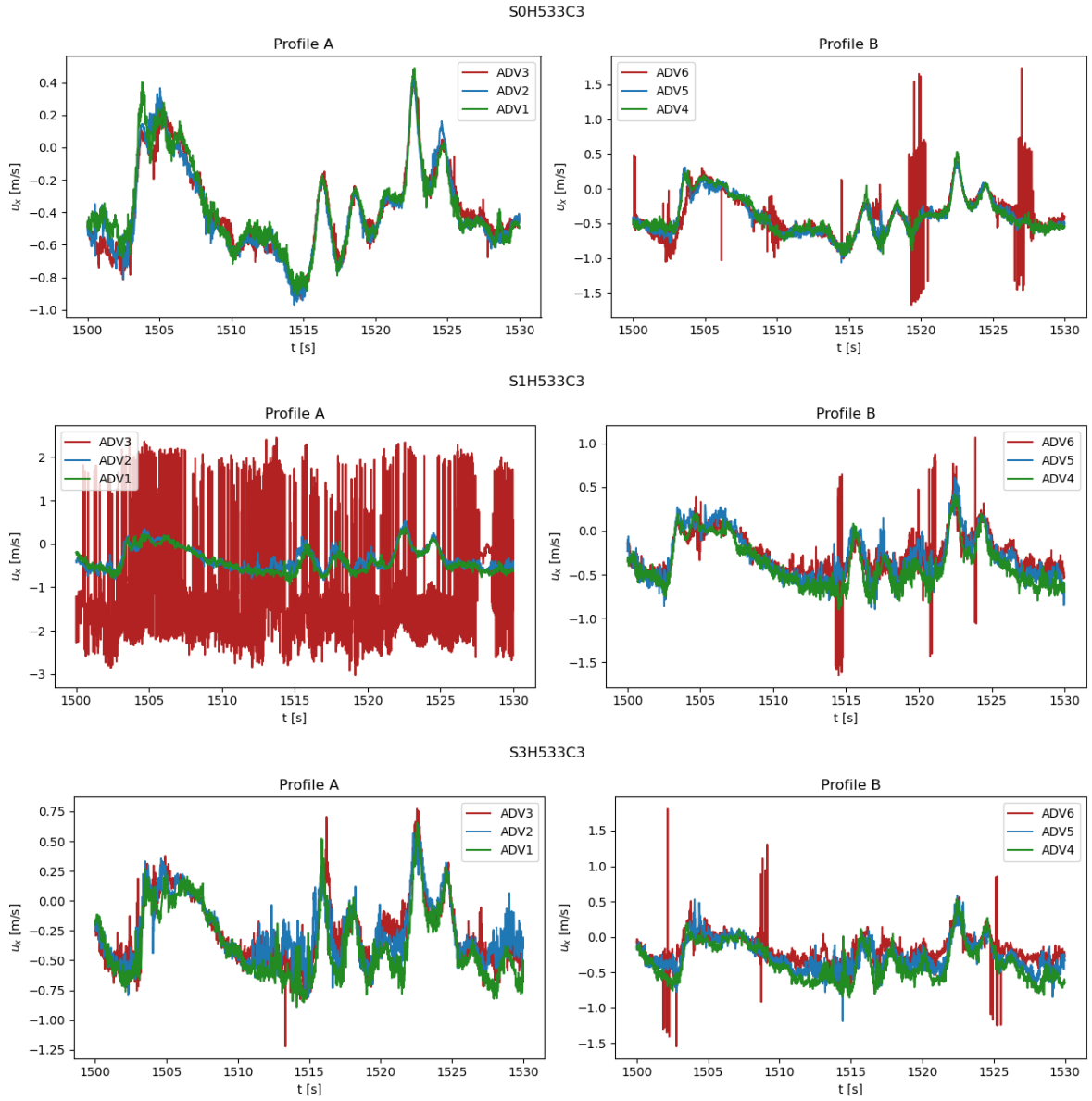

Figure D.1: Snippet of the ADV velocity timeseries as measured during run SxH533C3. Note the erratic behaviour of ADV3 in run S1H533C3 and the lower data quality of ADV3 during the S0H533C3 and S3H533C3 runs.

Table D.1: Overview of the ADV quality metrics as defined in section 3.4.1 for runs SxH533C1.

S0H533C1	outliers [%]	$\sigma^2_{noise}\ [m^2/s^-3]$	$corr._{<70,1}$ [%]	$corr._{<70,2}$ [%]	$\overline{SNR_1}$ [-]	$\overline{SNR_2}$ [-]
ADV1	0.14	0.54	1.59	4.89	29.0	28.8
ADV2	0.11	0.34	0.01	0.02	23.2	25.4
ADV3	0.11	0.42	3.41	1.23	20.9	24.3
ADV4	0.15	0.69	0.25	0.29	23.9	24.1
ADV5	0.09	0.60	0.80	3.31	23.3	23.1
ADV6	0.93	21.78	43.77	0.88	18.8	20.6
S1H533C1	outliers [%]	$\sigma^2_{noise}\ [m^2/s^-3]$	$corr._{<70,1}$ [%]	$corr._{<70,2}$ [%]	$\overline{SNR_1}$ [-]	$\overline{SNR_2}$ [-]
ADV1	0.18	1.31	4.24	7.98	30.1	29.9
ADV2	0.21	1.40	0.96	1.33	23.0	25.1
ADV3	0.00	813.34	5.65	87.96	4.0	0.1
ADV4	0.18	1.65	1.41	2.00	23.8	24.7
ADV5	0.14	2.64	3.59	7.06	22.5	22.4
ADV6	2.21	18.36	57.56	1.96	17.5	19.4
S3H533C1	outliers [%]	$\sigma^2_{noise}\ [m^2/s^-3]$	$corr._{<70,1}$ [%]	$corr._{<70,2}$ [%]	$\overline{SNR_1}$ [-]	$\overline{SNR_2}$ [-]
ADV1	0.18	1.58	2.46	5.28	27.9	26.5
ADV2	0.30	1.79	1.52	1.94	23.2	24.5
ADV3	0.21	1.78	7.66	3.57	10.3	0.4
ADV4	0.22	1.63	1.18	1.83	23.2	23.5
ADV5	0.28	3.01	2.74	5.19	21.9	22.5
ADV6	1.63	6.03	37.52	1.45	1.8	2.0

Table D.2: Overview of the ADV quality metrics as defined in section 3.4.1 for runs SxH533C3.

S0H533C3	outliers [%]	$\sigma^2_{noise}\ [m^2/s^-3]$	$corr._{<70,1}$ [%]	$corr._{<70,2}$ [%]	$\overline{SNR_1}$ [-]	$\overline{SNR_2}$ [-]
ADV1	0.28	1.35	2.45	6.19	27.7	27.4
ADV2	0.24	0.73	0.23	0.29	23.2	24.5
ADV3	0.15	0.75	4.26	1.64	14.9	19.5
ADV4	0.41	1.44	0.82	0.86	23.1	24.1
ADV5	0.21	1.14	1.37	4.27	21.9	21.8
ADV6	2.75	22.90	49.29	0.99	2.3	1.8
S1H533C3	outliers [%]	$\sigma^2_{noise}\ [m^2/s^-3]$	$corr._{<70,1}$ [%]	$corr._{<70,2}$ [%]	$\overline{SNR_1}$ [-]	$\overline{SNR_2}$ [-]
ADV1	0.24	2.13	4.80	8.21	27.5	27.3
ADV2	0.28	2.25	2.09	2.63	23.0	24.3
ADV3	0.00	1445.64	6.74	87.41	4.7	0.4
ADV4	0.33	2.48	2.52	3.00	23.8	24.0
ADV5	0.30	4.07	4.86	7.88	22.5	21.8
ADV6	1.99	9.78	53.57	3.51	17.7	18.9
S3H533C3	outliers [%]	$\sigma^2_{noise}\ [m^2/s^-3]$	$corr._{<70,1}$ [%]	$corr._{<70,2}$ [%]	$\overline{SNR_1}$ [-]	$\overline{SNR_2}$ [-]
ADV1	0.27	2.55	4.58	7.99	27.8	26.5
ADV2	0.30	2.99	3.30	4.23	23.1	24.5
ADV3	0.23	2.72	10.68	5.96	10.0	0.3
ADV4	0.32	2.74	2.98	3.90	23.9	24.2
ADV5	0.29	4.75	5.04	7.68	22.5	21.8
ADV6	1.67	7.30	44.74	3.27	12.1	8.4

Table D.3: Overview of the ADV quality metrics as defined in section 3.4.1 for runs SxH533C7.

S0H533C7	outliers [%]	$\sigma^2_{noise}\ [m^2/s^-3]$	$corr._{<70,1}$ [%]	$corr._{<70,2}$ [%]	$\overline{SNR_1}$ [-]	$\overline{SNR_2}$ [-]
ADV1	0.19	0.97	2.14	5.64	27.8	27.6
ADV2	0.18	0.79	0.23	0.31	23.2	24.5
ADV3	0.12	0.92	4.82	1.80	19.3	22.2
ADV4	0.13	1.06	0.40	0.52	23.2	24.2
ADV5	0.13	1.33	1.45	4.35	21.9	21.8
ADV6	3.01	17.05	42.19	1.09	12.5	8.6
S1H533C7	outliers [%]	$\sigma^2_{noise}\ [m^2/s^-3]$	$corr._{<70,1}$ [%]	$corr._{<70,2}$ [%]	$\overline{SNR_1}$ [-]	$\overline{SNR_2}$ [-]
ADV1	0.21	2.46	5.44	9.14	27.6	26.2
ADV2	0.30	3.05	3.47	4.39	23.0	25.3
ADV3	0.00	3333.04	8.51	78.04	4.5	0.3
ADV4	0.26	2.86	3.01	3.66	23.9	24.1
ADV5	0.45	6.18	7.54	11.68	22.5	22.4
ADV6	1.84	9.17	59.49	4.63	17.5	19.4
S3H533C7	outliers [%]	$\sigma^2_{noise}\ [m^2/s^-3]$	$corr._{<70,1}$ [%]	$corr._{<70,2}$ [%]	$\overline{SNR_1}$ [-]	$\overline{SNR_2}$ [-]
ADV1	0.25	3.10	6.25	10.06	27.8	24.5
ADV2	0.41	3.86	5.36	6.69	23.1	24.5
ADV3	0.28	3.58	13.08	8.45	10.3	0.2
ADV4	0.28	3.31	3.74	5.12	23.2	23.5
ADV5	0.33	6.19	7.12	9.92	21.8	22.5
ADV6	1.58	7.38	48.29	4.95	11.2	6.9

Table D.4: Overview of the ADV quality metrics as defined in section 3.4.1 for runs SxH533C9.

S0H533C9	outliers [%]	$\sigma^2_{noise}\ [m^2/s^-3]$	$corr._{<70,1}$ [%]	$corr._{<70,2}$ [%]	$\overline{SNR_1}$ [-]	$\overline{SNR_2}$ [-]
ADV1	0.56	1.75	2.78	6.28	27.8	27.6
ADV2	0.31	1.23	0.72	0.85	23.2	24.6
ADV3	0.18	1.32	4.4	1.47	16.1	20.6
ADV4	0.49	4.69	1.49	1.67	23.2	24.2
ADV5	0.31	1.93	1.57	3.85	21.9	21.7
ADV6	2.48	11.44	64.66	0.94	1.3	1.9
S1H533C9	outliers [%]	$\sigma^2_{noise}\ [m^2/s^-3]$	$corr._{<70,1}$ [%]	$corr._{<70,2}$ [%]	$\overline{SNR_1}$ [-]	$\overline{SNR_2}$ [-]
ADV1	0.37	3.72	6.33	9.67	29.1	29.0
ADV2	0.43	4.44	5.61	6.70	23.1	24.5
ADV3	0.00	3014.48	9.55	74.31	4.6	0.3
ADV4	0.44	4.42	4.82	5.52	23.9	24.2
ADV5	0.42	6.77	7.57	10.11	22.5	22.4
ADV6	1.22	7.86	56.51	6.34	18.1	18.9
S3H533C9	outliers [%]	$\sigma^2_{noise}\ [m^2/s^-3]$	$corr._{<70,1}$ [%]	$corr._{<70,2}$ [%]	$\overline{SNR_1}$ [-]	$\overline{SNR_2}$ [-]
ADV1	0.35	4.56	8.06	11.63	27.9	26.5
ADV2	0.42	5.36	8.24	10.08	23.1	24.6
ADV3	0.27	4.60	14.20	9.94	10.3	0.3
ADV4	0.37	4.60	5.84	7.00	23.9	24.3
ADV5	0.37	8.11	9.24	12.09	22.5	22.4
ADV6	1.16	7.59	49.18	6.82	11.8	7.7

Table D.5: Overview of the ADV quality metrics as defined in section 3.4.1 for runs SxH533C11.

S0H533C11	outliers [%]	$\sigma^2_{noise}\ [m^2/s^-3]$	$corr._{<70,1}$ [%]	$corr._{<70,2}$ [%]	$\overline{SNR_1}$ [-]	$\overline{SNR_2}$ [-]
ADV1	0.27	1.44	2.32	5.81	27.8	27.5
ADV2	0.22	1.13	0.57	0.71	23.2	24.5
ADV3	0.17	1.31	4.69	2.13	8.8	10.8
ADV4	0.34	3.27	1.17	1.46	23.1	24.2
ADV5	0.38	3.50	1.68	4.92	21.3	21.2
ADV6	3.17	18.50	46.61	1.13	1.6	1.6
S1H533C11	outliers [%]	$\sigma^2_{noise}\ [m^2/s^-3]$	$corr._{<70,1}$ [%]	$corr._{<70,2}$ [%]	$\overline{SNR_1}$ [-]	$\overline{SNR_2}$ [-]
ADV1	0.28	3.45	5.54	8.32	27.9	26.6
ADV2	0.36	4.18	5.50	6.58	23.1	24.5
ADV3	0.00	2248.74	8.87	71.08	4.4	0.2
ADV4	0.32	3.96	4.30	4.54	23.9	24.2
ADV5	0.40	6.77	7.28	9.16	23.2	22.4
ADV6	0.82	6.28	49.11	6.25	18.8	19.4
S3H533C11	outliers [%]	$\sigma^2_{noise}\ [m^2/s^-3]$	$corr._{<70,1}$ [%]	$corr._{<70,2}$ [%]	$\overline{SNR_1}$ [-]	$\overline{SNR_2}$ [-]
ADV1	0.42	4.53	7.49	11.28	27.9	26.5
ADV2	0.50	5.27	8.05	9.68	23.1	24.6
ADV3	0.31	4.46	13.08	8.89	10.4	0.3
ADV4	0.42	4.67	5.67	7.02	23.2	24.3
ADV5	0.40	8.04	8.86	11.38	22.5	22.4
ADV6	0.88	6.96	48.31	6.88	10.0	4.6

Table D.6: Overview of the ADV quality metrics as defined in section 3.4.1 for runs SxH567C1.

S0H567C1	outliers [%]	$\sigma^2_{noise}\ [m^2/s^-3]$	$corr._{<70,1}$ [%]	$corr._{<70,2}$ [%]	$\overline{SNR_1}$ [-]	$\overline{SNR_2}$ [-]
ADV1	0.05	0.48	5.38	10.84	26.7	25.1
ADV2	0.07	0.29	0.01	0.01	23.1	24.1
ADV3	0.32	0.61	6.23	6.49	13.0	17.7
ADV4	0.02	0.43	0.03	0.51	23.0	22.3
ADV5	0.15	0.61	3.12	7.27	20.8	19.5
ADV6	0.72	38.04	48.47	0.65	4.6	1.9
S1H567C1	outliers [%]	$\sigma^2_{noise}\ [m^2/s^-3]$	$corr._{<70,1}$ [%]	$corr._{<70,2}$ [%]	$\overline{SNR_1}$ [-]	$\overline{SNR_2}$ [-]
ADV1	0.07	0.59	3.11	6.66	26.0	24.7
ADV2	0.14	0.75	0.20	0.27	23.1	24.3
ADV3	0.00	672.23	6.83	58.36	4.9	0.5
ADV4	0.19	0.63	0.13	0.16	23.1	24.0
ADV5	0.32	1.59	2.46	5.55	22.5	22.4
ADV6	2.74	12.25	48.11	1.33	7.6	5.0
S3H567C1	outliers [%]	$\sigma^2_{noise}\ [m^2/s^-3]$	$corr._{<70,1}$ [%]	$corr._{<70,2}$ [%]	$\overline{SNR_1}$ [-]	$\overline{SNR_2}$ [-]
ADV1	0.12	0.76	4.16	23.36	27.1	23.6
ADV2	0.19	1.04	0.36	0.47	23.1	24.4
ADV3	0.39	1.66	9.50	5.74	10.1	0.3
ADV4	0.23	0.83	0.29	0.61	23.1	24.1
ADV5	0.49	2.20	2.99	5.96	22.5	22.5
ADV6	2.42	13.66	48.71	2.49	2.0	1.4

Table D.7: Overview of the ADV quality metrics as defined in section 3.4.1 for runs SxH567C3.

S0H567C3	outliers [%]	$\sigma^2_{noise}\ [m^2/s^-3]$	$corr._{<70,1}$ [%]	$corr._{<70,2}$ [%]	$\overline{SNR_1}$ [-]	$\overline{SNR_2}$ [-]
ADV1	0.09	0.73	3.16	6.56	28.7	27.2
ADV2	0.11	0.56	0.07	0.09	23.1	24.4
ADV3	0.40	0.78	8.06	4.41	9.7	0.2
ADV4	0.11	0.69	0.23	0.57	23.1	24.1
ADV5	0.16	0.89	1.62	4.36	22.5	23.2
ADV6	2.27	7.15	41.53	0.24	10.8	7.2
S1H567C3	outliers [%]	$\sigma^2_{noise}\ [m^2/s^-3]$	$corr._{<70,1}$ [%]	$corr._{<70,2}$ [%]	$\overline{SNR_1}$ [-]	$\overline{SNR_2}$ [-]
ADV1	0.08	1.28	2.39	5.22	26.3	24.1
ADV2	0.17	1.75	1.17	1.70	23.1	23.5
ADV3	0.00	1163.90	37.04	31.91	4.9	0.4
ADV4	0.23	1.44	0.84	0.96	23.9	24.1
ADV5	0.30	3.20	3.82	6.95	22.5	22.4
ADV6	1.84	7.99	48.62	3.49	17.0	19.4
S3H567C3	outliers [%]	$\sigma^2_{noise}\ [m^2/s^-3]$	$corr._{<70,1}$ [%]	$corr._{<70,2}$ [%]	$\overline{SNR_1}$ [-]	$\overline{SNR_2}$ [-]
ADV1	0.50	2.02	6.20	15.74	28.5	25.2
ADV2	0.23	2.46	2.49	3.15	23.1	25.3
ADV3	0.31	3.01	12.25	8.48	9.3	0.2
ADV4	0.21	2.05	1.66	2.47	23.9	24.1
ADV5	0.31	4.41	5.95	9.11	23.2	23.1
ADV6	2.29	16.48	42.19	5.02	17.9	20.0

Table D.8: Overview of the ADV quality metrics as defined in section 3.4.1 for runs SxH567C7.

S0H567C7	outliers [%]	$\sigma^2_{noise}\ [m^2/s^-3]$	$corr._{<70,1}$ [%]	$corr._{<70,2}$ [%]	$\overline{SNR_1}$ [-]	$\overline{SNR_2}$ [-]
ADV1	0.09	0.77	0.91	2.84	26.7	24.6
ADV2	0.12	0.72	0.12	0.15	19.9	19.9
ADV3	0.11	0.85	3.60	0.74	7.5	8.1
ADV4	0.07	0.87	0.15	0.23	16.8	15.5
ADV5	0.11	1.15	0.50	2.28	12.8	11.8
ADV6	1.58	3.37	42.27	0.07	2.4	1.8
S1H567C7	outliers [%]	$\sigma^2_{noise}\ [m^2/s^-3]$	$corr._{<70,1}$ [%]	$corr._{<70,2}$ [%]	$\overline{SNR_1}$ [-]	$\overline{SNR_2}$ [-]
ADV1	0.12	1.59	2.91	5.53	25.4	24.2
ADV2	0.17	2.04	1.74	2.36	23.1	23.6
ADV3	0.00	1097.30	7.71	56.16	4.9	0.4
ADV4	0.17	1.69	0.97	1.11	23.9	24.1
ADV5	0.24	3.55	3.49	6.15	22.5	22.4
ADV6	1.81	7.09	47.79	3.23	11.3	8.5
S3H567C7	outliers [%]	$\sigma^2_{noise}\ [m^2/s^-3]$	$corr._{<70,1}$ [%]	$corr._{<70,2}$ [%]	$\overline{SNR_1}$ [-]	$\overline{SNR_2}$ [-]
ADV1	0.28	2.03	5.07	9.87	28.7	26.0
ADV2	0.27	2.61	2.69	3.48	23.1	24.4
ADV3	0.30	3.15	12.59	8.61	10.2	0.3
ADV4	0.21	2.14	1.69	2.48	23.9	24.1
ADV5	0.33	4.49	5.69	8.75	22.5	23.1
ADV6	1.72	14.44	50.85	5.24	3.3	1.6

Table D.9: Overview of the ADV quality metrics as defined in section 3.4.1 for runs SxH567C9.

S0H567C9	outliers [%]	$\sigma^2_{noise}\ [m^2/s^-3]$	$corr._{<70,1}$ [%]	$corr._{<70,2}$ [%]	$\overline{SNR_1}$ [-]	$\overline{SNR_2}$ [-]
ADV1	0.16	1.25	1.24	3.32	27.9	25.5
ADV2	0.15	1.15	0.37	0.46	23.2	24.6
ADV3	0.10	1.21	2.96	1.12	20.3	23.7
ADV4	0.18	1.43	0.67	0.85	23.9	24.2
ADV5	0.13	1.80	0.73	2.30	23.2	23.1
ADV6	1.18	3.40	43.60	0.27	18.8	20.0
S1H567C9	outliers [%]	$\sigma^2_{noise}\ [m^2/s^-3]$	$corr._{<70,1}$ [%]	$corr._{<70,2}$ [%]	$\overline{SNR_1}$ [-]	$\overline{SNR_2}$ [-]
ADV1	0.23	2.57	3.35	5.21	25.6	24.6
ADV2	0.24	3.14	3.77	4.57	22.4	23.7
ADV3	0.00	1430.22	8.21	56.08	4.8	0.4
ADV4	0.23	2.70	2.36	2.60	23.2	23.5
ADV5	0.29	5.24	4.80	6.87	22.5	22.4
ADV6	0.87	5.81	48.96	5.32	11.6	7.4
S3H567C9	outliers [%]	$\sigma^2_{noise}\ [m^2/s^-3]$	$corr._{<70,1}$ [%]	$corr._{<70,2}$ [%]	$\overline{SNR_1}$ [-]	$\overline{SNR_2}$ [-]
ADV1	0.30	3.49	7.04	10.81	29.0	26.3
ADV2	0.40	4.33	6.12	7.45	23.1	24.5
ADV3	0.32	4.29	14.23	9.95	9.7	0.2
ADV4	0.30	3.51	4.03	5.06	23.2	23.5
ADV5	0.36	6.78	7.63	10.35	23.2	23.1
ADV6	1.27	8.03	49.69	6.84	19.2	19.9

Table D.10: Overview of the ADV quality metrics as defined in section 3.4.1 for runs SxH567C11.

S0H567C11	outliers [%]	$\sigma^2_{noise}\ [m^2/s^-3]$	$corr._{<70,1}$ [%]	$corr._{<70,2}$ [%]	$\overline{SNR_1}$ [-]	$\overline{SNR_2}$ [-]
ADV1	0.13	1.14	1.36	3.36	27.8	27.6
ADV2	0.16	1.08	0.34	0.46	23.2	25.4
ADV3	0.11	1.36	3.92	1.66	20.3	22.9
ADV4	0.14	1.24	0.48	0.67	23.9	24.2
ADV5	0.14	1.71	1.08	3.32	22.5	22.4
ADV6	1.79	5.11	47.55	0.37	18.4	19.9
S1H567C11	outliers [%]	$\sigma^2_{noise}\ [m^2/s^-3]$	$corr._{<70,1}$ [%]	$corr._{<70,2}$ [%]	$\overline{SNR_1}$ [-]	$\overline{SNR_2}$ [-]
ADV1	0.16	2.59	3.61	5.88	26.7	25.5
ADV2	0.25	3.29	3.63	4.36	23.1	24.5
ADV3	0.00	1794.84	8.29	63.53	4.7	0.4
ADV4	0.20	2.75	2.41	2.63	23.9	24.2
ADV5	0.29	5.17	4.35	6.17	21.9	22.5
ADV6	0.95	6.11	47.80	4.96	4.0	0.3
S3H567C11	outliers [%]	$\sigma^2_{noise}\ [m^2/s^-3]$	$corr._{<70,1}$ [%]	$corr._{<70,2}$ [%]	$\overline{SNR_1}$ [-]	$\overline{SNR_2}$ [-]
ADV1	0.23	3.41	6.34	10.08	27.8	26.4
ADV2	0.41	4.24	5.93	7.15	23.1	24.5
ADV3	0.24	4.37	13.95	9.74	10.3	0.4
ADV4	0.21	3.37	3.66	4.71	23.2	23.5
ADV5	0.37	6.88	7.61	10.49	22.5	22.5
ADV6	1.27	9.79	49.80	6.93	2.3	1.7

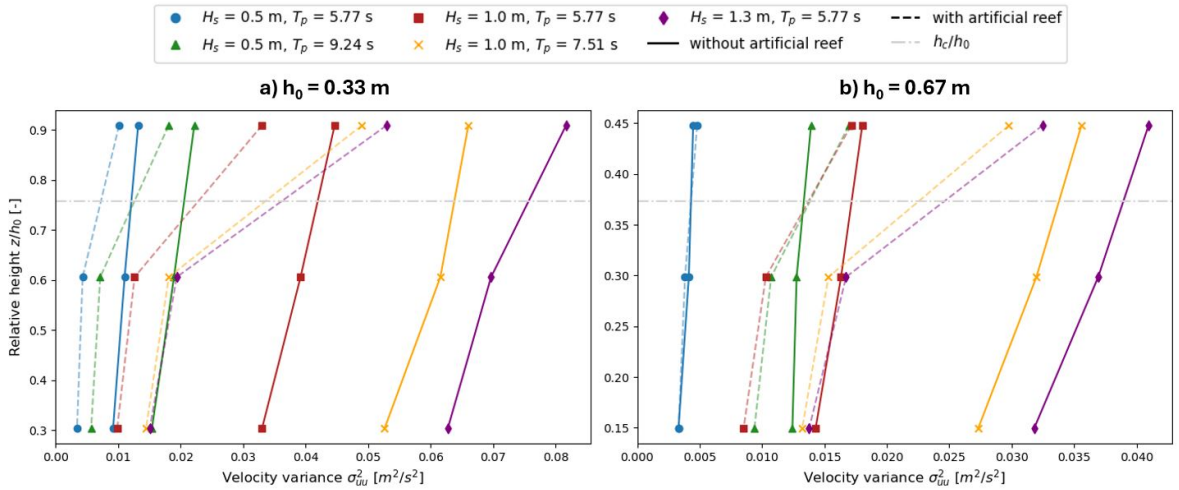

Figure D.2: Velocity profiles for all wave conditions with on the left the low water case and right the high water case. The variances are determined by averaging the variance of two ADVs at the same height. The solid lines depict the velocity profiles without artificial reef while the dashed lines depict the velocity profiles with artificial reef.

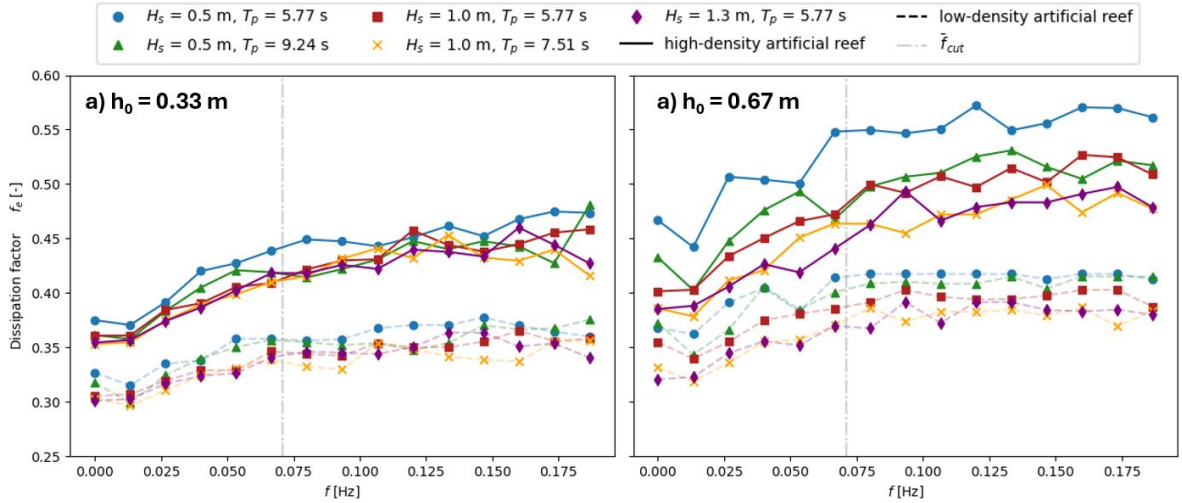

Figure D.3: Dissipation factor per wave component indicating to which extent a wave component is affected by the artificial reef. Panel a) shows the dissipation factors for the low water case, while Panel b) presents them for the high water case.

Table D.11: The ratios of Arms/S and intermediate steps in the calculation of this ratio. Note the large difference between Tm01 and Tm-1.0 and its effect on the Arms/S ratio

Run ID	Spacing	U_∞^{rms}	T_{m01}	$A_\infty^{rms}\ (T_{m01})$	$A_\infty^{rms}/S\ (T_{m01})$	$T_{m-1.0}$	$A_\infty^{rms}\ (T_{m-1.0})$	$A_\infty^{rms}/S\ (T_{m-1.0})$
S1H533C1	0.42	0.33	5.75	0.31	0.74	108.18	5.844	13.91
S1H533C3	0.42	0.38	7.20	0.45	1.06	256.91	15.930	37.93
S1H533C7	0.42	0.45	8.12	0.59	1.40	173.26	12.559	29.90
S1H533C9	0.42	0.49	8.64	0.69	1.64	325.80	26.033	61.98
S1H533C11	0.42	0.50	8.41	0.68	1.61	184.49	14.862	35.38
S1H567C1	0.42	0.27	3.91	0.18	0.42	38.29	1.725	4.11
S1H567C3	0.42	0.34	5.76	0.32	0.76	99.77	5.550	13.21
S1H567C7	0.42	0.37	5.70	0.35	0.83	88.06	5.371	12.79
S1H567C9	0.42	0.44	6.70	0.48	1.13	180.51	12.837	30.56
S1H567C11	0.42	0.45	6.69	0.49	1.16	114.90	8.351	19.88
S3H533C1	0.27	0.33	5.78	0.31	1.16	111.61	6.064	22.46
S3H533C3	0.27	0.38	7.16	0.44	1.63	261.63	16.103	59.64
S3H533C7	0.27	0.44	7.76	0.55	2.05	163.12	11.610	42.99
S3H533C9	0.27	0.48	8.12	0.64	2.36	297.53	23.331	86.41
S3H533C11	0.27	0.49	7.92	0.63	2.33	167.16	13.278	49.18
S3H567C1	0.27	0.27	3.90	0.18	0.66	37.75	1.726	6.39
S3H567C3	0.27	0.35	5.60	0.32	1.17	94.40	5.347	19.80
S3H567C7	0.27	0.37	5.44	0.34	1.24	80.48	4.956	18.36
S3H567C9	0.27	0.43	6.34	0.45	1.65	155.31	10.923	40.46
S3H567C11	0.27	0.44	6.33	0.45	1.68	102.77	7.354	27.23

E

Energy decrease and flow attenuation per wave component

E.1. Wave energy decrease across artificial reef per wave component

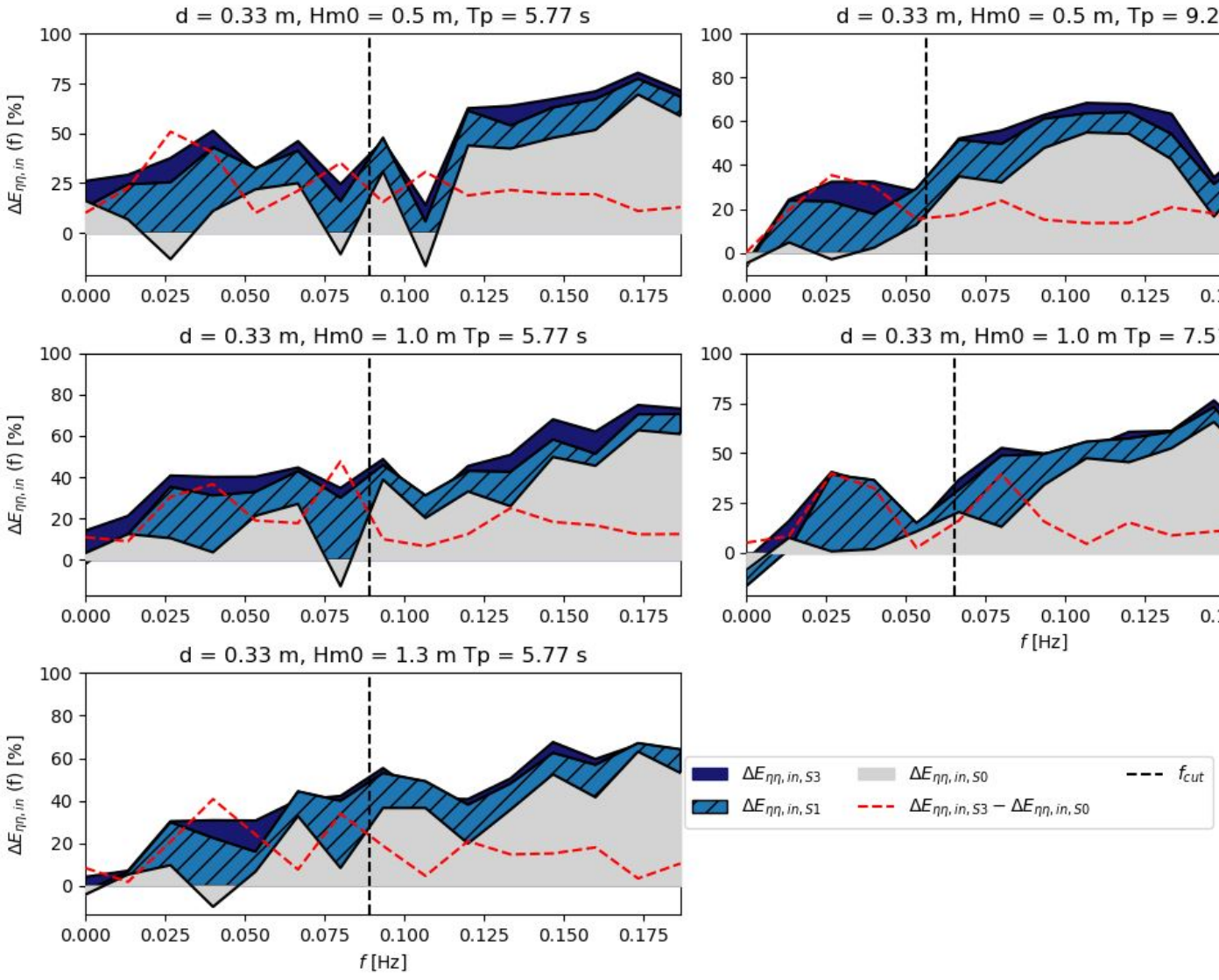

Figure E.1: Energy change per wave component as observed over the artificial for all wave conditions, for the **low water level** runs. Note that the percentages of energy changes are layered over each other. By visualizing this way, the grey area is the initial energy change during the bare reef case and the added blue area is the energy change added by introducing the artificial reef elements.

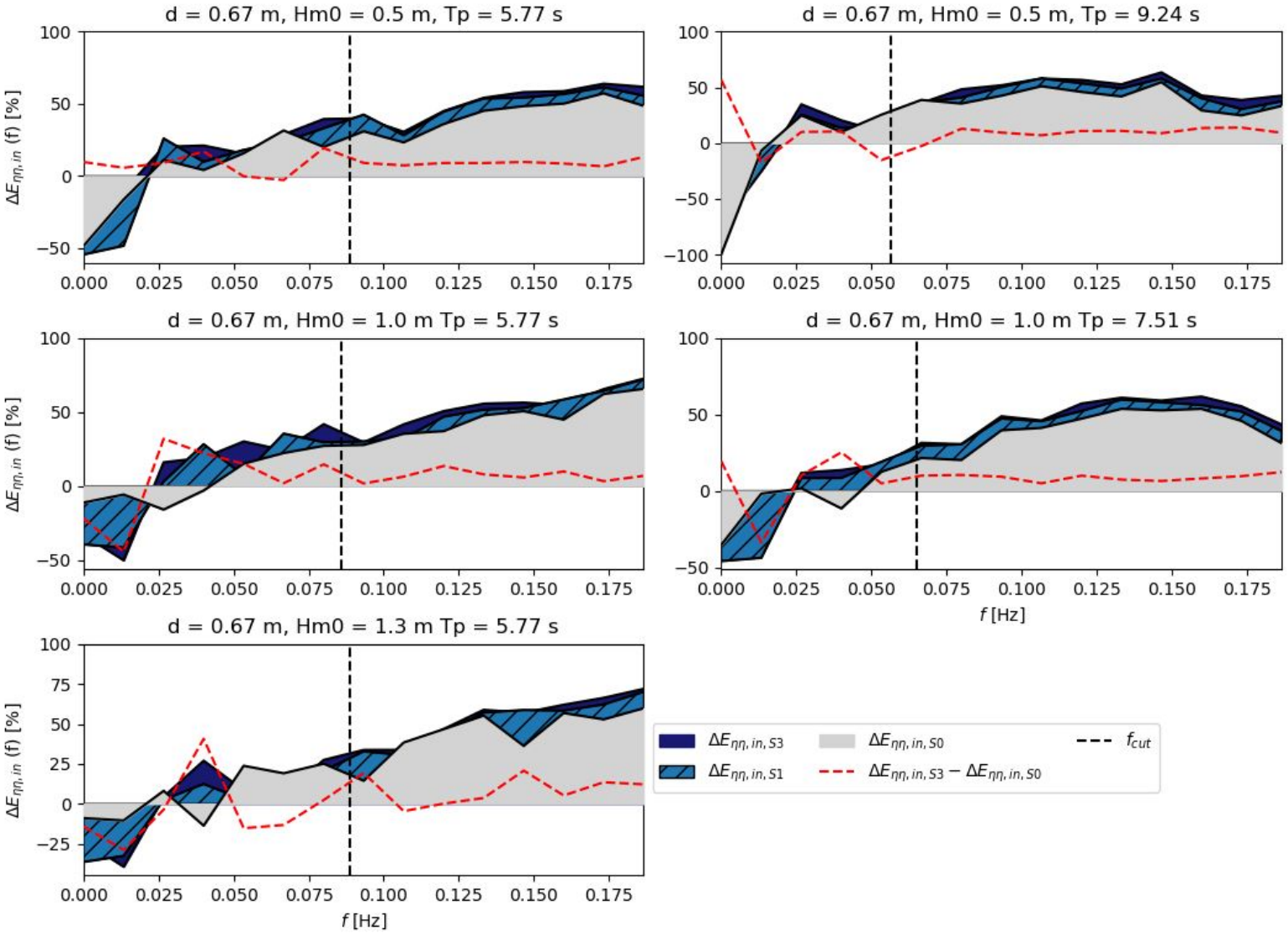

Figure E.2: Energy change per wave component as observed over the artificial for all wave conditions, for the **high water level** runs. Note that the percentages of energy changes are layered over each other. By visualizing this way, the grey area is the initial energy change during the bare reef case and the added blue area is the energy change added by introducing the artificial reef elements.

E.2. Flow attenuation per wave component

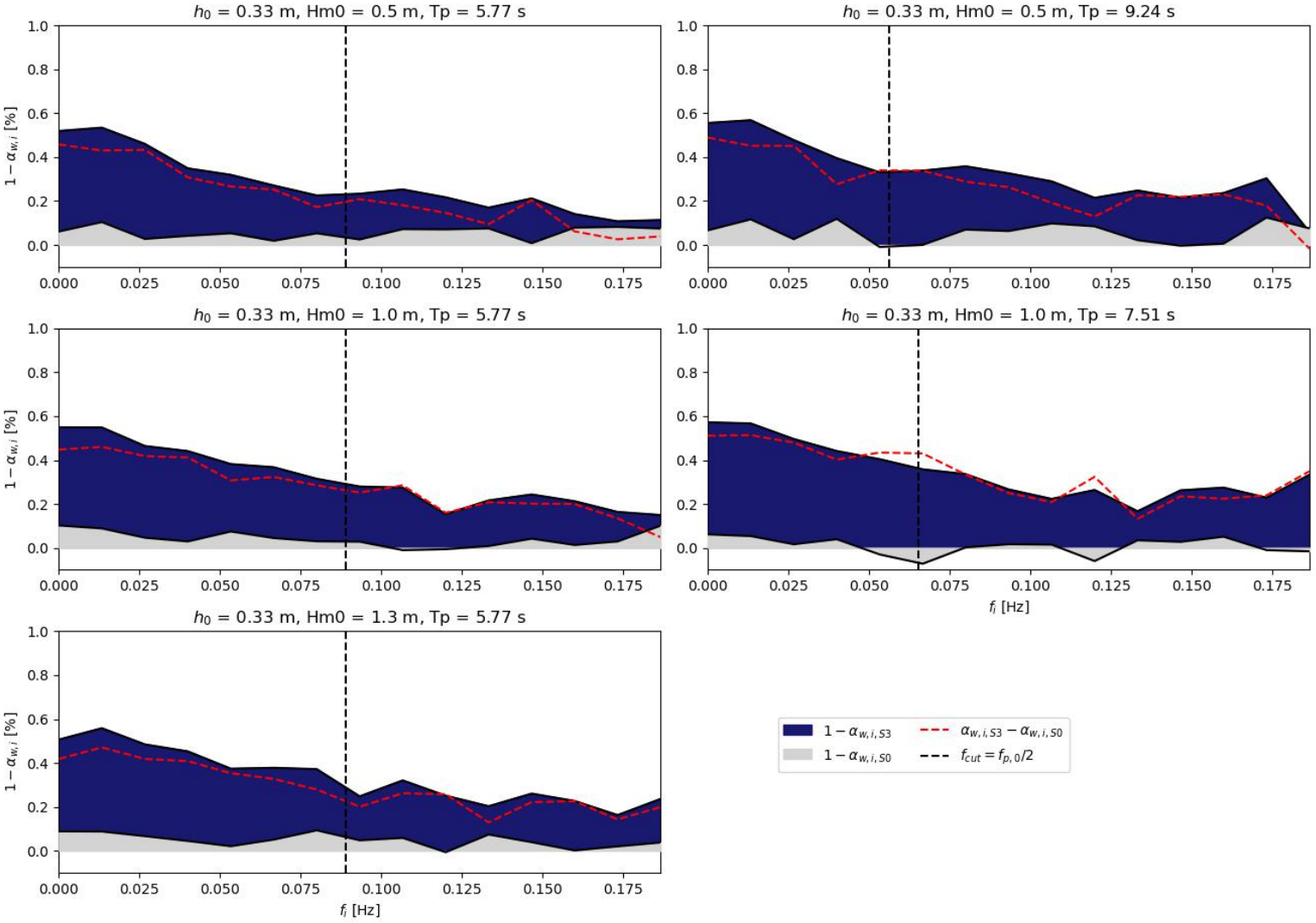

Figure E.3: Energy change per wave component as observed comparing the free-stream and in-canopy energy (**reprented by the four bottom ADVs**) for all wave conditions, for the high water level case. Note that the percentages of energy changes are layered over each other. By visualizing this way, the grey area is the initial energy change due to bottom friction and the added blue area is the energy change added by introducing the artificial reef elements. Higher values mean that less wave energy is able to penetrate into the canopy. The red line depicts the increased flow attenuation by placing the artificial reef elements.

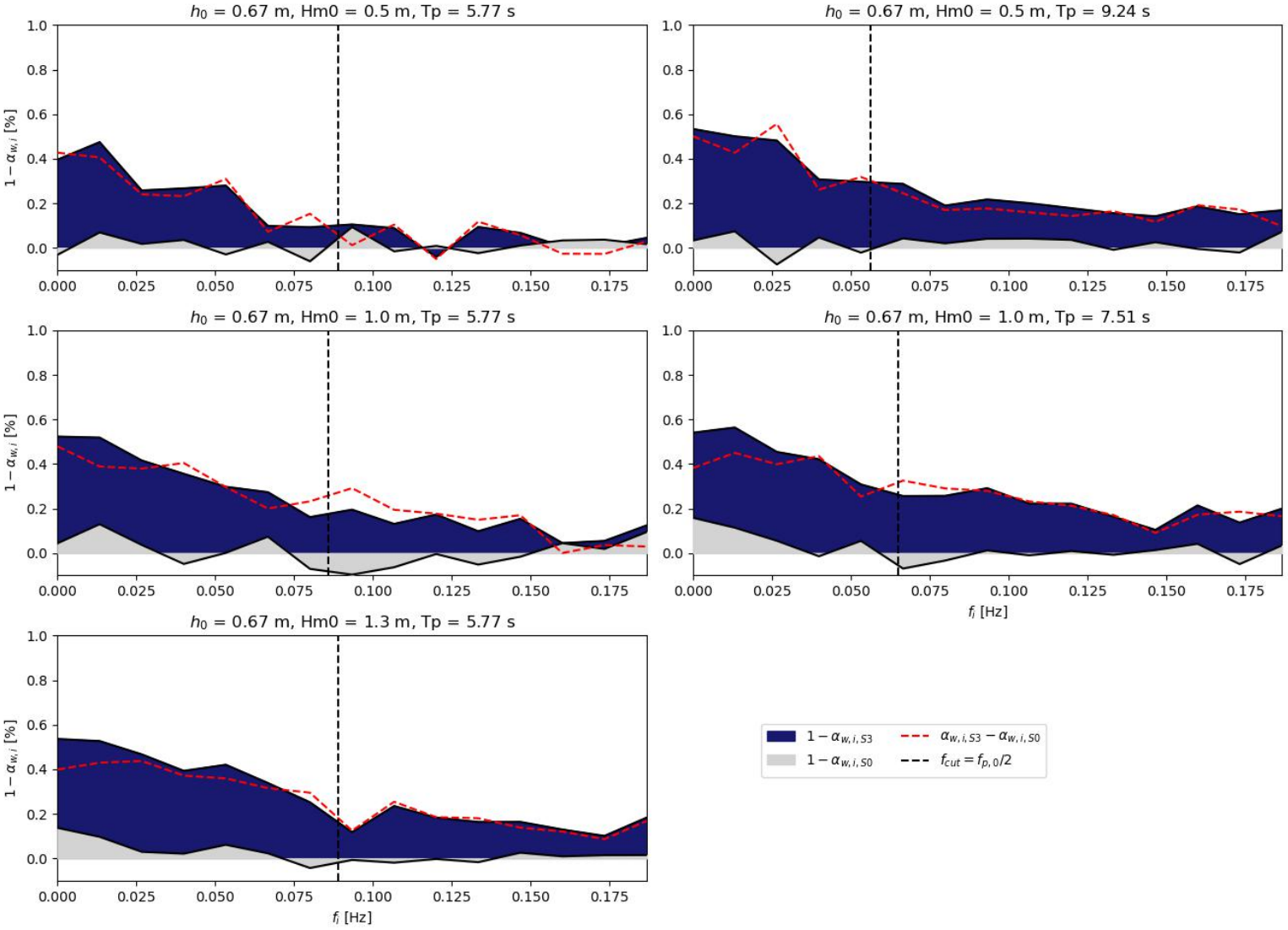

Figure E.4: Energy change per wave component as observed comparing the free-stream and in-canopy (**reprented by the four bottom ADVs**) energy for all wave conditions, for the low water level case. Note that the percentages of energy changes are layered over each other. By visualizing this way, the grey area is the initial energy change due to bottom friction and the added blue area is the energy change added by introducing the artificial reef elements. Higher values mean that less wave energy is able to penetrate into the canopy. The red line depicts the increased flow attenuation by placing the artificial reef elements.

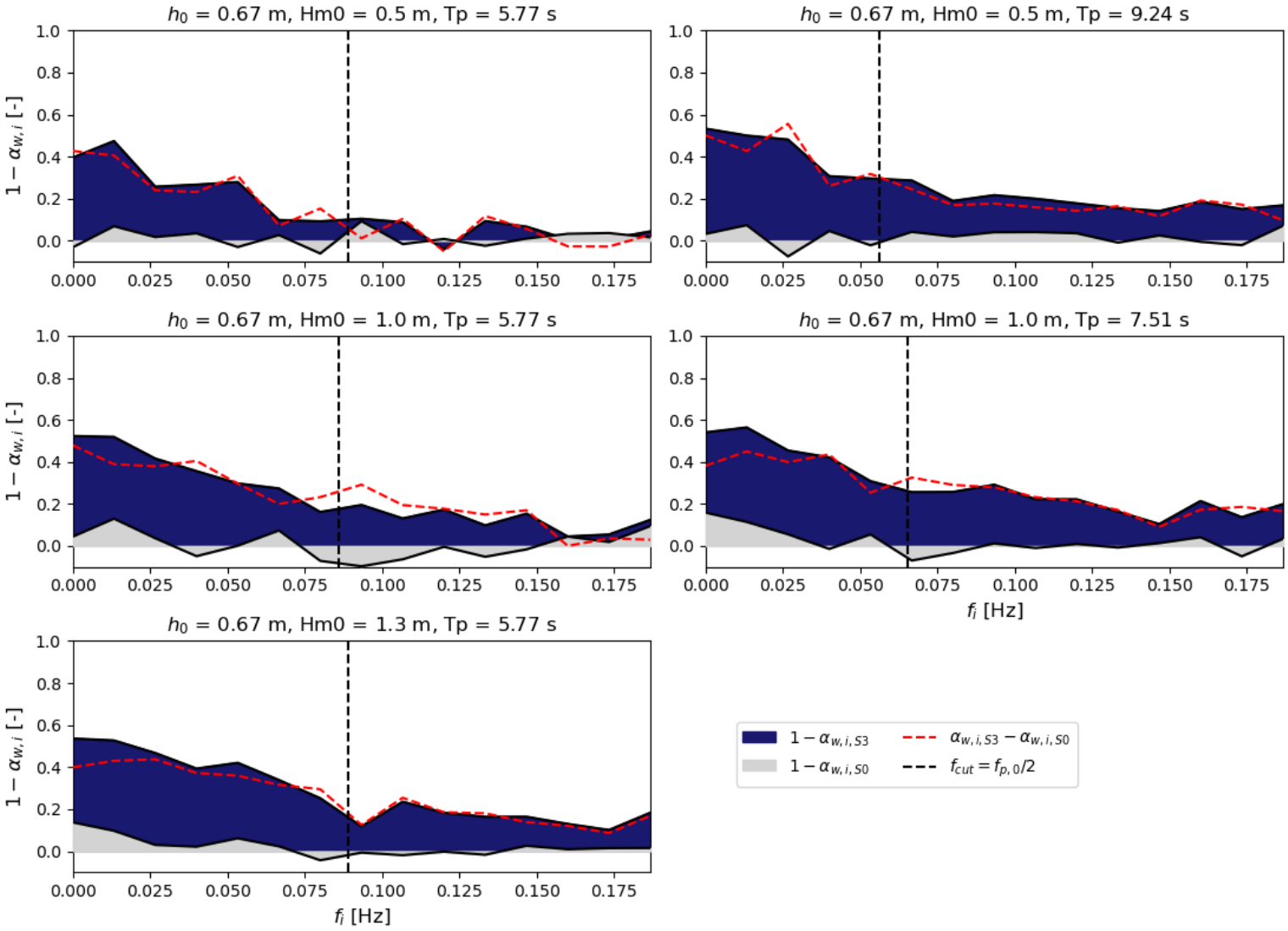

Figure E.5: Energy change per wave component as observed comparing the free-stream flow and in-canopy flow (**reprented by the two middle ADVs**) energy for all wave conditions, for the high water level case. Note that the percentages of energy changes are layered over each other. By visualizing this way, the grey area is the initial energy change due to bottom friction and the added blue area is the energy change added by introducing the artificial reef elements. Higher values mean that less wave energy is able to penetrate into the canopy. The red line depicts the increased flow attenuation by placing the artificial reef elements.

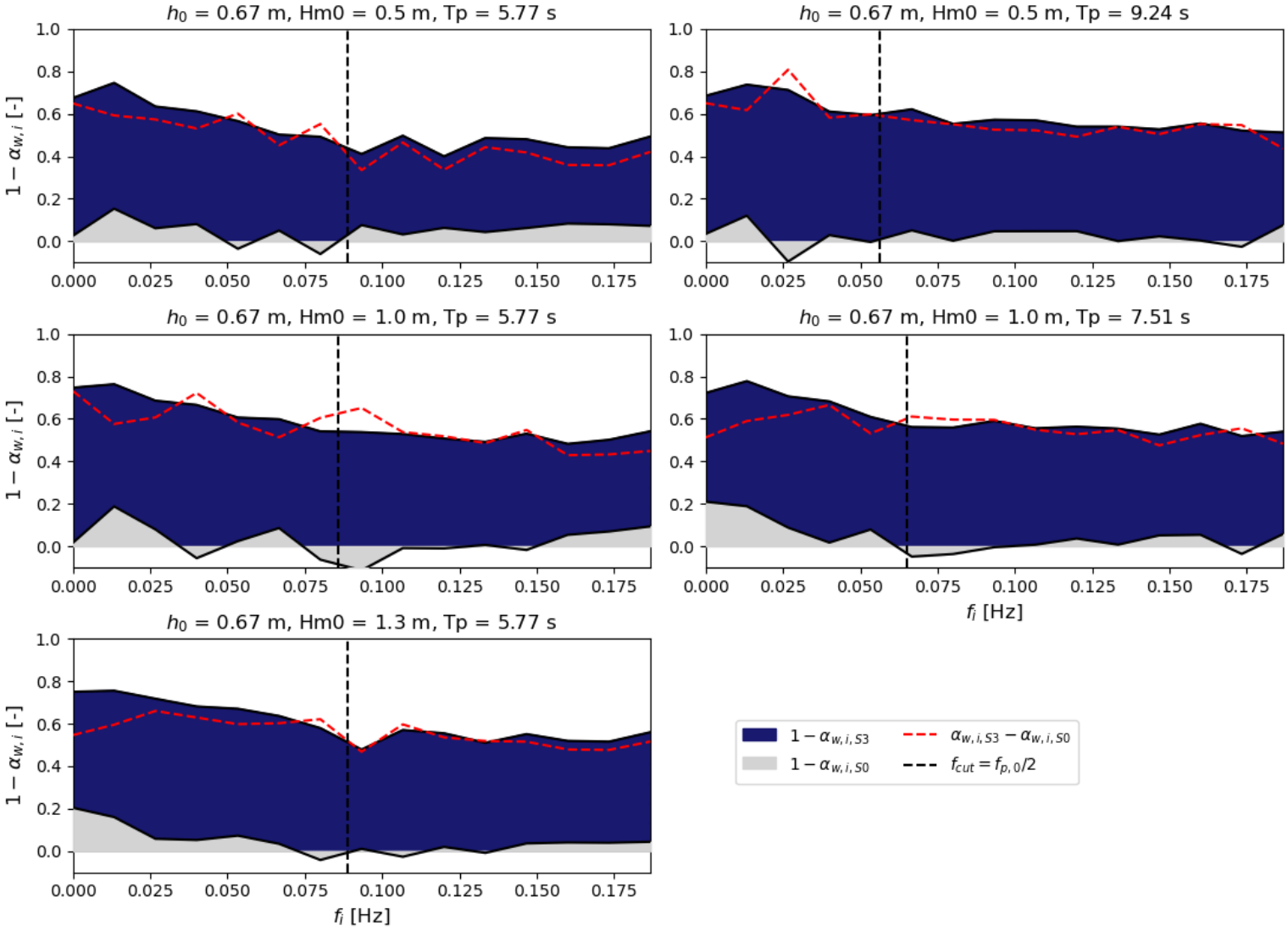

Figure E.6: Energy change per wave component as observed comparing the free-stream flow and in-canopy flow (**reprented by the four middle ADVs but with a convergence correction applied**) energy for all wave conditions, for the high water level case. Note that the percentages of energy changes are layered over each other. By visualizing this way, the grey area is the initial energy change due to bottom friction and the added blue area is the energy change added by introducing the artificial reef elements. Higher values mean that less wave energy is able to penetrate into the canopy. The red line depicts the increased flow attenuation by placing the artificial reef elements.